Three-photon microscopy : instrumentation and extension of the observable parameters

Júlia Ferrer Ortas

INSTITUT POLYTECHNIQUE DE PARIS

NNT: 2021IPPAX134

Thèse de doctorat

ÉCOLE POLYTECHNIQUE

IP PARIS

Three-photon microscopy: instrumentation and extension of the observable parameters

Thèse de doctorat de l'Institut polytechnique de Paris
préparée à École polytechnique

École doctorale n°626 : École doctorale
de l'Institut polytechnique de Paris (EDIPP)
Spécialité de doctorat: Physique

Thèse présentée et soutenue à Palaiseau, le 16 décembre 2021, par

Júlia FERRER ORTAS

Composition du Jury :

Patricia SEGONDS Prof. Univ. Grenoble-Alpes, Institut Néel	Présidente du jury
Valentina EMILIANI DR CNRS, Institut de la Vision, Paris	Rapporteuse
Cathie VENTALON CR CNRS, IBENS, Paris	Rapporteuse
Martin OHEIM DR CNRS, INPP, Paris	Examinateur
Emmanuel BEAUREPAIRE DR CNRS, LOB, Palaiseau	Co-directeur de thèse
Willy SUPATTO DR CNRS, LOB, Palaiseau	Co-directeur de thèse

Funding

Cette thèse a été financée par les institutions suivantes :

Elle a débuté à l'école doctorale *Interfaces* de l'Université Paris-Saclay. Polytech Paris-Saclay est l'institution où j'ai effectué ma mission d'enseignement.

Le Laboratoire d'Optique et Biosciences a été l'unité d'accueil.

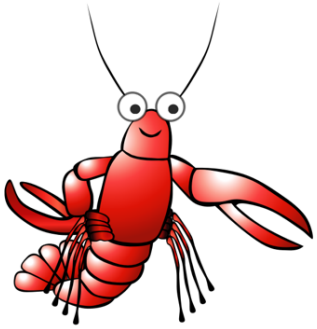

Acknowledgements

Plus de quatre ans de ma vie se sont écoulés ici entre lasers, poissons, manips, couleurs, sourires, lumières, photons... et aussi quelques larmes. Cette richissime explosion d'expériences a été possible uniquement car j'ai eu la chance d'interagir, travailler, discuter, réfléchir, vivre, cuisiner, chanter ou danser avec des personnes merveilleuses que je vais tâcher de remercier comme elles le méritent.

En premier lieu, je tiens à remercier les membres du jury de ma thèse. Merci à Cathie Ventalon et à Valentina Emiliani d'avoir lu de manière détaillée mon manuscrit et d'en avoir réalisé des rapports avec soin. Merci également à Cathie d'avoir fait partie de mon comité de suivi et d'avoir été aussi bienveillante durant toutes nos interactions. Merci aussi à Martin Oheim et Patricia Segonds d'avoir participé en tant qu'examinateurs et présidente. Merci à tous de l'intérêt montré pour mon travail et des riches discussions qui ont eu lieu. Je vous remercie aussi d'avoir rendu possible une soutenance en présentielle.

Rien n'aurait été pareil sans mes deux directeurs de thèse: Emmanuel et Willy. Ça a été une énorme chance de vous avoir et de travailler avec vous, je ressens une immense gratitude envers tout ce que j'ai reçu. Merci de votre soutien incessant, de votre aide et de votre enthousiasme. Willy, merci de ta rigueur, ton honnêteté et ta vision perspicace. Merci de ton temps et de ta patience pendant les semaines de correction du manuscrit. Merci de ne pas avoir lâché le moindre détail, la moindre précision ou la moindre opportunité de m'apprendre les secrets de la rédaction, à la fois les plus pertinents mais aussi les plus alcoolisés. Merci de ton équilibre et de ton exemple. Merci aussi d'avoir organisé les lab meetings et d'avoir fait l'effort de rendre possible ces échanges précieux même lors des différents confinements. Emmanuel, ou le sheriff au regard bleu profond, merci de m'avoir embarquée dans cette aventure multicouleur. Merci de ta sagesse, de ta patience, de ton calme, de ta confiance, de ton respect, de ton imagination et de ton humour qui m'auront accompagnée toutes ces journées. Merci d'avoir éclairé mon travail avec ton intuition fine et aussi avec la lumière de mon bureau en partant le soir. Merci d'avoir su me motiver, m'encourager et de m'avoir poussée à sortir le meilleur de moi-même. Merci pour tout ce que tu m'as appris, et pour toutes ces discussions scientifiques et non scientifiques. Merci également pour tes chocolats, tes nougats, tes croissants et tes salades de fruits. Ça a été un vrai plaisir.

On ne peut pas imaginer aujourd'hui faire de la recherche sans établir des collaborations. J'aimerais donc remercier toutes les personnes avec qui j'ai travaillé et qui, même si elles ne font pas partie de l'équipe, ont été d'une importance cruciale pour mes travaux. Merci à Frédéric Druon et Khmaies Guesmi (de l'équipe Lasers à l'Institut d'Optique) pour leur travail sur le premier prototype OPA et merci également à Alexandre Thai et Michele Natile (d'Amplitude) pour leur aide avec les prototypes qui ont suivi. Merci à Jean Livet,

Takuma Kumamoto et Mickaël Le (de l'Institut de la Vision), qui m'auront fourni inlassablement des échantillons arc-en-ciel. Merci aussi à l'intrépide Nicolas Dray (de l'Institut Pasteur) qui n'a pas eu peur de venir plonger avec des bouteilles d'azote dans notre salle de manip. Thanks also to Gert-Jan (Radbound University) for a very intense but fruitful experiments week.

Touts ces beaux moments ont été accompagnés par la bienveillance de l'ensemble des permanent.e.s du pôle *Microscopies Avancées* (et invités), qui ont joué le rôle d'une vraie famille lors de mon passage au LOB. Je remercie Pierre, le héros de l'optique; Marie-Claire, la reine du collagène et des chats lasséristiques; Gaël, à la sensibilité et l'écoute exceptionnelles; Nicolas O. et Debora, qui m'ont fourni en mangue séchée pendant toute ma rédaction et pour la relecture du Chapitre 3; Chiara, Anatole, Nicolas D., Guilhem et Karsten, à la ponctualité métronomique toujours accompagnée d'une chanson jolie mais pas trop joyeuse. Un merci spécial à Marie-Claire et Nicolas D. pour leur courageux travail à l'école doctoral de l'IPP (excellentissime institution dont, par hasard, l'acronyme se lit en anglais comme la phrase "Hay pipí" en espagnol). D'autres permanent.e.s du LOB ont également participé soit à mon travail, soit à mon bonheur. Un énorme merci tout d'abord à François Hache, qui a fait un travail exemplaire en tant que directeur du LOB pendant la durée de ma thèse. Avec ses magiques qualités scientifiques et humaines, il a su guider ce laboratoire pour tirer le meilleur de chacun. Je le remercie aussi pour ses efforts en tant que directeur de l'école doctorale Interfaces au début de ma thèse. Merci à Xavier pour son expertise électronique mais aussi pour ses prêts de matériel de camping et de ski. Merci pour son amabilité et aussi pour l'organisation des barbecues du LOB ! Merci à Jean-Marc pour sa précision mécanique. Merci à Isabelle, Nicolas D. et Émilie pour leur travail à l'animalerie qui a rendu possible une grande partie de mes expériences. Merci également à Émilie pour son magnifique accueil au bureau pendant les premières années de ma thèse. Un grand merci à Stéphane aussi pour m'avoir accueilli dans son bureau, avoir suivi avec moi la passionnante construction du lycée international ainsi que pour avoir réussi à me faire rire pendant les périodes de stress les plus critiques de ma rédaction. Merci à Ernan et à Jean-Christophe pour l'aide informatique et les tomates. Merci à Laure et à Christelle pour leurs efforts administratifs qui m'ont beaucoup facilité la vie. Merci beaucoup à Manuel, Adeline et Roby pour leurs bons conseils et pour tous leurs prêts de matériel et d'outils de caractérisation de faisceaux. Merci à Michel, le seul échantillon-chercheur de ce manuscrit. Merci à Cédric de m'avoir aidé avec l'organisation de mon séminaire de mi-parcours. Merci à Roxane, qui aura été suffisamment patiente quand les décibels dépassaient le seuil toléré lors de mes concerts vocaux improvisés dans la salle de manip. Finalement, un grand merci à Hubert, Antigoni, Jean-Louis, Lionel, Pascale, Rivo, Lucille, Caroline, Hannu, Anne, Marten, Alexey... Merci à Sylvain Gigain qui m'a accidentellement, grâce à une soirée fromages, éclairé le chemin jusqu'à ce merveilleux laboratoire ! Merci aussi à Fabian Zomer, Matthieu Lancry et Yves Bernard (de Polytech Paris-Saclay) de m'avoir permis de faire de l'enseignement avec eux.

Une grande partie du temps passé au laboratoire a été partagée avec d'autres camarades d'aventures, les jeunes LOBsters. Merci donc aux doctorant.e.s et postdoctorant.e.s que j'ai croisé.e.s le long de mon séjour. Merci à ceux qui étaient déjà sages quand je suis arrivée: Lipsa, Olga, Marco, Chao, Lamiae, Mayla, Nicolas P., Oscar et Son. Merci ensuite à Yoann, qui ne manquait jamais de blagues; à Guillaume, qui est parti apprendre au monde le coût de griller son pain du petit-déj; à Romain, qui avec son immense esprit

zen profitait de la moindre excuse gentille pour ne pas rédiger; à Dam-Bé pour sa bonne humeur. Merci à Xiujun, Thuy et Paul, mes copains de promo. Merci à Arthur, le rockeur aux cils bruns, pour son partage musical, les soirées jeux et pour l'organisation d'un magnifique weekend en Bretagne. Un très grand merci à Vincent, pour toutes ces ratatouilles partagées lors des repas de midi ainsi que pour son aide de relecture de quelques chapitres. Merci aussi à Marianne et à la petite et souriante Chloé. Je dois remercier ensuite mes LOBsisters: Margaux, Joséphine et Clothilde. Merci à Margaux, à l'oreille fine à la fois pour écouter une belle histoire et en tirer les conclusions les plus optimistes et à la fois pour placer les meilleures notes de poule hautboïstique. Merci d'avoir partagé avec moi les aventures les plus intenses et odorantes et de ne jamais perdre l'envie d'en vivre de nouvelles. Merci aussi à Joséphine pour toutes ces discussions philosophiques et psychanalytiques sur la réalité. Merci de m'avoir invitée à ces rêveries sans limites et d'avoir réussi en même temps à être un beau soutien sur terre. Enfin, merci énormément à Clothilde, avec qui j'ai vécu en parallèle ces derniers mois de la thèse. Ça a été une chance incalculable de faire ces derniers pas à tes côtés. Merci de ton soutien, de tes blagues, de nos RER synchronisés, de nos pauses-balades et de nos soirées rédaction. Tu as réussi à faire de cette étape l'une des plus belles de ma thèse. Ensuite, un gigantesque merci à Sophie, ma biologiste préférée aux super-pouvoirs, merci de ton aide avec les poissons. Merci pour tous les gâteaux (et biscuits à la cuillère), merci d'avoir pris soin de nous avant, pendant et après la rédaction. Merci de nous faire rigoler et sourire tous les jours, merci de tes bons conseils, et merci de ne jamais arrêter d'essayer de nous parler, car chacun de tes mots est, comme toi, extraordinaire. Merci aussi à Loïc, Alice et Couillouille pour leur joie et imagination illimitée. Merci à Maëlle pour son positivisme, pour sa musique et pour le pisse-debout. Thanks Seongbin for all these shared lunchtimes and interesting discussions. Merci également à Anastasia d'avoir partagé les midis avec nous. Enfin, merci beaucoup à Hugo, Maxime, Lien, Kevin, Bahar, Dale, Clément, Anaïs, Auriane, Amélie, Giulia, Blandine, Matthew, Hester... Merci à Ramy pour ses expériences de comptage des marches de Lozère. Un grand merci aussi à Stella, dont les efforts télescopiques font preuve d'un grand intérêt et patience. Je te souhaite tout le courage possible pour la suite !

Nulle part je n'ai ressenti une ambiance pareille à celle du LOB, certes. Mais pendant ces années à Paris, j'ai fait partie de certains groupes qui ont fortement concurrencé la sympathie des LOBsters. Lors de mon stage M2 j'ai pu profiter de la beauté de l'optique quantique en rencontrant des personnes fantastiques. Un énorme merci à Martin, qui m'a appris plein de secrets de l'optique expérimentale. Merci spécialement pour ce que tu m'as apporté humainement, ce stage a vraiment été beaucoup trop stylé, trop de la bombe et la pompélopie ! Merci également à Grogui, officiellement mon premier prof de français. J'espère que vous ne serez pas déçus par mon Duplo. Merci également à Vincent, Sylvain, Luis et Florence. Merci aussi à Alban et Solenne pour les moments de loisir et de vacances, pour leur proposition de co-fonder la *Ferme ta Gueule* et pour leurs fraises. I also want to thank Pipi and Lena Chichivitza, for all the good moments we shared during this period either in Marseille or Paris. Ensuite, je dois citer mes ami.e.s du chœur PSL. Infiniment merci pour ces doses inquantifiables de musique et de détente lors des répétitions tous les mardis soirs, concerts, tournées et autres évènements festifs. Votre aide a été fondamentale pour surmonter les plus sombres moments de cette thèse. Merci à Johan pour sa génialité, à Julien pour sa générosité et sa sincérité, à Adrian pour sa bonne humeur et sa vitalité, à Hélène pour son énergie et sa jukebox, à Megan et Adrien pour leur sourires. Merci également à Pierre, Philomène, Annya, Marie, Arthur,

Julia, Martine, Ariane, Aurore, Anne des F., Anne B., Alina, Véronique, Rita, Armine, Brigitte, Anne-Claire, Clotilde, Eliza, Isabelle... et autant d'autres belles voix qui ont été la bande très originale de ma thèse à travers le Requiem de Brahms, de Mozart ou de Fauré, la petite messe solennelle de Rossinni ou le Gloria de Poulenc. Una parte importante de este viaje la he compartido con Andrés. Me gustaría agradecerle que (A) me haya transmitido su entusiasmo por la vida desde las Calanques hasta Atizapán de Zaragoza, (B) me haya acompañado con su sentido del humor a través de varios traslados, y (C) me haya enseñado tantas cosas útiles como lo importante que es tener un cuchillo bien afilado o unos buenos zapatos. También le estoy muy agradecida, a él y a su familia, por la increíble acogida en México. Nada mejor me pudo haber permitido empezar este doctorado en unas tan buenas condiciones de salud mental. Gracias pues a Irene, a la tía Pitis, a Emilio, a la abuela, a las primas y al tío Alberto. Un énorme merci à mes garants : Jean-Paul et Françoise, sans qui je n'aurais jamais réussi à avoir mon bel appart à Bourg la Reine. Merci à Vladimir de m'avoir fourni sans cesse (même pendant les confinements) tous ces délices végétaux à travers les saisons.

Enfin, merci beaucoup Antoine pour tout. Merci d'avoir partagé toutes ces aventures gauloises avec ta gentillesse et ta bonne humeur. Merci de m'avoir apporté toutes sortes de remèdes quand j'en avais besoin et pour cette liste interminable de rêves que tu me proposes tous les jours. Quelle chance pour une goûteuse de potions magiques ! Merci également à Bruno et Cathy de m'avoir permis de me ressourcer avec l'air frais et pur du Morbihan.

Otro conjunto importante de personas me han acompañado desde la distancia. Moltíssimes gràcies als meus amics catalans (o quasi) de Física. Un especial agraïment a na Carlota per totes ses visites europees, a Álvaro por todos esos kilómetros vascos e irlandeses que nos llevarán quizás un día hasta Santiago, a en Raimoon per tantes idees i converses loques, a en Carles y los Rivero-Ferràs, per totes les acollides a Enric Granados. Gràcies també a n'Àlex, Javi, en Rai, en David, n'Anna, en Sergi, n'Andrés i na Gemmis. Gràcies per sa vostra alegria, el vostre suport i, sobretot, gràcies per la vostra CALOR! Però sa font més gran de descans i tranquil·litat, l'he trobada sempre a Mallorca. Seguiré doncs, amb es mallorquins i mallorquines (i convidats/des). Moltes gràcies a en Carlos i na Cristina, na Clara, n'Auba, na Paula, n'Henar i en Juan Vizcaíno, sa primera persona que me va desvelar sa bellesa de s'òptica. Moltes gràcies a sa representació des escoltes Nuredduna: n'Andrea i na Laura S., a los Mir Kato i a na Gibet. Gràcies a nes músics: en Joan, n'Izaskun, na Caterina, na Maria T. i na Maria V.

Finalment, gràcies Magí. Gràcies per ser-hi sempre, per sa teva intensitat i es teu entusiasme. I bé, sobretot tenint en compte sa meva llarga i boirosa companyia, tant de bo un dia puguem veurer-mos nítidament entre ses gotes. Aleshores sabrem, quan caurà la nit, si l'estel del vespre et fa estremir com a mi.

Venir, anar, tornar, romandre. Tant de moviment podria parèixer que seguesc una dansa erràtica però no és així. Cada paso está ligado a mi familia. Primero de todo, muchísimas gracias a mis hermanas/os. Compañeras/os de aventuras soleadas y felices, de cantos, risas y llantos, de energía positiva y repartición aritmética de patatas fritas. Gracias a Laia por su creatividad, sus voces de acompañamiento y su humor contagioso. Gracias a Ariadna por sus sonrisas, por sus melodías, por ser mi equipo de escambrí y de otros juegos familiares (¡10 puntos!). Gracias también a Javi y a Pablo. Muchas gracias a Pau, por su curiosidad científica y artística y por las emocionantes partidas de ajedrez. Muchas

gracias a mis padres por habernos dado todo lo que tenían en sus manos, en sus mentes y en sus almas. Por haber pasado todo ese precioso tiempo con nosotros y habernos enseñado, educado y guiado con su amor y esfuerzo. Gracias mamá por tu atención y buenos consejos. Gràcies papà per s'exemple d'eficàcia i també per tanta Viva la O ! Antes de terminar me gustaría agradecerles a mi tío Rafa, tía Ana, y tío Tuyi haberme estimulado y enseñado tantas cosas interesantes desde que era pequeña. También a Nuria, por haberme cuidado, por abrirme siempre su casa y por haber venido hasta París a apoyarme durante la defensa. Muchas gracias también a la tía Chelo y el tío Luís, Rocío, Cristina P., Rafa B., Joan J., Luisito, el tío Manolo, Olga y a todos mis primos y primas: Aitana, Sol, Cristina O., Mar, Sandra, Aina, Joan O., Isaac y Lola. Moltes gràcies també a ses xamarrines per es seu suport: a la tia Paca i el tio Joan, la tia Margarita, el tio Miquel i la tia Sari, na Margalida, en Xim, en Joan P. i en Lluc, n'Eva, en Dani, en Daniel i en Marc, na Lourdes i en David, na Neus, n'Albert i na Marina, en Llorenç i especialment na Rasa !

Las últimas líneas de estos agradecimientos son para la abuela. Ni lo que yo haya escrito en esta tesis ni ninguna otra ciencia podrá equipararse a todo lo que tú me has enseñado. Gracias por haber estado ahí siempre, como hija, hermana, madre, tía, abuela... Gracias por poderlo todo a la vez. Gracias por ser el corazón que bombea esta familia. Gracias por haberla tejido con esa fuerza extraordinaria. Gracias por cuidarnos, por abrazarnos y por querernos. Gracias por darlo todo por nosotros. Gracias por tus refranes, gracias por tus lentejas, gracias por tus risas, gracias por todo. Un último pensamiento va para el abuelo. Gracias por tu cariño y por haber sido una inspiración de paciencia, exactitud y perfeccionismo únicos.

Salut! Con esta palabra me despido, que significa *adiós* en francés et *santé* en catalan. Désolée for this language mess. Mais merci beaucoup à tous d'avoir été présent.e.s et d'avoir fait de ma vie une histoire si rayonnante. Je vous aime.

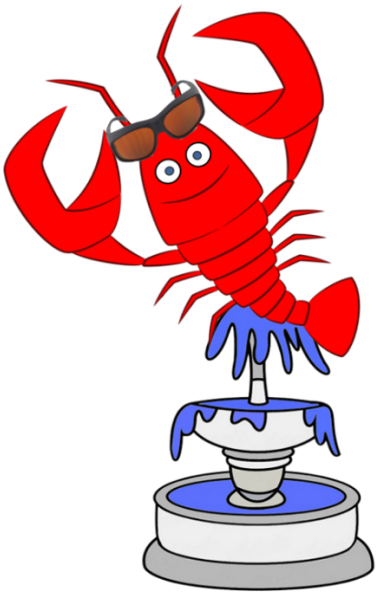

Résumé de la thèse en français

Cette thèse présente un projet développé au Laboratoire d'Optique et des Biosciences au sein du groupe *Microscopies avancées et physiologie des tissus*. Parmi les défis actuels de la microscopie optique, la microscopie multiphotonique (ou non linéaire) permet d'aborder l'imagerie en profondeur dans les échantillons diffusants. Ce travail a porté spécifiquement sur le développement et l'optimisation de la microscopie à trois photons (3P) en tant que méthode d'imagerie non linéaire quantitative pour les applications biologiques. Nous décrivons deux approches permettant d'étendre le nombre de paramètres observables avec cette méthode d'imagerie.

Dans le premier chapitre de ce manuscrit, nous présentons la microscopie multiphotonique comme une méthode efficace de sectionnement optique 3D. Nous décrivons ses principes et les caractéristiques qui la rendent efficace dans les milieux diffusants. Nous discutons ensuite la limite de profondeur d'imagerie en microscopie à deux photons, qui est principalement due à l'émission de lumière hors du plan focal. Nous décrivons comment la microscopie à trois photons surmonte cette limite grâce à son confinement optique plus fort. Ce sectionnement optique est ensuite analysé à l'aide d'un modèle numérique pour étudier l'effet des paramètres d'excitation sur le rapport signal sur bruit de fond à grandes profondeurs d'imagerie. Nous discutons enfin les limites actuelles de la microscopie à trois photons et nous proposons de relever deux défis : le développement de l'instrument (Chapitre 2) et l'extension du nombre de paramètres observables (Chapitres 3 et 4).

Dans le Chapitre 2, nous présentons notre travail sur le développement et l'optimisation d'un microscope à trois photons. Tout d'abord, nous décrivons la source laser, un prototype d'amplificateur paramétrique optique (OPA) construit en laboratoire et conçu pour les applications à trois photons. Fonctionnant à une fréquence de répétition de 1MHz, elle délivre des impulsions laser de l'ordre du microjoule, permettant l'excitation 3P à 1300 et 1700 nm, les bandes spectrales optimales pour l'imagerie 3P des tissus profonds. Ce chapitre présente les avantages et les inconvénients de cette source laser et des prototypes précommerciaux suivants, conçus pour notre laboratoire. Enfin, nous décrivons notre travail sur les voies de conditionnement des faisceaux et sur la conception du microscope pour optimiser l'imagerie 3P.

Dans le Chapitre 3, nous explorons la possibilité d'exciter à trois photons des protéines fluorescentes bleues, ce qui reste peu étudié jusqu'à présent. Les rapports les plus récemment publiés sur l'excitation à trois photons des protéines fluorescentes se concentrent sur les protéines fluorescentes vertes et rouges, qui peuvent être excitées dans la gamme de longueurs d'onde de 1300 à 1700 nm. Ils concluent tous que le spectre d'excitation multiphotonique ne peut pas être déduit du spectre d'excitation linéaire et peut présen-

ter des différences significatives. Pour cette raison, il n'est pas possible de prédire les propriétés d'excitation 3P de protéines fluorescentes spécifiques à partir de leurs spectres linéaires. Nous présentons ici une étude dans laquelle trois protéines fluorescentes bleues sont excitées à la longueur d'onde de 1030 nm afin de déterminer dans quelles conditions elles peuvent être utilisées en microscopie 3P.

Enfin, dans le Chapitre 4, nous mettons en œuvre et explorons une nouvelle modalité de contraste cohérent compatible avec la microscopie à fluorescence 3P et basée sur la génération de somme de fréquences du troisième ordre (TSFG). Une imagerie TSFG à plusieurs longueurs d'onde est obtenue par le mélange de fréquences de deux impulsions synchronisées. Nous étudions comment les signaux de TSFG et de génération de troisième harmonique (THG) peuvent être exaltés par la présence de résonances électroniques dans un milieu absorbant. Nous montrons qu'un tel effet résonant 3P est présent près de la bande de Soret de l'hémoglobine et nous l'utilisons pour réaliser une imagerie sans marquage spécifique à l'hémoglobine qui permet une segmentation automatique des globules rouges. Enfin, nous démontrons également comment cet effet, ainsi que les différences spectrales entre l'hémoglobine oxygénée et l'hémoglobine désoxygénée ont un potentiel pour l'imagerie fonctionnelle de l'état d'oxygénation des globules rouges.

L'ensemble de ces résultats contribue au développement instrumental de la microscopie 3P, ainsi qu'à l'ouverture de nouveaux domaines d'applications en bioimagerie.

Contents

Preamble

This thesis presents a project developed at the Laboratory for Optics and Biosciences within the *Advanced microscopies and tissue physiology* group. Among current challenges in optical microscopy, imaging deep inside scattering samples can be addressed by using multiphoton (or nonlinear) microscopy. This work specifically focused on the development and optimization of three-photon (3P) microscopy as a quantitative nonlinear imaging method for biological applications. We extended the number of observable parameters with this technique using two different approaches.

In the first chapter of this manuscript, we start by introducing multiphoton microscopy as an efficient 3D optical sectioning method. We describe its principles and the main characteristics which make it effective in scattering media. We then discuss the imaging depth limit in two-photon microscopy, which is mainly due to out-of-focus light emission. We describe how three-photon microscopy overcomes this limitation thanks to its stronger optical confinement. This optical sectioning is then analysed using a numerical model to investigate the effect of the excitation parameters on the signal to background ratio at large imaging depths. We then discuss the current limitations of three-photon microscopy and propose to address two challenges: the development of the instrument (Chapter 2) and the extension of the number of observable parameters (Chapters 3 and 4).

In Chapter 2, we present our work on the development and optimization of a three-photon microscope. First, we describe the laser source, a lab-built OPA prototype designed for three-photon applications. Operating at MHz repetition rate, it delivers microjoule laser pulses allowing 3P excitation at 1300 and at 1700 nm, the optimal spectral bands for deep-tissue 3P imaging. This chapter reports on the advantages and disadvantages of this laser source and the following pre-commercial prototypes that were designed for our laboratory. Finally, we describe our work on the beam conditioning paths and on the microscope design to optimize 3P imaging.

In Chapter 3, we explore the possibility of three-photon excitation of blue fluorescent proteins, which remains poorly investigated so far. Most recently published reports on three-photon excitation of fluorescent proteins focus on green and red fluorescent proteins, which can be excited in the 1300 - 1700 nm wavelength range. They all conclude that the multiphoton spectrum cannot be deduced from the linear one and might present significant differences. For this reason, it is not possible to predict the 3P excitation properties of specific fluorescent proteins from their linear spectra. Here, we present a study in which three blue fluorescent proteins are excited at a fixed wavelength to determine in which condition they can be used in 3P microscopy.

Finally, in Chapter 4, we implement and explore a new coherent contrast modality compat-

ible with 3P fluorescence microscopy and based on third-order sum frequency generation (TSFG). Colour TSFG is obtained by mixing two synchronized pulses. We discuss how TSFG and third-harmonic generation (THG) signals can be enhanced when real energy levels such as absorption bands are present near the virtual transitions. We show that such a 3P-resonant effect is present near the Soret band in hemoglobin, and use it to achieve label-free hemoglobin-sensitive imaging and automated red blood cells segmentation. Finally, we also demonstrate how this effect together with the spectral differences between oxygenated hemoglobin and deoxygenated hemoglobin have a potential for functional imaging of the oxygenation state of red blood cells.

Chapter 1

Introduction

Contents

1 Making visible the invisible

Antonie van Leeuwenhoek crafted the first high-resolution microscopes in the 17th century driven by his curiosity about microorganisms. With his hand-held instruments, he made visible what was invisible at that time, and pioneered the field of microscope making. Many developments have followed since then to fulfill the requirements of the scientists to perform observations at higher magnification, larger depth and higher speed. These improvements have been possible thanks to technological advances such as mastering the fabrication of lenses or the advent of the laser in the 1960's. Technology has enabled the development of new imaging methods and instruments, some of them so complex that they need the size of a whole room.
Figure 1.1 classifies several bioimaging techniques according to their spatial resolution and penetration in tissues. It illustrates that there is a global trade-off between spatial resolution and imaging depth. However, there are other important imaging properties that can be experimentally required for a particular application such as sensitivity or imaging speed. Such requirements have motivated the development of many imaging techniques focusing on the improvement of one or two of these parameters. In practice, a compromise must generally be found between spatial resolution, imaging depth, imaging speed, contrast specificity, and non-invasiveness.

Optical microscopy provides a spatial resolution on the order of the micrometer, which makes it ideal for the observation of biological objects at the cellular and sub-cellular scale. In addition, it offers high sensitivity and specificity through its combination with fluorescence labelling, which makes it unique for studying cell structure and function. On the other hand, light is strongly scattered when propagating in biological media, so that the imaging depth of optical microscopes in tissues is limited to a few hundreds of micrometers at best.
In this thesis work, we focus on three-photon microscopy, a recent approach providing enhanced penetration depth in tissues. Our aim will be to optimize both imaging depth and contrast specificity, while keeping an acceptable spatial resolution for studying cells *in situ*.

Let us first introduce some general concepts and methods relevant to in-depth microscopy. Wide-field illumination microscopy is the most standard approach in optical microscopy. As we will briefly review, it does not provide 3D information of the sample. This is a limitation inherent to the imaging process. Due to energy conservation, the amount of light illuminating any plane perpendicular to the optical axis is the same. It follows that the image of a thick 3D object consists of a sharp image of the plane of interest superimposed to blurred images of the other planes. This out-of-focus light produces a background that diminishes the image contrast, which can be quantified by means of the signal to background ratio (SBR).

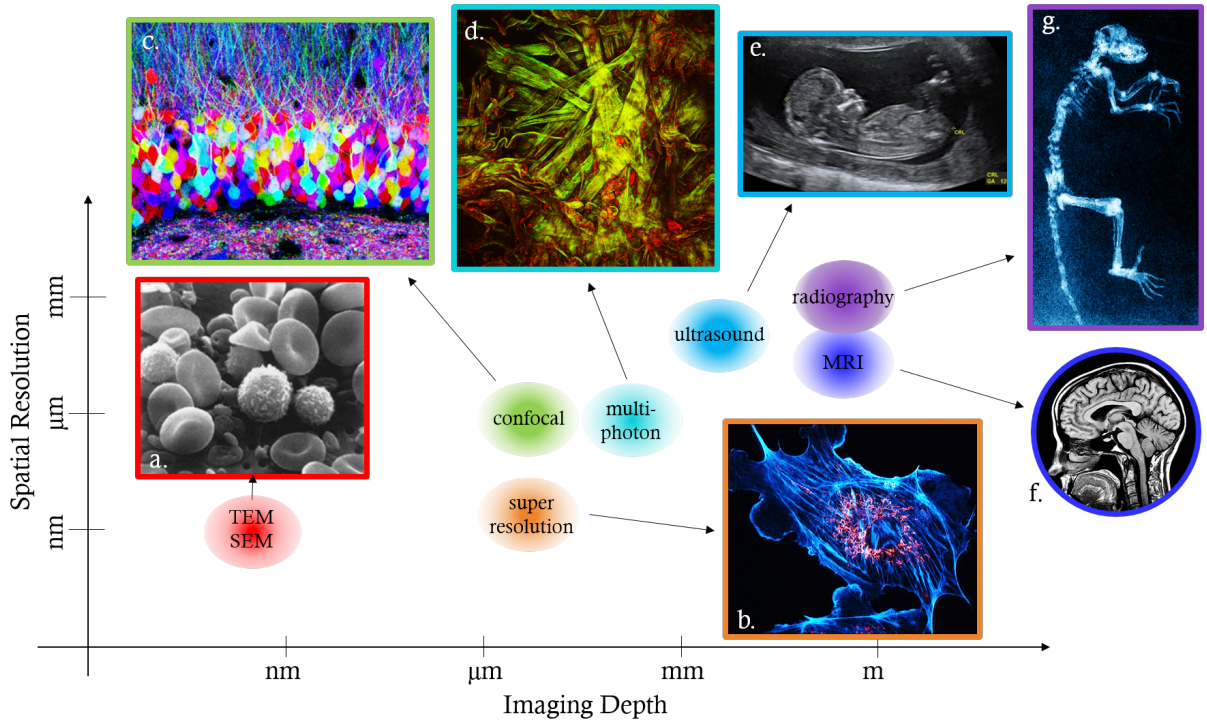

Figure 1.1: Illustration of several standard imaging techniques classified in terms of their spatial resolution and penetration depth. **a) Scanning Electron microscopy (SEM):** normal human blood. Source: NCI. TEM: transmission electron microscopy. **b) Super resolution microscopy:** bovine pulmonary artery endothelial cell, showing actin (blue) and mitochondria (orange). Source: NSW. **c) Confocal microscopy:** brainbow labelled neurons in the hippocampus of a mouse [1]. **d) Multiphoton microscopy:** second harmonic generation (green) and two-photon autofluorescence (red) image of collagen fibrils of a parchment [2]. **e) Ultrasound imaging:** a fetus in the womb at 12 weeks of pregnancy. Source: wikipedia (W. Moroder). **f) Magnetic Resonance Imaging (MRI):** sagittal section of the head of an adult human. Source: Radnet. **g) Radiography:** specimen of *Darwinius masillae* adapted from [3].

To achieve 3D resolution, two techniques have been principally developed using linear optics: confocal microscopy and light sheet microscopy. In Section 2, we briefly review the strategy used to avoid out-of-focus light in these two approaches. However, these linear microscopy methods fail to maintain 3D sectioning deep in scattering tissues. Indeed, as imaging depth increases, scattering results in a loss of signal and an increase in background scattered light. One workaround that maintains optical sectioning at larger depth is multiphoton microscopy, discussed in Section 2.3. In Section 3, we then present more specifically the differences between two-photon (2P) and three-photon (3P) fluorescence microscopy focusing on the details of the latter. Finally, in Section 4, we introduce the objectives of this thesis.

2 3D optical sectioning methods

2.1 Confocal microscopy

Confocal microscopy [4] was initially described by Marvin Minsky in 1953, and the first commercial instruments were produced in the 1980's thanks to the availability of efficient

laser sources, detectors and scanning methods. It is now a reference technique in cell biology.
The principle is the following: the illumination is focused onto a point in the sample, and a pinhole is placed in a conjugated position in the detector plane. The pinhole lets the light from the focus reach the detector, and blocks light coming from all other positions in the sample, in particular out-of-focus light. This is illustrated in Figure 1.2.

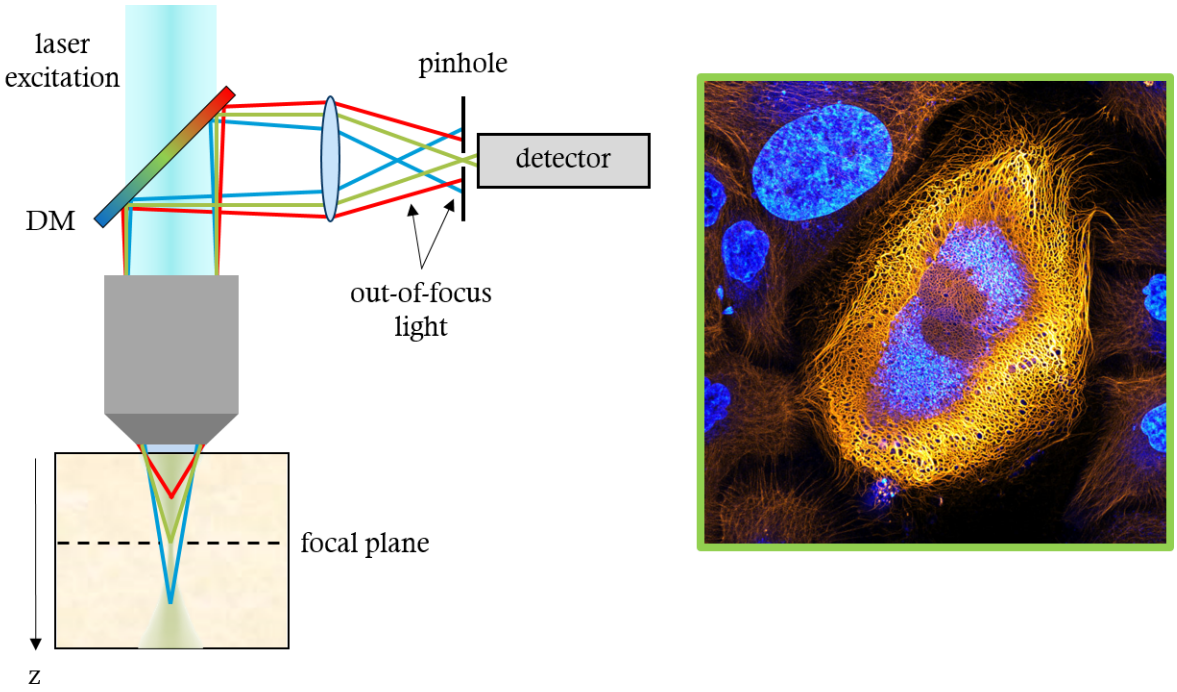

Figure 1.2: Scheme of the confocal microscopy principle (left). Only the photons coming from the focal plane enter the pinhole, which rejects all the out-of-focus light. DM: dichroic mirror. Example of a confocal image: immortalized human skin cells (HaCaT keratinocytes) expressing fluorescently tagged keratin (right). Source: The Netherlands Cancer Institute.

The excitation spot is then scanned in 2D or 3D across the sample, and an image is recorded in a point-by-point manner. This imaging method is known as point-scanning.
One limitation of the confocal microscope is its phototoxicity when it is used for 3D imaging. Indeed, by principle, each 2D confocal image requires to illuminate the sample over its entire thickness, and to then reject all the collected light that does not come from the focal plane. As a consequence, photo-perturbation becomes a limiting factor when performing 3D or sustained imaging of fragile samples. A second limitation of confocal microscopy is that its point-scanning acquisition principle necessarily limits the imaging speed.

2.2 Light sheet microscopy

Light sheet microscopy provides a solution to achieve faster and less-phototoxic 3D-resolved imaging than confocal microscopy. It is based on a different imaging geometry, as shown in Figure 1.3.a [5]. The excitation and the detection axes are orthogonal, generally including an objective lens each. In the most usual implementations, the illumination beam cone is shaped into a sheet of light either by means of a cylindrical lens, or with a rapid scanning mirror. Thus, only one plane is illuminated at a time and no out-of-focus

light is generated. This principle brings two additional advantages. The first one is that the imaging speed can be greatly increased since the acquisition is parallelized. In practice, a camera rather than a point detector is used to acquire 2D images. The second one is that, because only the imaged region is illuminated, photodamage is strongly reduced compared to confocal microscopy.

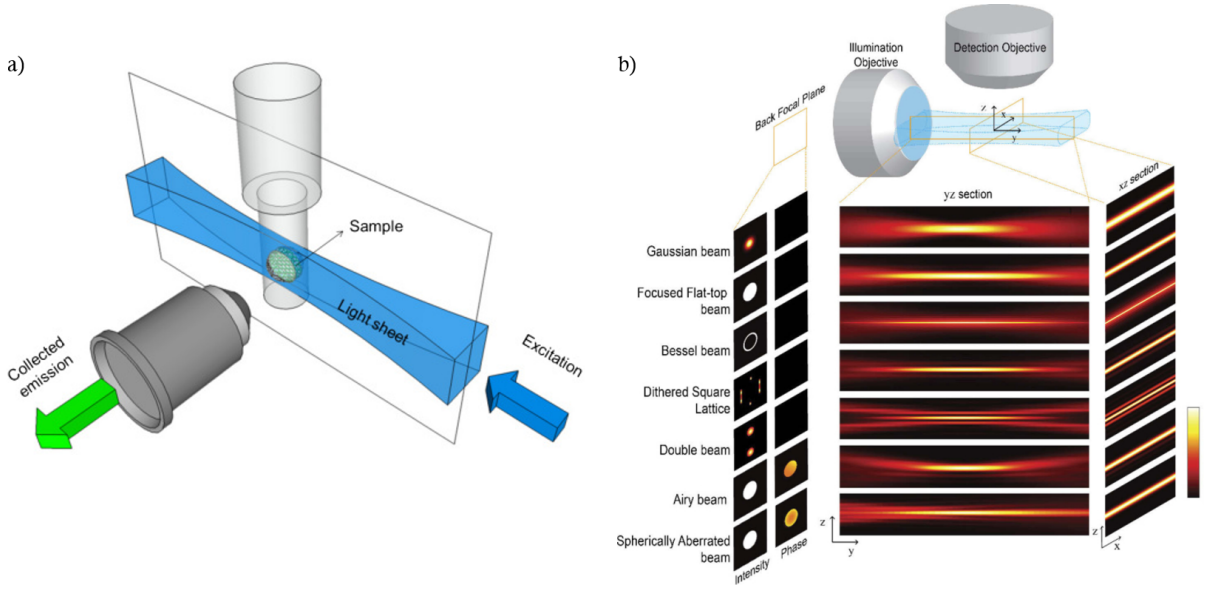

Figure 1.3: (a) Geometry of light sheet microscopy, adapted from [5]. (b) Examples of different possible light sheet shapes, adapted from [6].

Light sheet microscopy is a recent method and is still undergoing many technical and methodological developments. Due to the coupling between the axial and lateral dimensions in a focused beam, the thickness and the axial extension of the light sheet are also coupled. Thus, there is a trade-off in light sheet microscopy between axial resolution, related to the sheet thickness, and field-of-view (FOV), related to the sheet axial dimension. A current field of research is therefore to try to engineer optimal sheet shapes using phase masks at the back focal aperture of the illumination objective (see Figure 1.3.b).

2.3 Multiphoton microscopy

2.3.1 Principles

Multiphoton absorption is a process by which n photons of energy $\hbar\omega/\mathrm{n}$ combine their energies to allow an optical transition normally requiring a single photon of energy $E = \hbar\omega$. It was predicted by Maria Goeppert-Mayer in 1931 [7], and first applied to microscopy by Denk et al. in 1990 [8]. This latter group reported 3D-resolved microscopy based on two-photon excited fluorescence (2PEF) contrast, and pioneered the field of multiphoton microscopy.

The imaging principle at the heart of multiphoton microscopy is that, because of the nonlinearity of the contrast mechanism, excitation is intrinsically restricted to a small probe volume. For example in the case of 2PEF microscopy, fluorescence excitation is proportional to the square of the excitation intensity; when the excitation beam is focused by a high numerical aperture (NA) objective, the squared intensity distribution is confined to a micrometer-scale volume around the focal point, as we will detail in Section 3.2.1.

This property is illustrated in Figure 1.4. The micrometric probe volume is then scanned in 2D or 3D to form an image. Excitation confinement results in an intrinsic optical sectioning without the need for a pinhole to reject light from other planes like in confocal microscopy.

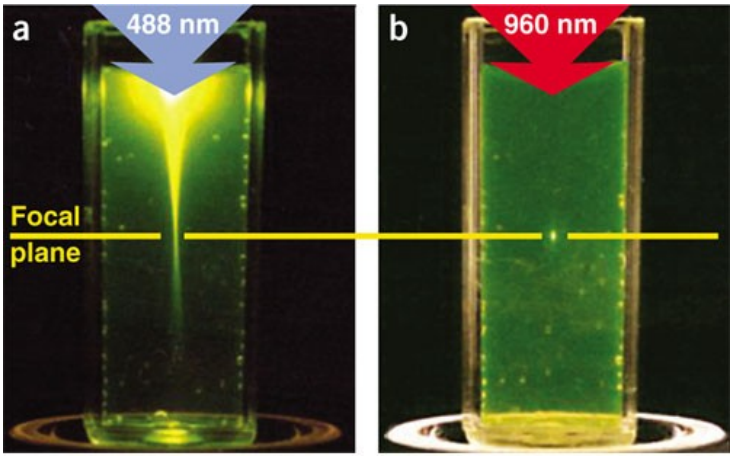

Figure 1.4: Localisation of linear excitation (a) and two-photon excitation (b) in a sample of fluorescein by focused 488 nm continuous-wave light and focused femtosecond 960 nm laser pulses (0.16 NA). Figure from [9].

Molecular two-photon absorption cross sections are very small (on the order of $10^{-48} cm^4$ for the green fluorescent protein [10]) so that laser light must be concentrated spatially and temporally to achieve efficient excitation. Spatial concentration is achieved by using a high numerical aperture (NA ≈ 1) microscope objective, but this is not sufficient to reach reasonable acquisition times. Experimentally, 2PEF microscopy has been made possible by the advent of femtosecond oscillators in the near infrared ($\approx$ 900 nm) wavelength range. Typical temporal parameters of these lasers are a pulse duration τ of 100 fs and a repetition rate $1/T$ of 80 MHz (Figure 1.5).

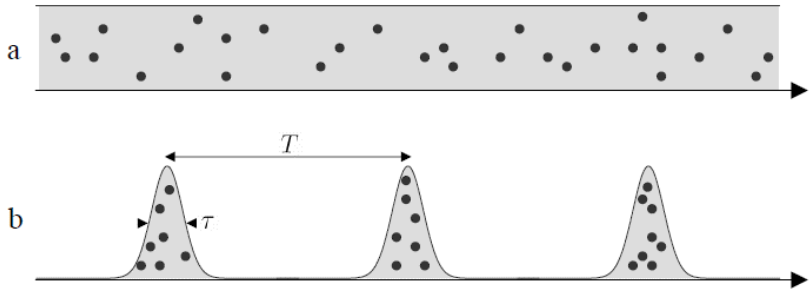

Figure 1.5: Temporal distribution of the photons (black dots) in the case (a) of a continuous-wave laser and (b) of a pulsed laser of pulse duration τ and repetition rate $1/T$. Figure from [11].

As summarized in Table 1.1[1], pulsed excitation increases the probability of nonlinear excitation for a given average excitation power P_0. This makes it possible to enhance nonlinear processes while minimizing sample heating by linear absorption.

[1] A detailed derivation of these dependences is included in Section 2.3 in Chapter 4 for the case of 3P excitation.

N = 1 (linear)	$S_{1P} \propto P_0$
N = 2	$S_{2P} \propto \left(\frac{T}{\tau}\right)\langle P_0\rangle^2$
N = 3	$S_{3P} \propto \left(\frac{T}{\tau}\right)^2\langle P_0\rangle^3$
N	$S_{\mathrm{NP}} \propto \left(\frac{T}{\tau}\right)^{\mathrm{N}-1}\langle P_0\rangle^{\mathrm{N}}$

Table 1.1: Dependence of linear and nonlinear optical processes on laser average power and temporal parameters. Explicit expressions of the signal (S) are given for 1, 2 and 3 photon processes, together with the general expression for a N-photon process.

Two distinctive advantages of multiphoton microscopy are that it performs better in scattering media than linear microscopy techniques, and it offers additional contrast modalities, as we will see below.

2.3.2 Advantages in scattering media

Multiphoton microscopy performs better in scattering media than linear techniques such as confocal microscopy, for three reasons: (i) longer excitation wavelengths experience reduced scattering; (ii) excitation confinement is preserved up to a few scattering lengths; (iii) detection is relatively unaffected by scattering.

Longer wavelengths provide reduced scattering

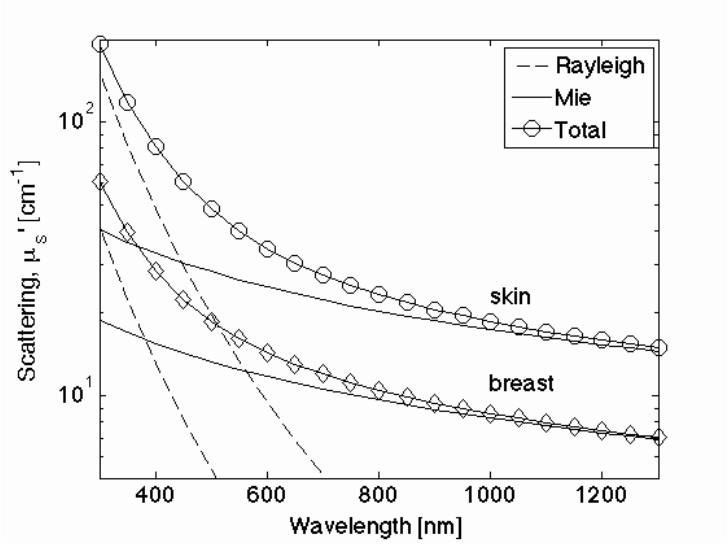

Figure 1.6: Scattering dependence on wavelength in skin and breast tissue. Adapted from [12].

Scattering is the phenomenon responsible for the change of light propagation direction occurring when a photon encounters an obstacle. Non-scattered photons with straight trajectories are usually termed ballistic photons. Microscopy, i.e. diffraction-limited imaging, relies on the detection of ballistic photons only. However, the scattering nature of tissues

makes in-depth microscopy difficult because the number of ballistic photons decreases with the propagation distance. This attenuation is described as an exponential decay of the intensity characterized by the scattering length or scattering mean free path l_s. It is defined as the distance after which the ballistic intensity is attenuated by a factor of $1/e$ and can also be understood as the average distance travelled by a photon between two scattering events. The scattering coefficient, μ_s, is the inverse of the scattering length and decreases with increasing wavelengths as shown in Figure 1.6 [12].

As discussed earlier, the SBR in confocal microscopy of a thick transparent object is high because the pinhole rejects out-of-focus light. However, its value decreases with increasing imaging depth inside a scattering sample, for two reasons. Firstly, some photons originating from the focal region are deviated and rejected by the pinhole, which reduces the signal. Secondly, some scattered photons originating from out-of-focus planes are not properly rejected by the pinhole and reach the detector, which increases the background. In light sheet microscopy, scattering also causes a similar effect by broadening the illuminated region.
Multiphoton microscopy presents a superior penetration inside scattering media compared to confocal and light sheet microscopy [13] because it uses longer excitation wavelengths in the infrared range, which experience less scattering in tissues.

Robustness of multiphoton optical sectioning in scattering media

The second advantage of multiphoton microscopy for tissue imaging is that the confinement of the excitation is relatively well preserved over $\approx$ 4 scattering mean free paths [14, 15]. This limit will be discussed in more detail in Section 3 of this chapter. This mechanisms result in a conservation of the SBR up to an imaging depth of a few hundreds of microns in practical applications.

Detection in multiphoton microscopy is little affected by scattering

The last step of the imaging process is the fluorescence collection. A strong advantage of multiphoton microscopy in scattering media is that fluorescence light does not need to be refocused on a pinhole before detection. Indeed, since the excitation is confined, all emitted photons originate from the focal region and contribute to the signal, whether they are ballistic or scattered. In the case of a non-scattering sample (Figure 1.7, left), confocal detection performs well through the whole sample volume. In a scattering sample (Figure 1.7, right) however, confocal microscopy fails to provide strong signal, as most of the photons are deviated and rejected by the pinhole. The absence of pinhole in multiphoton microscopy allows the collection of a larger amount of photons.

As a summary, the advantages of multiphoton microscopy for imaging inside a scattering medium are presented in Figure 1.8.

2.3.3 Contrast mechanisms

In addition to the superior performance for in-depth imaging of scattering media, another specific advantage of multiphoton microscopy is that it gives access to different contrast

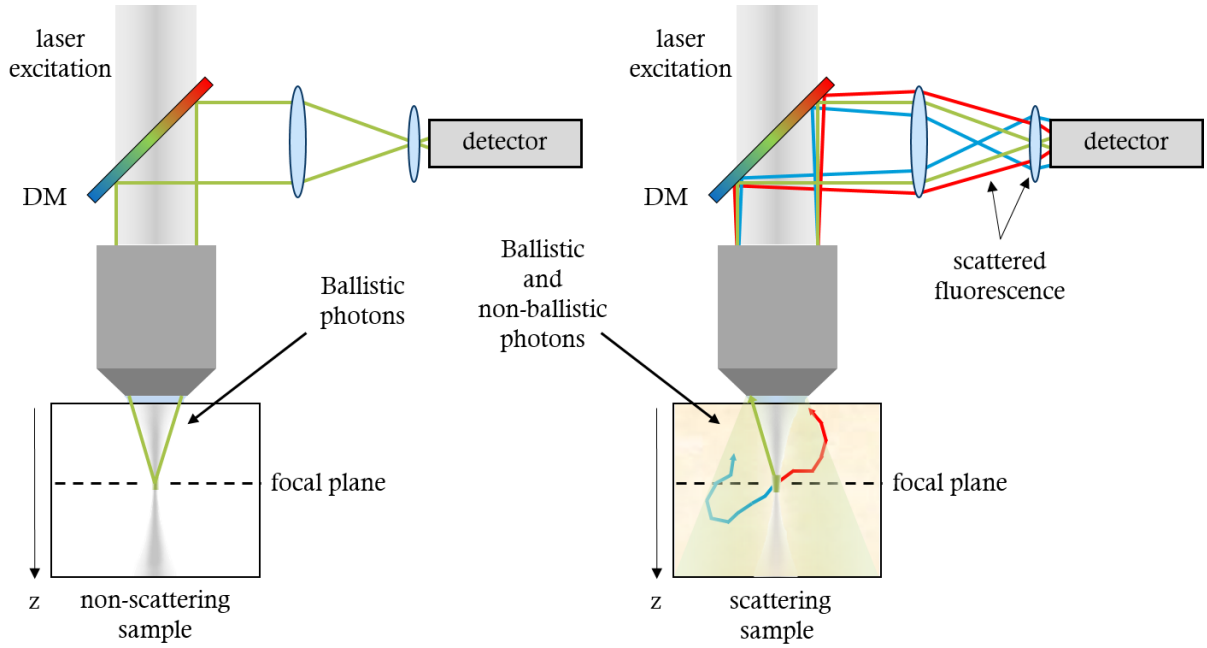

Figure 1.7: Collection efficiency in multiphoton microscopy. Non scattering sample (left): all the detected light consists of ballistic photons. Scattering sample (right): ballistic and non-ballistic photons contribute to the detected signal. Since all the fluorescence originates from the focal region, the detection of scattered light increases the signal without degrading the contrast.

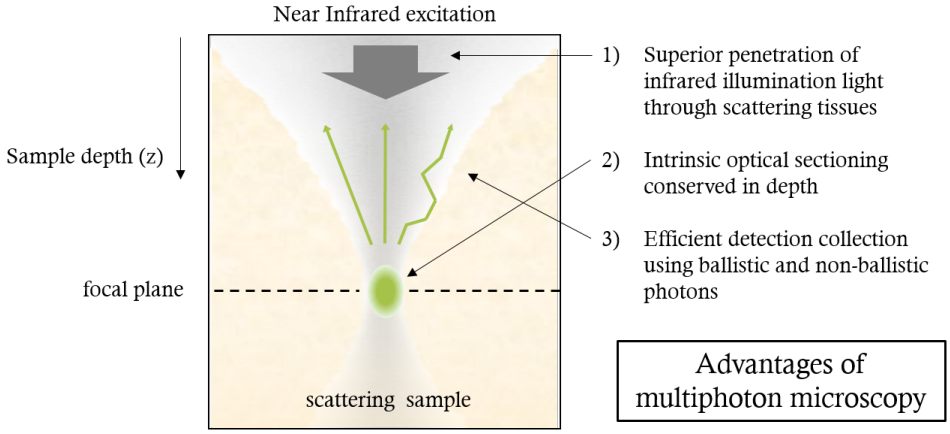

Figure 1.8: Scheme of the excitation, optical sectioning and collection in multiphoton microscopy. Inspired from [16].

mechanisms based on nonlinear optical processes, which can be combined to provide complementary information.

Figure 1.9 presents several processes that can be used as contrast mechanisms in multiphoton microscopy. First, chromophores can be excited using a two-photon or a three-photon process before emitting fluorescence (2PEF, 3PEF). 2PEF is the most widely used contrast modality in nonlinear microscopy. We will discuss 3PEF in more detail in Chapter 3. In addition, coherent nonlinear processes can be used as contrast mechanisms. These include second harmonic generation (SHG) [17–19], third harmonic generation (THG) [20, 21] or coherent anti-Stokes Raman scattering (CARS) [22–24]. SHG is specifically observed in non centrosymmetric media. It can be used to visualize in a label-free manner certain dense polarized biological structures such as collagen fibers, myosin filaments or micro-

tubule bundles. THG is sensitive to interfaces and can be used to visualize the presence of dense inclusions such as lipid droplets, interfaces, and pigments. We will discuss it in more detail in Chapter 4. CARS is sensitive to vibration modes and can be used to visualize the density of lipids, water and other tissue components.

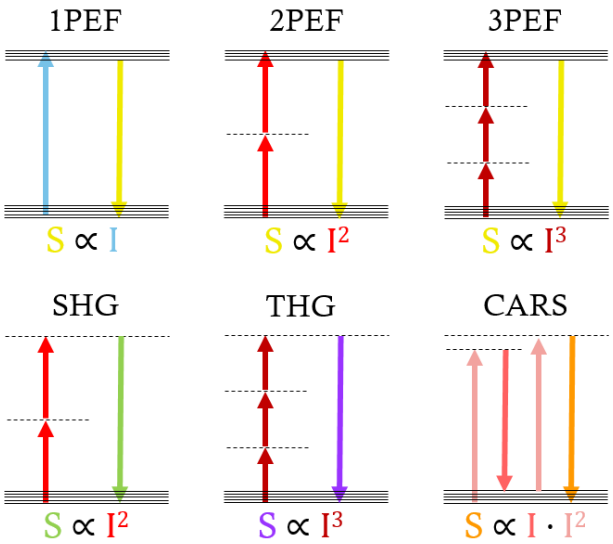

Figure 1.9: Schematic representation of several contrast mechanisms in multiphoton microscopy compared to one-photon excited fluorescence (1PEF). Real energy levels are represented by solid lines whereas dashed lines stand for virtual energy states. The dependence of the detected signal S on the excitation intensities I is shown with a colour code correspondent to the energy scheme.

The possibility to easily combine these signals in the same instrument is an important advantage of multiphoton microscopy. Fluorescence can be used to label specific components, while SHG and THG provide complementary structural information. Figure 1.10 presents an example of multimodal imaging where 4 different label-free nonlinear signals are detected simultaneously.

3 Three-photon microscopy

In this section we analyse the limits of 2P microscopy at large imaging depths and how 3P microscopy is able to overcome them. We present a more precise study of optical sectioning including an analysis of the SBR depending on several parameters.

3.1 Depth limit in 2PEF

As we have mentioned in the previous section, scattering is a parameter that limits the number of non-scattered photons reaching the focal plane as the imaging depth increases. Assuming that only these ballistic photons contribute to nonlinear excitation, the excitation intensity decreases exponentially in terms of the imaging depth z according to:

$$I(z) = I_0 \exp -\frac{z}{l_s}, \tag{1.1}$$

where I_0 is the excitation intensity at the surface of the sample and l_s the scattering length. We have also seen that 2P excitation is inversely proportional to the duty cycle

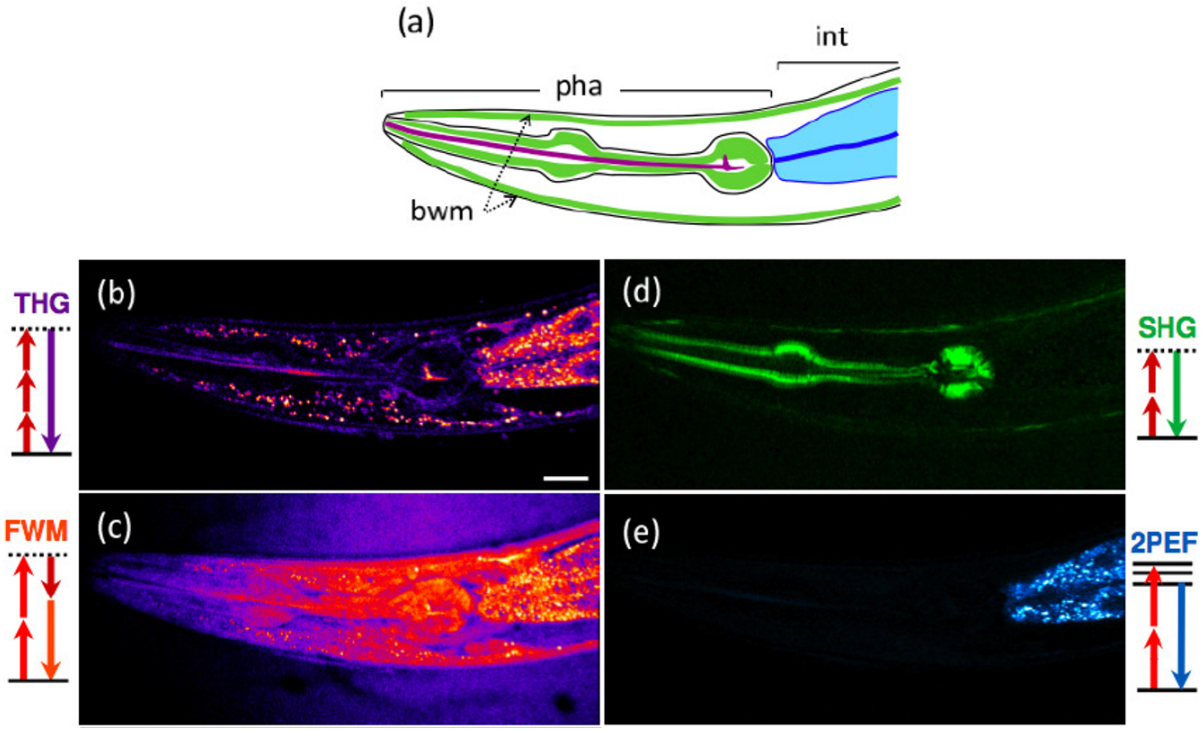

Figure 1.10: Pharynx of a *C. elegans* imaged with four simultaneous channels corresponding to label-free signals: THG (b), Four Wave Mixing (FWM) (c), SHG (d) and endogenous 2PEF. Adapted from [25].

of the laser (τ/T) and scales as the squared excitation intensity (Table 1.1). Thus, the generated 2PEF signal in depth can be expressed as:

$$S_{2PEF} \propto \frac{T}{\tau}\Big(I_0 \exp -\frac{z}{l_s}\Big)^2 = \frac{T}{\tau} I_0^2 \exp -\frac{2z}{l_s}. \tag{1.2}$$

For a given maximum available laser power, P_0, this exponential dependence results in a maximum imaging depth z_{max} at which the signal decays below the sensitivity of the microscope. In the absence of background, one can write [26]:

$$z_{max} \approx l_s \, ln(\alpha P_s \sqrt{\frac{T}{\tau}\phi(z_{max})}),$$

where α is a parameter including fluorophore efficiency as well as detector and shot noise. P_s is the average power available at the surface of the sample and $\phi(z)$ is the collected fraction of fluorescence.
In what follows we review some studies investigating strategies to increase the maximum imaging depth.

3.1.1 Longer excitation wavelengths

One of the parameters that can be adjusted in Equation 1.2 is the wavelength. As we have seen in Figure 1.6, longer wavelengths exhibit longer scattering lengths. With this property in mind, the authors in [27] demonstrated an important increase in imaging depth when using longer excitation wavelengths compared to shorter ones. As seen in Figure 1.11, they imaged the brain of mice *in vivo*. The vasculature of the cortex was labelled

both with fluorescein and Alexa680 emitting at the wavelengths of 515 nm and 700 nm, respectively. 2P excitation was performed sequentially at 775 nm and at 1280 nm. The maximum imaging depth achieved at 1280 nm is of the order of 1 mm whereas at 775 nm excitation the signal is lost at around 600 µm in accordance to other references [28, 29].

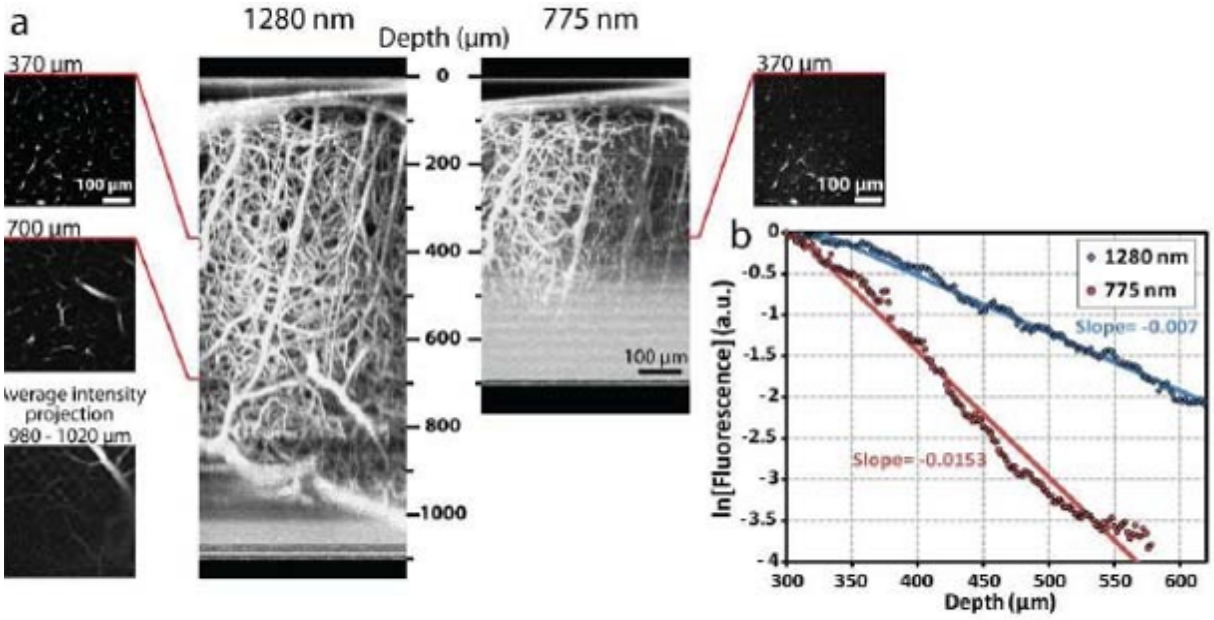

Figure 1.11: *In vivo* 2PEF imaging of mouse cortex vasculature. Normalized image stacks excited at 1280 nm and 775 nm (a) and attenuation of the average intensity in depth (b). The two different slopes correspond to different scattering lengths for each wavelength. Figure from [27].

3.1.2 Amplified pulses

Apart from using longer wavelengths, another parameter affecting the 2PEF signal for a given average excitation power P_0 is the duty cycle of the laser (τ/T).
Some efforts have been done to reduce the pulse duration to smaller values than the typical 100 fs [30,31]. Still, shortening the pulse duration below ≈ 20 fs is useless because the pulse spectral width becomes larger than the excitation spectrum of the fluorophores. Moreover, such short pulses experience considerable dispersion by microscope optical components. This complicates their use in microscopy applications. In practice, sub-20 fs pulses are very rarely used in 2PEF imaging.
The gain in imaging depth can be much more important by reducing the laser repetition rate. This strategy was introduced by Beaurepaire et al. [32] and by Theer and Denk [33]. They proposed the use of regenerative amplifiers on mode-locked lasers used for 2P microscopy. These lasers are typically Ti:Sapphire oscillators working at a repetition rate of 80 MHz. A regenerative amplifier is a device that by means of a switch increases the number of round trips of the pulse inside the resonator cavity. This increases the amplification of the pulses on the gain medium. This way, the average output power of the laser (typically 1 W) is unchanged, but energy is temporally redistributed into more energetic pulses with lower repetition rate. The pulse duration does not vary but the repetition rate can be of the order of 200 kHz. In the absence of saturation, the more energetic the excitation pulses are, the higher the generated fluorescence signal. However, saturation and photodamage thresholds impose a limit peak intensity per pulse I_{pmax}

which leads to a maximum fluorescence signal per pulse F_{pmax}. The total fluorescence signal is then F_{pmax}/T.
Figure 1.12 represents the fluorescence profile in depth. At low depths, excess power is available from the laser. Laser power is therefore adjusted to keep the intensity under the limit I_{pmax} at the focal plane. As imaging depth increases, the laser power is increased exponentially to compensate scattering and maintain a constant detected signal. At some point the power of the laser is tuned to its maximum and the fluorescence profile decreases exponentially with depth. The comparison of two different excitation regimes in Figure 1.12 illustrates how high repetition rates are advantageous at shallow depths since the generated fluorescence rate is high. At deeper planes, however, lower repetition rate lasers perform better.
This strategy comes at the price of a lower average fluorescence level. As the repetition rate decreases, the pixel dwell time needs to be increased if one wants to maintain a constant number of pulses per pixel and signal level. This results in a decrease of the imaging speed and thus, limits the temporal resolution.

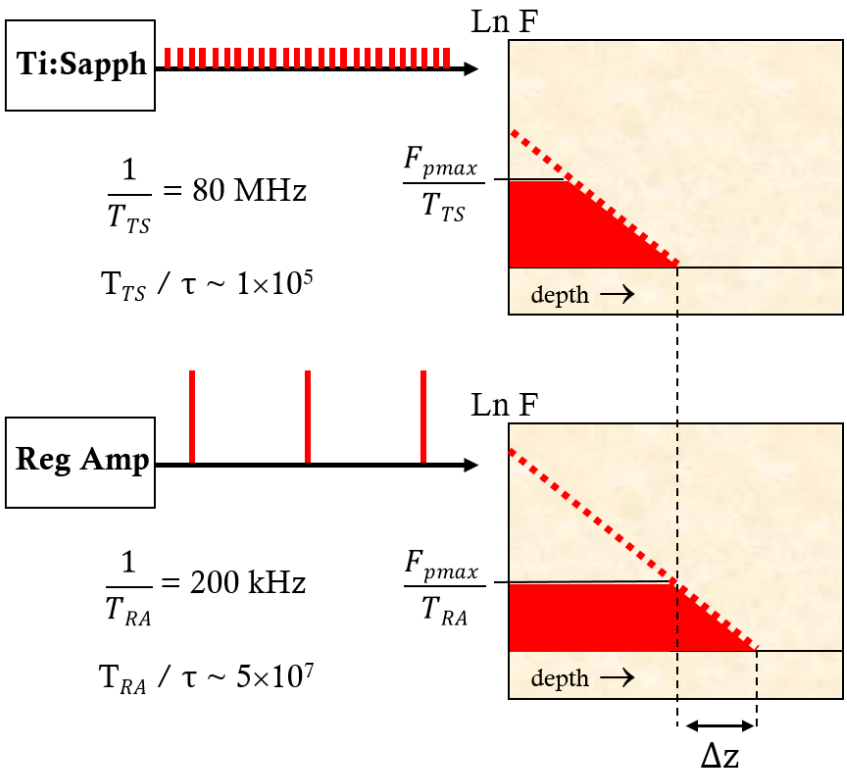

Figure 1.12: 2PEF signal profile in depth. In the first case, a high repetition rate laser gives a strong fluorescence signal at low depth, but the excitation is rapidly attenuated by scattering as the imaging depth increases. With a regenerative amplifier, imaging speed is slower for shallow depths but the low repetition rate allows deeper imaging for the same average excitation power. Inspired from [32].

3.1.3 Loss of SBR in depth in 2PEF

Theer and Denk [33] confirmed experimentally that regenerative amplifiers (200 kHz, 925 nm) can provide deeper 2PEF imaging in brain tissue. They estimated an improvement of ≈ 3 scattering lengths compared with standard mode-locked lasers.

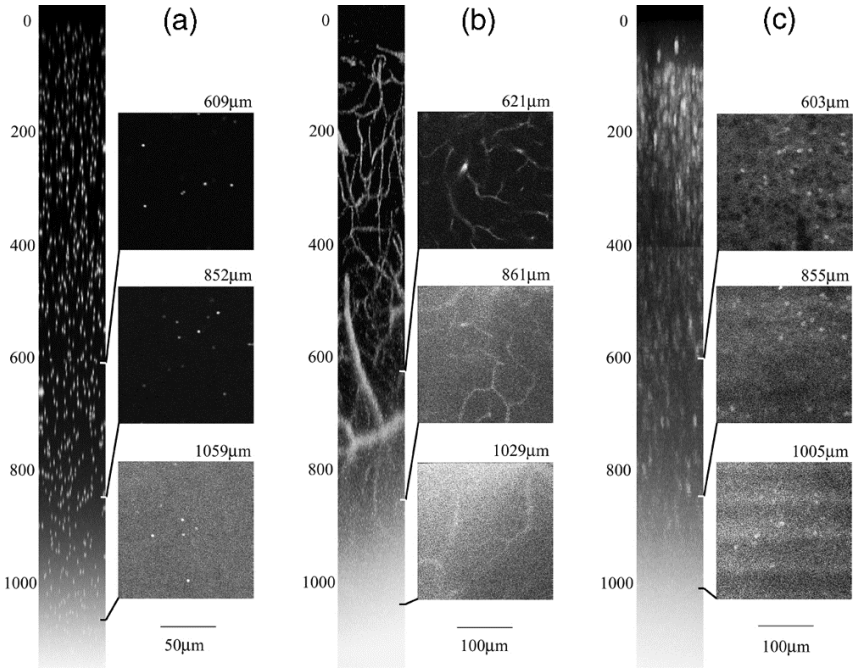

Figure 1.13: Z-stacks of images of tissue phantom made of fluorescent beads (a), stained vasculature in mouse brain (b) and fluorescent labelled mouse neurons (c). Taken from [33].

They demonstrated imaging up to 1050 µm deep in mouse brain with this strategy (see Figure 1.13) without being limited by the required laser power. However, they identified another depth limiting factor: at imaging depths greater than 800 µm, out-of-focus light starts to blur the images. This phenomenon is a fundamental limit of the 2P excitation process which causes a loss of contrast at large imaging depths in scattering samples.
In the next section we analyse in detail the origin of this limitation and present 3P microscopy as an alternative imaging method to overcome it.

3.2 Optical sectioning analysis

In this section we present a more detailed description of optical sectioning in multiphoton microscopy. First, we define the parameters of the focal volume as described by Zipfel et al. in [9] for the case of 2PEF. We generalize them to the case of N-photon excitation. Then, inspired on the model proposed by Xu's group introduced in [34], we derive an expression of the excitation profile in depth in the case of non-scattering and scattering samples. These expressions, also generalized to N-photon excitation, allow to explain some features observed in our experimental measurements. Moreover, based on these calculations, we complete the study with simulations of the SBR that allow to evaluate the effect of experimental parameters such as nonlinear order, excitation wavelength and focusing NA.

3.2.1 Excitation volume and spatial resolution

The dimensions of the focal volume give an estimation of the smallest structures that can be resolved in the images. In microscopy, the illumination intensity near the focus is usually described using the illumination point spread function (PSF). This concept can be generalised to multiphoton microscopy using the linear PSF raised to the power of N, the

order of the excitation process. After Zipfel et al. [9], we can approximate the nonlinear excitation volume as a gaussian-gaussian distribution centered at the focus, with lateral and axial half-widths at $1/e^2$ of this distribution given by:

$$r_{xy} = \begin{cases} \dfrac{0.320\sqrt{2}\,\lambda}{\sqrt{N}\,\mathrm{NA}}, & \text{for NA} \leq 0.7 \quad (1.3) \\ \dfrac{0.325\sqrt{2}\,\lambda}{\sqrt{N}\,\mathrm{NA}^{0.91}}, & \text{for NA} > 0.7 \quad (1.4) \end{cases}$$

$$r_z = \frac{0.532\sqrt{2}\,\lambda}{\sqrt{N}} \left(\frac{1}{n - \sqrt{n^2 - \mathrm{NA}^2}} \right) \quad (1.5)$$

λ is the wavelength at vacuum, N the excitation order of the process, NA the numerical aperture and n the refractive index of the immersion medium. Both expressions, r_{xy} and r_z are used in the following sections to simulate the axial excitation profile and the signal to background ratio.
The focal volume of N-photon excitation is defined as:

$$V_{NP} = \left(\frac{\pi}{2N}\right)^{3/2} r_{xy}^2 r_z$$

Except in the limit of very tight focussing, its dimensions scale with NA as follows: $r_{xy} \propto 1/\mathrm{NA}$, $r_z \propto 1/\mathrm{NA}^2$. Experimentally, the most convenient definition of the width of the spatial gaussian functions is the full width at half maximum (FWHM). Along this thesis we call spatial resolution δ the FWHM of the lateral (along x and y) and axial (along z) profiles measured on 3D stacks of images acquired on small objects, typically fluorescent beads of radius $\leq 0.5\,\mu\mathrm{m}$. This parameter is related to the previous ones by:

$$\delta_{xy} = \sqrt{2\ln 2} \cdot r_{xy} \qquad \delta_z = \sqrt{2\ln 2} \cdot r_z$$

Considering an excitation wavelength of 1300 nm and a water immersion objective of NA = 1.05, the axial resolution is $\approx 1.6\,\mu\mathrm{m}$ with 2P excitation and $\approx 1.3\,\mu\mathrm{m}$ with 3P excitation.

3.2.2 Dependence of 2P and 3P signals on NA

Based on the relations given above, it is also interesting to derive general rules on the dependence of two-photon and three-photon signals on excitation numerical aperture. Assuming moderate focusing for simplicity, we can consider that the excitation volume approximately scales as NA^{-4}, with an axial extent proportional to NA^{-2} and a transverse section S also proportional to NA^{-2}. For a constant incident power P, the intensity at the focus I scales as $P/S \propto \mathrm{NA}^2$. It follows that when the beam is focused in a homogeneous fluorescent medium (with extent larger than the excitation volume, as illustrated in Figure 1.14.a), the total two-photon fluorescence F_{2P} scales as $I^2 V_{2P} \propto \mathrm{NA}^0$ and therefore does not depend on NA. This is a known property of two-photon microscopy: an enlargement of the excitation PSF does not induce a large signal drop when imaging objects larger than the focal volume (for example cell bodies). In contrast, the 3P signal F_{3P} from a large homogeneous object scales as $I^3 V_{3P} \propto \mathrm{NA}^2$, and rapidly decreases when NA is reduced. Maintaining a tight focus is therefore more important in 3P microscopy than in

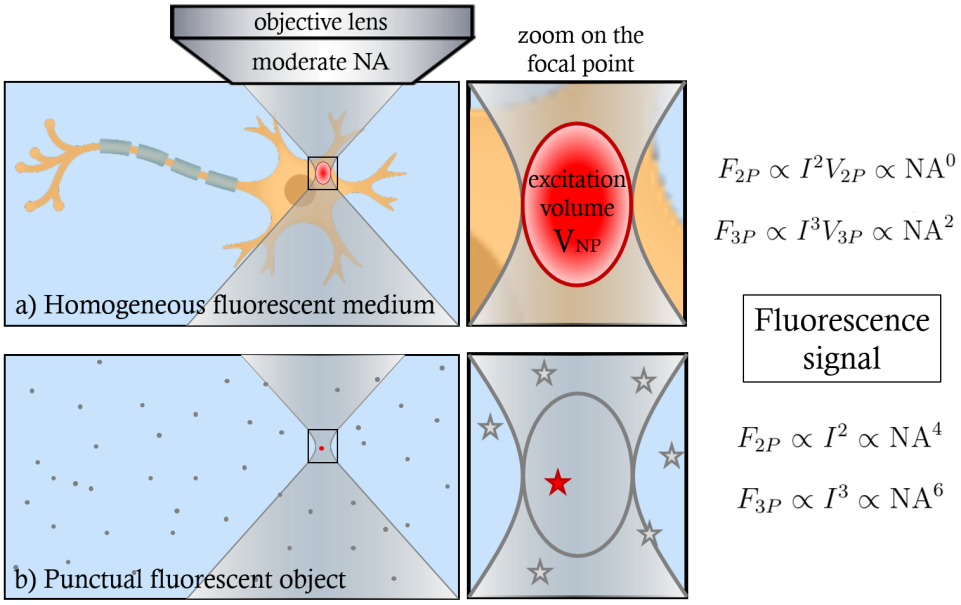

Figure 1.14: Illustration of the 2P and 3P fluorescence signal dependence on NA in the case of: (a) A homogeneous fluorescent medium. At the size scale of the excitation volume dimensions, a labelled cell body appears as a homogeneous medium. (b) A punctual fluorescent object smaller than the excitation volume. Examples of this case are nanoparticles in solution or small sample features.

2P microscopy. We can also note that in the case of a point-like object (Figure 1.14.b), 2P signals scale as $F_{2P} \propto I^2 \propto \mathrm{NA}^4$ and 3P signals have an even stronger dependence on NA scaling as $F_{3P} \propto I^3 \propto \mathrm{NA}^6$.

3.2.3 Axial Signal

As in light sheet microscopy, the optical sectioning in multiphoton microscopy is achieved by confining the excitation to the imaging plane. In the following section, we derive a simple model to compare the axial distribution of fluorescence excitation in multiphoton microscopy. This model will help us analyse the optical sectioning properties of multiphoton microscopy in transparent and scattering samples.
We define the axial signal, $S_N(z)$, as the total excitation intensity in each plane perpendicular to the optical axis raised to the power of the nonlinear order of the process N. It can be expressed mathematically as:

$$S_N(z) = \iint_{-\infty}^{+\infty} I^N(x, y, z)\, dxdy$$

Non-scattering sample

Let us consider a Gaussian profile for the excitation intensity as:

$$I(r, z) = I_0 \left(\frac{w_0}{w(z)} \right)^2 \exp\left\{ \frac{-2r^2}{w(z)^2} \right\},$$

where the beam radius at $1/e^2$ is defined as

$$w(z) = w_0\sqrt{1+\left(\frac{z}{z_R}\right)^2},$$

where w_0 is the beam waist and z_R the Rayleigh range defined as $z_R = \dfrac{\pi w_0^2 n}{\lambda}$, with n the refractive index and λ the wavelength of the beam in free space.
With this geometry it is more convenient to work in cylindrical coordinates:

$$S_N(z) = \int_0^{2\pi}\int_0^{+\infty} I^N(r,z)\,dr d\theta = 2\pi\int_0^{+\infty} rI^N(r,z)\,dr \tag{1.6}$$

Let us calculate this integral for the case of 1, 2 and 3P excitation.[2]

- **N = 1: linear excitation**

$$\begin{aligned} S_1(z) &= 2\pi\int_0^{+\infty} rI(r,z)\,dr = 2\pi I_0\left(\frac{w_0}{w(z)}\right)^2\int_0^{+\infty} r\exp\left\{\frac{-2r^2}{w(z)^2}\right\}dr \\ &= 2\pi I_0\left(\frac{w_0}{w(z)}\right)^2\frac{w^2(z)}{4} = \frac{1}{2}\pi I_0 w_0^2 \equiv P_0. \end{aligned}$$

  This result confirms that the excitation axial profile in linear microscopy is constant and equal to the excitation power, which explains why there is no optical sectioning. The out-of-focus light comes from all the planes at the same magnitude and degrades the image SBR. Techniques as confocal pinholes are needed to improve it.

- **N = 2: Two-photon excitation**

$$\begin{aligned} S_2(z) &= 2\pi\int_0^{+\infty} rI^2(r,z)\,dr = 2\pi I_0^2\left(\frac{w_0}{w(z)}\right)^4\int_0^{+\infty} r\exp\left\{\frac{-4r^2}{w(z)^2}\right\}dr \\ &= 2\pi I_0^2\left(\frac{w_0}{w(z)}\right)^4\frac{w^2(z)}{8} = \frac{P_0^2}{\pi w(z)^2} \propto \frac{1}{z^2}. \end{aligned}$$

  This result demonstrates the axial confinement in 2P microscopy. It indicates that the excitation decays as $1/z^2$ away from the focal plane, providing a strong sectioning.

- **N = 3: Three-photon excitation**

$$\begin{aligned} S_3(z) &= 2\pi\int_0^{+\infty} rI^3(r,z)\,dr = 2\pi I_0^3\left(\frac{w_0}{w(z)}\right)^6\int_0^{+\infty} r\exp\left\{\frac{-6r^2}{w(z)^2}\right\}dr \\ &= 2\pi I_0^3\left(\frac{w_0}{w(z)}\right)^6\frac{w^2(z)}{12} = \frac{4}{3}\frac{P_0^3}{\pi^2 w(z)^4} \propto \frac{1}{z^4}. \end{aligned}$$

  This result shows that the axial sectioning in 3P microscopy is stronger than that of 2P microscopy. The excitation in this case decays as $1/z^4$ away from the focal plane.

[2]The following result is used for the integration of S_N in each case: $\int_0^{+\infty} x\exp\{-2N(\frac{x}{a})^2\}\,dx = \frac{a^2}{4N}$. This solution is easily achieved by the following change of variable $u = -2N\left(\frac{x}{a}\right)^2$.

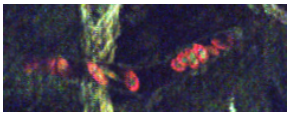

- **General case: N-photon excitation**
  The previous results can be summarized in a general expression for the axial confinement:

$$S_N(z) = \frac{P_0^N}{N}\left(\frac{2}{\pi w(z)^2}\right)^{N-1} \propto \left(\frac{1}{z^{N-1}}\right)^2.$$

These expressions have been adapted to compare the axial signal in linear, 2P and 3P excitation. The simulations use an excitation wavelength of $\lambda = 1300\,\text{nm}$ and a typical scattering length of $l_s = 315\,\mu\text{m}$. As in our experimental system described in Chapter 2, we use a NA = 1.05. Figure 1.15 shows the axial signal in terms of imaging depth when the laser is focused 1500 µm deep inside a transparent medium.

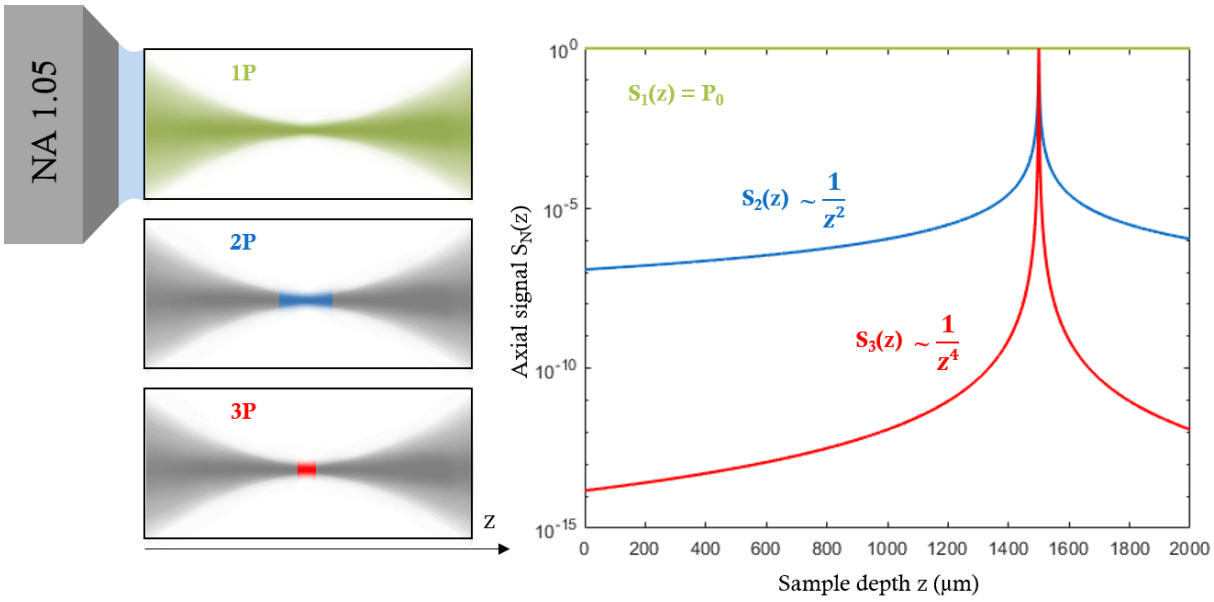

Figure 1.15: Calculations of axial signal in a transparent medium. Simulation parameters: excitation wavelength $\lambda = 1300\,\text{nm}$, scattering length $l_s = 315\,\mu\text{m}$, objective lens numerical aperture NA = 1.05, focusing depth $z_f = 1500\,\mu\text{m}$.

In the graph in Figure 1.15 it can be observed that the signal coming from other planes is orders of magnitude lower than that from the focal plane in multiphoton microscopy. For the case of 2P, for instance, in the simulated conditions, excitation at the surface is seven orders of magnitude below the near-focus fluorescence, causing no background. For non-scattering samples, thus, 2P microscopy performs well in depth. Let us analyse now the case of a scattering sample.

Scattering sample

In this case we consider the same excitation profile as in the previous case but with an exponentially decreasing factor according to Equation 1.1:

$$I(r,z) = I_0\left(\frac{w_0}{w(z)}\right)^2 \exp\left\{\frac{-2r^2}{w(z)^2}\right\} \exp\left\{\frac{-z}{l_s}\right\}.$$

The results of the integral in Equation 1.6 for this case can be similarly derived since the scattering factor does not depend on the surface coordinates:

- **N = 1: linear excitation**

$$S_1(z) = \frac{1}{2}\pi I_0 w_0^2 \exp\left\{\frac{-z}{l_s}\right\} = P_0 \exp\left\{\frac{-z}{l_s}\right\}.$$

- **N = 2: Two-photon excitation**

$$S_2(z) = \frac{P_0^2}{\pi w(z)^2} \exp\left\{\frac{-2z}{l_s}\right\} \propto \frac{1}{z^2} \exp\left\{\frac{-2z}{l_s}\right\}.$$

- **N = 3: Three-photon excitation**

$$S_3(z) = \frac{4}{3}\frac{P_0^3}{\pi^2 w(z)^4} \exp\left\{\frac{-3z}{l_s}\right\} \propto \frac{1}{z^4} \exp\left\{\frac{-3z}{l_s}\right\}.$$

- **General case: N-photon excitation**

$$S_N(z) = \frac{P_0^N}{N}\left(\frac{2}{\pi w(z)^2}\right)^{N-1} \exp\left\{\frac{-Nz}{l_s}\right\} \propto \left(\frac{1}{z^{N-1}}\right)^2 \exp\left\{\frac{-Nz}{l_s}\right\}.$$

The expressions show that all excitation profiles are attenuated by an exponential decay. In practice, this attenuation is compensated by increasing the laser power with imaging depth, in order to maintain a constant intensity in the focal plane and therefore a constant signal level. The consequence is that more fluorescence is generated in the superficial regions of the sample. This is visible in the simulation in Figure 1.16, where 2P and 3P excitation profiles are normalized to unity at the focal plane.

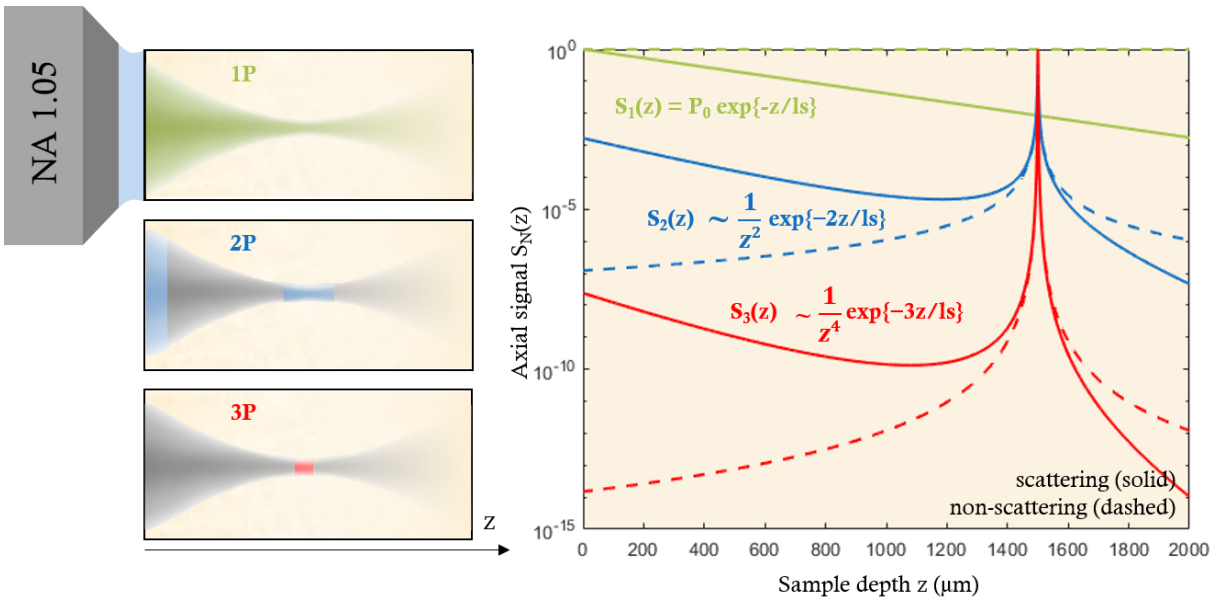

Figure 1.16: Calculations of axial signal in a scattering medium (solid lines), and in a non-scattering medium (dashed lines). Simulation parameters: excitation wavelength $\lambda = 1300\,\text{nm}$, scattering length $l_s = 315\,\mu\text{m}$, objective lens numerical aperture NA = 1.05, focusing depth $z_f = 1500\,\mu\text{m}$. The multiphoton axial signal profiles are normalized to keep constant excitation at the focus as laser power is increased to keep a constant signal in depth.

In other words, the SBR of 2P microscopy degrades at large depths in scattering samples. Indeed, the exponential decay factor on the axial signal profile (blue solid line in

Figure 1.16) results in out-of-focus light generated at the surface of the sample. As illustrated in the simulation, 2P fluorescence produced in superficial regions is comparable to that produced near focus when the beam is focused at ≈ 4 scattering lengths below the surface. 3P excitation is an efficient strategy to overcome this limitation. Since the axial confinement is stronger for 3P processes (decaying as z^{-4} away from the focal plane in transparent media) the superficial 3P excitation remains orders of magnitude smaller than the near-focus signal even at depths exceeding 6 scattering lengths (see Figure 1.16). Out-of-focus 3P excitation in a scattering medium remains even lower than out-focus 2P excitation in a transparent sample (blue dashed line).

We did an experimental demonstration of this 3P advantage for deep imaging in a scattering sample with the system described in Chapter 2. Our collaborators at Institut de la Vision (Jean Livet's team) provided us with a fixed P14 cytbow mouse brain, which exhibits dense cytoplasmic tdTomato labelling. We imaged this brain at increasing depths with 2P excitation at 1030 nm and with 3P excitation at 1700 nm. Figure 1.17 illustrates how the SBR decreases with depth in the case of 2P microscopy, while it is maintained with 3P excitation. The degradation of SBR with depth in 2P imaging can be attributed to the presence of out-of-focus fluorescence produced near the surface and producing a homogeneous background.

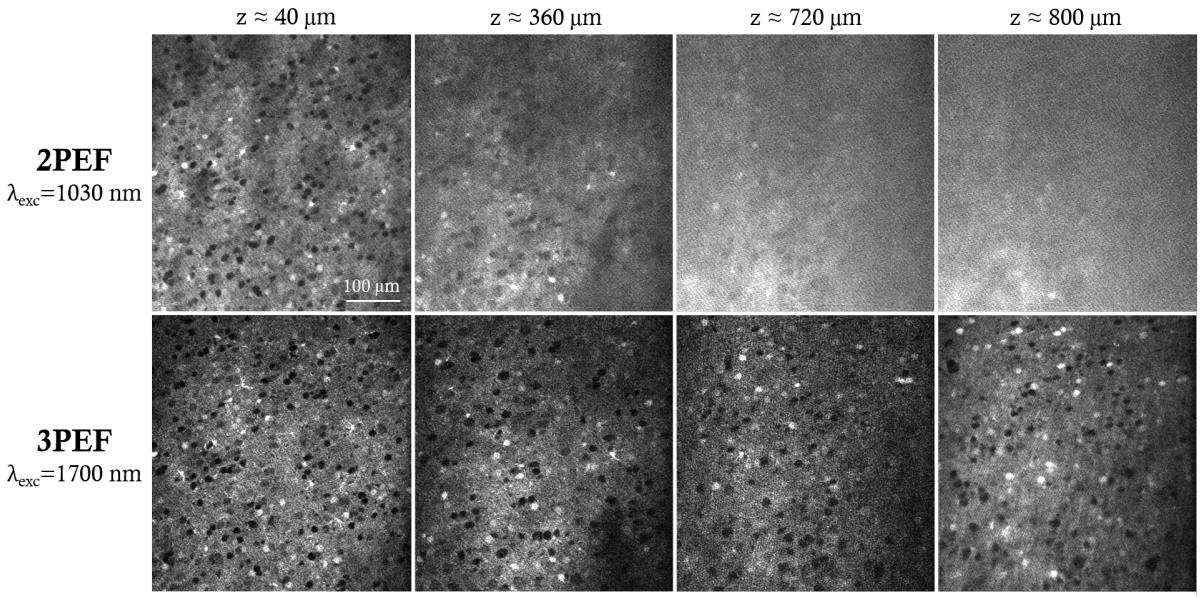

Figure 1.17: Comparison of 2P and 3P imaging at different depths of a P14 cytbow (tdTomato labelling) mouse brain. The SBR decreases with depth in 2P microscopy images due to the presence of background fluorescence produced in superficial regions.

3.2.4 Signal to Background Ratio

Following the analysis of Horton et al. [34], the expressions of the fluorescence axial distribution derived in the previous section can be used for calculations of the SBR.

We define the **signal** as a quantity proportional to the integral of the axial signal within the excitation volume. The proportionality constant depends on experimental parameters such as the absorption cross section and quantum yield of the fluorophores as well as the

collection and detection efficiency of the system.

Concerning the background, we can distinguish between two types [35]: bulk background and defocus background. The first one accounts for the out-of-focus light mainly generated at the surface due to the loss of axial confinement combined with the compensation of power loss due to scattering in depth. With the same constant as for the signal, we define this bulk **background** proportional to the integral of the axial signal within one scattering length of the tissue from the surface, since the out-of-focus light is mostly generated there. Both integrals, signal and bulk background, are represented as the surface under the axial signal curve in Figure 1.18.a. The defocus background has a different origin. The focussing PSF degrades due to tissue aberrations becoming a larger spot rather than a sharp focal point. The side lobes of this distorted PSF, though less important than in 2P microscopy, result in a background which can appear even at shallow depths. In the following simulations we take only the bulk background into account to study the effect of the imaging depth.

Consequently, the SBR is:

$$SBR_N(z) = \frac{\int_{z_f - r_z}^{z_f + r_z} S_N(z)\, dz}{\int_0^{l_s} S_N(z)\, dz},$$

where z_f is the focussing depth and r_z refers to the axial extension of the N-photon excitation volume as defined in Equation 1.5.

This simple model does not take into account the degradation of the illumination PSF in depth caused by scattering and aberrations. PSF degradation causes a reduction of the intensity at focus and of the signal, particularly in the case of 3P excitation. For this reason, the absolute SBR values given in the following simulations are overestimated and should not be taken as a quantitative reference to which compare experimental data. Nevertheless, the model allows relative comparisons of the SBR and is accurate to understand the effect of the experimental parameters. The integrals were performed numerically and are shown in Figure 1.18.b for the case of non-scattering and scattering samples.
It can be seen that in the case of the simulation parameters (1300 nm excitation, l_s = 315 µm, NA = 1.05 and z_f = 1500 µm), at a focusing depth of 750 µm the SBR at 3P on scattering samples is already superior than that of 2P in transparent samples. The figure also shows that when imaging through scattering samples of this thickness the SBR at 2P strongly decreases resulting in blurred images as shown in Figure 1.17, whereas 3P excitation presents a SBR six orders of magnitude higher. This model considers a uniform labelling of density 1 of the sample volume. Less dense labelling results in a lower axial signal profile, proportional to the label density. Non-uniformly labelled samples present changes on the profile. The labelling density also affects the bulk background since sparser labelling results in less fluorescence. At 2 % of labelled volume fraction as in brain vasculature, the maximum imaging depth in 2P excitation is predicted to be ≈ 5 l_s (where the SBR approaches 1) [14, 33, 36]. Experimentally, this limit at ≈ 920 nm excitation has been measured to appear at a depth ranging from 450 to 850 nm in the

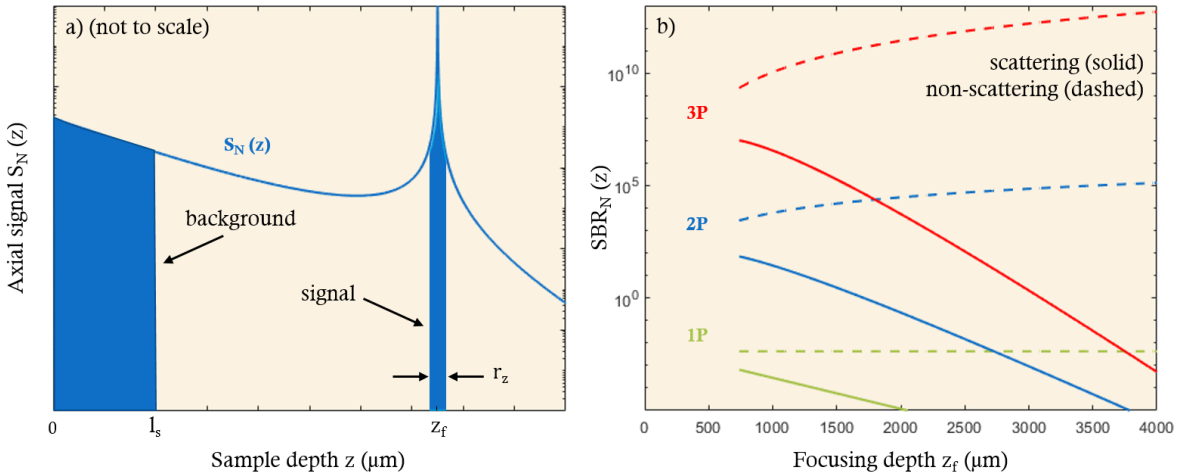

Figure 1.18: a) Signal and background integrals representation as the surface under the axial signal curve. The scattering lentgh and the excitation volume are not to scale to help the visualisation. b) SBR comparison for 1, 2 and 3P excitation in the case of non-scattering (dashed lines) and scattering sample (solid lines). Simulation parameters: excitation wavelength λ = 1300 nm, scattering length l_s = 315 µm, objective lens numerical aperture NA = 1.05, focusing depth z_f = 1500 µm.

mouse cortex depending on the sample variation and density of the labelling [33, 37, 38]. Different alternatives have been proposed to reduce this background, such as low-density labelling, layer specific labelling or neocortex removal [35].
On the other hand, 3P microscopy maintains image contrast at larger depths. SBR was measured to be ≈ 40 at a depth of 2100 µm excited at 1700 nm, corresponding to ≈ 5 l_s [39].
Figure 1.18.b also illustrates well the absence of optical sectioning that provides poor contrast in linear microscopy, justifying the use of confocal pinholes or other strategies. This result is consistent with those presented by Horton et al. [34]. In the supplementary information they present the following expressions of SBR for 2P and 3P excitation:

$$SBR_{2P} \approx \frac{6(NA)^2 z^2}{\lambda\, l_s} \exp\left\{-\frac{2z}{l_s}\right\} \tag{1.7}$$

$$SBR_{3P} \approx \frac{14.7(NA)^6 z^4}{\lambda^3\, l_s} \exp\left\{-\frac{3z}{l_s}\right\} \tag{1.8}$$

With the model we have described, we simulate in the following sections the effect that several parameters (NA, λ, l_s and absorption) have on the axial signal and on the SBR.

3.2.5 Effect of the numerical aperture

Figure 1.19 shows the importance of using high NA objectives, especially for 3P excitation (SBR_{3P} scales as NA^6 according to Equations 1.7 and 1.8). In the case of an excitation at 1300 nm and l_s = 315 µm, an order of magnitude improvement in SBR is predicted at 750 µm of imaging depth by exciting with a NA of 1.1 instead of 0.7. This can be understood as follows: higher NA means higher angle of the illumination cone. This results in a stronger focussing at the focal plane (enhancing the signal) and a larger illuminated area at the planes close to the sample surface, resulting in lower intensity for the same

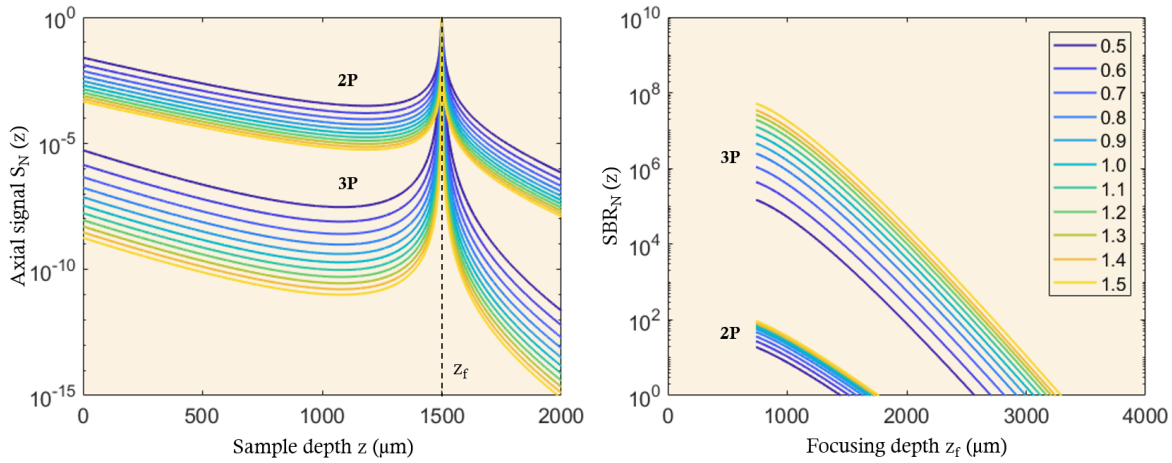

Figure 1.19: Axial signal at a focusing depth of $z_f = 1500\,\mu m$ (left) and SBR (right) simulated for different values of the numerical aperture for 2P and 3P excitation. Simulation parameters: excitation wavelength $\lambda = 1300\,nm$, scattering length $l_s = 315\,\mu m$, immersion liquid refractive index $n = 1.33$.

excitation power compared to lower NA excitation (reducing the background). However, not many high NA objectives are available providing both a large working distance and good infrared transmission. Being usually used also for epidetection, an ideal objective for 3P microscopy should transmit a remarkably large range of wavelengths ranging from 350 to 1700 nm, which is not commonly available.

3.2.6 Effect of the wavelength

Now we examine the dependence of the axial signal and the SBR on the wavelength.

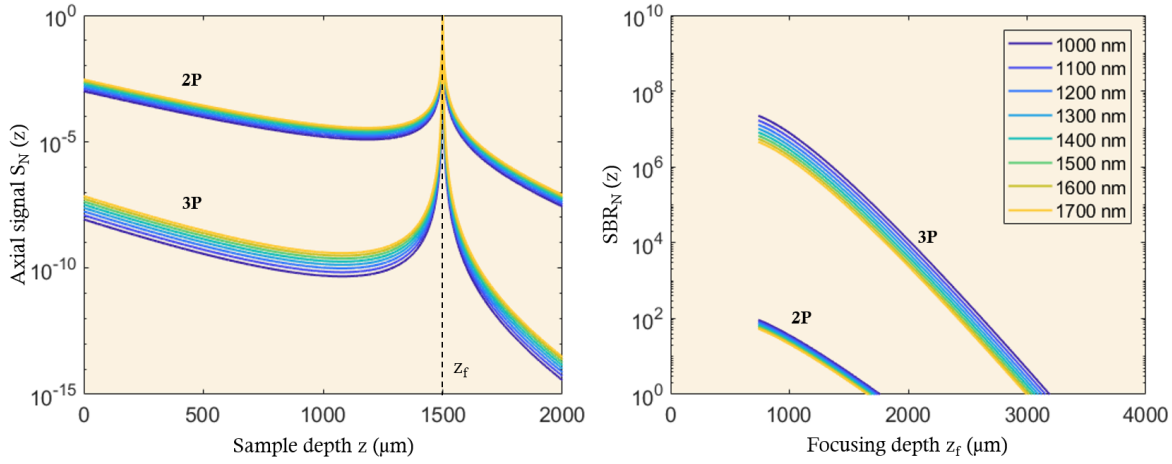

Figure 1.20: Axial signal at a focusing depth of $z_f = 1500\,\mu m$ (left) and SBR (right) simulated for different wavelengths using 2P and 3P excitation assuming constant l_s. Simulation parameters: scattering length $l_s = 315\,\mu m$, objective lens numerical aperture NA = 1.05, immersion liquid refractive index $n = 1.33$.

Figure 1.20 presents a theoretical simulation where the wavelength varies while l_s is kept constant. The SBR is improved when imaging with shorter wavelengths, although the

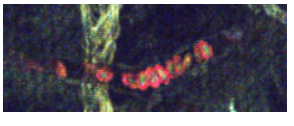

effect is limited, in accordance to Equations 1.7 and 1.8. As shown above (Figure 1.6), however, l_s does depend on the wavelength. The effect of this dependence is analysed in the following analyses.

3.2.7 Effect of the scattering length

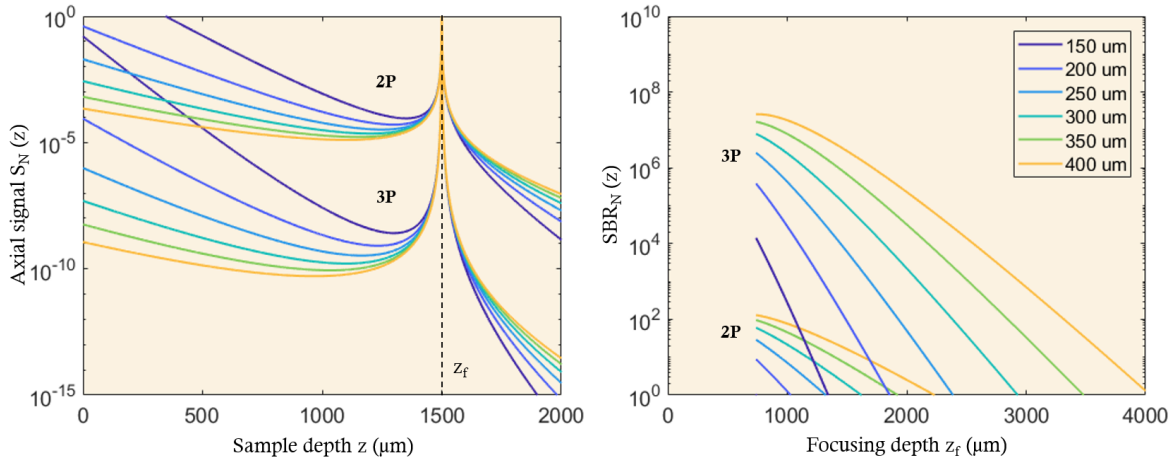

Figure 1.21: Axial signal at a focusing depth of $z_f = 1500\,\mu m$ (left) and SBR (right) simulated for different scattering mean free paths for 2P and 3P excitation. Simulation parameters: excitation wavelength $\lambda = 1300\,nmm$, objective lens numerical aperture NA = 1.05, immersion liquid refractive index $n = 1.33$.

Figure 1.21 confirms that the scattering properties of the tissue have a drastic effect on the axial signal and SBR as predicted by Equations 1.7 and 1.8. The shorter the scattering length, the shorter the light penetration depth inside the tissue, resulting in a loss of SBR. On the other hand, shorter scattering lengths are associated with shorter wavelengths (see Section 2.3.2), for which we have just seen that the SBR is improved compared to longer wavelengths. For this reason, it is more realistic to include the dependence of the scattering length on the wavelength to evaluate both effects simultaneously. This dependence is analysed together with absorption in the following section.

3.2.8 Effect of the absorption

Until the development of 3P microscopy, absorption has often been considered to play a negligible role compared to scattering in multiphoton microscopy. The reason is that the excitation wavelengths commonly used lay within the so-called optical window of biological tissues. This wavelength range located between 0.7 and 1.3 µm corresponds to the region for which light absorption by tissue components (water, blood, lipids) is minimal. At the longer excitation wavelengths used for 3P excitation, however, tissue absorption is an important parameter to take into account. It contributes significantly to the attenuation of the excitation light reducing the number of photons that reach the focal point, and to tissue heating. Figure 1.22 presents the spectral properties of the main biological absorbers.
The absorption coefficient is the inverse of the absorption length l_a, a parameter that describes the exponential decay of excitation light in depth caused by absorption in an

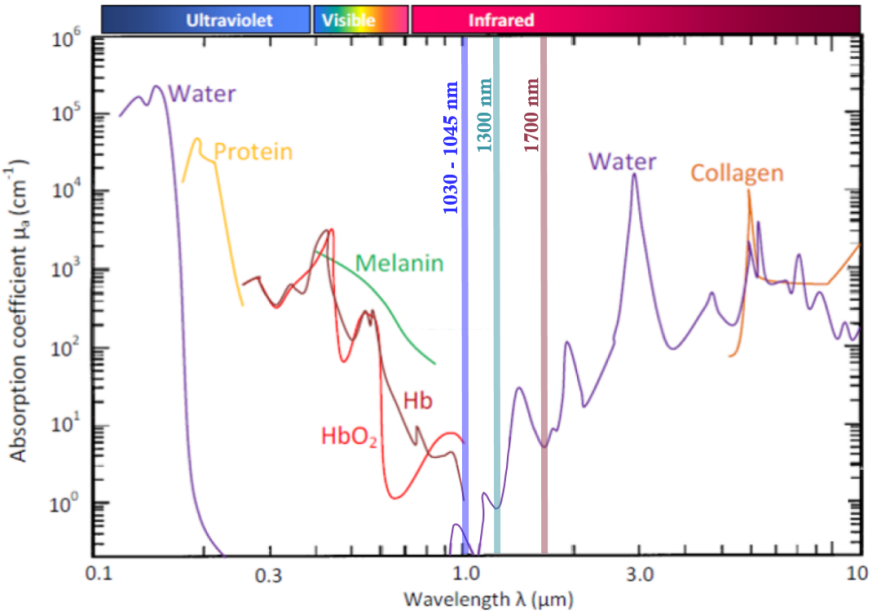

Figure 1.22: Absorption coefficient of the main components of biological tissues including water, proteins, melanin, oxygenated (HbO_2) and de-oxygenated (Hb) hemoglobin and collagen. The main excitation wavelengths (from 1030 to 1700 nm) used in this thesis have been indicated with vertical lines. Adapted from [40].

equivalent way as that of scattering. Therefore, the two effects can be combined and quantified by means of the effective attenuation length, l_e, defined as:

$$\frac{1}{l_e} \equiv \frac{1}{l_a} + \frac{1}{l_s}.$$

Water is the main component of tissues, and as seen in Figure 1.22 its absorption is low between 200 and 1000 nm. For this reason, signal attenuation with depth in 2P microscopy is dominated by scattering.

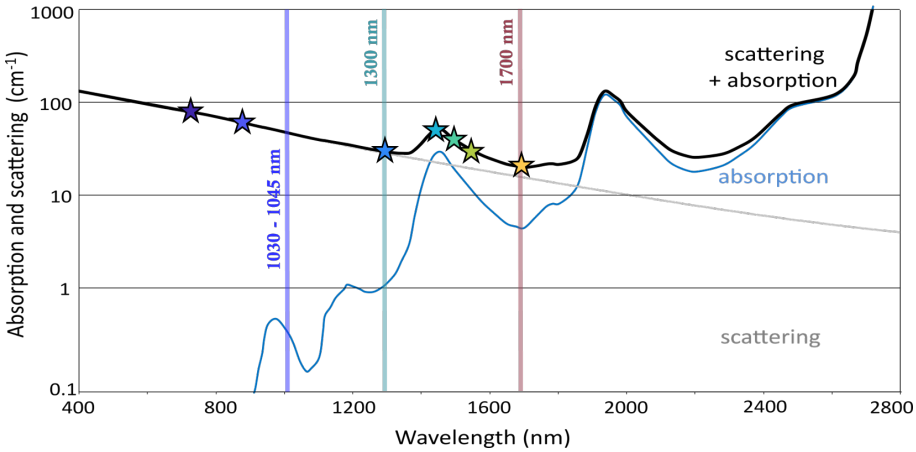

Figure 1.23: Tissue scattering (grey) and water absorption (blue) coefficients and the combination of the two effects (black) plotted together with experimental points reviewed or measured in [41] (coloured stars). The main excitation wavelengths (from 1030 to 1700 nm) used in this thesis have been indicated with vertical lines. Adapted from [42].

3P microscopy needs longer wavelengths to excite the same fluorophores and thus water

absorption becomes a concern. Xu et al. [41] conducted a study in which a theoretical model of the attenuation inside the *in vivo* mouse brain is validated through experimental measurements. The authors conclude that up to 1300 nm, attenuation is dominated by scattering. For longer wavelengths, however, water absorption increases and the combination of the two effects needs to be taken into account. Beyond this wavelength, the assumption that longer wavelengths penetrate deeper inside the tissue is no longer valid as shown by the black curve in Figure 1.23.
From the figure, it can be concluded that the best wavelengths to perform 3P excitation minimizing the combined effect of absorption and scattering are 1300 and 1700 nm. Although this is a very valuable information, one must bear in mind that it is valid for the mouse cortex, but that scattering properties depend on the tissue and slightly different minima may be found in other cases. Nevertheless, no significant changes are expected since water absorption remains the same for all tissues. These results give good indicative values for deep tissue imaging. The following table summarizes the effective attenuation values at different wavelengths [41] inside the mouse cortex (coloured stars in Figure 1.23):

λ (nm)	775	920	1300	1450	1500	1550	1700
l_e (µm)	131	155	315	191	246	286	375

We have used this data to simulate the axial signal and SBR in mouse cortex in more realistic conditions than in the previous sections where the parameters varied independently. The results are shown in Figure 1.24 and confirm that the best SBR are achieved indeed at 1300 and 1700 nm excitation, although the precise minima depend slightly on the tissue l_s. The dependence of l_e on wavelength has a strong effect on imaging depth. If we consider that the minimal acceptable SBR is 2, it can be seen in Figure 1.24 that the maximum 3P imaging depth in the mouse cortex is increased by a factor of more than two by changing from 1450 to 1700 nm excitation.

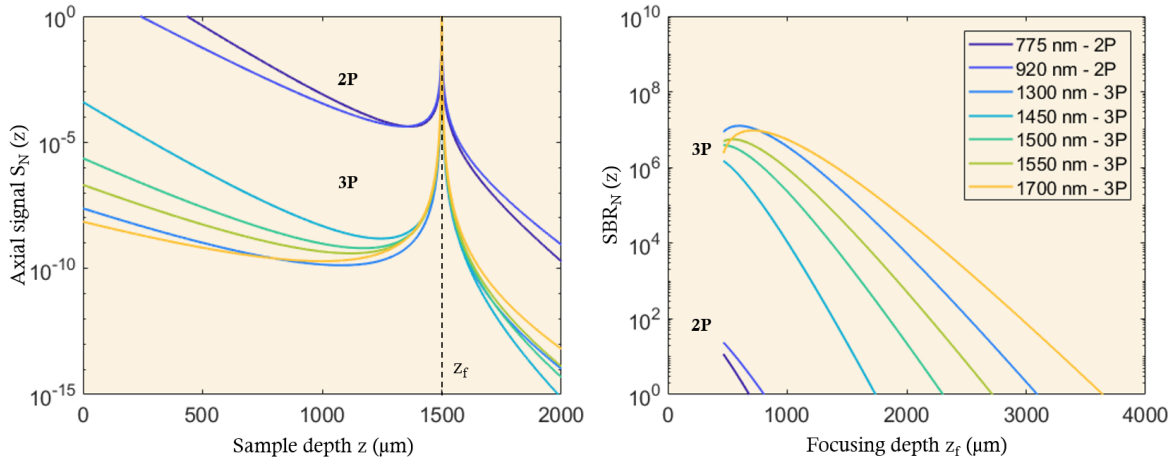

Figure 1.24: Axial signal at a focusing depth of $z_f = 1500$ µm (left) and SBR (right) simulated for different typical conditions at 2P and 3P excitation. Simulation parameters: objective lens numerical aperture NA = 1.05, immersion liquid refractive index $n = 1.33$, l_e values are those referenced for the mouse cortex on the table above.

In conclusion, these simulations show together that the important excitation parameters affecting the imaging depth are NA and the effect of the wavelength on scattering and

absorption. High NA and excitation around 1300 and 1700 nm are preferred for deep imaging.

3.3 State of the art (2018) of 3P microscopy

Initial demonstrations of 3P microscopy were reported in 1996 by three different research groups [43–45], but its potential for deep imaging was not completely identified at that time. Technical difficulties were undeniably present: 3P imaging required both higher excitation pulse energy than that needed for 2P excitation and also longer excitation wavelengths, which seemed difficult to obtain with the available commercial sources of the time. Additionally, there were concerns about tissue heating as well as technical difficulties which delayed the development of laser sources adapted to 3P microscopy.

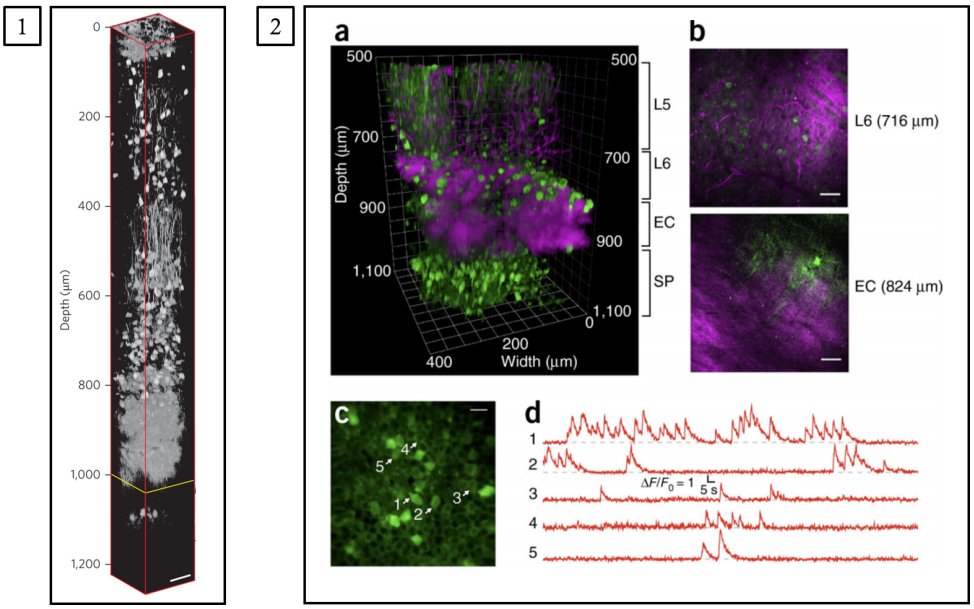

Figure 1.25: 1. Three-dimensional reconstruction of a z-stack of 3P images of a labelled brain containing RFP on pyramidal neurons excited at 1700 nm. Adapted from [34]. **2.** 3P images of spontaneous activity in neuronal population labelled with GCaMP6s in the SP layer of the CA1 region of the mouse hippocampus (green, fluorescence; magenta, THG). (a) 3D reconstruction of 3PM images of GCaMP6s-labelled neurons in the mouse cortex and the hippocampus. (b) Selected XY frames at various depths in a. THG visualizes blood vessels and myelinated axons. Scale bars, 50 µm. (c) Activity recording site in the SP layer of the hippocampus located at 984 µm beneath the dura. Scale bar, 20 µm. (d) Spontaneous activity recorded from the labelled neurons indicated in c. Figure from [46].

A more active research on the topic awakened in the beginning of the 2010s pioneered by the group of Chris Xu at Cornell University. In 2013 [34], they analysed some of the parameters involved in 3P excitation and identified 1300 and 1700 nm as the best candidate wavelengths taking into account scattering and absorption as seen in the previous section. They demonstrated the axial sectioning performance of 3P microscopy (Figure 1.25.1, [34]). In addition, the emergence of new commercial and lab-built [42] laser sources delivering µJ femtosecond pulses in the short wavelength infrared (SWIR) range facilitated the development of 3P microscopy in the following years. In 2017, the recently developed

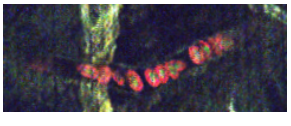

GCaMP6 calcium indicator allowed the first 3P excitation (at 1300 nm) of neuronal activity in the hippocampus in an intact mouse brain [46]. The authors demonstrated the acquisition of the spontaneous activity of 150 neurons at 1 mm depth and with high spatial and temporal resolution as shown in Figure 1.25.2. Moreover, in 2018, 1300 nm-excited 3P functional imaging at single-cell resolution was demonstrated at a depth of 500 µm through the intact skull of a mouse [47].

3.4 Limitations in 3P microscopy

In Section 3.2 we have discussed why 3P microscopy is superior to 2P microscopy for imaging deep inside scattering tissues. However, there are technical and experimental issues associated with the efficient implementation of 3P microscopy. These are principally: (i) the need for adapted laser sources; (ii) the limited number of parameters and signals that can be observed on a 3P microscope; (iii) the reduced imaging speed, and (iv) the potentially increased photodamage. The first two limitations are discussed in more detail in Chapters 2, 3 and 4 of this thesis in which we present the efforts that we have done to overcome them. In the remaning part of this section, we briefly discuss the two last issues.

3.4.1 Compromise between imaging speed and imaging depth

We have stated in Section 3.1.2 that to extend the imaging depth in 2P microscopy the laser duty cycle can be reduced. According to the expressions in Table 1.1, 3P excitation depends on the duty cycle raised to the power of -2. This reveals that the temporal parameters of the laser are critical for the optimisation of the signal. Therefore, microscopists seek to reduce both the repetition rate and the pulse duration of the laser. In this section, we focus on the decrease of the repetition rate, which provides a lower fluorescence signal per unit of time at the surface of the sample but allows a higher imaging depth.
To compensate for signal attenuation caused by scattering and absorption in depth, the laser power can be increased. The rate of this increase is determined by l_e (Section 3.2.8). Without any means of attenuation compensation (which happens in depth when the laser has reached its maximum power), an exponential decay of the signal is observed in depth. An alternative way to keep a constant signal is then to scan several times the sample and cumulate all the frames.
These two strategies both result in slowing down the imaging speed. Indeed, reducing the duty cycle results in less pulses per second. The pixel dwell time is increased to keep the number of pulses per pixel constant. Thus, a compromise between imaging depth and imaging speed must be made depending on the application.

3.4.2 Photodamage

Photodamage can be present in the form of thermal effects (linear) or in the form of nonlinear effects [48].

Heat-induced damage affects the entire illuminated volume of tissue and depend mostly on the average power administered to the sample, but also on the FOV size and on imaging depth. Due to the increased absorption coefficient of water corresponding to

longer wavelengths, 3P excitation causes more tissue heating than 2P for the same average power [12, 49, 50].

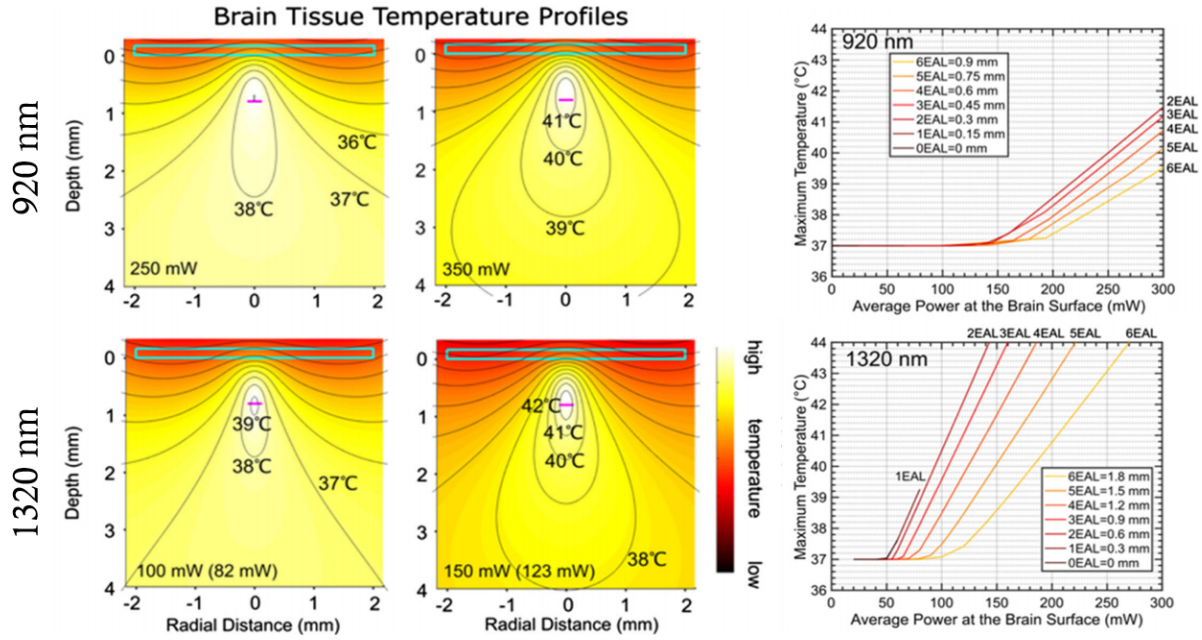

Figure 1.26: Left: light intensity distribution and brain temperature profile simulated for 920 nm 2PM and 1320 nm 3PM, after 60 s of continuous scanning (sufficient to reach steady states) at the given average power (the bottom left corner of each plot). For 1320 nm, the distinction is made between the average power after the objective lens and at the brain surface (in brackets), due to the absorption by the immersion water (H2O). The absorption by immersion water is negligible at 920 nm, and the power at the brain surface is equal to that after the objective lens. Right: The maximum brain temperature as a function of imaging depth and average power, calculated by Monte Carlo simulation for 920 and 1320 nm. Figures adapted from [38, 35].

Xu et al. developed numerical simulations to investigate tissue heating during 3P imaging. They used a Monte Carlo method to estimate the temperature profile inside the mouse brain comparing it to experimental data [38,51]. These studies compare 2P excitation at ≈ 920 nm and 3P excitation at ≈ 1320 nm. They demonstrate that heat dissipation through a cranial window on top of the mouse brain allows keeping the tissue at a physiological temperature ≤ 37 °C down to a certain depth. As imaging depth increases, attenuation losses are compensated by an increase in power. However, the window dissipation is not enough to compensate for the increased heating. This continuous heating perturbs normal physiological functions such as the neuron firing rate or the immune responses. According to the simulations, ≈ 63 % of the excitation photons at 1320 nm are absorbed by the tissue contributing to heating in the illuminated volume, in comparison to ≈ 20 % at 920 nm 2P excitation. In the simulations on the left-hand side of Figure 1.26 it can be seen that 2P excitation at 920 nm allows using 250 mW of average power without exceeding reasonable temperatures, whereas 3P excitation at 1320 nm is limited to 82 mW. On the right-hand side of the figure, the maximum brain temperature is plotted depending on the average power at the surface of the sample and the effective attenuation length (EAL or l_e). It is visible that the tissue temperature increases faster with increasing average power at 1320 nm. Moreover, the numerical values given here depend strongly on the tissue and on the experimental conditions of heat dissipation and cannot be straightforwardly generalized to other experiments, which will require an equivalent phototoxicity study.

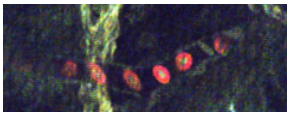

They show that the effect of pulsed excitation has a negligible effect on temperature increase on the tissue [35] as expected from Table 1.1. The main concern when using high peak intensities is nonlinear effects, related to the spot size, pulse energy and pulse duration. First of all, high peak intensities can lead to fluorophore saturation, which reduces the excitation efficiency and enlarges the focal spot [52]. Secondly, at higher peak intensities than those of fluorophore saturation, ionisation and recombination of molecules can happen under strong electric field excitation damaging the tissue beyond a given threshold [35]. As shown in Figure 1.27, this damage on fluorescent samples often results in an irreversible increase of brightness.

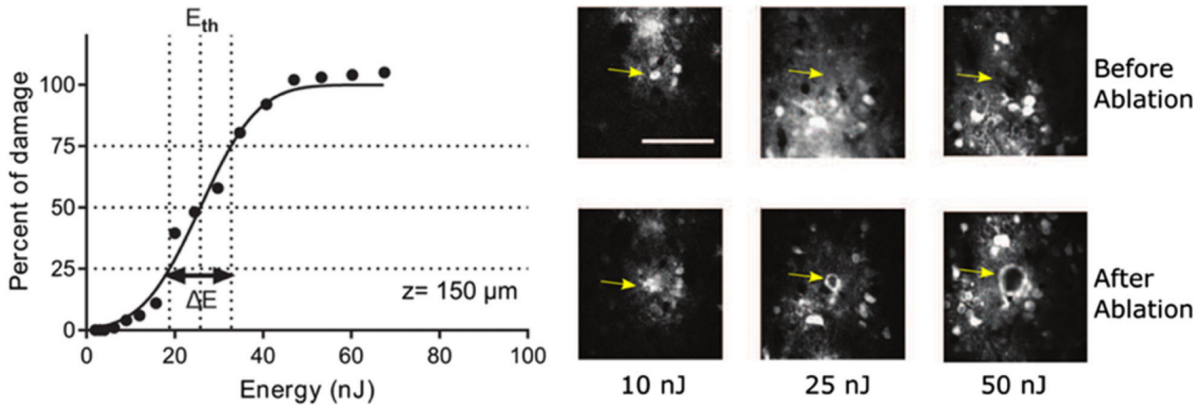

Figure 1.27: Tissue ablation induced by intense excitation pulses at the focus ($\lambda = 1320\,\text{nm}$). Probability of damage (damaged area/total scanned area) versus pulse energy (40 fs pulse duration, 1.0 NA, focused at 150 µm depth), left. Tissue appearance before and after the ablation, right. Scale bar: 100 µm. Adapted from [53].

3.4.3 Excitation parameters optimisation in 3P microscopy

Taking into account the limitations discussed above, the authors in [35] propose guidelines for the adjustment of the excitation parameters. At first and to maximise the signal, the peak intensity should be set to the maximum acceptable value. That is to say just below the threshold for nonlinear damage at shallow depths. Then, the repetition rate can be increased to improve the imaging speed until absorption starts to be an issue through tissue heating. These optimisations can be deduced from the parameter maps in Figure 1.28.

If the resulting repetition rate is not enough for the time dynamics of the application, other faster scanning strategies might be considered. Some examples are temporal focusing, 3P Bessel beam, remote focusing, reverberation microscopy or 3P light sheet microscopy reviewed in [35]. These maps help making the good choice of parameters. For instance, as shown by the white arrows in the left plot, it is much more interesting to double the pulse energy than the repetition rate: the signal is multiplied by 8 on the first case and only by two on the second situation even when the average power increase is the same in both of them. The limit for average power is not well determined and it depends also on the size of the FOV.

The authors conclude that the optimal repetition rate can be deduced by dividing the maximum average power by the pulse energy at the surface of the sample. But as the imaging depth increases, the average power is increased exponentially to compensate for

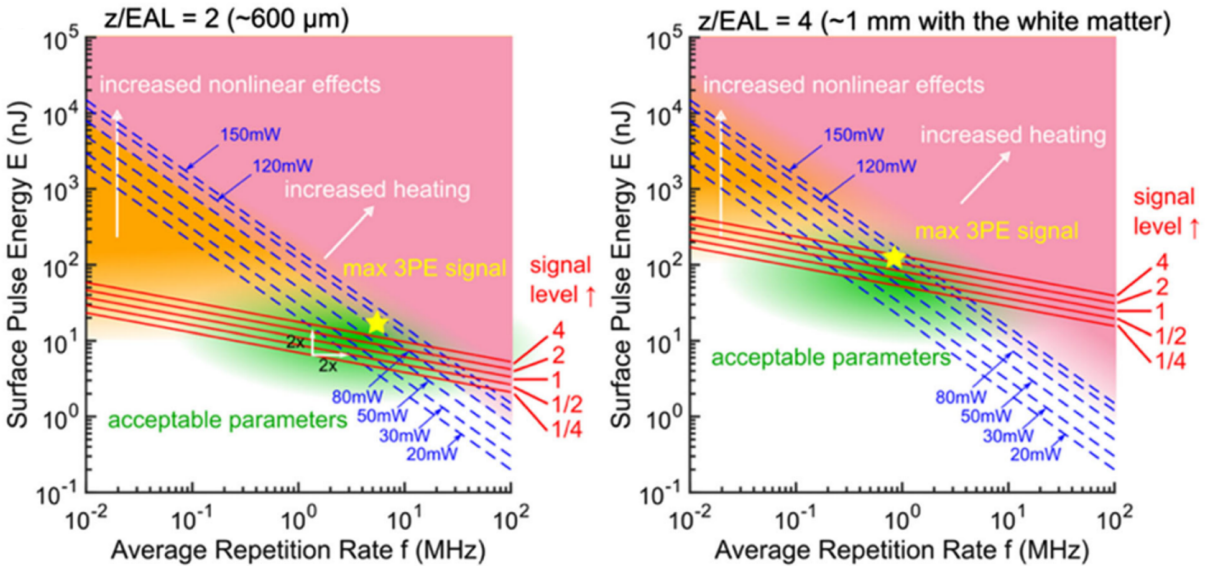

Figure 1.28: Surface pulse energy against repetition rate in 3P excitation at two different imaging depths. The green regions represent the combination of average power (blue dashed lines) and repetition rate that are tolerated by the tissue. The yellow star represents the maximisation of the signal (red solid lines) within the *safe* area, shadowed in green. The pink and orange zones correspond to combination of parameters that can cause measurable brain heating responses and adverse nonlinear effects, respectively. Pulse energy was calculated taking into account a pulse duration of 60 fs and a NA of 0.7. Figure from [35].

attenuation and the heat dissipation is not enough to avoid heating. That is why the optimal repetition rate decreases with imaging depth as seen in Figure 1.28 ($\approx$ 7 MHz at 600 µm and $\approx$ 1 MHz at 1 mm in the mouse brain.).

In general, commercial lasers for multiphoton microscopy do not allow varying the repetition rate, which hampers the investigation of photodamage. In practice, the repetition rate sets the maximum imaging depth attainable with 3P microscopy before tissue heating becomes too important.

4 Challenges and objectives of this thesis

4.1 Technical developments for 3P microscopy

As we have discussed in this chapter, 3P microscopy requires laser sources providing short pulse duration and working in the MHz repetition rate regime. Moreover, the optimal excitation wavelengths have been identified to be 1300 and 1700 nm due to reduced scattering and absorption of biological samples. However, the domain is still relatively new and although commercial sources adapted for 3P microscopy have become available, there is still room for technological improvements, and new sources will certainly push the field further.

During this thesis work, we developed and optimised a 3P microscope based on a prototype multibeam OPA source operating at $\approx$ 1 MHz repetition rate. In Chapter 2 we describe the details of this multicolour source and report on its advantages and disadvantages. We also discuss the consequences of the characteristics of this source on the design and optimization of the microscope and describe how we addressed the main issues

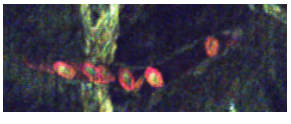

encountered.
We conclude by showing initial imaging demonstrations.

4.2 Observable parameters

In the second part of this thesis, we address another current limitation of 3P microscopy which is the reduced number of observable parameters. Indeed, the available data on 3P excitation of fluorophores is limited to few green and red fluorescent proteins that can be excited at 1300 and 1700 nm, respectively. In consequence, 3PEF imaging is generally restricted to one or two spectral channels and cannot benefit from the possibilities provided by multicolour labelling approaches.
In this work we first try to extend the available colour palette by exploring 3PEF of blue fluorescent proteins. In Chapter 3, we present a characterization of the 3P excitation properties of three blue fluorescent proteins, along with preliminary imaging demonstrations.
In Chapter 4, we develop a complementary approach to extend the number of observable parameters in a 3P microscope. We demonstrate and characterize a new third-order coherent imaging modality based on third-order sum frequency generation (TSFG) providing information at several wavelengths. We demonstrate that this contrast modality is sensitive to hemoglobin in blood, and is potentially applicable to label-free reporting on red blood cells oxygenation.

5 Conclusion and perspectives of Chapter 1

In this chapter, we have presented multiphoton microscopy as an efficient 3D imaging technique to image deep into scattering samples. We have discussed its principles, main advantages and the imaging depth limit of 2P microscopy. We then have shown how 3P fluorescence microscopy overcomes this limitation using a model to study the axial confinement. Through these simulations, we have analysed the effect on the SBR of several parameters of the excitation such as numerical aperture, scattering mean free path or absorption. It allowed us to confirm that the optimum excitation wavelengths for 3P microscopy are the bands at 1300 and 1700 nm, as reported in the literature. However, we noted this model overestimates the SBR. Indeed, it does not take into account the degradation of the PSF in depth due to scattering and aberrations nor the contribution of the scattered photons to the background. Therefore, one perspective of this study is to refine our model to include such processes [54].
In the last part of this chapter we have presented several technical and experimental bottlenecks limiting the development of 3P microscopy: (i) the lack of adapted laser sources and instrumentation, (ii) the limited number of observable parameters, (iii) the compromise between imaging speed and imaging depth governed by the laser repetition rate and (iv) the potential photodamage. Finally, we have presented the main goals of this thesis to address (i) and (ii) and contribute to improve the performances of 3P microscopy.

Chapter 2

Sources and instrumentation for 3P microscopy

Contents

1 Introduction to Chapter 2

This chapter presents the work done during this PhD to build and optimize an imaging platform for 3P microscopy. Focusing on the laser source first, let us introduce two families of sources used to reach wavelengths beyond 1050 nm for 2P and 3P microscopy: optical parametric oscillators and optical parametric amplifiers.

- **Optical parametric oscillators (OPO):** An optical parametric oscillator is based on a cavity similar to that of a laser, with the difference that the amplification medium is a nonlinear crystal instead of a material inducing population inversion for stimulated emission (Figure 2.1). The configuration is otherwise very similar: a pump beam (generally from a laser) is injected in an oscillating cavity. In a resonator, the repetition rate is related to the length of the cavity through the speed of light. A commonly used repetition rate for 2P imaging is 80 MHz, related to a cavity length of $L = c/80\,\text{MHz} = 3.75\,\text{m}$, with $c = 3 \times 10^8\,\text{m/s}$.

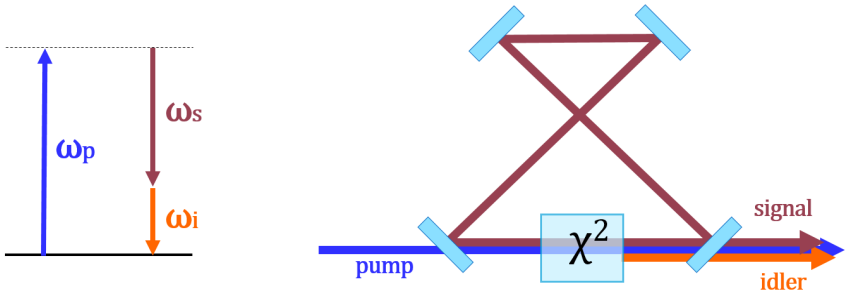

Figure 2.1: Energy diagram of the difference frequency generation process governing the energy conversion on an OPO (left) and ray diagram of the oscillator and the different beams involved (right).

  The nonlinear crystal, which presents non-zero second order susceptibility ($\chi^{(2)}$), is chosen to phase match the desired conversion, for which one pump photon (of frequency ω_p) gives one signal photon (ω_s) and one idler photon (ω_i) following the energy conservation expression: $\omega_p = \omega_s + \omega_i$. This process is usually called difference frequency generation. One of the advantages of this system is that the phase matching of the crystal can be adjusted to match a different conversion, resulting in a wavelength tunable source. This configuration provides a large range of wavelengths that can be used for microscopy. In Chapter 4, we present results obtained using a commercial femtosecond OPO (Insight X3, *Spectra-Physics*) with available wavelengths ranging from 760 to 1300 nm. Specifically, we will present spectroscopic THG experiments performed in the range 1120 to 1300 nm with this source.

- **Optical parametric amplifiers (OPA):** Given the lower repetition rate requirement of 3P microscopy (discussed in Section 3.1.2 in Chapter 1), an OPO system would involve a very long cavity ($L = 300\,\text{m}$ for 1 MHz repetition rate) which is impractical. For this reason, a more viable option for 3P microscopy is to use OPA sources. An OPA is also based on the process of difference frequency generation, but without a resonator. Output pulses with higher energy are obtained using a powerful pump laser (20 to 60 W). Additionally, OPAs usually need a seed pulse at either the signal or the idler wavelength allowing to drive the specific energy conversion. This small seed pulse is amplified during the conversion process, hence the term 'optical parametric amplifier'. If the obtained output power is not sufficient, two OPA stages can be implemented sequentially. In this configuration, a first OPA is optimized to provide a clean seed pulse train for a second one, which allows to reach higher conversion rates.

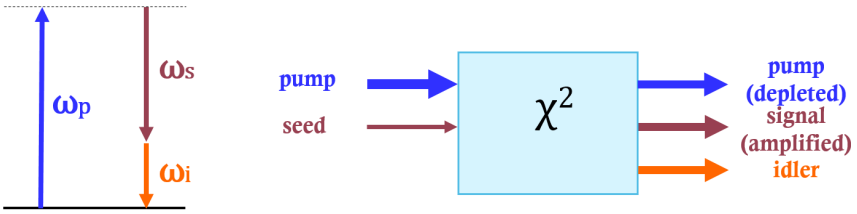

Figure 2.2: Energy diagram of the difference frequency generation process governing the energy conversion on an OPA (left) and ray diagram of the the different beams involved (right).

During this thesis work we characterized and used several generations of OPA prototypes designed for 3P microscopy. We started with a lab-built multibeam OPA source designed by Frédéric Druon's team at Laboratoire Charles Fabry (LCF) at Institut d'Optique, Palaiseau. One distinctive characteristic of this source is that it provided efficient excitation simultaneously at 1300 and 1700 nm [42]. As we will see, however, we concluded that despite its potential for colour imaging, the original design proved to be too unstable for developing biological applications. Based on this feedback, two pre-industrial OPA prototypes were then successively implemented by the LCF-Amplitude common laboratory hosted by Institut d'Optique, and benchmarked during the thesis. In Section 2 we present these various sources along with their advantages and disadvantages.
In Section 3 we present how we control the different parameters of the excitation beams, the necessary steps to pre-compensate their dispersion, and how they are combined and routed into the microscope. Finally, we describe the main elements forming the microscope installed and optimised during this thesis, and present some first imaging demonstrations.

2 OPA sources used in this thesis

In this section we present the most essential element of our 3P microscope: the laser source. We have stated in Chapter 1 the need of sources optimized for this regime, requiring µJ-range pulses with MHz repetition rate at 1300 and 1700 nm.
Our team has worked on this topic in close collaboration with the group of Frédéric Druon (at LCF) whose research is devoted to the development of laser sources for biophotonics, and with the LCF-Amplitude joint lab at IOGS.

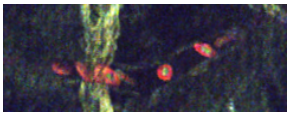

The LCF group initially developed an original OPA scheme producing simultaneously two pulse trains at 1300 nm and at 1700 nm with characteristics appropriate for 3P microscopy. The general structure of the source starts with a high-power beam at 1030 nm. It is the pump of the OPA process and is also used to generate a supercontinuum from which a seed/signal beam at 1700 nm is amplified. The corresponding idler beam at 2600 nm is then frequency-doubled, resulting in 1300 nm pulses. This approach provides two beams at wavelengths targeting the most appropriate spectral ranges for 3P microscopy (Section 3.2.8 in Chapter 1), and enables the simultaneous optimal excitation of green and red fluorophores. In addition, the design is based on a double OPA stage, which enables to reach an average power of ≈ 4 W in the 1700 nm beam, which was significantly higher than the performance of commercially available OPAs in 2018. One first objective of this thesis at the time was to also inject the pump beam in the microscope, and explore the possibilities of 3P imaging at 1030 nm in addition to 1300 and 1700 nm.
Although the design and performance of this source were very attractive for developing 3P bioimaging applications, in practice it exhibited important stability issues which strongly restricted its use for that purpose. Prior to this thesis work, initial proof-of-principle experiments had been done in presence of the OPA builder (Khmaies Guesmi), who ensured its proper operation for each test. When starting this thesis, there was a transfer of expertise to the LOB and we took the task of realigning the source when needed.
In practice, the first two years of this thesis work turned out to be largely devoted to the maintenance and upgrade of the source because of its complexity. One first important period of time was needed to master the alignment of the various stages of the dual-output OPA. Then, we spent another period characterizing and trying to improve its optical stability. Temperature and humidity were identified to have a critical influence on the source performance. However, after a lot of efforts we concluded that despite its unique characteristics, this first OPA prototype was not stable enough to enable sustained imaging sessions of biological samples.

In parallel, an alternative option was developed at the LCF-Amplitude joint laboratory by Alexandre Thai, Frédéric Druon and coworkers. This second prototype was installed at LOB in October 2019. It lacked the output at 1300 nm due to difficulties with the doubling stage, but exhibited stable performance at 1700 nm and enabled us to focus on microscope optimization and on the temporal compression of a fraction of the 1030 nm pump beam for use in the microscope.

By July 2020, a third prototype was installed at LOB, which enabled the use of all three beams: at 1030, 1300 and 1700 nm.

2.1 First prototype

In this section we describe the first prototype of the source. Because it was lab-made and we were managing it on our own, it is the prototype that we know in greater detail.

2.1.1 Structure and stages

As illustrated in Figure 2.3, two consecutive OPA stages (OPA_1 and OPA_2) form the basis of the source. The pump ($\lambda_p = 1030$ nm) and the signal ($\lambda_s = 1700$ nm) are mixed in a periodically poled lithium niobate (PPLN) crystal giving as a result an amplification of the signal and an idler ($\lambda_i = 2600$ nm), according to energy conservation. The idler is

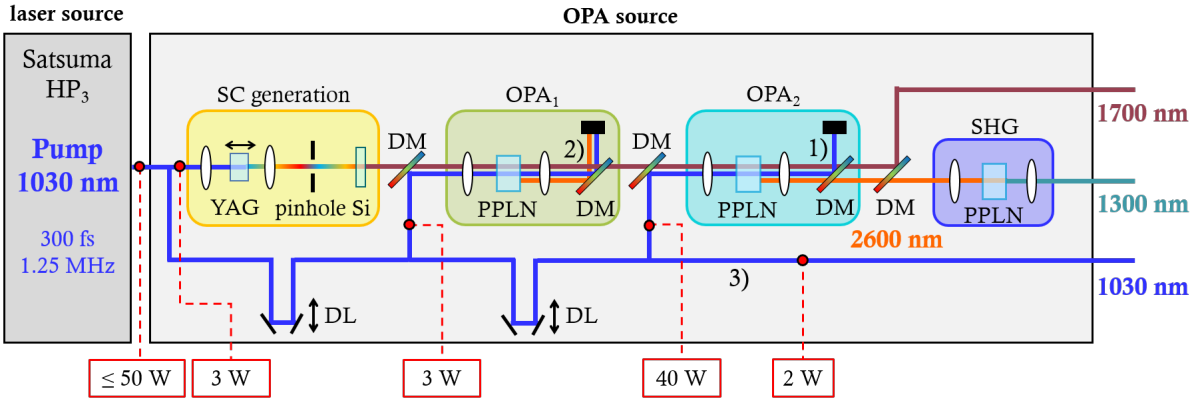

Figure 2.3: Simplified scheme of the different stages of the OPA source including power indications for the different pump fractions. SC: supercontinuum, Si: Si plate, DM: dichroic mirror, DL: delay line, PPLN: periodically pooled lithium niobate, SHG: second harmonic generation. Numers 1), 2) and 3) indicate the locations where pump pick-ups where tried for imaging at 1030 nm as described in Section 2.1.3.

then doubled in frequency to produce a beam at $\lambda_{SHG} = 1300\,\text{nm}$. Previous to the OPA stages, a seed at $\lambda_s = 1700\,\text{nm}$ is obtained through supercontinuum generation.

The pump of the OPA is a high-power commercial ytterbium femtosecond fibre Laser (Satsuma HP^3, *Amplitude*), which provides a pulsed beam at 1.25 MHz repetition rate, centered at $\lambda_p = 1030\,\text{nm}$ with pulse duration $\tau_p = 300\,\text{fs}$. The average power of this pump laser is $P = 50\,\text{W}$, requiring a water-cooling system.

The first step of the OPA system is to generate the seed, a beam at $\lambda_s = 1700\,\text{nm}$ to be amplified in stage OPA1. Therefore, a fraction (3 W) of the pump laser is focused onto a 10 mm YAG crystal where supercontinuum (SC) generation is achieved. A pinhole is used to reject the colour cone (off-axis frequencies, see Figure 2.4) of the SC and to homogenize it. Then, a 3 mm Si plate stretches the pulses as in chirped pulse amplification also working as a spectral longpass filter. The length of this plate was chosen so that a proper temporal overlap is achieved between the seed (the spectral component of the SC spectrum at $\lambda_s = 1700\,\text{nm}$) and the pump (at $\lambda_p = 1030\,\text{nm}$). Another $\approx 3\,\text{W}$ fraction of the 1030 nm main beam is used as the pump in this first OPA stage, and focused onto the first PPLN crystal. The remaining power on the main beam ($\approx 40\,\text{W}$) is used as pump in the second OPA stage OPA2, which uses the signal generated at OPA1 as its seed.
In both stages, a delay line is introduced in the pump path to allow temporal synchronisation with the signal. Adjusting the pump delay line is particularly critical in OPA1 because of the signal chirp. Depending on the relative delay between the two beams, the pump can be mixed with the spectral component at λ_s or with another one, which would result in an undesired energy conversion. For this reason, to adjust the delay line, the resulting signal wavelength is measured with a spectrometer. This wavelength-selection mechanism is not present in OPA2 because the seed for this second stage comes from OPA1 and is narrow-band. Thus, the adjustment of the delay line is simpler.
Apart from being temporally synchronised, the two beams need to be spatially overlapped on the nonlinear crystal position. This is achieved using a pair of mirrors for each beam. It is also critical to control the relative diameters of the two beams. The pump spot on the crystal needs to be at least as large as the signal one to achieve a homogeneous gain on

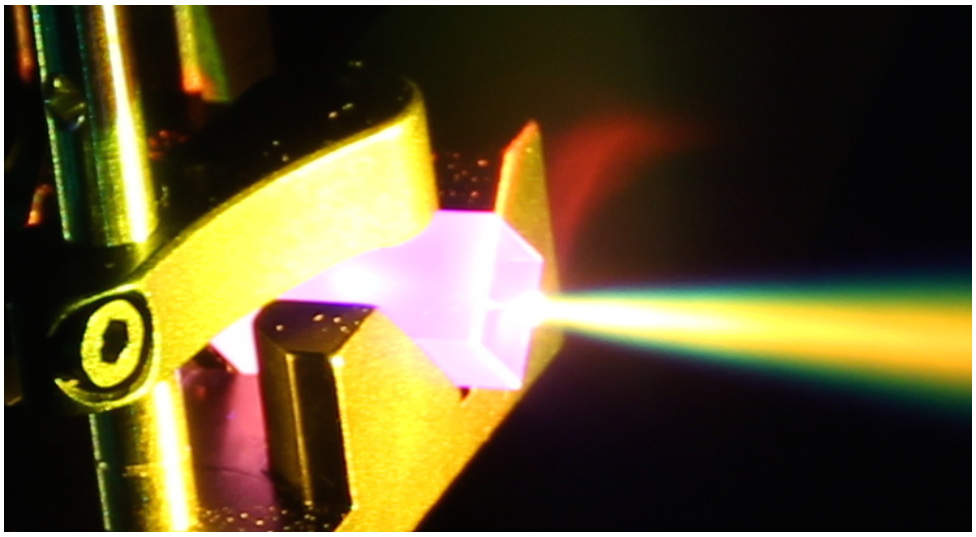

Figure 2.4: Picture of the supercontinuum generation on a yz profile. The generated colour cone can be observed including off-axis angles which are rejected in our source by the pinhole.

the signal beam. Otherwise, the output signal exhibits an inhomogeneous pattern with an amplified region (corresponding to the pump-signal overlapping region) well distinguished from a non-amplified part of the profile (corresponding to the non-overlapping region). Therefore, telescopes are included to control the beam dimensions.

After OPA1, the signal is amplified reaching an average power of $\approx 200\,\text{mW}$, and the idler and the non-converted pump are filtered out spectrally (DM in Figure 2.3). The overall efficiency of OPA2 is $\varepsilon = (P_s + P_i)/P_p \approx 0.17$, where P_s and P_i are the output signal and idler average powers respectively, while $P_p = 42\,\text{W}$ is the average power of the incident pump (the incident signal power is negligible compared to this value). At the output of the source, the average power of the signal beam ($\lambda_s = 1700\,\text{nm}$) is $\approx 4.3\,\text{W}$.
Finally, the three beams are spatially separated after OPA2 using dichroic mirrors. A third PPLN crystal is used to perform idler frequency doubling with 40 % efficiency, producing a beam at 1300 nm with average power 1.15 W.

2.1.2 Phase matching and PPLN crystals

Frequency conversion efficiency in a nonlinear crystal is generally limited by the phase mismatch between the input and output beams that build up during propagation in the crystal, due to refractive index dispersion. Phase matching is usually achieved through the use of birefringent crystals, either by angle tuning or temperature tuning [55]. The first method involves precise angular orientation of the crystal with respect to the incident polarisation of the waves involved in the process whereas the latter uses the strong dependence of birefringence on temperature.
The nonlinear processes in our OPA source are based on quasi phase matching. This alternative technique uses a periodically poled nonlinear medium (Figure 2.5.a), i.e. consisting of stacked layers of a birefringent material with alternate orientations of one of the crystalline axis [55]. This change of orientation can compensate for a wavevector mismatch inverting the coupling of the interacting waves. The different domains are regularly spaced with a period Λ chosen to match the coherence length of the nonlinear process

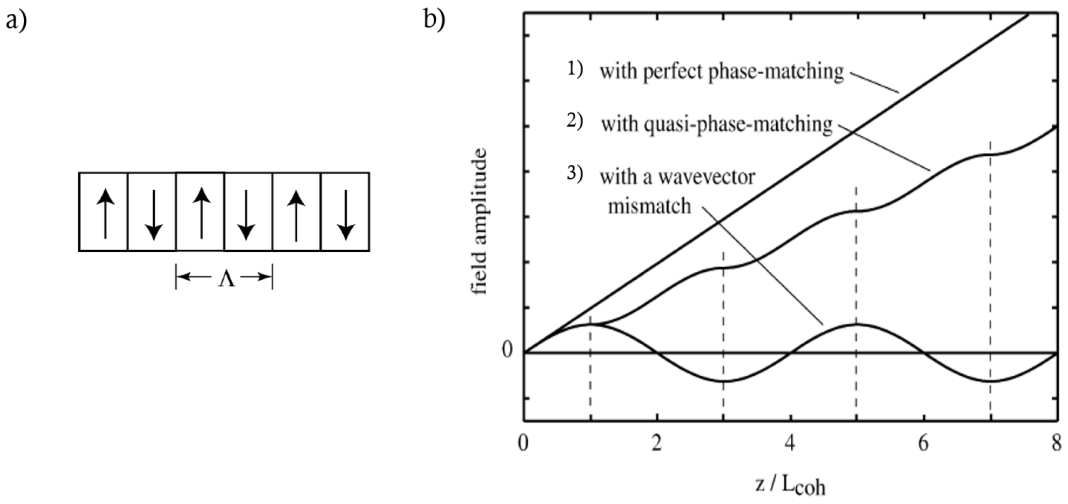

Figure 2.5: a) Illustration of a periodically-poled nonlinear medium. The inverted orientation domains alternate with a spatial period Λ. b) Amplitude of the generated field on a nonlinear process represented along the propagation length inside the nonlinear medium. The case of quasi phase matching is compared to a perfect phase matching and with the case in which there is a wavevector mismatch. Figure adapted from [55].

resulting in a monotonically increase of the generated field amplitude (Figure 2.5.b). In our case, magnesium-doped periodically-poled lithium niobate (PPLN) crystals are used in OPA_1, OPA_2 and SHG stages (Figure 2.3). The coherence length of the OPA processes is on the order of 30 µm but not precisely known. For this reason, several crystals with slightly varying periods between neighbours (ranging from $\Lambda_1 = 29.52$ µm to $\Lambda_5 = 31.59$ µm) are stuck to one another. This way one can select the periodicity providing the most efficient conversion experimentally, which was obtained with $\Lambda_3 = 30.49$ µm. Finally, the efficiency of the process is optimised by precise temperature tuning of the crystals. A dedicate oven for each crystal keeps it at a constant temperature through a proportional-integral-derivative (PID) system: 115 °C for the two OPA crystals and 30 °C for the SHG crystal.

2.1.3 Stability issues

In this section we summarize the main points in which this first prototype lacked the required stability for imaging experiments.

Temperature-related issues

Thermal effects were the major cause of stability issues experienced with this first prototype. First, the stabilization time after which the maximum power is reached was about 3 h after switching on the pump. Therefore, the source was generally turned on on Monday mornings and switched off on Friday evenings to guarantee the best possible stability. Then, we realized that the source was very sensitive to temperature changes in the room. When the room was kept closed for a day, we could measure OPA power fluctuations correlated with the cooling cycles of the room air conditioning system, as illustrated in Figure 2.6.
We reduced these effects by building an OPA enclosure with passive ventilation openings

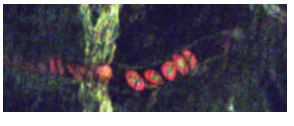

to allow efficient dissipation of the heat produced by pumped optical components, with minimal perturbation from the air conditioning flow in the room. Although the enclosure did improve the source stability, we could not fully compensate the effects of the poor performance of the room air conditioning system.

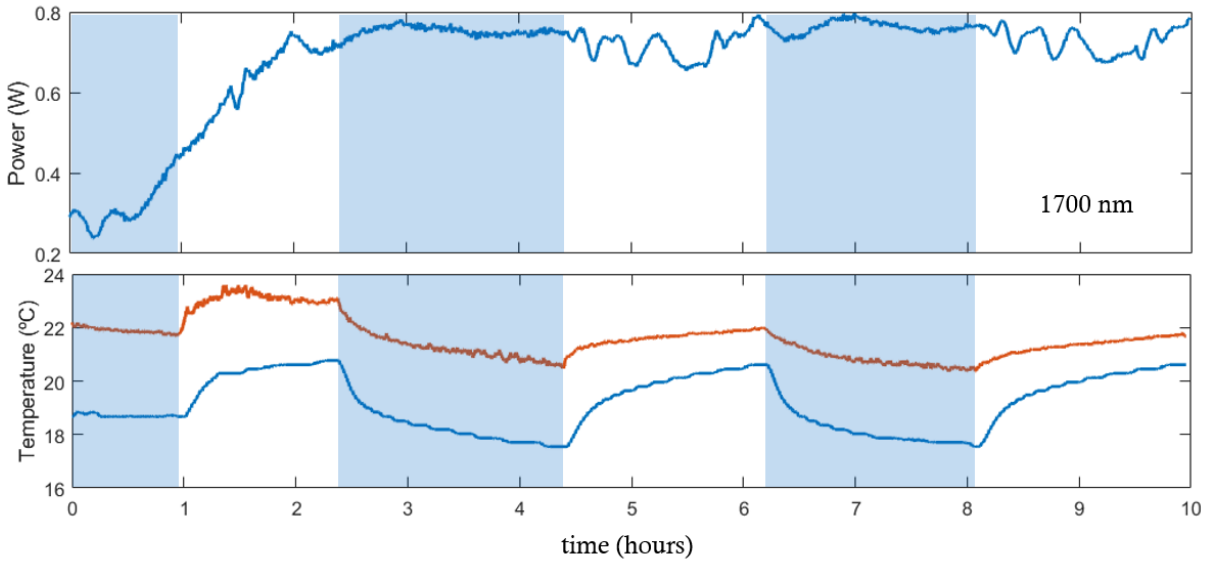

Figure 2.6: The upper graph shows the power measurements on a fraction of the output power at 1700 nm measured during 10 h in one of the source's most stable days. The first 3 hours correspond to warming up and stabilization time. Then a succession of stable and fluctuating periods is visible. The bottom graph shows corresponding temperature measurements by two probes located inside the OPA enclosure (orange) and on the optical table (blue). Cooling periods are shadowed in blue, and are correlated with higher stability of the source.

Another cause of power drop was related to temperature perturbations on the oven sensors. Sometimes, due to a thermal drift, the heat dissipated by the pump on the crystal reached a temperature sensor causing the oven to stop heating. The temperature needed was no longer maintained and thus phase matching was no longer obtained, resulting in a conversion efficiency drop.

Consequence for alignment stability at the output of the source

In addition to the OPA efficiency issues, temperature also had important effects on beam pointing stability at the output of the source. We observed that the alignment of the beams from the source to the microscope was not stable over a few hours and presented a continuous drift out of the optimum point during the day. This probably originated from a slow thermal stabilisation of the optomechanical elements inside the source. Sometimes, it also correlated with instabilities in the air conditioning system related to weather changes, and on other times the cause remained unclear.

We also note that the presence of an important misalignment inside the OPA cavity could be dangerous for the optical elements. The average pump beam powers (3 W for OPA_1 and 40 W for OPA_2) can indeed cause damage to many materials. For example, the ovens were equipped with a cover enclosing the crystal with a small entrance for the pump

beam. When drift or misalignment of the pump beam became large, this cover could be hit by the laser. On occasions, this produced smoke or ashes falling on nearby optics or the crystal itself, causing irreversible damage.

Issues with 1030 nm beam pickup

Another consequence of these instabilities was a difficulty to pick up a stable fraction of the 1030 nm beam for imaging purposes. One of the objectives of this thesis project was to explore the use of this wavelength in combination with 1300 or 1700 nm beams in the context of three-photon microscopy. A first straightforward implementation of this idea was to use for this purpose the remaining pump from OPA_2, of average power ≈ 10 W (labelled as *1)* in Figure 2.3). An optical path was installed to route this beam to the microscope, but we then realized that because of the fluctuations in the OPA conversion efficiency, this remaining pump beam also exhibited important power and pointer fluctuations. We then decided to use a portion of the beam that does not go through the second OPA stage, which exhibited the highest fluctuations. We therefore installed a pickup of the remaining pump of the first OPA stage (labelled as *2)* in Figure 2.3), but unfortunately we also observed fluctuations at this stage. The best option was finally to extract a part of the main pump before it entered the second OPA stage, which turned out to be as stable as the main pump laser. This pickup (beam labelled as *3)* in Figure 2.3), of power up to 2 W was performed by adjusting the angular position of a half wave plate, resulting in a moderately diminished OPA power.

Issues with SHG stage

The SHG stage producing a 1300 nm output from the 2600 nm idler beam is a critical module of the source. This stage is in fact even more sensitive to stability issues than the steps discussed previously. First, intensity fluctuations in the idler are of course raised to the power of two in the 1300 nm output. Secondly, the idler wavelength (2600 nm) is strongly absorbed by water and sensitive to room humidity (see Figure 1.22). Therefore, the optical path length of this beam between OPA_2 and the SHG stage was minimized in the source design. Still, we found that SHG efficiency was very unstable both in output intensity and beam pointing. We considered the option of enclosing this path in a chamber filled with a neutral gas such as N_2; this could have been a useful solution for a future version, although our collaborators at the LCF-Amplitude joint lab decided to first go for a simpler design for the following prototypes described below.

Hands-on feedback on the first prototype

All these instabilities made our multibeam OPA source much less adapted for bioimaging applications than we originally thought. Firstly, power oscillations which could be as important as 50 %, as illustrated in Figure 2.7 resulted in a high uncertainty on the power at the sample plane, which in fact requires precise control. Secondly, these fluctuations affected also the beam pointing directions. After propagation through the paths on the optical table, these fluctuations caused misalignments and even larger power drops at the objective focal plane. In practice, microscope realignments were needed every ≈ 2 h.

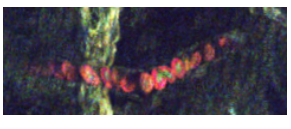

Although the injection beam paths were re-designed to make this task relatively simple, this requirement combined with daily alignment and care of the source prevented us from developing bioimaging experiments going beyond initial proofs of principle with this system.

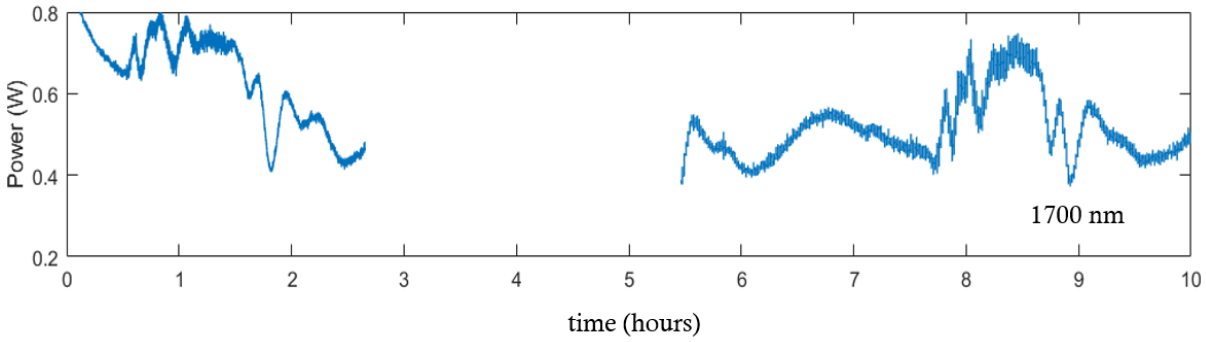

Figure 2.7: Power on a fraction of the 1700 nm beam recorded along several hours on a typical day of poor stability of the source. These fluctuations made the source unpractical for biological imaging.

2.2 Second prototype

A second prototype was designed by Alexandre Thai (Amplitude), Frédéric Druon et al. at the LCF-Amplitude joint lab with the goal of building a simplified system with stable characteristics, at the cost of reduced efficiency. This system was implemented in an industrial package (Satsuma mechanical frame) and used only one OPA stage (see Figure 2.8). It used a different pump laser (Satsuma HP^2, *Amplitude*) with the following

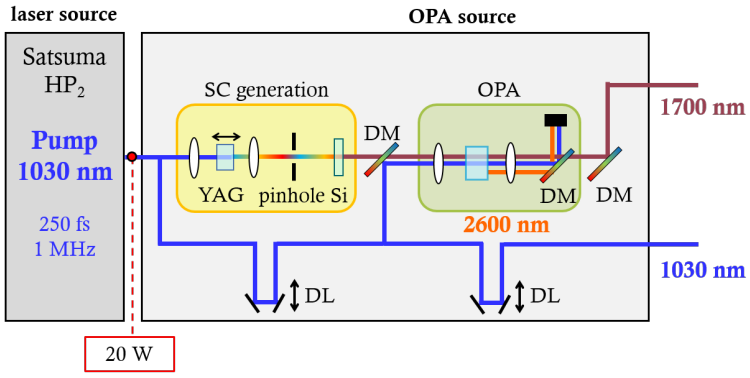

Figure 2.8: Simplified representation of the compact design of the second prototype of the OPA source built by the LCF-Amplitude lab.

characteristics: 1030 nm center wavelength, 20 W average power, 250 fs pulse duration and 1 MHz repetition rate. This pump beam was guided inside the OPA frame which was much more compact than the previous lab-made system (Figure 2.8). Three mechanical shutters were installed on the three output beams with 3.1 W available at 1700 nm (minimum pulse duration $\approx$ 80 fs), 500 mW available at 1030 nm, and only 80 mW available at 1300 nm. Alexandre Thai et al. experienced difficulties for the optimization and stabilization of the SHG stage. They had to perform a systematic study of the doubling crystals available

on the marked for this purpose, which turned out to be a complicated task. In practice, the beam at 1300 nm was not available on this prototype (see Figure 2.15). While the issue was being solved, this version of the source was used for developing 3P imaging experiments with 1030 and 1700 nm excitation. Unlike the first prototype, this model was very stable in terms of output power and beam pointing.

2.3 Third prototype

The third OPA prototype used during this thesis is in fact an upgraded version of the second one. This source provides 2.9 W at 1700 nm, 500 mW at 1300 nm and 550 mW at 1030 nm. The minimum pulse durations of the OPA beams were $\approx$ 80 fs whereas the pump pulse duration was on the order of 250 fs. It is as compact and stable as the second version (Figure 2.9), requiring alignment only once a month: the pump injection mirror can be adjusted and there are two screws per crystal to optimize each nonlinear process. The SHG stage is especially delicate and it is the one which needs the most frequent tuning. After testing different types of crystals for the SHG stage, our collaborators chose the best possible option but this stage could be further improved. One of the main issues encountered by the builders of the source is the difficulty to find companies able to provide frequency doubling crystals for these conditions.

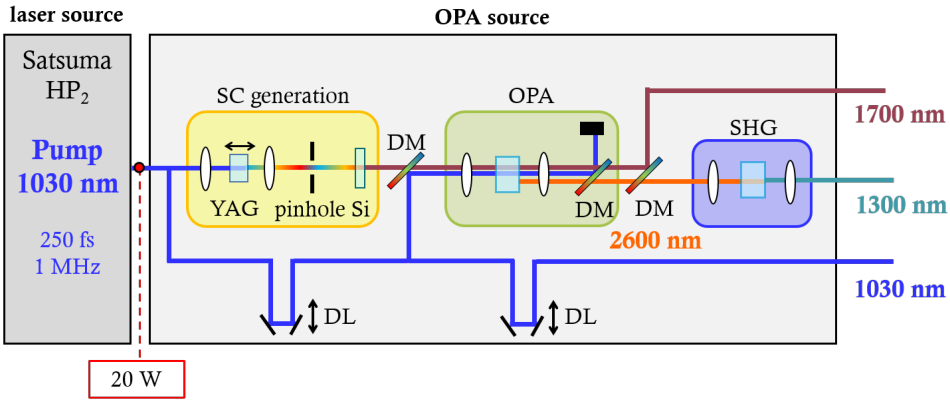

Figure 2.9: Simplified representation of the compact design of the third prototype of the OPA source built by the LCF-Amplitude lab.

3 Beam conditioning paths

In this section we describe the optical paths of the beams and the different stages they go through from the output of the source up to their injection into the microscope. Much effort and attention has been given to the optimization of these stages, which have been progressively adapted and improved for each source version.

3.1 General design principles for the optical paths

A few basic design rules have been used when implementing optical paths for our multi-beam microscope.

- **Length minimization**
  As a first general principle, we seek to minimize the length of the beam paths

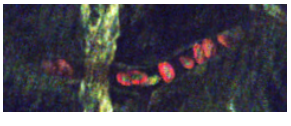

between the laser and the microscope. One reason is to minimize beam divergence caused by propagation over long distances, because it must be compensated with additional collimation optics which may introduce aberrations in the initially clean beam profiles. Another reason is to avoid unnecessary mirrors and related power losses. Silver mirrors (PF10-03-P01, *Thorlabs*) were used for the 1300 and 1700 nm beams (3 and 4 % of losses respectively at 45° of incidence). For the 1030 nm pump pick-up beam, dielectric mirrors (custom made, *Eksma Optics*) were used with higher reflectivity (>99 %). Similar care was given to select all the optics coatings.

- **Beam stirring and alignment modularity**
  Another guideline is to have a modular design with two stirring mirrors between each alignment-sensitive key element in the path: source output, pulse compressor, beam size controller, microscope injection point. This arrangement is important to compensate for possible source pointing instabilities and proved to be essential when using the first prototype of the source. Each pair of beam-stirring mirrors is followed by a relatively long straight path where the laser is aligned using a classical beam-walking strategy: a first diaphragm is located close to the second mirror, and a second diaphragm is placed far from the two mirrors. The beam is iteratively centered on each diaphragm with its associated mirror until it goes through both targets. This procedure allows to efficiently recover the alignment up to the microscope even in the case of a large pointing change of the source.

- **Beam height**
  In addition, the paths were designed so that all beams propagate at the same height on the table. A single movable pinhole has been calibrated to the height of the microscope entrance ($\approx$ 13.5 cm above the table), and is used all along the paths as an alignment reference. To reach this beam height at the laser output, a periscope was installed on each beam to raise it from its original height (8 cm for the second and third prototypes) to that of the microscope entrance.

In the following sections we present the details of the different modules.

3.2 Power control

For each beam at the output of the source, the first element is a power control system consisting of a half wave plate (HWP) on a motorized rotation mount and a polarizing beamsplitter (PBS). The linear polarization of the beam rotates with respect to the axis orientation of the HWP. The PBS then projects the polarization along the horizontal and vertical axes. The vertical component is blocked and the horizontal one is let to propagate on the optical table. The angular position of the HWP is set with a labVIEW function in which the percentage of power reaching the microscope has been calibrated taking into account Malus' law.

3.3 Spectral filtering

In the case of the first OPA prototype in which many unwanted additional wavelengths were generated, spectral filters were necessary at the output of the source to prevent them entering the microscope. It was particularly important to block unwanted components in the the visible range (515 and 650 nm) and remaining leaks of the pump laser. The

excitation beams at 1030, 1300 and 1700 nm were cleaned with the following filters FF01-715/LP, BLP01-1064R and BLP02-1319R (*Semrock*), respectively.

3.4 Dispersion control and pulse compression

The temporal profile of the excitation pulse train is a critical parameter in 3P microscopy. As we have seen in Chapter 1 (Table 1.1), 3P signals are proportional to the laser duty cycle τ/T to the power of -2. Minimizing the pulse duration is therefore very important to maximize the signal obtained with a constant average excitation power. In the case of our source, pulse shortening after the objective is achieved with three different strategies depending on the wavelength. Before describing them, let us remind some definitions:

- **Group velocity**
  The group velocity is the velocity at which the envelope of a wave packet progresses in space. It is equal to the inverse derivative of the wavenumber with respect to the angular frequency: $v_g = [dk/d\omega]^{-1}$.

- **Group velocity dispersion (GVD)**
  The GVD characterises the frequency dependence of the group velocity in a medium. It is expressed mathematically as the derivative of the inverse of the group velocity with respect to the angular frequency: $GVD = \frac{\partial}{\partial\omega}\frac{1}{v_g} = \frac{\partial^2 k}{\partial\omega^2}\Big|_{\omega_0}$. It is used to characterise changes in pulse duration during propagation in a dispersive medium. It is usually expressed in fs^2/mm, can be positive or negative, and is a function of the wavelength.

- **Chirped pulses and Fourier transform limited pulses**
  A chirp is defined as a temporally dependent instantaneous frequency. Unchirped pulses exhibit the minimum value for the time-bandwidth product (product of their temporal duration and spectral width) and are usually termed Fourier transform limited (TL) pulses. In other words, TL pulses present the shortest possible duration τ_0 for a given spectral width. A polychromatic TL laser pulse passing through a medium presenting non-zero GVD becomes chirped, and this chirp results in temporal broadening: the pulse spectrum is unchanged but its duration increases. For a Gaussian pulse, the final duration τ of a pulse propagating through a medium with GVD and length L is:

$$\tau(L) = \tau_0\sqrt{1 + \Big(\frac{4\ln 2[GVD]L}{\tau_0^2}\Big)^2}.$$

In out setup, pulse durations can be measured on the optical table and at the the focus of the objective with a dedicated microscopy autocorrelator (Carpe, *APE*). This system is very convenient as we seek to minimize the pulse duration at the sample plane and pre-compensate the dispersion caused by all optical elements including the microscope optics.
In our multibeam system, we need to design different strategies for the three beams. The 1030 nm pulses produced by the pump laser are relatively long (τ_0 = 250-300 fs) and experience little temporal broadening on its propagation up to the microscope focus.

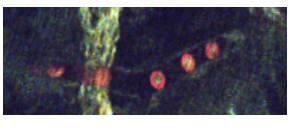

However, shorter pulses are desirable for 3P microscopy, and we therefore implemented a nonlinear compressor system for this beam. The 1300 and 1700 nm pulses produced by the successive OPA prototypes are spectrally broad with $\tau_0 = 60$-80 fs, and thus, experience significant dispersion through the beam conditioning paths and microscope optics. This dispersion can be pre-compensated, but the method is different for each beam.

3.4.1 1700 nm pulse dispersion control

Recompressing 1700 nm pulses is relatively simple because in this wavelength range there exist transparent materials presenting a positive GVD values and others presenting negative values. For instance, positive dispersion can be introduced with silicon (Si, 986.60 fs^2/mm), and negative dispersion can be introduce with silica (SiO_2, $-47.585\,fs^2/mm$). In the successive versions of our source, after measuring pulse durations for various thicknesses of dispersive material, the optimum pulse duration was found by inserting Si plates (1 or 3 mm). We obtained pulse durations at the sample plane of $\tau = 77$ fs, very close to the TL pulse duration calculated from the spectrum ($\tau_0 \approx 60$ fs). Compared to the uncompensated pulse duration of $\tau = 117$ fs at the sample plane, dispersion pre-compensation provided a gain on the 3P signal of: $G = (117/77)^2 = 2.3$.

3.4.2 1300 nm pulse dispersion control

The task is more complicated at 1300 nm because most materials present a dispersion close to zero at this wavelength. Therefore, impractically large (≈ 2 m) thicknesses of dispersive materials would be needed to recompress the pulses in the same manner as for the 1700 nm case. A more suited approach is to implement a compressor based on dispersive prisms [56]. Such a system introducing larger amounts of dispersion was provided by Alexandre Thai from the LCF/Amplitude joint laboratory. Its structure is schematized in Figure 2.10.

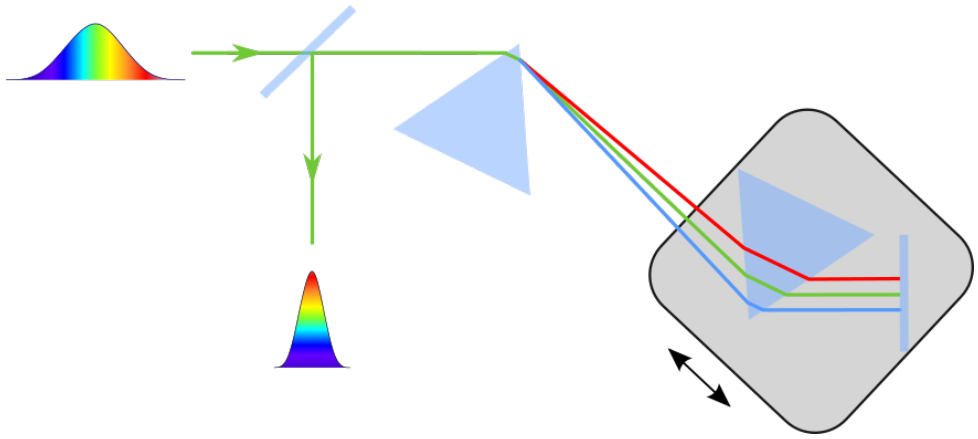

Figure 2.10: Prism-based compressor for the 1300 nm beam. Spectral components are spatially separated in the first prism, and travel different optical lengths in the second prism. By translating the stage with the second prism, one can change the amount of negative dispersion introduced in the pulse after spectral recombination. In the illustration, a chirped pulse is recompressed after passing through the prism pair.

The system can introduce both positive and negative dispersion. Positive dispersion is added by increasing the optical path inside the prisms, which are made of a material presenting high positive dispersion (SF11 in our case, GVD = $76.75\,fs^2/mm$ at 1300 mm).

Negative dispersion is induced by the angular deviation (illustrated in Figure 2.10) and its amount can be tuned adjusting the distance between the two prisms. After tuning the compressor, we obtained a pulse duration of 196 fs at the sample plane.

3.4.3 1030 nm pulse compression

Compressing the 1300 nm pulses from the pump laser down to a duration of $\approx$ 100 fs is slightly more complicated. Indeed, these pulses have a limited spectral bandwidth. They are already TL with a pulse duration of $\tau_0 = 250$ fs. Therefore, to reach shorter durations, we first need to enlarge their spectrum. A suitable compressor design was proposed by the team of Frédéric Druon (Figure 2.11). To generate additional spectral components, the beam is focused onto a first 1 mm YAG crystal. The beam is then recollimated and compressed with a pair of chirped mirrors (on which reflection path depends on the wavelength). The output beam then goes through a second stage of spectral broadening in a second YAG crystal and compression with chirped mirrors.

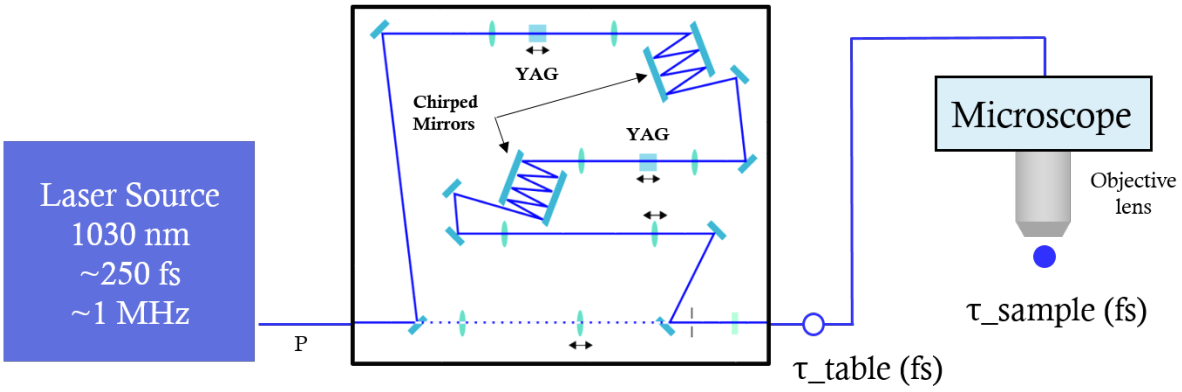

Figure 2.11: Module for temporal compression of the 1300 nm pulses. Two successive stages of spectral broadening in YAG crystals and pulse compression in chirped mirrors are implemented. The entire system can be bypassed (dashed lines) to enable comparisons between compressed and uncompressed pulses. The positions where the pulse durations in Figure 2.13 were measured are indicated.

The system was tested with different pump powers and number of bounces on the chirped mirrors. The two YAG crystals were mounted on micrometric translation stages to provide a fine control of the nonlinear effects. During alignment, the spectral profile was monitored on a spectrometer while tuning the YAG position relative to the beam focus, with the aim of obtaining the largest possible spectrum. Figure 2.12 shows the pulse spectra measured before and after the compression module, showing the increase in spectral bandwidth.
The number of reflections on the chirped mirrors was then optimized to achieve the shortest pulse duration at the microscope focus. In our case, an optimum was found with 6 reflections on the first mirror pair and 8 on the second one. A measurement of the pulse duration in the microscope and on the table as a function of pump power is shown in Figure 2.13.
According to the data in Figure 2.13, the pulse can be compressed down to $\tau = 80$ fs. At this minimum, however, the temporal profile starts to exhibit important distortions, so the compressor was set to achieve $\tau = 100$ fs at the sample plane. The enhancement of 3P excitation resulting from this compression is: $G = (250/100)^2 = 6.25$.

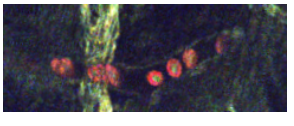

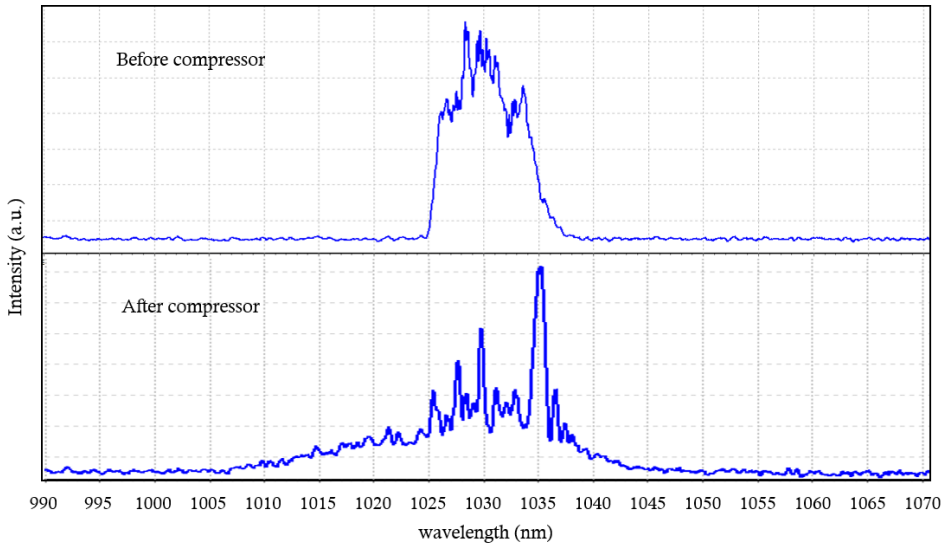

Figure 2.12: Spectrum of the pump before and after the compression stages. Significant spectral broadening is achieved thanks to nonlinear processes in the YAG crystals.

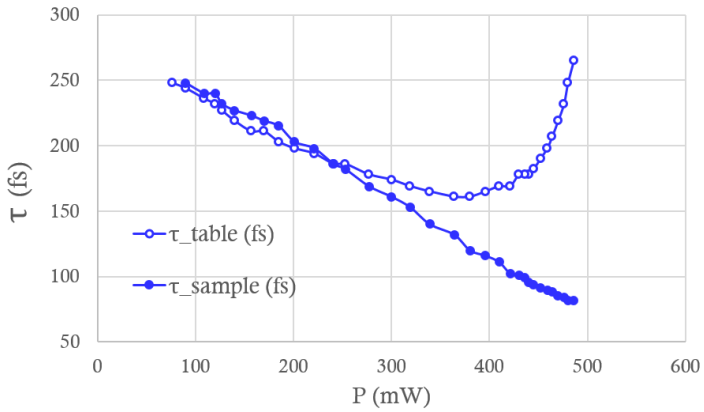

Figure 2.13: Pulse duration measured on the sample plane and on the table depending on the power at the entrance of the nonlinear compressor.

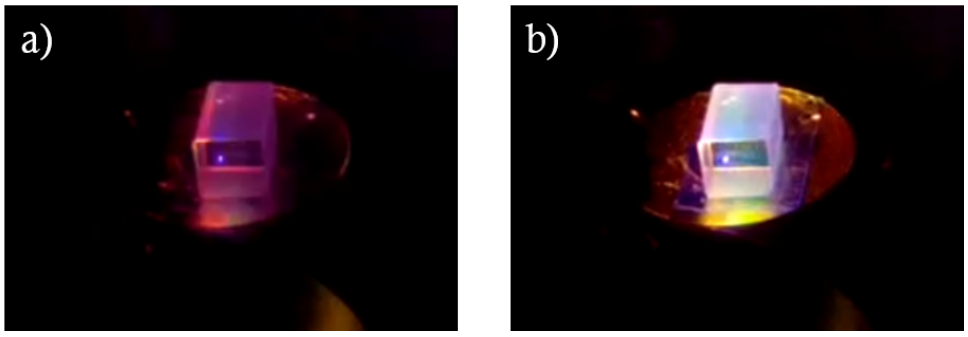

Figure 2.14: YAG crystal on the nonlinear compressor being excited with adequate power level (a) and with too much power, exceeding the threshold for SC generation spanning the entire visible spectrum (b). The laser light present in (a) is short wavelength IR to which the camera is sensitive. The laser can be identified as the small purple spot.

We should point out that the large spectrum in Figure 2.12 is obtained by establishing a high intensity in the YAG crystals (typically 450 mW focused by a f = 50 mm lens).

However, this pump power must be kept below the threshold for supercontinuum generation in the YAG crystals. If this happens, the spectrum exhibits a dramatic broadening including unwanted visible components. These are shown in Figure 2.14.b, compared to 2.14.a, in which only scattered 1030 nm light is observed.

3.5 Beam metrology

The beam size and divergence at the entrance of the microscope objective have a critical effect on imaging performance in three-photon microscopy.

- **Beam size**
  The beam diameter at the back focal plane of the objective is an important parameter in 3P microscopy. When the back focal aperture is underfilled, the effective numerical aperture (NA) is reduced, which reduces both the resolution and the signal level. We have seen in Section 3.2.2 in Chapter 1 that in the case of 3P excitation of a homogeneous medium, the signal approximately scales as NA^2 for a constant power incident on the sample. In general, the effective focusing NA is maximized for a flat beam profile at the objective entrance [57, 58]. This condition can be experimentally approached by overfilling the back focal aperture with a Gaussian beam [15,59]. On the other hand, largely overfilling the objective back focal aperture results in important laser power losses. This should be avoided because, as we have seen in Chapter 1, in 3P microscopy the power delivered to the sample surface needs to be increased with imaging depth to compensate for scattering and absorption. It is important to ensure that 100-200 mW can be delivered to the sample, and thus, to minimize power losses between the source and the sample plane.

- **Divergence**
  Microscope objectives are designed to operate best when a flat wavefront is incident at the objective back focal aperture. In principle, we would like to have three collimated beams at this plane. In practice, we need to find a compromise for the following reasons. First, the size and divergence of each beam are controlled by telescopes placed on the optical table before the microscope. As we will discuss below, the two parameters are partly coupled, so it is not possible to adjust the beam size without changing its divergence. Second, we seek to have all three beams of the microscope focused ideally to the same plane. However, because of the axial chromatic aberration of the objective over the 1030-1700 nm wavelength range, collimated incident beams are focused to different planes. This mismatch can be as high as 10 µm. In practice, we minimize this chromatic effect by adjusting the relative divergence of the beams.

Telescopes for beam conditioning

In short, beam size and divergence need to be adjusted to find a compromise between the maximum available power after the objective and the best spatial resolutions while dealing with chromatic issues. The essential tools used to handle these parameters are telescopes installed on each beam. In our setup all the telescopes consist of two convergent lenses arranged in a nearly 4-f configuration. In a 4-f arrangement, a collimated beam is incident on the first lens and focused at the image focal plane of this lens. The second lens is placed so that its object focal plane coincides with the beam focus, resulting in

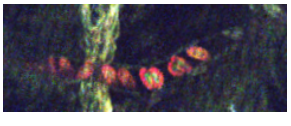

a collimated beam after the telescope with a magnification factor equal to the ratio of the two lenses focal lengths. From this arrangement, the beam divergence at the exit of the telescope can be adjusted by changing the distance between the lenses. In order to achieve a (partly) independent control of beam size and divergence, two telescopes can be installed on each beam. A first one is placed far from the microscope and in 4-f configuration, in order to mostly alter beam size at the microscope after propagation. A second one is placed close to the microscope scanning system and has a magnification equal to one. This second telescope, when detuned from 4-f configuration, allows to modify the divergence of the beam incident on the scanners without altering its dimensions.
In practice, since the power of the 1300 nm beam was limited in our OPA systems, we implemented only one telescope on this path to minimize power losses. With such a configuration, the multibeam alignment strategy is to first optimize the 1300 nm excitation beam path (effective NA and available power), and then adjust the telescopes on the other beam paths to achieve foci matching in the microscope. Finally, because the 1030 nm beam experiences more propagation distance in the table, an additional telescope was implemented on this path close to the laser output to prevent excessive divergence.

Spatial resolution measurement

The choice of the lenses and alignment of all these telescopes is achieved in an iterative way, by monitoring both the overall power transmission with a power meter at the sample plane and the axial resolution (δ_z). Axial resolution is estimated by recording an axial image series (z-stack) of a point-like object, and estimating the FWHM of its axial profile. In practice, point-like objects should be chosen smaller than the axial resolution. We typically use fluorescent beads embedded in agarose (*ThermoFisher Scientific*), or non-fluorescent polystyrene beads producing THG. Indeed, axial resolution can be alternatively estimated from the THG axial profile through a horizontal water-glass interface [11, 60].

In all the successive versions of the setup, we achieved similar axial resolutions ranging from 2.1 to 2.8 µm for all beams. An axial mismatch smaller than 1 µm was achieved except with the third prototype, for which the axial mismatch between the 1700 nm and the two other beams could not be made smaller than $\Delta z = 5.5$ µm without large power losses. This issue is probably related to the initial divergences of the beams in this particular source design. We plan to solve it soon after the installation of a fourth source prototype, and if necessary by introducing a phase mask in the 1700 nm beam.

Beam profilometry

A complementary measurement of the beam size on the table can be achieved more rapidly with an IR beam profilometer. During initial alignments of a new source, this is very useful not only to check the beam dimensions but also to detect possible issues in the spatial profiles. An example of defective beam profile at 1300 nm can be seen in Figure 2.15 compared to normal beam profiles at 1030 and 1700 nm. It shows beam profile measurements from the second source prototype, which had important issues in the 2600 nm doubling stage.

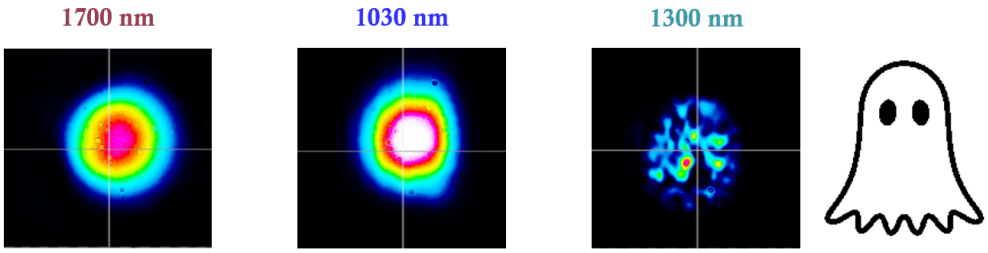

Figure 2.15: Example of beam profile measurements done on the optical table with the IR profilometer. The second prototype of the source arrived at LOB in 2019 around Halloween with a phantom 1300 nm beam profile well suited for the occasion!

3.6 Pulse synchronisation

One of the foreseen applications of this microscope is to investigate the use of non-degenerate multiphoton processes. This consists for example in exciting a fluorophore through a wavelength mixing approach, where photons of different energies are combined to reach the excited state. At LOB, this method has been previously developed in the context of two-photon microscopy to provide additional excitation routes and enable multicolour two-photon imaging [61]. Another possibility is to perform sum-frequency generation at different colours, as we will discuss in Chapter 4. Experimentally, this requires to temporally synchronise in the microscope the pulse trains from two different beams. This requires specific care in the case of 1 MHz pulse trains, because the pulse-to-pulse distance is on the order of 300 m. To enable pulse synchronization in the microscope, the paths of all three beams must therefore be designed to have the same optical lengths between the source and the microscope. The 1030 nm beam exiting the source is directly extracted from the main pump laser, meaning that it has propagated along a shorter distance than the 1300 and 1700 nm pulses, which result from propagation in the successive OPA stages. This delay was measured with a fast IR photodiode on an oscilloscope and found to be 1.98 m in equivalent light-travelled distance, for the second and third prototypes. Therefore, the 1030 nm pulse needs to propagate through this rather long additional distance compared to the 1300 and 1700 nm pulses in order to be synchronized on the sample, which complicates path design. For this reason, the 1300 and 1700 nm beams paths are shortened as much as possible and, before implementation, the design of the routing paths was drawn to scale allowing pulse synchronisation with sub-centimeter precision (i.e. sub-30 ps). To finally enable precise synchronization, a motorized optical delay line (ODL220/M, *Thorlabs*) was installed in the 1030 nm beam path.

3.7 Beam combination and injection in the microscope

The microscope entry point is close to the scanning system. As in the case of other key locations on the table, beam injection in the microscope is achieved using two mirrors targeting two points at the entrance and inside the microscope.
The combination of the three beams is done using dichroic mirrors. The beam at 1700 nm is the one aligned from further away from the microscope using two mirrors. The 1300 nm beam is then inserted by reflection on a dichroic located between the last 1700 mirror and the microscope. Finally, the 1030 nm is inserted by reflection on a second dichroic.

This details together with a summary of the different modules described in this section

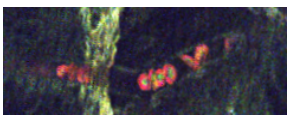

are illustrated in Figure 2.18.

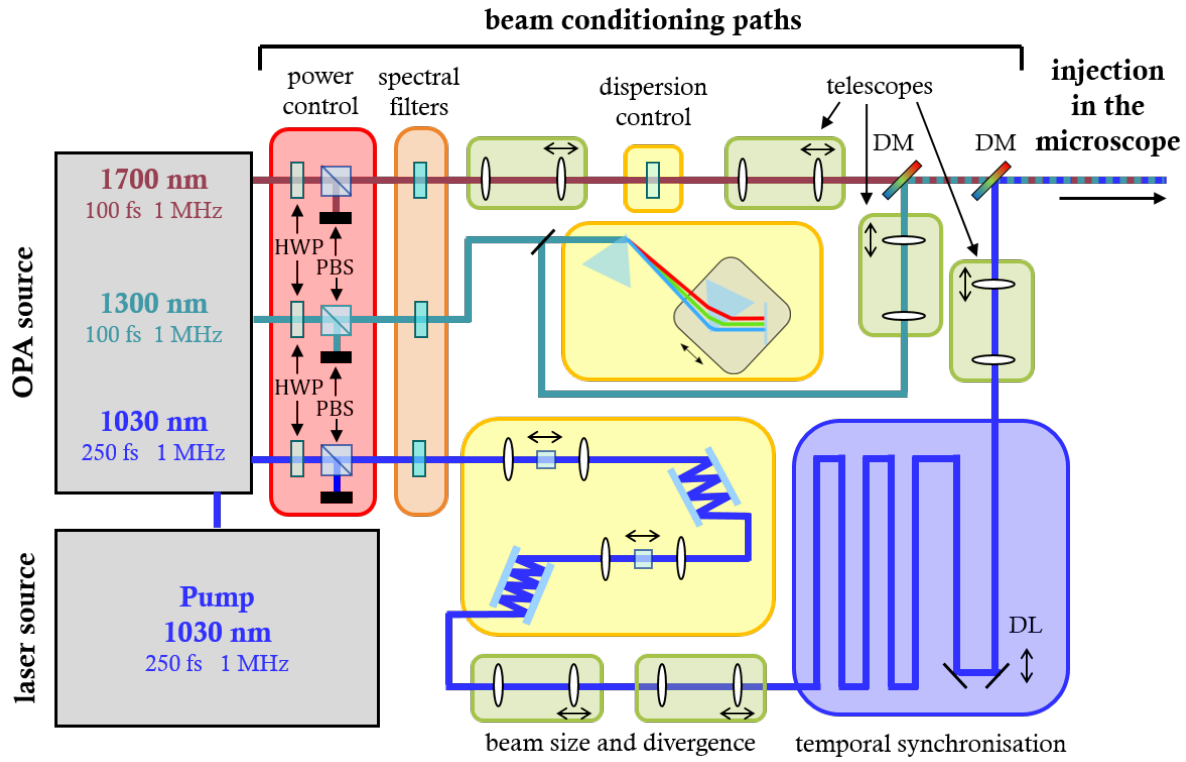

Figure 2.16: Schematic view of the structure of the different modules the beams go through from the OPA source to the microscope. HWP: half wave plate, PBS: polarising beam splitter, DM: dichroic mirror.

4 Microscope

4.1 Optomechanical design and control software

The microscope was originally designed and built by Pierre Mahou and is being gradually updated and improved according to project requirements. The frame and optomechanical components mostly consist of commercial components (*Thorlabs*), and the overall geometry is an upright configuration.

4.1.1 Objective lens and 3D imaging

The objective we use is a 25x water immersion (XLPLN25XWMP2, *Olympus*), with NA = 1.05, working distance = 2 mm, and back focal aperture diameter ≈ 15 mm. This objective is equipped with a correction collar and samples can be imaged either in direct immersion, or though a glass coverslip. As seen in Figure 2.17, it provides relatively a good transmission in the range of wavelengths involved in our projects spanning from 370 to 1600 nm (at 1700 nm we measured ≈ 50 % of transmittance). It is mounted on a motorized 25 mm translation stage (M-126, C-863, *PI*) moving along the optical axis (z direction) to adjust the imaging plane.

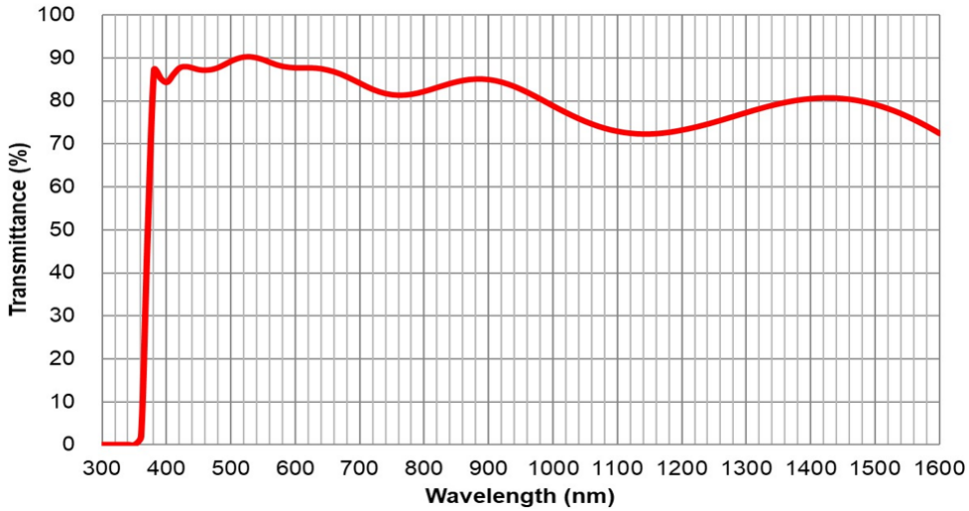

Figure 2.17: Transmittance data of the objective used in our system provided by the manufacturer.

4.1.2 Beam scanning and sample stage

A pair of 6 mm galvanometer mirrors (8315KB, Driver: 671, *Cambridge Technologies*) scan the excitation beam(s) in the x and y directions. The first scanning mirror is imaged onto the second one by a telescope with a magnification of 1, and the plane of the second mirror is in turn relayed to the back focal plane of the objective by a telescope of magnification 4. We note that since the diameter of the objective back aperture is $\approx$ 15.1 mm, the beam size at the entrance of the microscope should be approximately 4 mm. In addition, the sample holder is equipped with x and y 26 mm computer-controlled translation stages (L-505.02, C-663, *PI*) for large-scale positioning.

4.1.3 Control software

The microscope elements are controlled on the computer and synchronized through a multipurpose I/O board (PCI6115, *National Instruments*). Two software systems have been adapted for the setup and can be used alternatively.

- **Lab-written LabVIEW software**
  Control of most microscope elements is included in a LabVIEW program developed at LOB for operating multiphoton microscopes. For this reason, its main advantage is that it can be entirely modified. In particular, it gives access to power control of the different excitation beams, z objective stage motion, and acquisition of image sequences.

- **ScanImage control software**
  As a complementary option to control the 3P setup for application-oriented experiments, we also installed ScanImage. This is a MATLAB-based control software originally developed as an open-source code for the neuroscience multiphoton community. Now it is also available as a commercial product (currently supported by *Vidrio Technologies LLC*). Although less customizable than our LabVIEW code, some of its advantages are its robustness, real-time visualization functions, and the availability of bidirectional scan patterns.

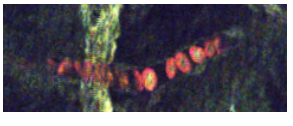

4.2 Detection

4.2.1 Detection modules

The microscope is equipped with a 4-port epidetection module, and a 2-port removable transmitted-light detection module.

Epidetection

The epidetection system is depicted in Figure 2.18. A main dichroic mirror (longpass filter at 850 nm, *Chroma*) installed just above the objective lens is used to transmit all relevant excitation wavelengths and reflect visible light towards the detectors. Laser light is further blocked by a short pass filter (890 nm) placed at the beginning of the detection system to protect the detectors. A two-lens system relays the objective back aperture plane to the entrance of a multi-port detection module. A classical configuration of this detection module is to use three ports for detecting fluorescence (for example blue, green, and red spectral ranges) with GaAsP detectors (H7422-40, *Hamamatsu*) sensitive in the 300 to 740 nm range. The fourth port is used alternatively for wide-field imaging with an IR camera while the sample is being illuminated by a 735 nm LED (or a white light lamp). For example, dichroics centered at 561 nm, 475 (or 495)nm, and 700 nm can be installed to separate blue, green, red and IR light.

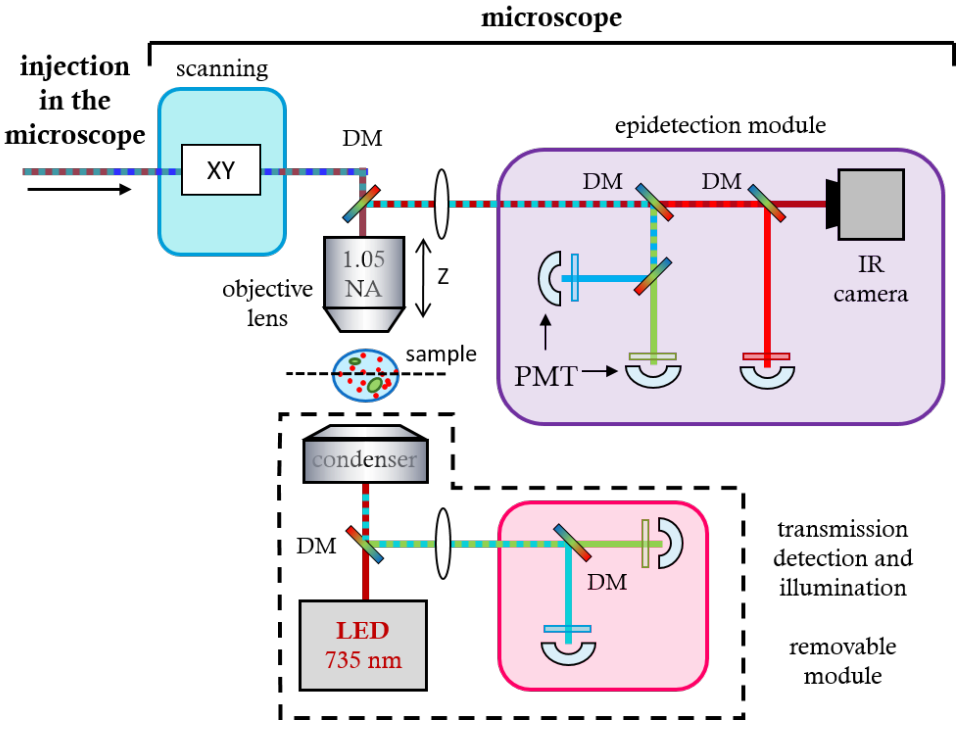

Figure 2.18: Schematic view of the structure of the different elements of the microscope that the beams encounter after the conditioning path.

Forward detection

The microscope is also equipped with a forward detection module to detect for example forward propagating THG and SHG signals from thin or transparent samples (Figure

2.18). This module contains a condenser lens and a dichroic mirror directing light in the 300 - 700 nm range to the detectors. A second dichroic then splits it into two channels, usually above and below 473 nm. This module also contains the 735 nm LED which can be used as a transmitted light source for wide-field imaging in combination with the camera in the epidetection module. The entire transmission module can also be removed to accommodate a large sample.

These details and a summary of the microscope elements discussed in this section are illustrated in Figure 2.18.

4.2.2 Detection electronics

An appropriate signal digitization approach must be developed when detecting signals produced using a pulsed excitation. Historically, the microscopy group at LOB has implemented strategies for detecting small signals (such as endogenous fluorescence or THG) obtained with 80 MHz oscillators and OPOs. All the detection systems at the beginning of this thesis relied on photon counting, which provides the highest sensitivity when working with small signals. However in the photon counting regime, only one signal photon can be detected per laser pulse. Indeed, the average count rate should be kept lower than one detected photon every 5 pulses to minimize the probability of having two "simultaneous" photons counted as one. Beyond this count rate, the response of the detection chain saturates and is no longer linear. With a 80 MHz source, the maximum count rate is therefore $80/5 = 16$ detected photons/µs. For example, if the pixel rate is set to 200 kHz (5 µs/pixel), there are 400 laser pulses per pixel. To avoid photon counting saturation effects, the maximum count rate is 400/5=80 counts/pixel, which sets a reasonable dynamic range of $\approx$ [0,80] in the images. However, this maximum count rate is only 1 in the case of 1 MHz excitation and 200 kHz pixel rate, resulting in a very low dynamic range. In order to maintain a high pixel rate (200 kHz - 1 MHz), it is therefore necessary to perform an analog digitalization of the PMT pulses and to detect several photons per laser pulse.

An alternative detection system was therefore designed for that purpose by Xavier Solinas in our laboratory. Instead of using a thresholding discriminator, the system performs an integration of the current pulses produced by the PMTs. The electronic diagram is shown in Figure 2.19. A condenser charges during the pixel dwell time specified in the acquisition software. After one pixel cycle, the condenser is discharged and the acquisition board (PCI6115, *National Instruments*) digitalizes the pixel value. The acquired signal is therefore proportional to the area under the curve of the detector current, and the dynamic range is then increased compared to the photon counting case.
In practice, three potentiometers allow tuning the integration parameters:

- **Offset:** It initializes the offset of all the electronic components of the system to zero. This potentiometer is used to adjust the value of the signal received by the integration system at the beginning of the integration time, which can be checked on an oscilloscope.

- **Null integrator:** This potentiometer ensures that the integral value is zero when no photons arrive on the PMT. To do that, the integrated signal is analysed with an oscilloscope with the PMTs on but no laser excitation and its slope is adjusted with the potentiometer until the curve is flat.

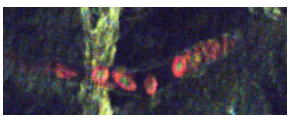

- **Gain:** This potentiometer regulates the multiplicative factor of the integral. It is useful to enhance the signal on the channels collecting low intensity signals.

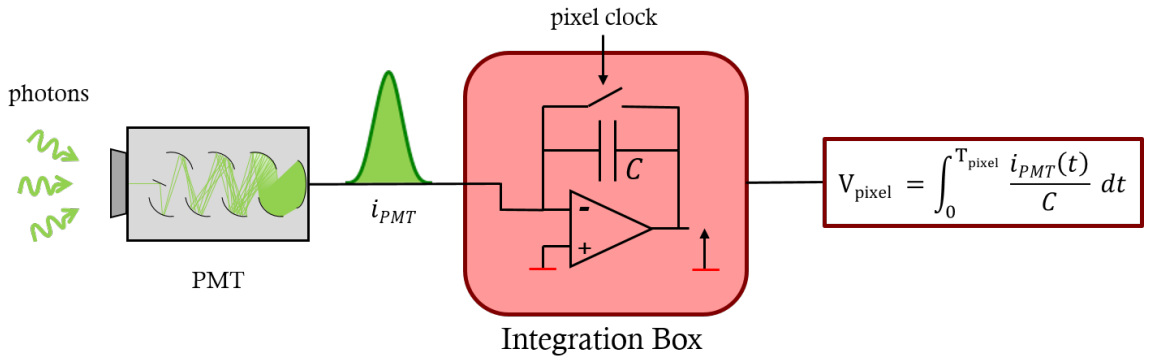

Figure 2.19: Diagram of the working principle of the integration detection system. It is triggered by a clock signal working at the pixel rate (pixel clock). PMT: photomultiplier tube.

4.2.3 Calibration and linearisation of the detection chain

The high-gain GaAsP detectors provide a high sensitivity of weak signals, however they have a limited dynamic range and do not exhibit a linear response with intensity. This causes difficulties for image interpretation, as pixel values are not proportional to the fluorescence flux on the detector.

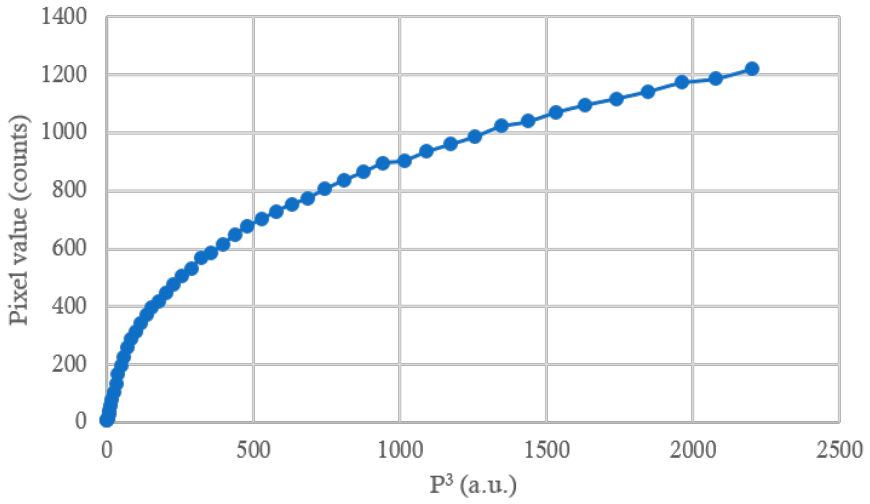

Figure 2.20: Nonlinearity of the detection chain. A THG signal represented in terms of the excitation power cubed is expected to be linear. Instead, the measure illustrates that the detection chain saturates.

For this reason, a calibration step is required for quantitative imaging. This calibration was done by measuring the THG signal of a water-glass interface for increasing excitation power. Figure 2.20 presents the response of the detector when imaging a THG signal as a function of the excitation power raised to the power of 3. If the detection was linear, this curve should be a straight line because THG is proportional to the cube of

the excitation intensity. Rather, this curve demonstrate the nonlinearity of the detection chain. Therefore, we used it to linearise the intensity values in our imaging experiments, as follows. The curve in Figure 2.20 is inverted, and fitted by a polynomial which is then used as a correction function to linearise all the images.

5 Illustration of in-depth imaging with MHz 1700 nm pulses

To conclude this chapter, we present some imaging demonstrations performed with the second source prototype, illustrating the ability of our setup to perform in-depth imaging of different biological tissues with high-energy 1700 nm pulses.

Zebrafish embryo

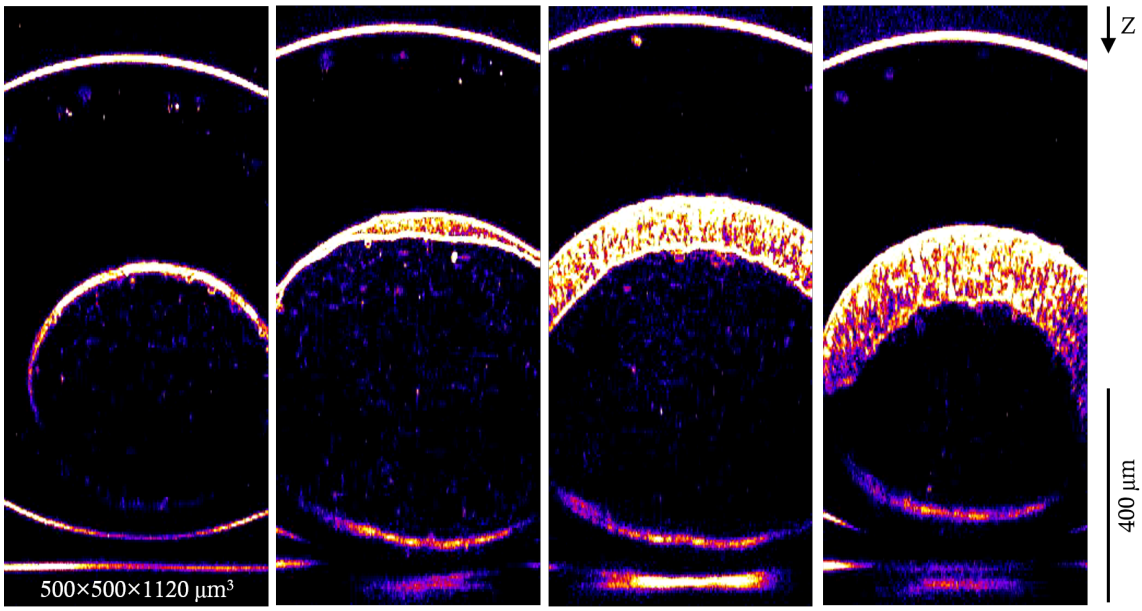

Figure 2.21: THG imaging of a 24 hpf zebrafish embryo inside its chorion using 1700 nm OPA excitation. The figure shows xz re-slices from a series of xy images. The excitation beam is focused from the top and detection was done in transmission.

As a first illustration, Figure 2.21 presents THG images of a 24 hpf (hours post fertilization) zebrafish embryo imaged directly inside its chorion. It was lying on a glass slide, immobilized in a low density agarose gel, and imaged with direct immersion in water. THG signals at 567 nm were recorded in transmission. The images shown are xz re-slices of a series of xy images encompassing the entire embryo. THG signals highlight the chorion, the embryo internal interfaces including cell boundaries [62], and the upper interface of the microscope slide. It is remarkable that THG signals can be recorded over the entire chorion (≈ 1 mm in diameter) despite the presence of aberrations caused by the embryo shape which reduces the contrast at large depths. This is generally not feasible in THG imaging with 80 MHz, 1100 nm excitation as usually performed at LOB [62] because signals are much weaker. This experiment illustrates the potential of high energy 1700 nm

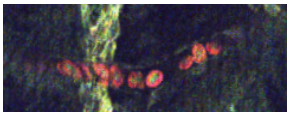

pulses for in-depth THG imaging.

Drosophila embryo

As a second example, Figure 2.22 presents THG images of a Drosophila embryo at the onset of gastrulation. Drosophila embryos at early stage are extremely scattering because they contain large amounts of lipid vesicles of various sizes. We could record contrasted THG images of the innermost yolk regions over 3/4 of the total embryo thickness, as seen in the xz re-projection in Figure 2.22. These images were recorded with up to 44 mW excitation power on the sample, and 200 kHz pixel rate. As a comparison, we note that THG imaging beyond the equatorial plane is not practical with conventional OPO excitation (80 MHz, 1100 nm, 120 fs, NA=1, 90 mW on the sample, 2-10 µs/pixel) [48,63] because of the strongly scattering nature of the embryo yolk and the rapid signal degradation with depth. This example illustrates further the potential of high energy 1700 nm pulses for enhanced THG imaging in scattering media beyond brain tissue applications.

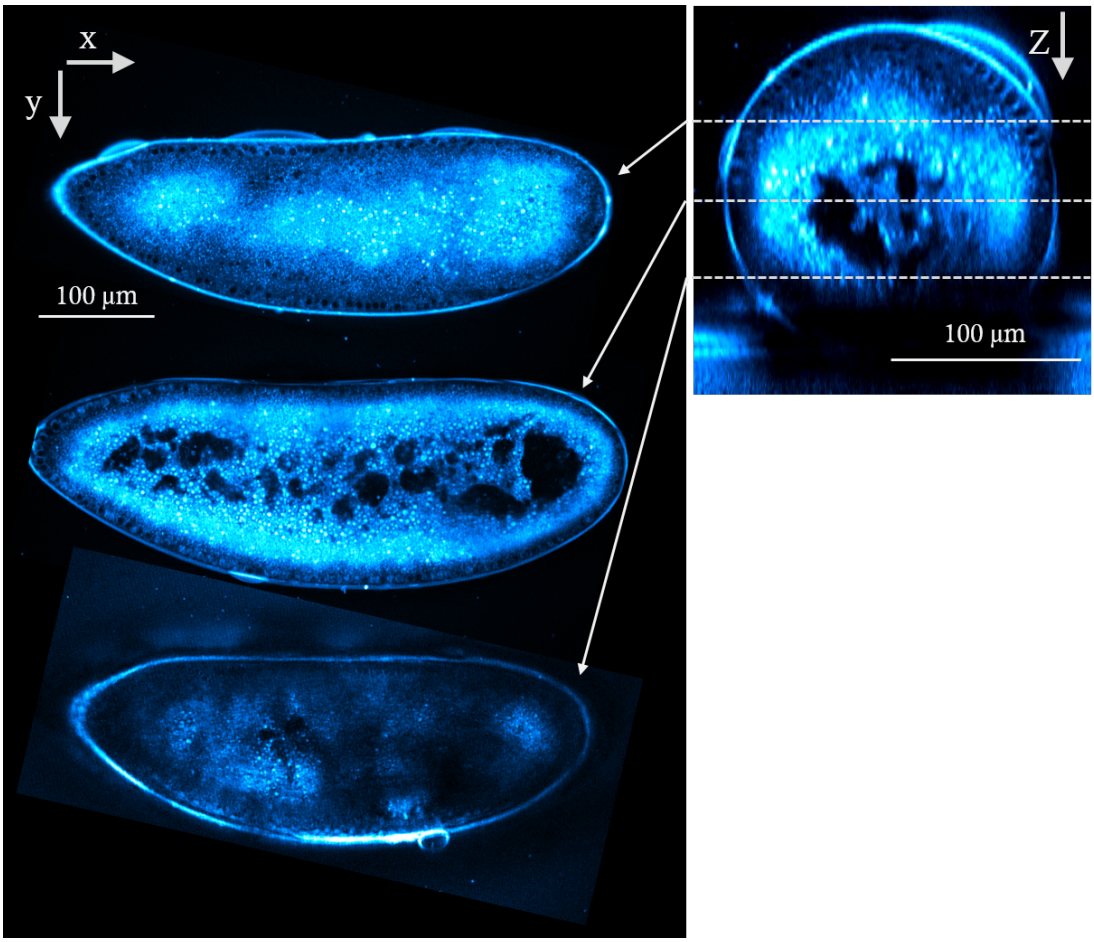

Figure 2.22: THG imaging of a Drosophila embryo at the onset of gastrulation using 1700 nm OPA excitation. Images of the innermost regions remain highly contrasted beyond the equatorial plane despite the highly scattering nature of embryo yolk.

Fixed mouse brain

As a last illustration more relevant to brain tissue imaging, Figure 2.23 presents an example of 3PEF and THG images recorded in a fixed P14 cytbow mouse brain. The brain was provided by the team of Jean Livet (Institut de la Vision). Cytbow corresponds to a cytoplasmic labelling of cells with a brainbow combinatorial approach [1,64]: cells express a random ratio of tdTomato, YFP and CFP. Since the excitation is done here at 1700 nm, Figure 2.23 shows red 3P fluorescence (from tdTomato) and THG at 567 nm. The images shown were recorded in the hippocampus at depths of 1.1 - 1.3 mm. A high power was used for this demonstration (up to 218 mW excitation power on the sample, and 100 kHz pixel rate) in order to ensure contrast preservation at such large depths. The fluorescence contrast on the hippocampal neurons, as well as the THG contrast from myelin fibers of the corpus callosum are remarkable.

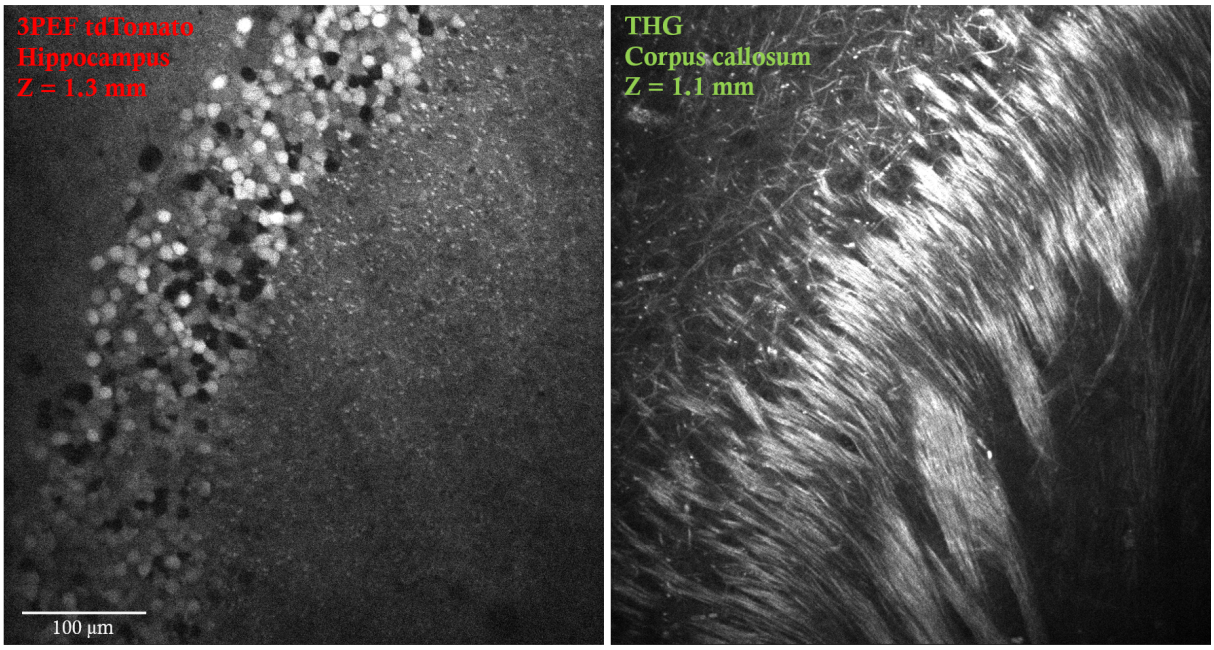

Figure 2.23: In-depth 3PEF and THG imaging of a fixed P14 mouse brain. The sample is a cytbow brain with dense cytoplasmic tdTomato labelling. The 3PEF image (left) was recorded in the hippocampus at a depth of 1.3 mm. The THG image (right) was recorded in the corpus callosum at a depth of 1.1 mm and reveals myelinated axons.

6 Conclusion and perspectives of Chapter 2

Conclusion

In this chapter, we addressed several technical limitations in 3P microscopy. To efficiently generate a third order nonlinear process, it is first critical to use high laser peak intensities. They can be reached by using a laser at constant average power but lower repetition rate compared to OPO sources used for 2P microscopy (typically working at 80 MHz). Thus, we presented a lab-made OPA source working at ≈ 1 MHz and providing microjoule pulses at 1030, 1300 and 1700 nm. Such performances were more adapted for 3P microscopy than what was possible with available commercial lasers. However, we showed that this OPA source suffered from important stability issues that prevented imaging applications beyond proof-of-principle demonstrations. We also briefly presented more stable and compact pre-commercial prototypes of this OPA, which were developed based on our feedbacks and on specific technical developments. We then explained the design of our lab-built 3P microscope. First, we described the conditioning of excitation beams before they are combined and injected in the microscope. It includes power control, spectral filtering, dispersion control, beam metrology and temporal synchronisation of the pulses. We carefully controlled spectral dispersion, since 3P signals strongly depend on pulse duration. We described how pulse compression is achieved with different strategies for each wavelength. Finally, we presented the structure of the microscope and discussed how it was optimised for low repetition rate imaging. In particular, we have shown why photon-counting detection systems used in 2P microscopy are not adapted for 3P microscopy and result in strongly reduced imaging speed or dynamic range. We then proposed an alternative detection system designed in our lab based on the integration of the current pulses produced by the detectors. Together with a calibration of the detection path, our microscope provides fast and high dynamic range 3P imaging. As a conclusion, the development of the OPA source together with our work on the beam conditioning paths and on the improvements of the microscope resulted in a working 3P microscope with a strong potential for biological imaging applications.

Perspectives

Implementing the next generation of the OPA source and further improving the microscope for 3P imaging are the main perspectives of the work presented in this chapter. A fully commercial version of the laser source presented in this chapter, called Satsuma Niji by *Amplitude*, was delivered and installed in our lab at the end of October 2021. This new version is based on two independent OPA paths, one which produces a beam at 1300 nm and a second one producing the 1700 nm output. This new design improves the output power compared to the original one using the doubling stage. Moreover, in this new laser source, the TL pulse duration of the OPA beams is ≈ 50 fs, delivering similar average power than the pulses of the third prototype ($\tau_0 \approx 80$ fs). In practice, this can result in a 3P signal enhancement of ≈ 2.5. Additionally, this OPA source allows wavelength tuning in a ≈ 100 nm range, which can be useful to optimize the central wavelength of the beam spectra depending on the imaging application. To improve our experimental setup, we will implement this new commercial laser source from Amplitude and address several issues. First, the beam paths designed for the third prototype will be adapted to

this new laser source. In addition, we plan to further reduce the axial mismatch between the foci at 1030 and 1700 nm, which was of 6 µm in the third prototype case. We also plan to simplify the control of beam divergence and size by replacing the iterative telescope adjustment by the use of phase masks. Finally, we observed a scanning artefact with striped patterns superimposed to the signal in our images (Figure 2.24), which we will address. This artefact is due to the random phase between the pixel acquisition rate and the laser repetition rate. Indeed, using a laser source at 1 MHz and a pixel rate of 200 kHz, we obtain an average of 5 pulses/pixel. However, the lack of synchronization between the pixel acquisition and the laser pulse train, results in a one-pulse fluctuation from one pixel to its neighbour. Such variation has a significant impact on the detected signal due to the low number of pulses per pixel and the third order signal process. We note that such signal variation is not observed in 2P microscopy since the number of pulse per pixel is several order of magnitude higher (typically 400 pulses/pixel when using 80 MHz laser repetition rate and 200 kHz pixel rate). To remove this artefact, we will synchronise the laser pulse train and the detection rate by triggering the detection electronics using the laser pulse time.

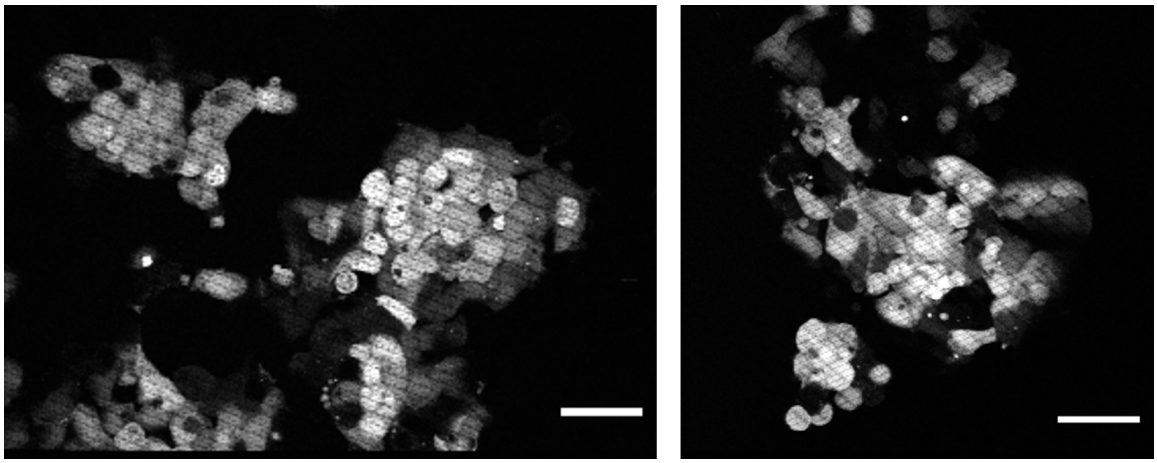

Figure 2.24: Stripped pattern superimposed to images of HEK cells labelled with EGFP excited with 3P at 1300 nm. It is due to fluctuations of the number of pulses per pixel as a consequence of the low repetition rate.

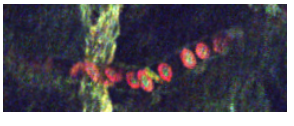

Chapter 3

3P excitation of blue fluorescent proteins

Contents

1 Fluorescence microscopy

In this chapter we focus on three-photon excited fluorescence. In this section, we first review the basis of this source of contrast and its main properties in the linear excitation regime. Then, we discuss the particularities of multiphoton excitation of fluorescence compared to 1P excitation. We underline the lack of published characterisation data of 3P excited fluorescent proteins emitting in the blue spectral range, which limits the amount of observable parameters in deep tissue imaging. Therefore, the objective of this project is to investigate the 3P excitability of different blue proteins with the system presented in Chapter 2 to extend the chromatic palette of 3P microscopy. In Section 2, we present the details of the experimental procedure which allowed to study the performances of three blue fluorescent proteins and how they compare with 3P excitation of red and green fluorescent proteins. In the last section, preliminary demonstrations of 3P blue fluorescence imaging in thick tissues are presented.

1.1 Basic concepts

1.1.1 Definition

Fluorescence is a phenomenon of light emission exhibited by some molecules during their relaxation from an excited electronic state. This excited level is usually reached through the absorption of a photon from an excitation light source, typically a laser in optical fluorescence microscopy. The emitted fluorescence light is red-shifted with respect to the excitation light as shown in the example of Figure 3.1. The energy difference between the maximum of the excitation spectrum and the maximum of the emission spectrum is known as the Stokes shift.

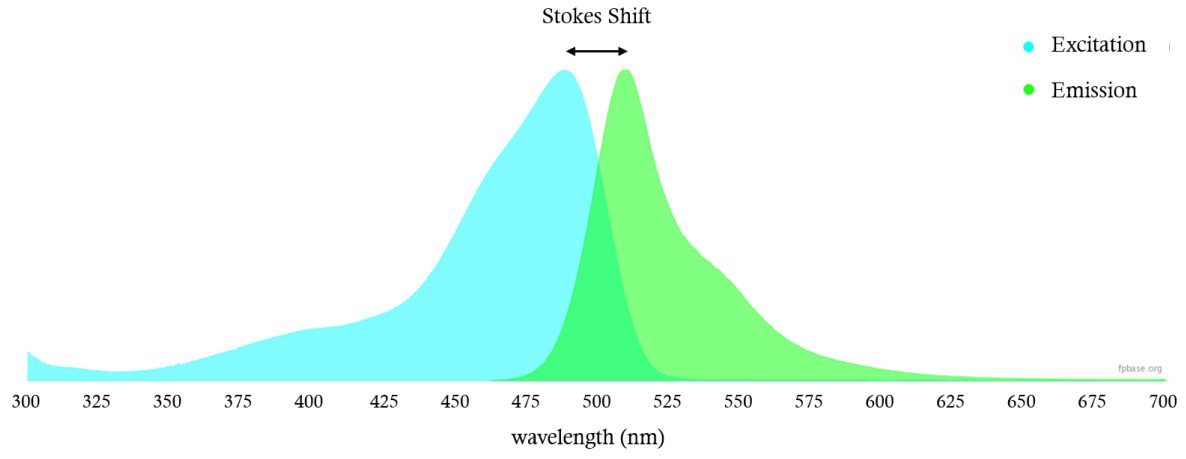

Figure 3.1: Excitation (blue) and emission (green) spectra of the green fluorescent protein (EGFP). Source: [65].

Fluorescence microscopy can use fluorescent substances naturally present in cells and tissues (endogenous fluorophores) as well as artificially introduced labels (exogenous fluorophores) as the source of contrast.

1.1.2 Mechanism

The absorption, excitation and emission processes can be represented by the energy diagram of the electronic orbitals of the fluorescent molecule or fluorophore. This representation is known as the Jablonski diagram (Figure 3.2). It also includes the vibrational energy sublevels existing around the electronic states.
When a photon of energy $E_{exc} = \hbar\omega_{exc}$ is absorbed, a transition from the ground state to an excited vibrational level of the excited electronic state takes place within a time of the order of the femtosecond. The de-excitation process starts through the relaxation of the vibrational level in a non radiative form followed by the electronic transition to the ground state through the emission of a photon of energy $E_{em} = \hbar\omega_{em}$. The internal vibrational transitions take several ps, whereas the lifetime of the electronic excited state is typically between 1 and 10 ns.
Yet, this is not the only de-excitation path that the molecule can follow. There are other possibilities such as the transfer of energy to another molecule or other non-radiative decays usually in the form of thermal transitions in which no light is emitted.
To describe the physics of these competing processes we define the radiative de-excitation rate k_r as the probability of radiative de-excitation per unit time, and $\sum k_{nr}$ as the sum of the probabilities of other non-radiative de-excitation processes. This allows us to mathematically define the **fluorescence quantum yield**:

$$\eta = \frac{k_r}{k_r + \sum k_{nr}},$$

which describes the probability of a photon being emitted when a photon has been absorbed. This quantity is determined by the internal energy organisation of the molecule and its chemical environment, therefore, it is different for each fluorophore. When a fluorophore is illuminated by a laser source of intensity I and absorbs a number of photons N_{abs}, we define the **absorption cross section** σ_{abs} as

$$N_{abs} = \frac{I\sigma_{abs}}{\hbar\omega_{exc}}.$$

It is the parameter that quantifies the absorption capability of the fluorophore.
Similiarly, the **action cross section** σ_{em} is the probability of emitting a photon and is defined as:

$$N_{em} = \frac{I\sigma_{em}}{\hbar\omega_{exc}},$$

where N_{em} is the number of emitted photons.
The brightness of the fluorescence signal for each fluorophore is proportional to $\sigma_{em} = \eta \cdot \sigma_{abs}$. For this reason the action cross section is commonly used to characterise the response of the fluorophore.

1.1.3 Photobleaching

Fluorescent molecules experience a finite number of excitation-emission cycles before definitive extinction of fluorescence. This phenomenon which can be measured experimentally is called photobleaching. Although the detailed energy transition mechanisms are not fully understood for all molecules, a model to explain them is the following (Figure 3.2). According to electronic selection rules, during excitation, the transition from the ground state S_0 is necessarily to a singlet state S_1 (antiparallel electron spins). The

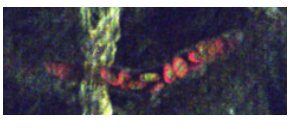

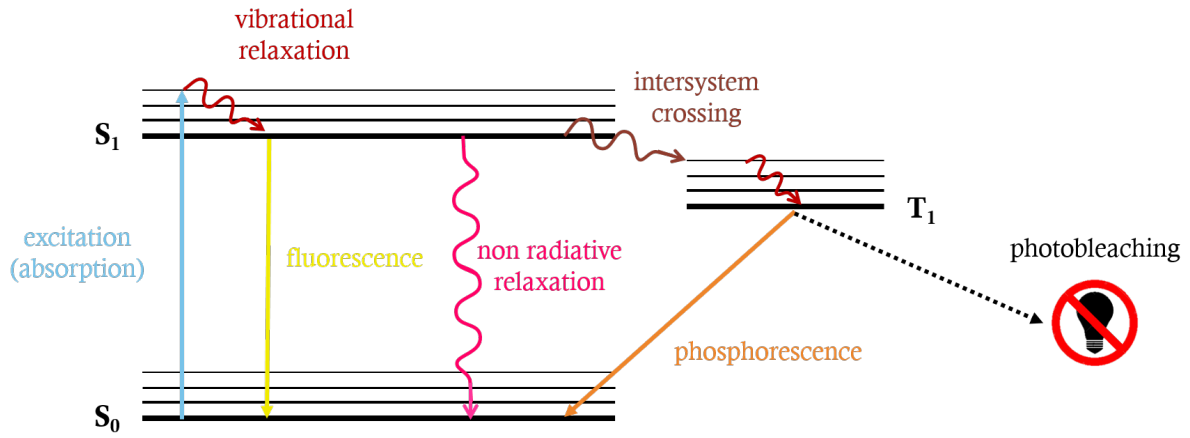

Figure 3.2: Jablonski diagram of a fluorescent molecule and the possible transitions. Electronic levels are represented in bold whereas the thinner lines represent vibrational states.

de-excitation process, however, which usually brings the system to the ground state, can also bring it to a triplet state T_1 (parallel spins), with very rare radiative de-excitation due to its long lifetime (phosphorescence $\approx$ ms). While the system stays in this state, no absorption-radiation cycles happen. Although this situation can be reversed, the triplet state is reactive, especially in the presence of oxygen radicals found in solutions. This can cause the fluorophore degradation up to complete extinction.

The consequences of bleaching in microscopy are an exponential decay of the fluorescence signal as a function of time under continuous exposure as well as a limited number of emitted photons per fluorescent molecule, known as the photon budget. For this reason, it is important to limit the light exposure of the sample.

1.1.4 Fluorescent probes

Not all the molecules are fluorescent. Indeed, when $\sum k_{nr} >> k_r$ (fast vibrational relaxation), the de-excitation takes place before there is time for the emission of a photon. These molecules are considered absorbers, since they distribute the energy of the absorbed photons to the system in the form of thermal energy. Among the existing fluorophores we distinguish three main groups:

- **Organic Dyes:**
  They are synthetic molecules such as fluorescein. They were the first to be used in biological imaging. Nowadays there exist a large choice of derivatives that have been improved to be more photostable and robust. One of the advantages of organic dyes is that they are generally smaller than other fluorophores (e.g. fluorescein size is of the order of a few Å), which makes them less invasive. On average, they are also brighter than other fluorophores.

- **Quantum Dots (QD):**
  They are engineered fluorescent nanocrystals [66,67]. Their main advantage is that their spectral properties can be designed with high specificity because they depend mostly on their size. A drawback for biological imaging is that their compounds are often toxic, and although they can be encapsulated in bio-compatible materials,

there is always a risk of degradation of this shell. Moreover, because of their size (2 to 50 nm) their invasivity is higher than that of other fluorophores.

- **Fluorescent Proteins (FP):**
  Green Fluorescent Protein (GFP) was first discovered in the jellyfish *Aequorea victoria*. Since then, this protein and others have been cloned and engineered to be gene expression reporters [68]. Consequently we now have a large palette (Figure

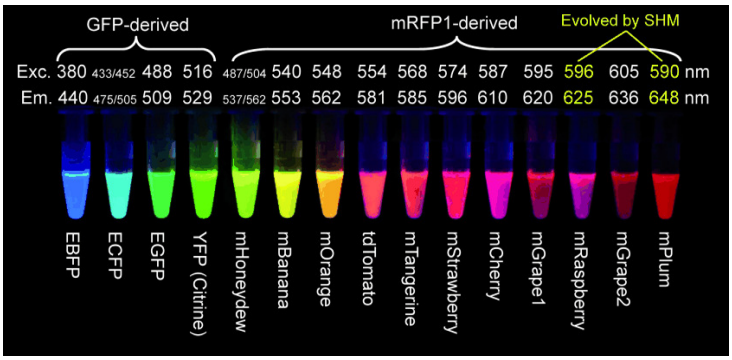

Figure 3.3: Chromatic palette showing some of the existing fluorescent proteins and their linear excitation and emission peaks. Adapted from [69].

3.3) of genetically encoded labels providing high biological specificity. An important development in FP biotechnologies has been to bind the fluorescence response of these proteins to physiological parameters such as the release of Calcium ions related to neuronal activity. This lets the fluorophore act as a neuronal activity reporter.

1.2 Multiphoton fluorescence

To optimize the use of a fluorophore, it is important to know its spectral response, i.e. the spectral dependence of its action cross section. Choosing the excitation wavelength at the absorption peak maximises the number of emitted photons, resulting in a stronger signal. These spectral responses have been studied and reviewed for linear excitation of fluorescent proteins [65, 68, 70, 71]. The excited state of fluorescent molecules can also be reached with multiphoton excitation as shown in Figure 3.4.

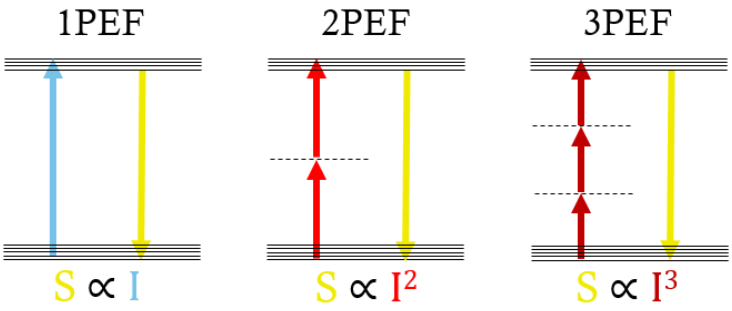

Figure 3.4: Energy diagram for linear, two-photon and three-photon excited fluorescence (EF).

1.2.1 Multiphoton fluorescence excitation

Although many questions on the details of the excitation process remain unanswered, precise 2P spectra have been reported for the most common fluorophores [45,72–74]. The two-photon absorption cross section can be measured through an absolute method, or more often, by means of a relative measurement calibrated with a known fluorophore. A common conclusion of these studies is that the multiphoton excitation spectrum of a fluorophore can generally not be predicted from its linear spectrum, probably due to differences in the selection rules for 1P and 2P transitions. The authors of [74] observe that for some fluorescent proteins the spectrum perfectly matches that of linear excitation (with the wavelength multiplied by 2) whereas in some other cases there is a significant shift or changes on the spectral shape. Similar observations can be done on the available data on 3P excitation [75–79]. An example is shown in Figure 3.5.

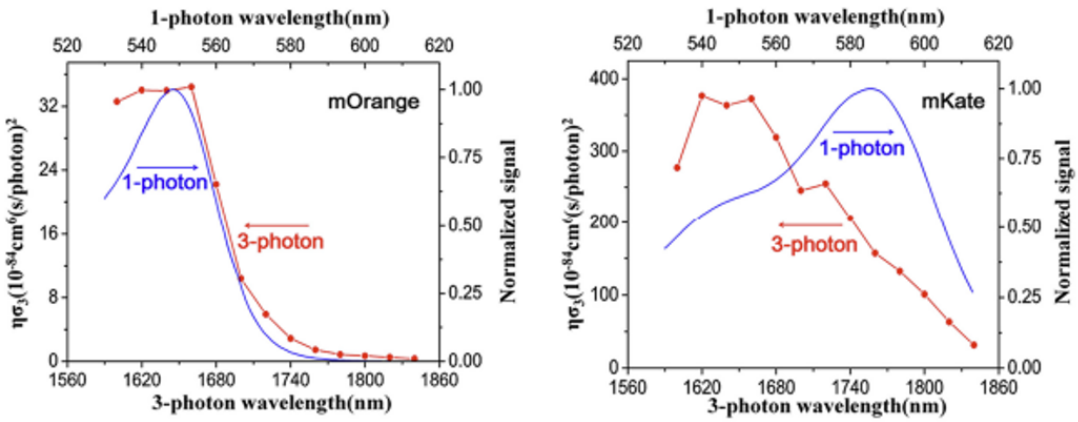

Figure 3.5: 3P excitation spectra compared to linear excitation. In some cases the excitation peak appears to match (mOrange, left) whereas for some others there is a visible shift (mKate, right). Adapted from [79].

The interpretation of these features is complex because different kinds of transitions can arise from the high excitation intensities involved. Moreover, other conditions such as pH, temperature or concentration also affect the spectral properties. For example, the authors of [78] measured differences on the spectral signatures of tdTomato between the purified protein and the protein in stained HeLa cells. Modelling the relation between the structure of a chromophore and its action cross section spectrum would be very interesting, but it is not straightforward. The lack of published FP 3P spectra complicates the choice of dyes and excitation wavelengths for 3P excitation hampering its development, for the moment limited to the few proteins characterised so far.

1.2.2 Multiphoton fluorescence emission

Regarding the emission, there is a rule in linear fluorescence microscopy known as Kasha's rule [80]. It states that the fluorescence of polyatomic molecules always occurs from the lowest excited state, independently of which state was initially excited. This means that the emission spectrum is independent of the excitation wavelength because vibrational relaxations previous to photon emission lead the system always to the same exited level. Very few violations of these rule have been observed. When translated to multiphoton

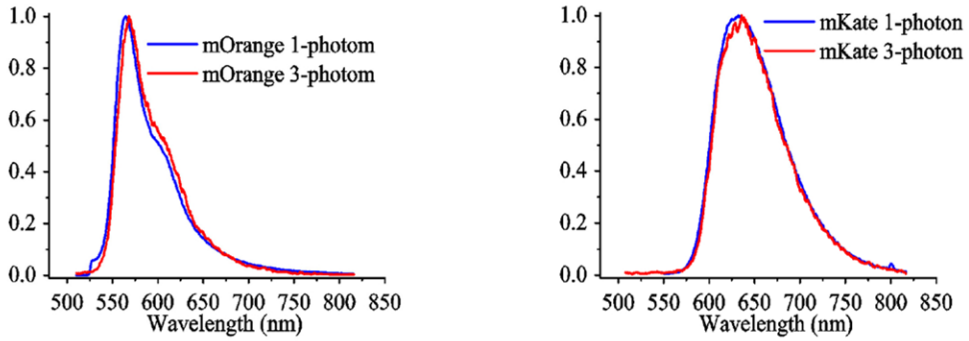

Figure 3.6: 3P emission spectra compared to linear spectra for mOrange (left) and mKate (right). The authors verified the validity of Kasha's rule in 3P excitation. Adapted from [79].

excitation, this rule results in the same conclusion for 2P and 3P excitation as for the linear case (emission spectrum independent of the excitation wavelength) but moreover it also means that the emission spectrum is independent of the modality of the excitation (1P, 2P or 3P). This fact as been confirmed in [79] even for the proteins for which the 3P excitation spectrum does not match the linear one as shown in the example of mKate (Figure 3.6).

1.3 Deep blue imaging

Since it was established that the optimal windows for 3P excitation and tissue penetration reside in the 1300 and 1700 nm bands, most of the recent studies measuring the action cross section have focused on green and red fluorescent proteins.
This results in a gap in the blue emission range, where almost no 3P imaging of fluorescent proteins has been reported yet. The identification of efficient 3P excited blue fluorescent proteins would be an advantage which would extend the number of independent tissue parameters that can be labelled and detected simultaneously. Eventually, it would also open the possibility of deep imaging using combinatorial multicolour labelling techniques such as brainbow [1]. In this approach, a transgene is built coding for three different proteins, typically a red protein, a yellow protein and a blue protein. The expression is regulated by a recombination of specific DNA sites triggered by the enzyme *Cre recombinase*, which results in an arbitrary expression of one of the three proteins. When several copies of the transgene are present in the same cell, the random combination mechanism results in multiple possible combinations that can be detected as independent colours.

In this chapter, we study multiphoton excitation of three different blue fluorescent proteins to evaluate if they can be excited with 3P at 1030 nm. This wavelength is available from the pump of most current OPA systems (including the microscope described in Chapter 2) and seems spectrally well suited for 3P excitation of blue fluorescence. Certainly, without a spectral analysis we miss the step of optimising the excitation wavelength, but comparing 3P absorption efficiencies of several FPs at this particular wavelength should already indicate which ones are most promising.
We use a pragmatic approach described in Section 2.1 in which fluorescent proteins are characterised directly in transfected cells instead of being purified and imaged in solution. This method can lead to higher uncertainties since the level of expression of the protein might exhibit some cell-to-cell variability. On the other hand, the sample preparation is

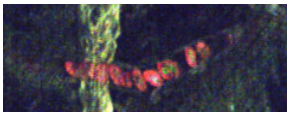

simpler and the results should be more representative of real experimental conditions in biological applications.

1.4 The blue FPs of interest

Three different blue proteins were chosen for the study: EBFP2, mCerulean and mTurquoise2. The linear photophysical properties of these proteins are summarized in Table 3.1 and their linear excitation spectra are plotted in Figure 3.7. The parameters for EGFP and mCherry, used as green and red controls, respectively, are also reported.

Protein	λ_{ex} (nm)	λ_{em} (nm)	EC ($M^{-1}cm^{-1}$)	η	Brightness	Lifetime (ns)	Reference
EBFP2	383	448	32000	0.56	17.92	3	[81, 82]
mCerulean	433	475	33000	0.49	16.17	-	[83]
mTurquoise2	434	474	30000	0.93	27.9	4	[84]
EGFP	488	507	56000	0.6	33.54	2.6	[85, 86]
mCherry	587	610	72000	0.22	15.84	1.4	[87, 88]

Table 3.1: Linear excitation parameters of the fluorescent proteins studied in this chapter. λ_{ex}: maximum excitation wavelength, λ_{em}: maximum emission wavelength, EC: extinction coefficient (absorption cross section normalized by the number of absorbing molecules per unit volume), η: fluorescence quantum yield, Brightness: calculated as the product of EC and QY, Lifetime: the time it takes for 1/e of an excited population of molecules to relax.

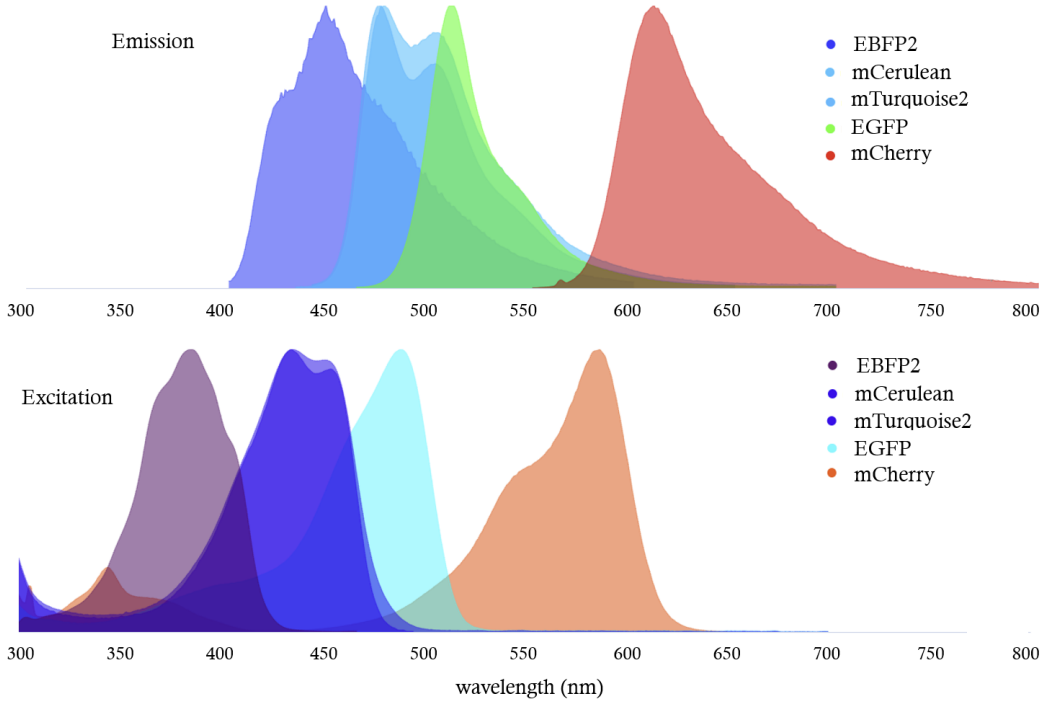

Figure 3.7: Linear excitation (bottom) and emission (top) spectra of the fluorescent proteins used in this chapter. Source: [65].

The samples were provided by our collaborators (prepared by Takuma Kumamoto and Mickaël Le in the team of Jean Livet) at Institut de la Vision and prepared as follows.

HEK-293 cells were grown for 24 h in 6-well plates (5 x 10^5 cells per well) and transfected with 1 µg of DNA plasmids encoding the protein of interest under the strong CAG or CMV promoter using Lipofectamine 2000 (*Invitrogen*). After 24 h, the transfected cells were deposited onto a 13 mm glass coverslip coated with collagen (50 µg/mL, *Sigma*), and cultured for an additional 24 h period. Then, the cells were fixed with 4 % paraformaldehyde (PFA, Antigenfix, *Diapath*) and mounted in mowiol medium (*Sigma*).

2 Experiments and results

Figure 3.8 presents examples of 3P images of the samples.

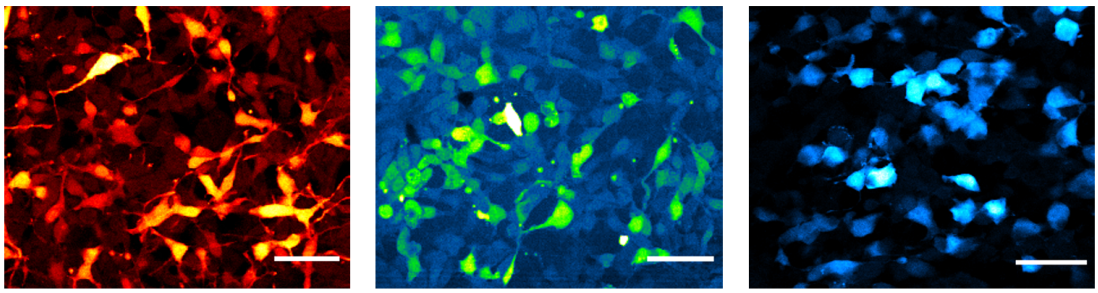

Figure 3.8: 3P images of HEK-293 cells labelled with mCherry, EGFP and mTurquoise2 (from left to right). Scale bar 50 µm.

2.1 Experimental procedure

The method to determine if a protein can be efficiently excited through a 3P process is relatively simple. As we stated in Chapter 1 (Table 1.1), the fluorescence signal of order N depends on the excitation power P raised to the power of N among other parameters:

$$S_{\mathrm{NP}} \propto P^{\mathrm{N}}.$$

Here, we used this dependence to determine the order of the excitation. A series of images was taken with increasing excitation powers (from P_{min} to P_{max}). Then the signal was fitted with a power law model. The exponent of the fit (slope in log-log scale) indicates the order of the excitation process:

$$\log S_{\mathrm{NP}} \propto \mathrm{N} \log P.$$

2.1.1 Image acquisition and identification of power ranges

The images were acquired in epidetection using a power stack (P-stack) mode, coded on the LabVIEW interface of the microscope. In this mode, the user can choose the values of P_{min} and P_{max} defined as a percentage of the maximum power, and the number of total images acquired as a stack. After the imaging session, a power calibration curve was carefully registered. This step is crucial for an accurate extraction of the nonlinear order because a power offset can strongly bias the fitted slope as shown in the following example. On the left-hand side of Figure 3.9, we have simulated a signal scaling as the

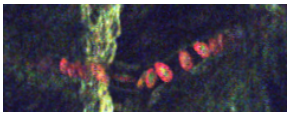

power cubed (straight line of slope 3 in log-log representation). In the right-hand side, we have plotted the same signal with different power offsets P_0. These offsets result in a region (indicated with the red rectangle) in which the power dependence of the signal presents slope values ranging between almost nearly 0 and 3. Experimentally, such a threshold can originate from an imperfect cancellation of the transmitted excitation on the power controller. A similar bias of the response curve is observed in power regions for which the signal is of the order of the noise floor offset and is limited by the detection sensitivity.

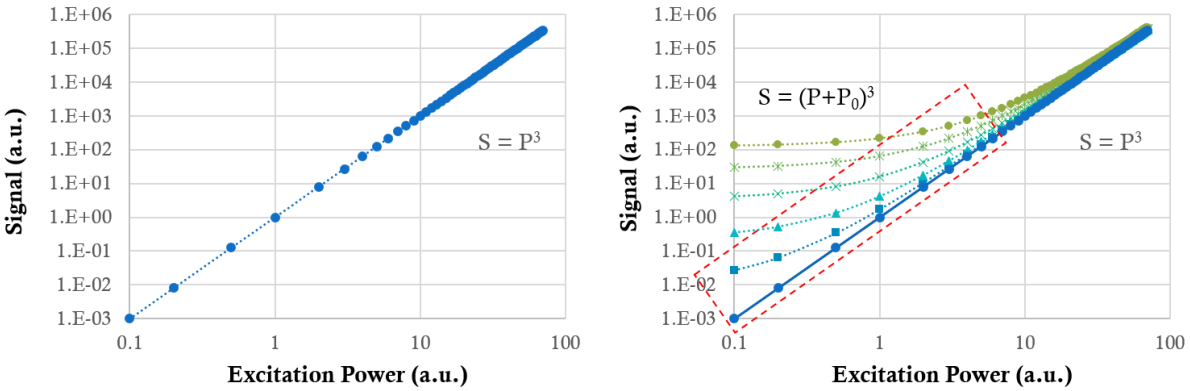

Figure 3.9: Simulations showing the effect of a power offset. On the plot to the right, the values of this power offset P_0 are 0, 0.2, 0.6, 1.5, 3 and 5 a.u..

We expect all the proteins to present similar relative behaviours along the excitation power response curve, but the absolute power values of the different regimes might vary. At the beginning of the curve the excitation power is not sufficient for multiphoton excitation and the signal is below the background. As the excitation power increases, we expect to reach a regime where the signal follows a power law of 3 with the excitation. At higher excitation powers, saturation of the fluorophore or higher order nonlinear effects generally occur. Saturation leads to lower excitation coefficients, while higher nonlinear orders result in brighter fluorescent signals with strong nonlinear coefficients as described in [35] (Figure 1.27, Chapter 1). In practice, the power range for which the signal scales as a cubic law is relatively narrow, usually less than the 3-fold of the minimum power value on the examples found in the literature [77,79,89]. For this reason, this power range is non-trivial to identify and might be missed if the power steps are too large during the P-stack. On the other hand, taking smaller power steps results in more images, which increases appearance of photobleaching, and leads to a decrease of the apparent nonlinear excitation order. A compromise, therefore, needs to be found. In general, several trials are needed to identify first the 3P excitation range and then a more accurate P-stack is recorded in this specific range of excitation powers. This study is then completed with repetitions of the experiment to obtain statistical and meaningful results.

The importance of the power offset described above depends on the comparison of P_0 to the power excitation values for which 3P excitation is achieved, P_{3P}. If $P_0 << P_{3P}$, the slope artefact is minimized, but if the two values are comparable, the results are strongly biased. Since P_{3P} is not known *a priori* for each protein, it is more convenient to minimize the power offset. If this problem cannot be resolved, the full calibration of the power variation is necessary.

2.1.2 Extracting the nonlinear order of the excitation

We analysed the images as follows. First, the signal was normalized by the collected fraction of the emission spectrum defined by the dichroic mirrors and detection filters. This allows to compare the brightness of the different proteins (assuming that the expression level is similar for all the cell preparations). Then, with ImageJ, we manually selected regions of interest in the center of the cells. There are differences of fluorescence expression resulting in a variability of brightness from cell to cell. The analysed regions were chosen on the brightest cells to maximise SBR. 10 to 20 cells were measured from different sample wells and different stacks series to average experimental conditions. For each cell, the averaged signal in the region of interest was measured and plotted against the excitation power.
In log-log graphs, we fitted a power law of coefficient γ. The criterion used to decide the limits of the fit was the R^2 parameter, which was accepted equal to 0.98 in the worse case. From these fits, parameters such as the signal level, average power and peak power were extracted. An average curve was also computed as the average of all the measured cells and used as a representative behaviour.

2.1.3 Validation of the method

To check the validity of this method, we applied it first to EGFP excited at 1300 nm and mCherry excited at 1700 nm, protein-wavelength pairs for which 3P excitation has already been shown [77, 42]. The resulting average curves are shown in Figure 3.10 in terms of the average power (P) and peak power P_p. The relationship between the two is $P_p \approx 0.94\frac{T}{\tau}P$ for gaussian shaped pulses. The pulse duration on the sample plane were in this case 170 fs and 80 fs at 1300 and 1700 nm, respectively (first OPA prototype).

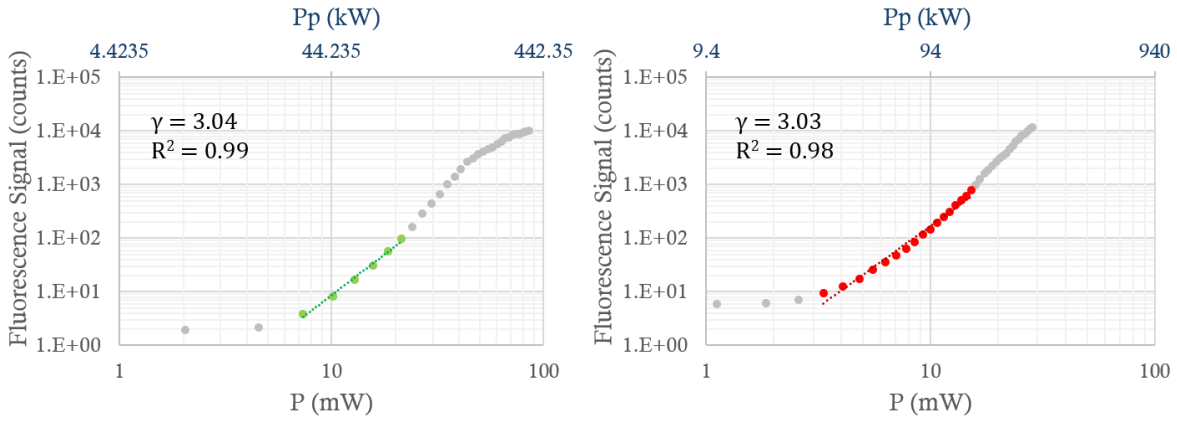

Figure 3.10: Signal dependence on the excitation power for EGFP (left) and mCherry (right). The curves are an average of 15 and 17 different measured cells respectively. The data highlighted in colour is fitted by a power law of γ (straight line).

In both cases it can be observed that for low powers the signal rises from the noise level and reaches the 3P excitation power range. The data in this region is highlighted in colour and fitted by a power law of γ (straight line). For higher excitation powers, higher nonlinear effects start to occur causing the slope to increase. In the case of EGFP a saturation of the curve is also visible for the highest excitation power values used.

2.2 Results and discussion

This method was applied to the three blue fluorescent proteins, excited at 1030 nm. We refer now to Section 3.4.3 in Chapter 2, about the nonlinear compressor for this wavelength. Uncompressed and compressed pulse durations of 250 and 115 fs, respectively, were compared in these experiments. The beam paths were designed such that the alignment is conserved while bypassing or entering the compressor, allowing sequential experiments.

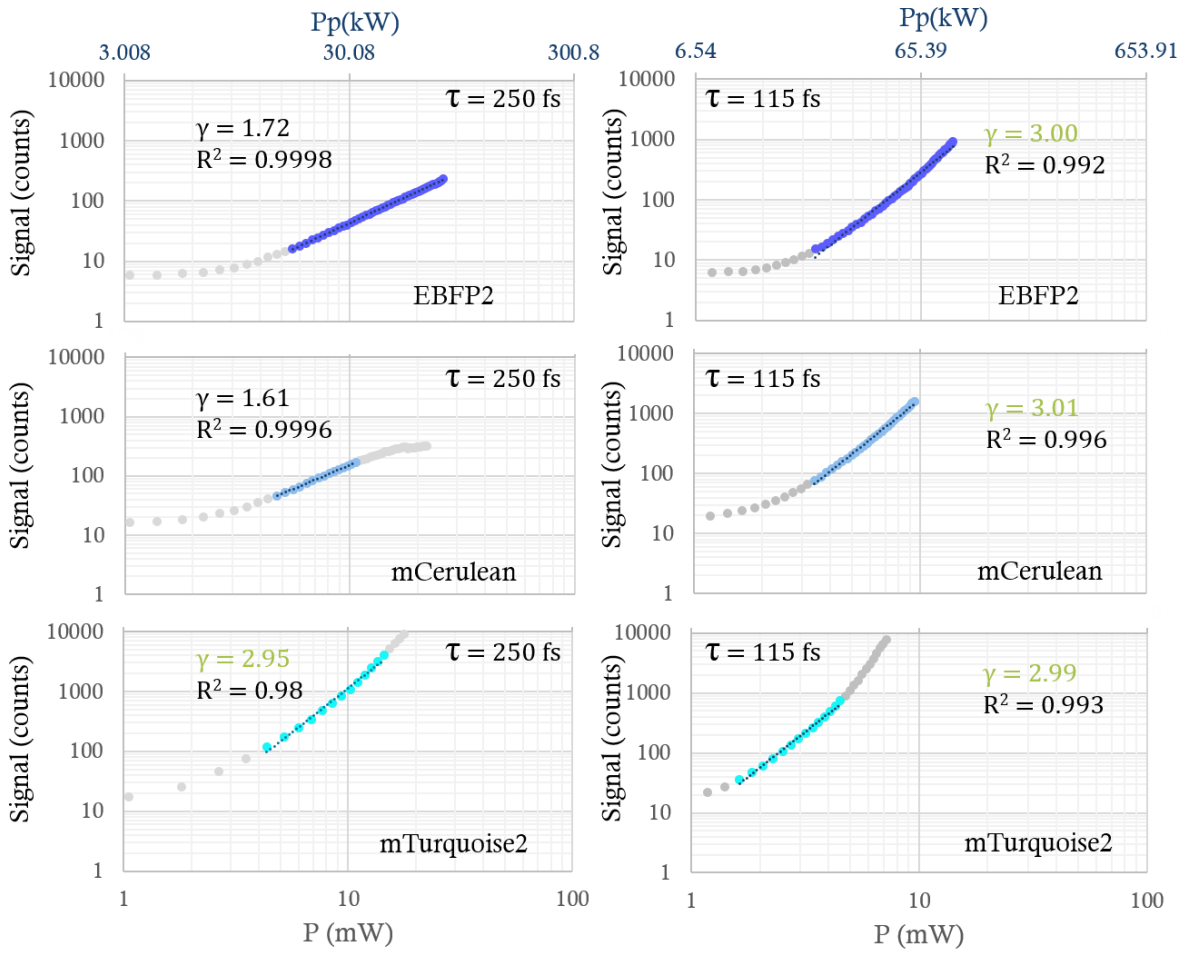

Figure 3.11: Signal dependence on the excitation power for cells labelled with EBFP2, mCerulean and mTurquoise2 excited at 1030 nm. The curves on the left-hand column show the results for the experiments done with 250 fs pulses excitation. The curves are an average of 15, 15 and 28 different cells for each protein respectively. The curves on the right-hand column show the results for the experiments done with 115 fs pulses excitation. The curves are an average of 23, 14 and 12 different cells for each protein respectively. The data highlighted in colour is fitted by a power law of γ (straight line).

2.2.1 Uncompressed 1030 nm pulses (τ = 250 fs)

The average curves of the experiments done with the uncompressed pump on the three blue selected proteins are presented in the left-hand column of Figure 3.11. From these results, we can draw our attention to different points. First of all, only mTurquoise2 seems to be excited at 3P (γ = 2.95) and presents a behaviour similar to EGFP or mCherry. The measured data for mCerulean seems to saturate at the highest excitation

power, but the excitation coefficient is $\gamma = 1.61$. The response of EBFP2 does not reach a saturation plateau and the coefficient $\gamma = 1.72$ is far from proving 3P excitation. The second remark concerns energy conservation issues. Indeed, even considering the detected signals to be around the higher limit of our spectral filter (FF02-447/60, *Semrock*), the energy corresponding to two excitation photons at 1030 nm ($\omega = \frac{2\pi c}{\lambda} = 1.83 \cdot 10^{15}$ rad/s) is not enough to excite fluorescence emitted at ≈ 475 nm ($\omega = 3.97 \cdot 10^{15}$ rad/s).

2.2.2 Compressed 1030 nm pulses ($\tau = 115$ fs)

In the right-hand side column of Figure 3.11, we present the average curves of the experiments done with the compressed pump. In this case, the three proteins exhibit an excitation coefficient close to 3. This suggests that different excitation paths are possible in terms of energy including real states within the main excitation gap. If a real energy level exists close to the one or two photon absorption gaps, they are likely to populate [90]. For example, if a 2P absorption is possible and its lifetime is higher than the time between two laser pulses (T, the inverse of the repetition rate), fluorescence might be excited with a combined effect of 2 plus 1 photon absorption processes in chain. This would cause the emission to depend as a superposition of orders 1 and 2 of the excitation power and could explain the measured values of γ between 1 and 2 found on the uncompressed pump experiments. As the energy per pulse grows higher, however, higher order processes are favoured and dominate upon lower order ones. This can explain why 3P absorption is visible for mTurquoise2, mCerulean and EBFP2 with compressed pulses whereas only mTurquoise2 presents this behaviour with longer pulses (with which higher excitation average powers are needed). This protein is probably the most indicated to use with 3P excitation.
Although the details of the energetic transitions occurring during excitation are complex and will deserve further investigation, we have obtained a first interesting result which is to experimentally determine appropriate 3P excitation conditions of blue fluorescent proteins.

2.2.3 Comparative analysis

As a summary, we display in Figure 3.12 the excitation orders found experimentally for the different proteins analysed.
A rigorous comparison of all the proteins is difficult to achieve because the focusing parameters vary slightly from one beam to the other. This affects the excitation volume, thus the intensity for a given power value. Moreover, although the signal is normalised by the collection of the filters, the spectral response of the detector is not completely flat on the visible range but slightly increasing for longer wavelengths. Therefore, blue signals are slightly underestimated compared to red signals. Another assumption needed for the comparison is that the expression level of the fluorescent proteins is similar among the different samples and cells measured. This should be the case as a first approximation, according to our collaborators who prepared the samples, but there is inevitably some variability in these expression levels. In short, this comparison is most reliable among blue proteins excited with the same pump duration. The comparison with the other proteins should be viewed as an approximation which also reflects the parameters in our microscope.
In Figure 3.13 we display the average values of the average power and the peak power

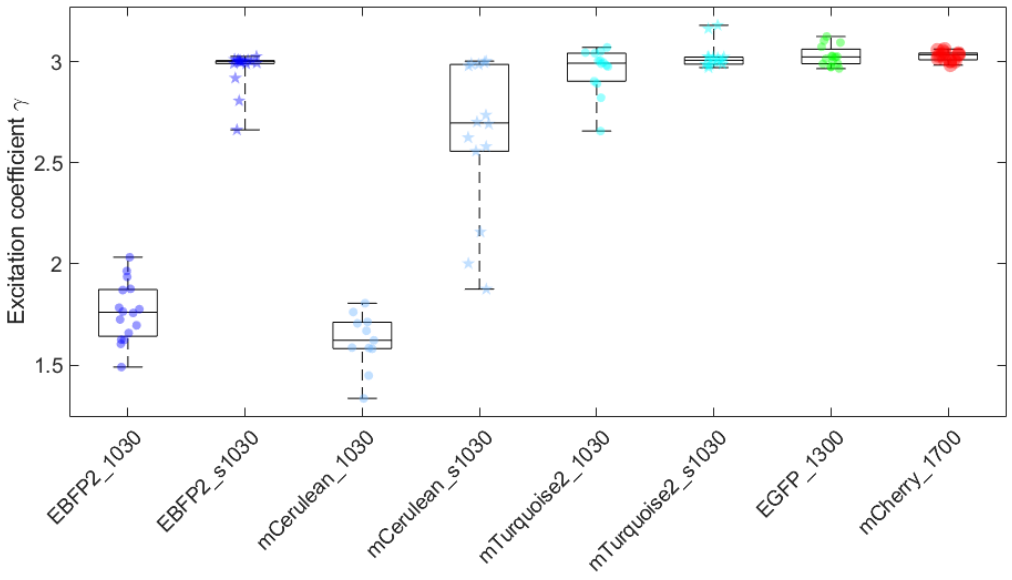

Figure 3.12: Nonlinear order excitation coefficient measured for the different proteins of the study. Stars indicate the experiments done with the compressed pump (s1030 for short-1030) in comparison to the circles, corresponding to the uncompressed pump.

required to achieve 3P excitation of the proteins together with the filter-normalized signal. These experiments were done on the first prototype of the OPA source for which the OPA beams were not very stable. This explains the larger spread of the green and red points, corresponding to uncertainty on the power measurement.

Achieving 3P excitation of EBFP2 (see Figure 3.11) is encouraging because its emission spectrum is well separated from that of EGFP. This facilitates the task of separating channels for multicolour applications. On the other hand, the results show that the required excitation power is higher for this protein than for others, which is a disadvantage for deep tissue imaging applications because of increased photodamage. Considering that mCerulean and mTurquoise2 share the same emission spectrum, it seems that mTurquoise2 is the best choice because it requires a lower excitation power for a similar signal level. mTurquoise2 exhibits 3P excitation both with compressed and uncompressed pulses. This means that the important factor determining the 3P excitation regimes is the peak power because it is the common parameter when we compare the two cases. It might be surprising that the signal obtained with the uncompressed pump is much higher than with the compressed beam. The explanation is that similarly high signal levels are also obtained with the compressed pump, although they appear in a regime of the curve for which the excitation coefficient is higher than 3. Therefore, they are not reflected in this figure. Whether the use of proteins in higher nonlinear excitation regimes is beneficial or detrimental is not clear, and the interpretation would require further experiments studying photodamage. Comparing signal levels is simpler when they are normalized by the excitation power cubed. This gives a measure of the efficiency of the protein on 3P excitation. As shown in Figure 3.14, this analysis reveals that the most efficient combination is mTurquoise2 excited with compressed pulses.

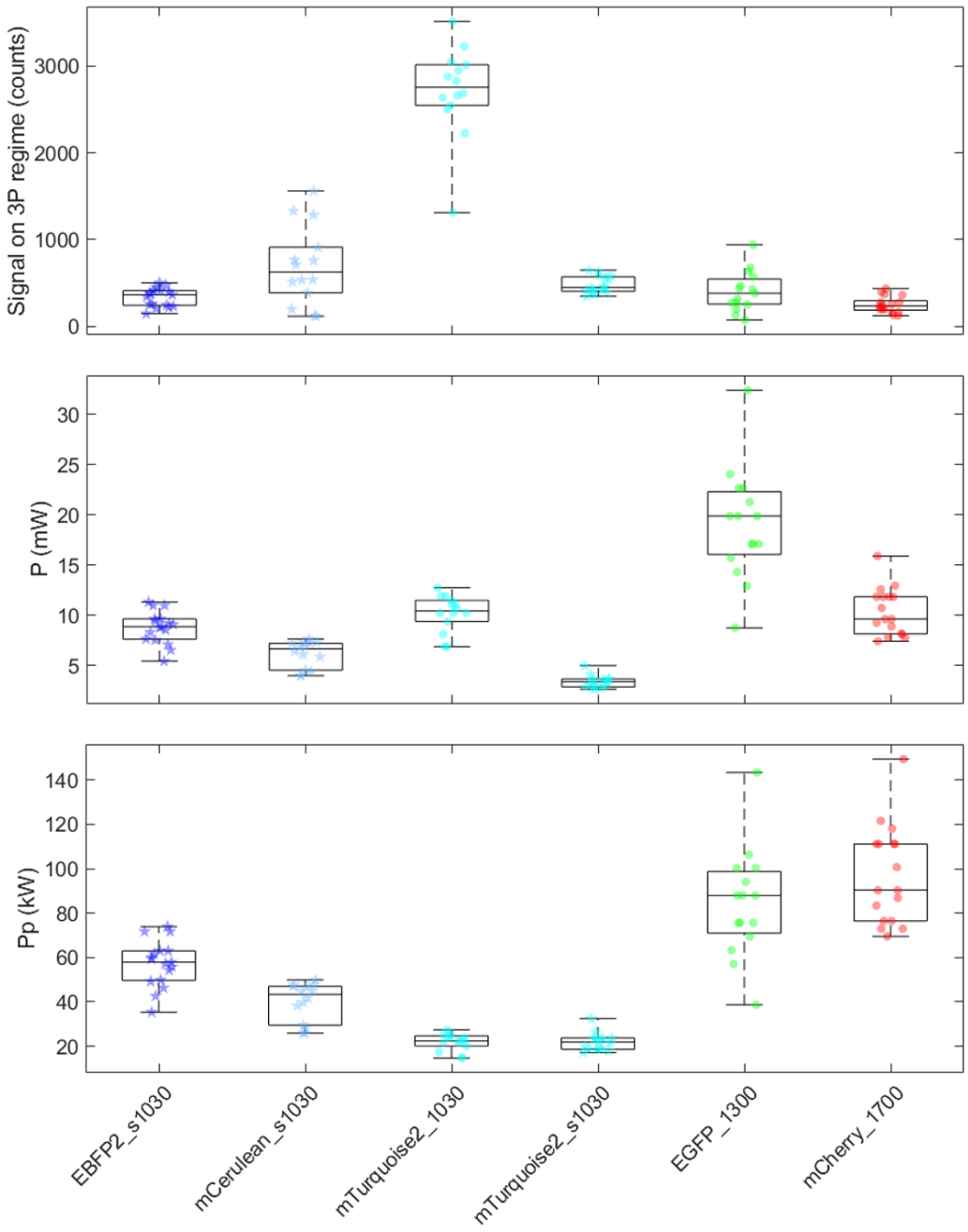

Figure 3.13: Absolute signal, average power and peak power corresponding to the 3P excitation regimes identified through the fitted areas. Stars indicate the experiments done with the compressed pump (s1030 for short-1030) in comparison to the circles, corresponding to the uncompressed pump.

2.3 Deep tissue demonstration

To conclude this chapter, we present preliminary demonstrations of in-depth blue imaging of two different types of tissues. mTurquoise2 was chosen for these tests because it showed the most promising performances in terms of efficiency and "clean" 3P excitation order.

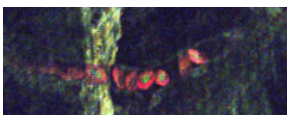

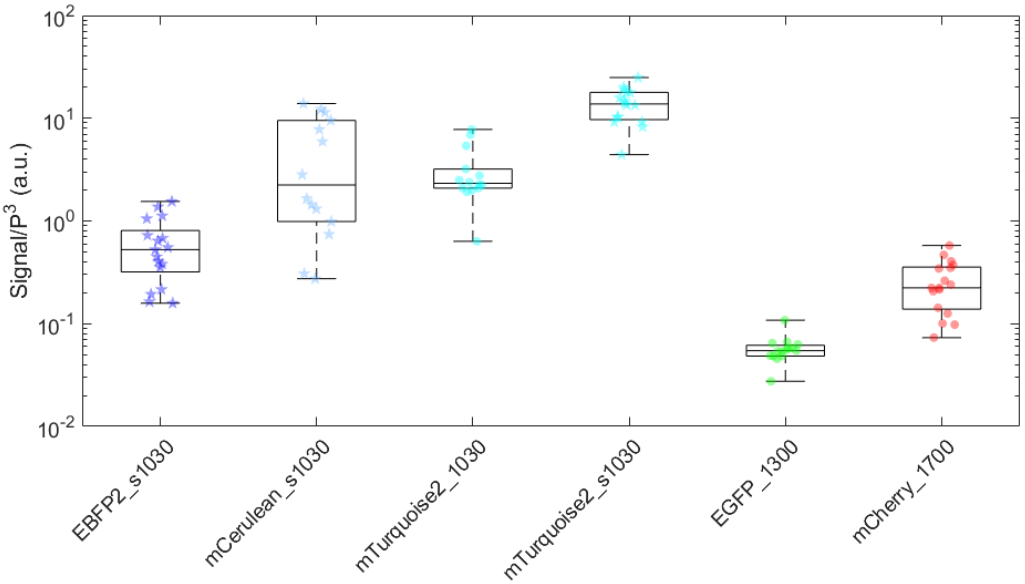

Figure 3.14: Signal normalised by the cube of the excitation power corresponding to the 3P excitation regimes identified on the fitted power ranges. Stars indicate the experiments done with the compressed pump (s1030 for short-1030) in comparison to the circles, corresponding to the uncompressed pump.

Mouse Brain

As in Section 5 in Chapter 2, we have used here a P14 Cytbow mouse brain. The labelling includes both red and blue fluorescence (tdTomato and mTurquoise2). It was provided by our collaborators from the group of Jean Livet (Institut de la Vision). The *ex-vivo* brain was stored in a PB solution (Phosphate buffer: 0.42g/L Monobasic sodium phosphate, 0.92g/L Dibasic sodium phosphate.). It was prepared following the *Agarose Embedding* part of the protocol in [91]. The agarose used here was prepared at 4.5 %. After embedding, the brain was cut in two parts horizontally and the superior half was glued in the bottom of a Petri dish, which was filled with PB as the immersion medium for imaging. The excitation was done on the vertical direction sequentially with the compressed pump at 1030 nm and with the beam at 1700 nm. In Figure 3.15 we present some of the acquired images.

First of all, these images allow the comparison of 2P and 3P imaging of tdTomato at similar imaging depths. It can be observed from the image that the SBR with 2P excitation is lower than with 3P, which presents sharper features.
Secondly, the third image (Figure 3.15.c) is a deep tissue blue imaging demonstration. It can be seen that the SBR at a depth of $\approx 800\,\mu$m is similar to that of tdTomato excited with 3P. As an approximative quantification of the SBR, we have measured the profiles of the brightest features on the three images. They are normalised and plotted in Figure 3.16, leading to an approximate value of SBR.

2P excitation presents a SBR ≈ 2 whereas the two 3P excitation images exhibit SBR ≈ 5 to 8 , measured on the sharpest features in each case. This indicates that mTurquoise2 is excited with 3P, confirming the results of the excitation order analysis presented above.

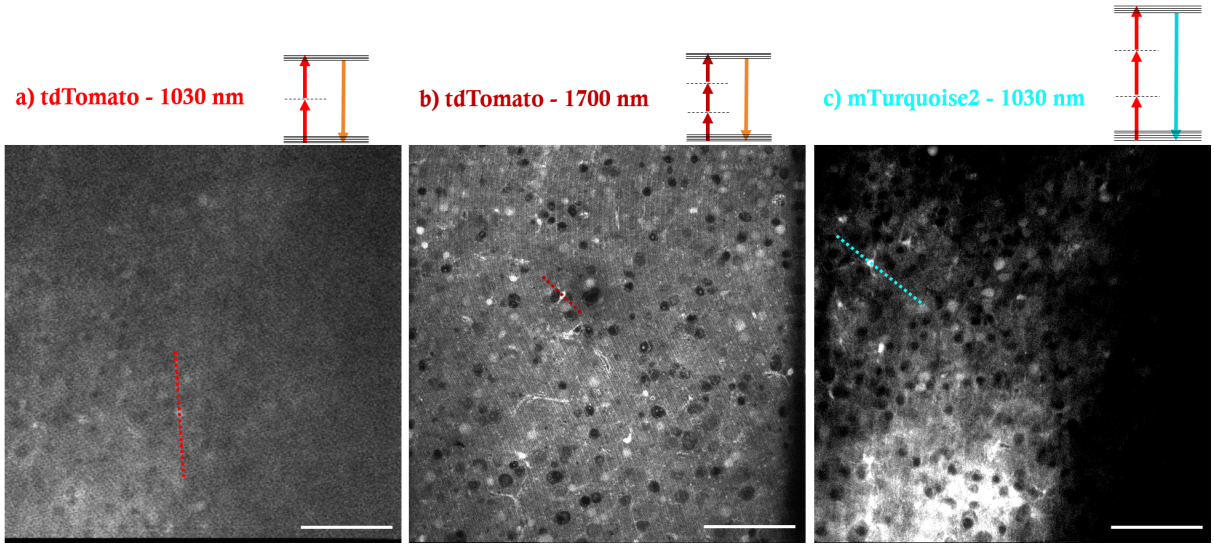

Figure 3.15: Images of a P14 Cytbow mouse brain labelled with tdTomato and mTurquoise2. a) Red channel excited with the compressed pump at 1030 nm (2PEF). Imaging depth z = 760 µm. b) Red channel excited at 1700 nm (3PEF). Imaging depth z = 790 µm. c) Blue channel excited with the compressed pump at 1030 nm (3PEF). Imaging depth z = 795 µm.

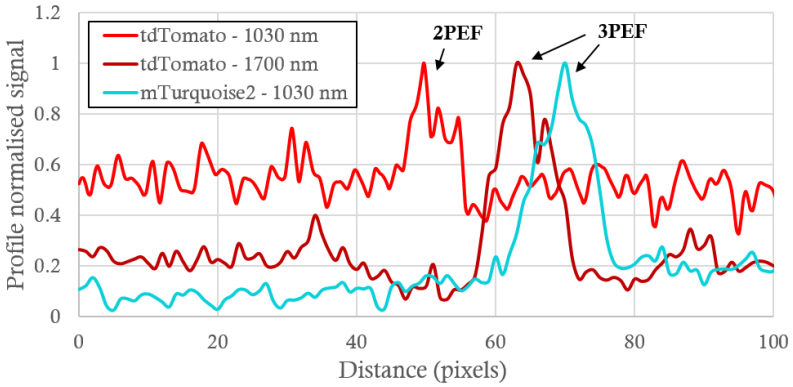

Figure 3.16: Normalised signal profiles of the images in Figure 3.15.

Chick embryo Spinal Cord

The second sample for our 3P blue fluorescence demonstration is a horizontal section of an electroporated chick embryo spinal cord (E-12) expressing mCherry and mTurquoise2, also prepared by our collaborators at the Institut de la Vision. Moreover, in this case, some cells express both red and blue fluorescence, allowing direct comparison between 2P and 3P signals excited at 1030 nm and 1700 nm as shown in Figure 3.17.

Comparing the signal of the profile drawn on a cell labelled with red and blue fluorescence we demonstrate that 2P excitation at 1030 nm provides a SBR $\approx$ 2 whereas the blue signal excited with the same laser exhibits SBR $\approx$ 5 The red fluorescence image of the cell excited with 3P at 1700 nm exhibits the same SBR level, confirming 3P excitation of mTurquoise2. The absence of background in Figure 3.17.b suggests that the background observed in the 2P image is due to out-of-focus light generated at the planes close to the surface of the sample. We can conclude that the SBR improvement in 3P excitation compared to 2P excitation is already present at this imaging depth of 600 µm.

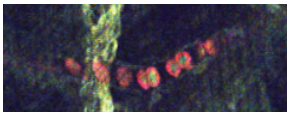

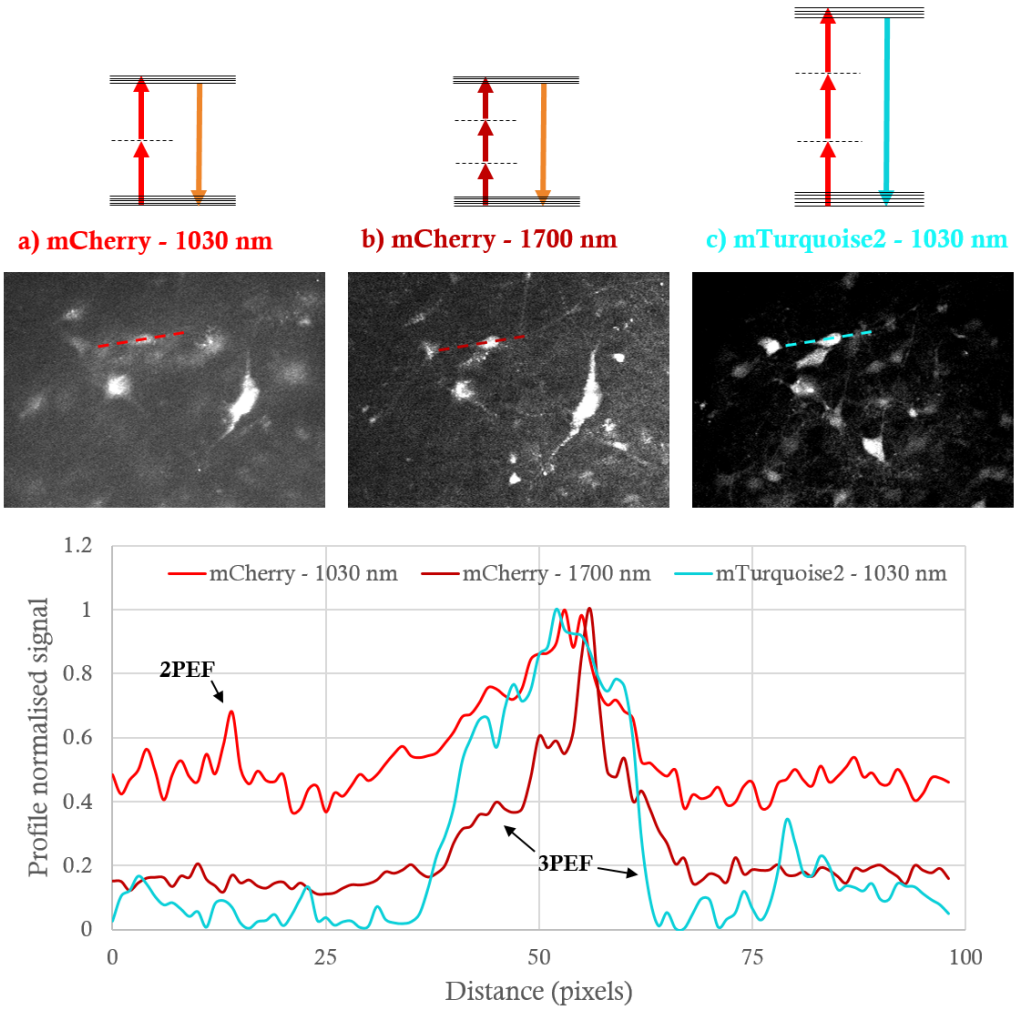

Figure 3.17: Chick embryo spinal cord images recorded at a depth of 600 µm. a) mCherry 2P fluorescence excited at 1030 nm. b) mCherry 3P fluorescence excited at 1700 nm. c) mTurquoise2 3P fluorescence excited at 1030 nm. Bottom: normalised signal profiles of the images.

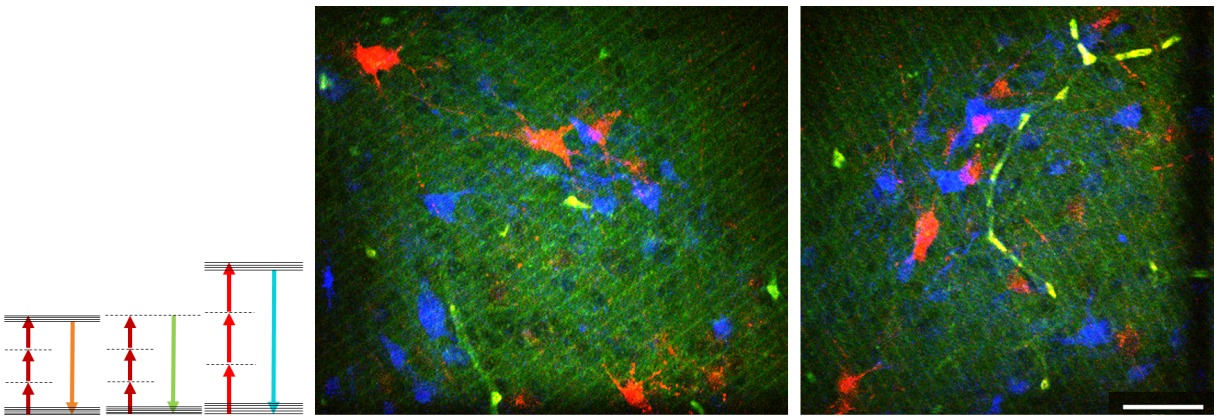

Figure 3.18: Chick embryo spinal cord images at 380 µm (right) and 390 µm (left) of imaging depth. Scale bar 50 µm. Red: mCherry excited at 1700 nm. Green: THG signal at 1700 nm. Blue: mTurquoise excited at 1030 nm.

With sequential excitation at 1030 nm and 1700 nm, we also performed a demonstration of three-colour 3PEF/THG imaging. In Figure 3.18, the red channel corresponds to 3P excitation of mCherry at 1700 nm, the green channel corresponds to the THG signal from this beam (at 567 nm) and blue fluorescence is excited with 3P from the compressed pump at 1030 nm.

3 Conclusion and perspectives of Chapter 3

In this chapter we have focused on extending the observable parameters in 3P microscopy through the study of 3P excitation of blue fluorescent proteins (FPs) at 1030 nm, which was not previously addressed in the literature. We first recalled the basic principles of fluorescence with linear and nonlinear excitation. In the few published studies on 3P excitation of red and green FPs, the emission spectrum has been shown to be very similar when using either linear or multiphoton excitation; however, the multiphoton excitation spectrum can differ significantly from the linear excitation spectrum. This makes it difficult to predict the optimal 3P excitation conditions for each FP.

Using a power-dependence analysis of FPs expressed in cells, we studied the behaviour of three blue FPs (EBFP2, mCerulean and mTurquoise2) with 1030 nm excitation. For comparison, we also included in our study 3P excitation experiments of EGFP at 1300 nm and mCherry at 1700 nm.

One first finding of our experiments is that EBFP2, mCerulean, and mTurquoise2 can all be 3P-excited with 1030 nm 1 MHz excitation. Among these three blue FPs, mTurquoise2 appears to be the most promising for 3P microscopy because of its efficiency and brightness. We also found that EBFP2 excitation at 1030 nm was not as efficient as expected from its linear absorption spectrum. This confirms the principle that the non-linear excitation spectrum cannot generally be deduced from the linear spectrum.

We have also shown that the pulse energy range actually resulting in 3P excitation for a particular FPs is in practice relatively limited. Extended power-dependence curves are usually not shown in the literature. Our data confirm the importance for 3P microscopy of (i) carefully controlling the excitation power, and (ii) working with short pulses. The design of robust power controllers and pulse compressors remains an important subject that needs to be addressed by laser developers.

Our comparison of blue FPs excitation at 1030 nm with EGFP excitation at 1300 nm and mCherry excitation at 1700 nm is only qualitative, due to the instability of the OPA used for this part of the study (first prototype) in terms of output power and beam spatial profile. It will be interesting and important to complement these experiments with new data acquired with the current version of the OPA source, which is much more stable in terms of output power and beam spatial profile. It will also be informative to perform additional experiments on purified FPs in solution, which would reduce the biological variability present in cell-based experiments. Despite their limitations however, our experiments suggest that mTurquoise2 has performance equivalent to EGFP, if not superior, for 3P microscopy.

Finally, we have presented a preliminary confirmation of deep-tissue 3P imaging of mTurquoise2 with 1030 nm excitation, along with red fluorescence and THG imaging

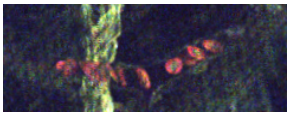

with 1700 nm excitation. Indeed, our demonstration that 1030 nm can be used as an excitation wavelength for 3P microscopy is interesting in the context of multicolour imaging. Moreover, it should be noted that this wavelength is generally available from the pump beam of many OPA sources.
Nevertheless, a systematic study is now needed to characterize the nonlinear photodamage effects at this wavelength. Indeed, some amino acids possess UV absorption peaks which could be reached through e.g. 4-photon effects and lead to phototoxic reactions.
Beyond the already mentioned experiments, our preliminary results suggest additional perspectives for further extending the number of detected signals. The availability of three different excitation wavelengths in our laser source seems particularly interesting for this analysis and for multicolour applications. First of all, screening additional FPs will most likely reveal unexpected properties. In particular, it would be useful to investigate the poorly characterized 3P properties of green-yellow FPs such as NeonGreen or EYFP. Another perspective is to synchronise two beams to enable wavelength mixing [61]. In the case of three-photon excitation, two-beam mixing provides four equivalent 3P excitation wavelengths, which further expands the excitation possibilities. The recent progress in numerical unmixing techniques should also help resolving signals from multiple fluorophores [92, 93]. As a word of caution, we note that a careful analysis of the nonlinear excitation regime will be needed for each combination of FPs and excitation conditions, in order to minimize unwanted 2P excitation during 3P experiments. For instance, during 3P imaging of red and blue FPs using 1700 and 1030 nm, we needed to record the signals sequentially, since red FPs are 3P-excited at 1700 nm and 2P excited at 1030 nm (Figures 3.15 and 3.17). In the next chapter, we will explore how wavelength mixing can give access to additional information through the detection coherent third-order signals.

Chapter 4

TSFG imaging of red blood cells

Contents

1 Introduction to Chapter 4

This chapter describes the development of a new contrast modality based on third-order sum frequency generation (TSFG) and demonstrates its sensitivity to hemoglobin. TSFG is a third-order nonlinear process similar to THG but involving more than one excitation wavelength. We propose a colour TSFG scheme (Figure 4.1) where signals at different wavelengths are simultaneously obtained by wavelength mixing of two laser beams.

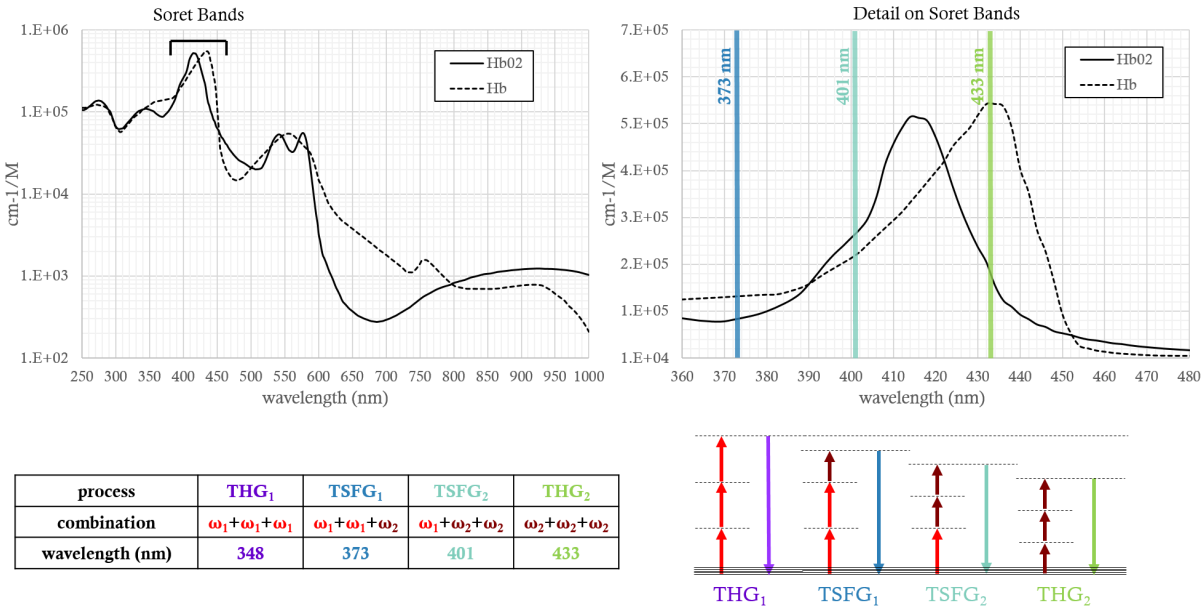

process	THG_1	$TSFG_1$	$TSFG_2$	THG_2
combination	$\omega_1+\omega_1+\omega_1$	$\omega_1+\omega_1+\omega_2$	$\omega_1+\omega_2+\omega_2$	$\omega_2+\omega_2+\omega_2$
wavelength (nm)	348	373	401	433

Figure 4.1: Molar extinction coefficient for Hb and HbO_2 in water. Data adapted from [94]. On the right-hand side, we show a detail on Soret bands representing by vertical lines the three wavelengths with which we probe hemoglobin later in this project using the wavelength mixing combinations described in the table and energy level schemes.

We show that this approach can be used for probing the absorption properties of non-fluorescent molecules, such as hemoglobin, by taking advantage of absorption-related resonances in their TSFG spectrum. In the next sections, we first review the currently available methods for imaging blood oxygenation. We then introduce coherent 3P imaging based on THG and TSFG, and present a complete experimental characterisation of colour TSFG microscopy. We then show that this modality provides a blood-specific contrast. We show that it can be used to selectively detect red blood cells in a label-free manner, and to report on their oxygenation state in zebrafish embryos. Finally, we show that colour TSFG can be implemented using the OPA technology described in Chapter 2

to achieve deep-tissue blood imaging in live adult zebrafish, while being compatible with 3P fluorescence microscopy.

1.1 Red blood cells and oxygenation

Blood[1] is the fluid circulating through our body as one of the main elements of the cardiovascular system, composed also by the heart and the blood vessels. Along with regulation and protection, transportation of oxygen and other nutrients is one of its main functions. Its normal temperature in humans is around 38 °C and its pH is slightly alkaline in between 7.35 and 7.45. It is formed by two main portions: blood plasma, a liquid containing dissolved substances, and formed elements (cells, vesicles or cell fragments). 99 % of the total formed elements are red blood cells (RBCs) or erythrocytes (Figure 4.2), resulting in ≈ 45 % of the blood volume (hematocrit), and only 1 % of formed elements corresponds to white blood cells and platelets.

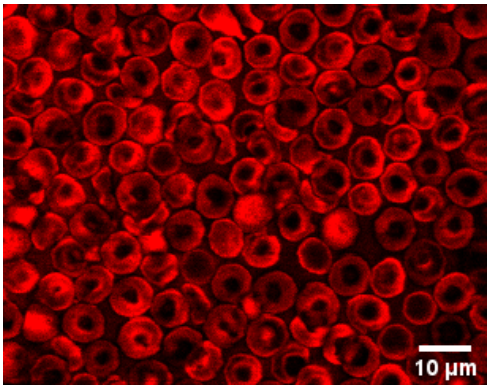

Figure 4.2: Human RBCs in a liquid isotonic solution imaged with THG contrast in our laboratory.

RBCs are responsible for oxygen transport from the lungs (or gills in the case of fish) to the cell bodies and they also enhance carbon dioxide transport on the opposite direction. RBCs concentration in human blood is around 5 million per µL. They are biconcave discs averaging ≈ 8 µm in diameter. This biconcave geometry present in mammals is achieved by the loss of the nucleus and maximizes the surface area for its volume (compared to a sphere or a cube) allowing easier diffusion of gas molecules into and out of the cell. They do not have organelles neither, therefore they cannot divide or carry extensive metabolic activities. On the other hand, this geometry makes them more flexible and thus able to squeeze into small capillaries. Physical wear and tear have an important destruction impact resulting in a lifetime of around 120 days. Their high renewal rate of ≈ 2 million per second by the bone marrow (in humans) compensates for this loss.
They consist mostly in a selectively permeable plasma membrane, cytosol and hemoglobin. The latter is a metalloprotein containing four iron atoms to which oxygen molecules bind. This protein responsible for the red colour of whole blood, is essential for oxygen transport because oxygen molecules do not dissolve easily in water. Only 1.5 % of the carried molecules are dissolved, while 98.5 % are bound to hemoglobin.
In the human lungs, there is a partial oxygen pressure of $P_{O_2} \approx 100$ mmHg. At this pressure, hemoglobin becomes fully saturated with oxygen in the capillaries adjacent

[1] Information about the cardiovascular system and hemoglobin presented in this section was adapted from [95] and [96].

to the alveoli, meaning that all four iron ions Fe^{2+} bind O_2. The iron-dioxygen bond acquires a $Fe^{3+} - O_2^-$ character with a partial charge $delta^-$ localized on dioxygen [97]. This character is reversible with the release of O_2 and differs from auto-oxydation which produces the unliganded Fe^{3+} ferric state. In this case we refer to it as oxyhemoglobin HbO_2 as opposed to deoxyhemoglobin, Hb, with no oxygen bound. When P_{O_2} decreases to $\approx 40\,\text{mmHg}$ as in mixed venous blood returning to the lungs, hemoglobin is only 70-75 % saturated with oxygen. This means that 1/4 of the bound oxygen is delivered to the tissues.

$$Hb + O_2 \rightleftharpoons HbO_2 \tag{4.1}$$

Equation 4.1 expresses the reversible process of binding and release of oxygen molecules performed by hemoglobin. This equilibrium is influenced not only by oxygen partial pressure but also by other parameters such as carbon dioxide partial pressure, acidity or temperature. Oxyhemoglobin and deoxyhemoglobin present significant differences on their linear absorption spectrum, shown in Figure 4.1. Particularly, the highest absorption peaks are centered at 415 and 430 nm for HbO_2 and Hb respectively, and are known as the Soret bands [98].
As said above, even in the least oxygenated blood of our body (expected in the veins), there are still 3 out of 4 iron atoms carrying a bound oxygen molecule in average. RBCs keep hemoglobin in a high oxygenated state, meaning that the pure deoxyhemoglobin spectrum is never observed in physiological conditions *in vivo*. The venous spectrum is expected to be similar to the oxyhemoglobin spectrum slightly shifted towards the deoxyhemoglobin spectrum.

1.1.1 Blood oxygenation measurement methods

There exist different approaches for probing oxygenation *in vivo*. The least invasive method is known as functional near infrared spectroscopy (fNIRS). It can be applied to humans and includes a variety of implementations such as through-skull monitoring brain hemodynamics or pulse oxymetry. These techniques use the spectral differences between oxy- and deoxyhemoglobin shown in Figure 4.1. In the case of the pulse oximeter for instance, the sample is illuminated at two different wavelengths, one around 700 nm and another around 900 nm, usually provided by LEDs. They are chosen below and above 800 nm, at which hemoglobin presents isosbestic point, i.e. where the absorbance is constant and independent of the oxygenation state. The transmitted light through a relatively thin part of the body (generally a finger or an earlobe) is measured for each wavelength enabling calculations of the absorbance values and their ratio. The system is calibrated to translate these parameters into peripheral oxygen saturation, a measure of oxygen saturation in blood. Approaches with the same working principle are also implemented in larger regions of the human body and are able to give useful information [99, 100]. However, their spatial resolution is very limited resulting in strong background and low specificity.

For imaging smaller samples at high resolution, the authors in [101] proposed an adaptation of this spectroscopic principle to wide-field microscopy. They used hemoglobin absorption measurements around the Soret band in developing zebrafish up to 12 days post fertilization (dpf). They put embryos in hyperoxic conditions and used the absorption values as a calibration point of 100 % oxygen saturation in blood. Then they measured absorption values in normoxic conditions to obtain a relative oxygen saturation value.

According to these measurements, hemoglobin leaving the heart through the dorsal aorta (main central artery connected to the heart) is saturated with oxygen at 92 % at 2dpf. This value eventually decreases as the fish develops. This observations tend to confirm that at early stages of development, oxygen transportation happens mainly by diffusion through the thin tissues instead of convection resulting from the bloodstream circulation. This corroborates a previous observation that zebrafish can develop up to 12dpf in absence of circulatory system without oxygen supply troubles [102]. Despite these interesting results, this technique has a limited spatial resolution and does not provide 3D information.

A more efficient method for high-resolution measurements of oxygenation is based on phosphorescent markers derived from porphyrins. These sensors can be injected on the blood and used for phosphorescent lifetime imaging microscopy (PLIM). The lifetime dependence on the partial pressure of oxygen allows absolute measurements which were demonstrated in murine tumors *in vivo* [103]. Such measurements were also done on 2dpf zebrafish embryos showing strong differences between normoxic and hypoxic conditions and slight differences between dorsal aorta and caudal vein (the main central vein connected to the heart) [104]. These PLIM reporters have more recently been modified and optimized for 2P microscopy [105–107]. This approach enables high-resolution measurements of the oxygen partial pressure in intact tissues, and has been used for several applications in the mouse brain. In [108], the authors used 2P-PLIM imaging to conclude that brain oxygenation significantly increases with locomotion and that it is strongly correlated to the respiration cycle. Nevertheless, this method still has limitations. One first issue concerns the specificity of the measurement: markers are injected in the blood plasma and do not report on oxygen level inside RBCs; additionally, they rely on an indirect contrast mechanism to probe hemoglobin. A second and more important limitation of this technique is its low temporal resolution. The phosphorescence lifetime of the sensors is on the order of hundreds of milliseconds, which prohibits full 2D imaging with a point-scanning approach. Instead, specific points in the sample are chosen and measured. With one of the fastest 2P probes, it takes 0.5 s to measure 12 points in a 2P image [107].

In this chapter we propose an alternative method based on spectroscopic coherent third-order nonlinear microscopy providing at least 1000 times higher temporal resolution than phosphorescent probes, along with RBC specificity. We also show that this approach can be implemented on a 3P microscope to detect RBCs in a label-free manner deep inside tissues.

1.2 THG microscopy

1.2.1 Coherent Contrast Mechanisms

In Chapter 1 we have discussed nonlinear microscopy based on fluorescence (2PEF and 3PEF). In this chapter we consider coherent multiphoton processes. The most commonly used coherent modalities in nonlinear microscopy are second harmonic generation (SHG) and, to a lesser extent, third harmonic generation (THG). These signals can be detected in most multiphoton microscopes and provide complementary information. SHG depends on the second-order nonlinear susceptibility, $\chi^{(2)}$, which is null in centrosymmetric materials. SHG microscopy provides a contrast specific to non-centrosymmetric materials and allows their 3D characterisation. The main source of SHG constrast in biological tissues are fibrillar collagen (present in many connective tissues including tendon, skin, cornea, bone or

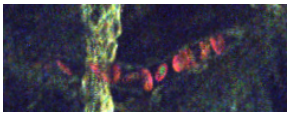

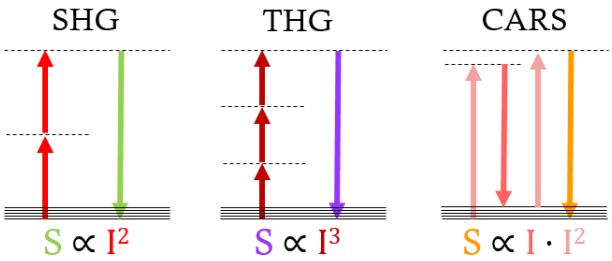

Figure 4.3: Energy schemes of SHG, THG and CARS processes. Solid lines represent real energy states while virtual energy levels are represented in dashed lines. The dependence of the detected signal S on the excitation intensities I is shown with a colour code correspondent to the energy scheme.

stroma in internal organs) [109–112], myofilaments (present in muscles) [113] or polarized microtubule assemblies (such as the mitotic spindles during cell division) [114, 62]. THG is a contrast mechanism governed by the third-order nonlinear susceptibility $\chi^{(3)}$. THG microscopy highlights interfaces and heterogeneities in the sample, resulting in images similar to those obtained with dark-field microscopy [115]. This imaging method is discussed in more details in the next section.
SHG and THG contrasts are easily combined in a nonlinear microscope to provide multimodal label-free imaging [116, 117, 62]. So far, SHG and THG microscopy have been mainly used for structural imaging in combination with specific labelling using fluorescent markers.

Another common multiphoton contrast mechanism is coherent anti-Stokes Raman scattering (CARS). The energy diagram for CARS is represented in Figure 4.3 alongside with those for SHG and THG. CARS is a four-wave mixing process excited with two synchronized lasers: the pump/probe field of angular frequency ω_p, involved twice in the process and the Stokes field of angular frequency ω_S, involved once. The two wavelengths are chosen such that $\omega_p - \omega_S = \Omega_{vib}$, where $\hbar\Omega_{vib}$ is the energy of a targeted vibrational level. This makes CARS specific to chosen vibrational transitions [118]. One characteristic of CARS imaging is that the susceptibility $\chi^{(3)}$ involved on the process has two components: a resonant one containing the Raman spectral information, and a non-resonant one with no chemical specificity. The interference between these two components is generally observed in CARS images, which can complicate their interpretation.

1.2.2 Third Harmonic Generation

In this section, we summarize the theoretical description of THG imaging contrast, which is now well described in the literature. This will be useful for introducing TSFG microscopy afterwards. We first introduce the process of third harmonic generation; we then discuss the mechanisms governing THG with plane waves and focussed beams (as it is the case in microscopy); and we finally review the topic of THG resonant enhancement in the presence of molecular absorbers such as hemoglobin.
The field of nonlinear optics deals with phenomena induced by intense light fields. When an electric field E(t) is applied to a material, it induces a polarisation P(t) (dipole moment per unit volume) which can be described as:

$$P(t) = \varepsilon_0 \chi^{(1)} E(t),$$

where ε_0 is the free space permitivity and $\chi^{(1)}$ is the linear optical susceptibility. As the applied field becomes stronger this expression is not enough to describe the occurring processes and requires adding nonlinear terms. The definition of the polarisation is then generalised as a power series of the field strength:

$$P^{NL}(t) = \varepsilon_0[\chi^{(1)}E(t) + \chi^{(2)}E^2(t) + \chi^{(3)}E^3(t) + \dots] \equiv P^{(1)}(t) + P^{(2)}(t) + P^{(3)}(t) + \dots,$$

where $\chi^{(N)}$ is the Nth-order nonlinear susceptibility. This quantity is a $N+1$ rank tensor. Since in this work we only consider the case of homogeneous and isotropic media, the $\chi^{(3)}$ can be reduced to a single independent element. $P^{(N)}(t)$ is defined as the Nth-order nonlinear polarisation and varies in time as a result of the action of the field. A time-varying polarisation can be understood as accelerated charges, consequently, it can act as the source of new electromagnetic field components. This coupled interaction is described by the nonlinear wave equation:

$$\nabla^2 E(t) - \frac{n^2}{c^2}\frac{\partial E(t)}{\partial t^2} = \frac{1}{\varepsilon_0 c^2}\frac{\partial^2 P^{NL}(t)}{\partial t^2}, \tag{4.2}$$

where n is the linear refractive index and c is the speed of light in vacuum.

THG with Plane Waves

Let us first consider the case of THG when the incident fundamental field is a monochromatic plane wave of frequency ω:

$$E(z,t) = E_\omega e^{-i\omega t} + c.c. = A_\omega e^{i(k_\omega z - \omega t)} + c.c.,$$

with $k_\omega = n_\omega \dfrac{\omega}{c}$ the wavevector. The induced third-order polarisation is:

$$P^{(3)}(t) = \varepsilon_0 \chi^{(3)}[{E_\omega}^3 e^{-i3\omega t} + 3{E_\omega}^2 {E_\omega}^* e^{-i\omega t} + c.c.]. \tag{4.3}$$

We observe that two terms of different frequency appear to drive new field components oscillating at those frequencies. The first term corresponds to the third harmonic wave:

$$E_{\mathrm{THG}}(z,t) = E_{3\omega} e^{-i3\omega t} + c.c. = A_{3\omega} e^{i(k_{3\omega} z - 3\omega t)} + c.c.,$$

The second term can be interpreted as an intensity-dependent refractive index effect, which can lead to processes such as the self-focusing effect. Indeed, we can identify a product $E_1 E_1^* = I_1$ followed by a field oscillating at the fundamental frequency.

Under the slowly varying amplitude approximation, the nonlinear wave equation leads to:

$$\frac{\partial}{\partial z} A_{3\omega}(z) \propto A_\omega^3 e^{i\Delta k z},$$

where we define the wavevector mismatch $\Delta k = 3k_\omega - k_{3\omega} = \dfrac{3\omega}{c}(n_\omega - n_{3\omega})$, which is the phase difference between the propagating fundamental and harmonic waves. This result indicates that the intensity of the harmonic wave scales as the cube of the intensity of the excitation field and oscillates depending on the value of Δk. If we integrate it, we find

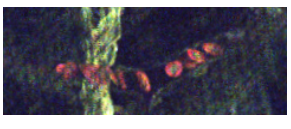

that the intensity of the harmonic wave after an interaction distance L within a material presenting non zero $\chi^{(3)}$ is of the form:

$$I_{3\omega}(z=L) \propto I_1^3 L^2 sinc^2(\frac{\Delta kL}{2}).$$

This intensity oscillates with the wave vector mismatch and with the distance propagated inside the nonlinear medium. As seen in Chapter 2 (Section 2.1.2), different methods can be used experimentally to achieve phase matching in a nonlinear material such as critical phase matching (using birefringence), temperature tuning (temperature controlled anisotropy) or quasi phase matching (with engineered periodic materials that compensate phase differences). In the case of perfect phase matching ($\Delta k = 0$), the intensity of the generated wave scales as: $I_{3\omega} \propto I_1^3 L^2$. In this case, THG intensity increases with interaction distance. On the contrary, when there is a phase mismatch $\Delta k \neq 0$, $I_{3\omega} \propto \frac{I_1^3}{(\Delta k/2)^2} sin^2(\frac{\Delta kL}{2})$ oscillates with L. Its amplitude is inversely proportional to the square of the phase mismatch, and its period is $\Delta kL/2$. THG reaches its maximum after an interaction length $L_c = \pi/\Delta k$, called coherence length.

THG with Focused Gaussian Beams

In THG microscopy, the fundamental beam is focussed onto the sample plane. The excitation should be modelled as a focussed Gaussian beam rather than a plane wave. In this case:

$$A_\omega(r,z) = \frac{\mathcal{A}_\omega}{1+i\xi} e^{-\frac{r^2}{\omega_0^2(1+i\xi)}},$$

with $\xi = \dfrac{2z}{b}$, where ω_0 is the excitation beam waist or twice the lateral beam radius at $1/e^2$ and $b = k\omega_0^2$ is called the confocal parameter.

To solve the nonlinear wave equation, we use the trial solution: $A_3(r,z) = \frac{\mathcal{A}_{3\omega}}{1+i\xi} e^{-\frac{3r^2}{\omega_0^2(1+i\xi)}}$, which gives the dependency:

$$\mathcal{A}_{3\omega}(z) = \frac{i3\omega}{2nc}\chi^{(3)}\mathcal{A}_{3\omega}^3 J(\Delta k, z_0, z).$$

where

$$J(\Delta k, z_0, z) = \int_{z_0}^{z} \frac{e^{i\Delta k z'}}{(1+\frac{2iz'}{b})^2} dz'$$

and z_0 is the value of z at the entrance of the $\chi^{(3)}$ medium.
In the case of a Gaussian beam tightly focused inside the nonlinear medium, the integration limits can be replaced by $-\infty$ and $+\infty$. The evaluation by contour integration gives [55], (Figure 4.4):

$$J(\Delta k, z_0, z) = \begin{cases} 0, & \text{for } \Delta k \leq 0 \quad (4.4) \\ \dfrac{\pi b^2 \Delta k}{2} e^{-b\Delta k/2}, & \text{for } \Delta k > 0 \quad (4.5) \end{cases}$$

We find the surprising result that there is no signal in the case of perfect phase matching. In order to obtain some intensity at the third harmonic wavelength, a positive phase

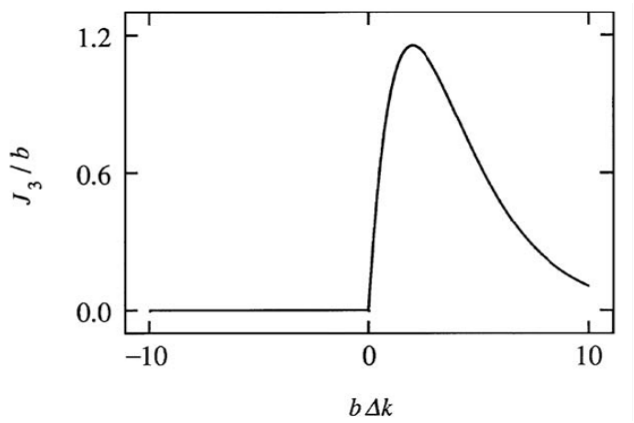

Figure 4.4: Representation of the $J(\Delta k, z_0, z)$ integral in terms of the phase mismatch for the case of strongly focused gaussian beams. Taken from [55].

mismatch is required. This phenomenon can be explained by considering the effect of the Gouy phase shift, which is the π radians cumulated axial phase shift experienced by a Gaussian beam near its focus. The direction of the Gouy shift is opposite to the propagation direction. An interpretation for the case of THG is the following. Three excitation photons are coherently scattered close to the focal point. At this region, the wavevectors are distributed symmetrically around the optical axis in a cone related to the aperture angle of the focusing lens. In average, the off-axis component of the excitation wavevectors cancels out due to cylindrical symmetry. Consequently, the three excitation wavevectors add up to a resulting axial wavevector which is smaller than in the case of collinear excitation wavevectors (plane waves). The momentum difference of the collinear case and the effective axial projection of the excitation wavevectors case is the total Gouy phase shift $3k_G$. This is illustrated in Figure 4.5 where k_ω is the magnitude of the excitation wavevectors (shown in red) and $k_{3\omega}$ is the magnitude of the wavevector of the THG signal (shown in purple). The axial projection of $k_{3\omega}$ is represented for the different phase mismatch values. In the case of THG with strongly focused light, due to the shorter resulting excitation wavevector, the two waves are phase matched when $\Delta k > 0$. This case is usually summarized by the following scalar expression: $3(k_\omega - k_G) - k_{3\omega} = 0$.

Most materials exhibit normal dispersion over the visible and infrared range: their refractive index decreases with increasing wavelength, resulting in $\Delta k < 0$. As a consequence, there is no THG signal in isotropic homogeneous normally dispersive media. This mechanism has important consequences for THG microscopy: THG images generally highlight interfaces over a dark background.

THG signal in a homogeneous medium (i.e. not near an interface) can nevertheless be obtained in the following cases. First, it is observed in the rare case of media presenting anomalous dispersion. Second, it can be obtained in birefringent media if birefringence is large enough to compensate for the Gouy phase shift. Calcite for instance, is a negative uniaxial crystal ($n_e \leq n_o$, where n_o and n_e are the ordinary and extraordinary refractive indices respectively) and thanks to birefringence, types I, II and III phase matching associated to an extraordinary harmonic index result in $\Delta k \geq 0$ [119]. Apart from these cases, the main source of THG constrast in biological images arises from interfaces and heterogeneities which introduce a supplementary phase mismatch term. The intensity of the generated signal depends both on the relative differences of the optical properties ($\chi^{(3)}$ and n) of the two media and on the micrometer-scale geometry of the sample near focus. An

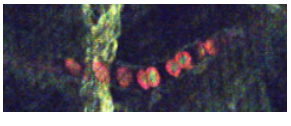

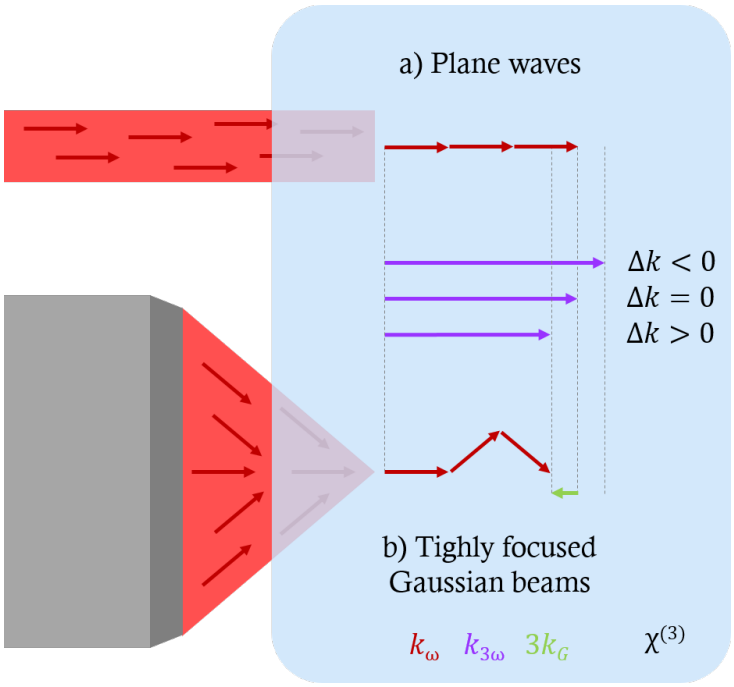

Figure 4.5: Phase matching in THG. In the case of plane waves (a), the two waves are phase-matched for $\Delta k \neq 0$. In the case of strongly focused Gaussian beams, the two waves are matched when $\Delta k > 0$. We remind the definition of the wave mismatch: $\Delta k = \frac{3\omega}{c}(n_\omega - n_{3\omega})$.

analytical form of the THG signal can be derived for simple geometries such as a horizontal interface, but numerical methods are more suited for more complex sample geometries.

In THG microscopy, the effective coherence length of the process can be expressed as:

$$L_{C,eff} = \frac{\pi}{|3(k_\omega - k_G) - k_{3\omega}|} \propto \frac{\pi}{3k_G}.$$

This approximation is valid in the limit of strong focusing, where the effect of the Gouy shift is dominant compared to dispersion [120]. Using numerical models, the authors of [121] estimate the coherence length as $L_C \approx 0.7\lambda$.

THG is mostly forward directed [11], i.e. it propagates in the same direction as the excitation light. In thick samples, however, THG can be conveniently epidetected by taking advantage of incoherent backscattering of the forward-generated THG [122].
In biological tissues, lipid droplets have been identified as a strong source of THG contrast [115] due to the strong optical contrast between lipids and water. For the same reason, THG has been shown to be an effective technique for imaging myelin in the central nervous system [123].

1.2.3 Resonance enhanced THG

In this section we discuss how THG signal can be enhanced in the presence of molecular absorbers such as pigments. An illustration of this effect may be visible in early works on THG microscopy: in [21], the authors reported images of plant samples where chloroplasts show clear contrast; in [124], the authors detected THG signals from red blood cells. Although the possibility of resonant enhancement was not analyzed at the time,

these images retrospectively suggest that THG enhancement could result from the strong absorption of chlorophyll and hemoglobin at the third-harmonic wavelength. Later studies reported that the presence of hematoxylin, a commonly used dye in histology, enhance THG contrast from nuclei [125], and that large THG signals are observed from hemozoin pigments present in malaria-infected cells [126].
The possibility of THG enhancement near absorption bands was later more specifically investigated in a few studies [127–129], where the authors performed spectral THG analyses.
Indeed, THG can in principle be resonantly enhanced if real transitions exist at frequency ω, 2ω or 3ω, where ω is the illumination frequency. Using a formalism similar to the one used in CARS microscopy, we can write the third-order susceptibility responsible for THG in the form :

$$\chi^{(3)} = \chi^{(3)}_{nonresonant} + \chi^{(3)}_{resonant}.$$

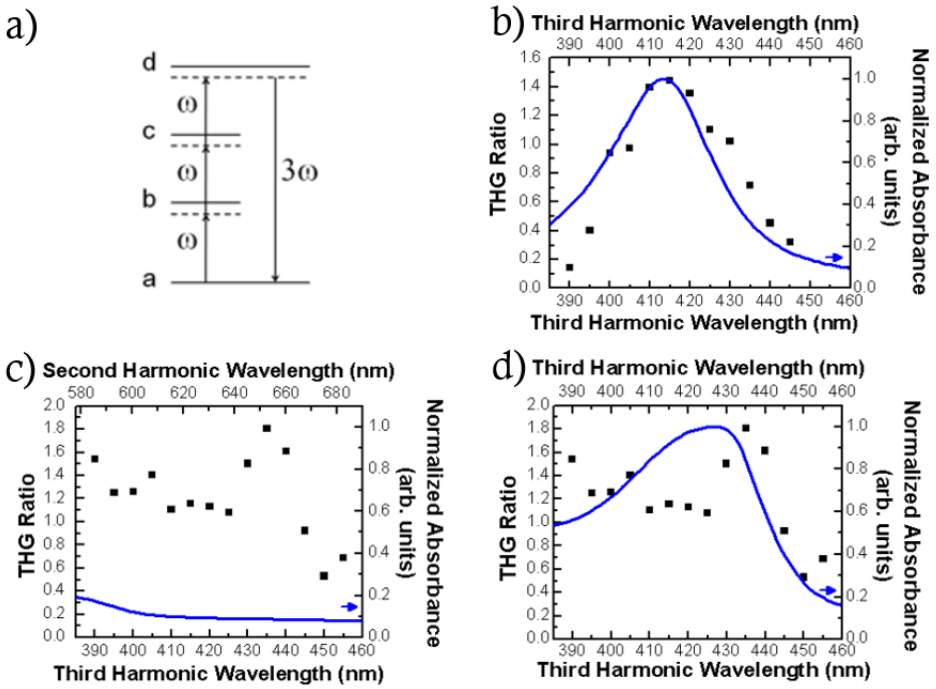

Figure 4.6: a) Energy level scheme. Real states are represented by solid lines and dashed lines correspond to virtual energy levels. b) HbO_2: third harmonic intensity spectrum (black squares) plotted with the linear absorption at 3ω (blue line). c) Hb: third harmonic intensity spectrum plotted with the linear absorption at 2ω. d) Hb: third harmonic intensity spectrum plotted with the linear absorption at 3ω. The signal is labelled *THG ratio* because THG from the samples is normalized by a THG of a non-resonant sample in the same conditions. Adapted from [129].

To describe the form of the resonant term, Clay et al. [128] and Chang et al. [129] proposed the energy transition scheme in Figure 4.6.a. The density matrix formalism and the perturbation theory give the expression:

$$\chi^{(3)}_{resonant}(3\omega,\omega,\omega,\omega) = \frac{\mathcal{N}}{\hbar^3}\frac{\mu_{ad}\mu_{dc}\mu_{cb}\mu_{ba}}{[(\omega_{da}-3\omega)-i\gamma_{da}][(\omega_{ca}-2\omega)-i\gamma_{ca}][(\omega_{ba}-\omega)-i\gamma_{ba}]},$$

where $\mathcal{N}$ is the atomic number density, μ_{lm} is the electric dipole moment between states l and m and γ_{lm} is the dephasing rate of the coherence between states l and m. The

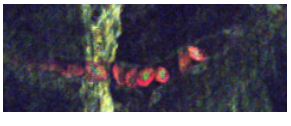

quantities $\hbar\omega_{da}$, $\hbar\omega_{ca}$ and $\hbar\omega_{ba}$ correspond to three-, two- and one-photon THG resonances associated to real transition energies, respectively. The THG signal intensity associated to the resonant term of $\chi^{(3)}$ is given by:

$$I_{3\omega} \propto \left|P^{(3)}(3\omega)\right|^2 \propto \left|\chi^{(3)}_{res}(3\omega)\right|^2 \propto \frac{1}{[(\omega_{da}-3\omega)^2+\gamma_{da}^2][(\omega_{ca}-2\omega)^2+\gamma_{ca}^2][(\omega_{ba}-\omega)^2+\gamma_{ba}^2]}.$$

It can be shown [55] that the factors multiplying on the denominator are inversely proportional to A_{ad}, A_{ac} and A_{ab}, absorbances at the third harmonic, second harmonic and fundamental wavelengths. This means that the THG intensity is affected by an absorption effect at those three frequencies, as $I_{3\omega} \propto A_{ad}A_{ac}A_{ab}$. This can be a single absorption effect (there exists important absorption at one of the three frequencies) or a combined effect (there is absorption at two or more frequencies). The results from [129] show that oxyhemoglobin enhancement can be explained by absorption at the third harmonic only (Figure 4.6.b), as the THG intensity correlates well with the linear absorption curve at 3ω. In the case of deoxyhemoglobin (Figure 4.6.c and 4.6.d), however, this absorption curve does not explain the shape of the THG spectrum between 390 and 425 nm as shown in Figure 4.6.d. The spectral shape correlates better with the linear absorption at 2ω (Figure 4.6.c) suggesting that both absorptions on deoxyhemoglobin affect THG intensity in this range.
This interpretation is consistent with the experimental measurements. However, these studies did not get to imaging applications.

1.3 Third-order Sum Frequency Generation signal

In this section we introduce third-order sum frequency generation (TSFG), which can be obtained when illuminating a nonlinear medium with two different frequencies. New frequency components are generated in the induced third-order polarisation. Experimentally, the two frequencies correspond to two laser beams represented by the electric field amplitudes E_1 (which we call the pump) and E_2 (which we call the OPO beam), oscillating at frequencies ω_1 and ω_2, respectively.
The total incident field introduced in Section 1.2.2 can then be written as:

$$E(t) = E_1 e^{-i\omega_1 t} + E_2 e^{-i\omega_2 t} + c.c..$$

And the induced third-order contribution to the nonlinear polarisation can be expressed as:

$$\begin{aligned} P^{(3)}(t) = \varepsilon_0\chi^{(3)}[&{E_1}^3 e^{-i3\omega_1 t} + {E_2}^3 e^{-i3\omega_2 t} \\ &+ 3{E_1}^2 {E_1}^* e^{-i\omega_1 t} + 3{E_2}^2 {E_2}^* e^{-i\omega_2 t} + 6E_1E_2{E_1}^* e^{-i\omega_2 t} + 6E_1E_2{E_2}^* e^{-i\omega_1 t} \\ &+ 3{E_1}^2 {E_2}^* e^{-i(2\omega_1-\omega_2)t} + 3{E_2}^2 {E_1}^* e^{-i(2\omega_2-\omega_1)t} \\ &+ 3{E_1}^2 E_2 e^{-i(2\omega_1+\omega_2)t} + 3{E_2}^2 E_1 e^{-i(2\omega_2+\omega_1)t} \\ &+ c.c.]. \end{aligned} \tag{4.6}$$

As seen in Section 1.2.2, these terms act as the source term of the driven wave equation, leading to electric fields oscillating at these new generated frequencies. The terms on the first line correspond to frequencies $3\omega_1$ and $3\omega_2$, i.e. the THG of the incident frequencies.

The terms on the second line are again intensity-dependent refractive index effects (we can identify a product $E_i E_i^* = I_i$ followed by a field oscillating at one of the incident frequencies). The terms on the third line of the expression can be referred to as third-order difference frequency generation (TDFG), we will not focus our interest in them because they are out of the wavelength detection range of our microscope. We are concerned about the last terms, oscillating at frequencies $2\omega_1 + \omega_2$ and $2\omega_2 + \omega_1$, which are called third-order sum frequency generation (TSFG) signals. The energy transition schemes are represented in Figure 4.7, summarizing that with two lasers, four different energy sums are available.

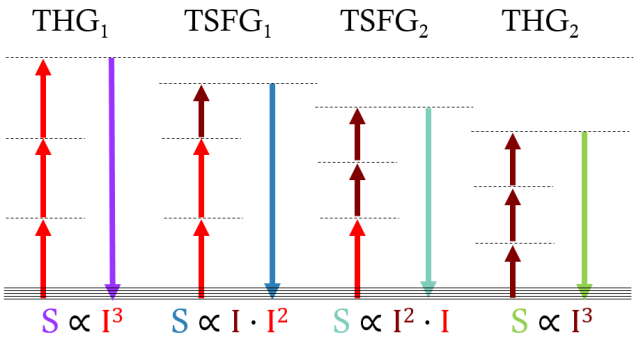

Figure 4.7: The four possible resulting frequencies in third-order sum frequency generation. THG can be understood as a degenerated TSFG.

A first report of TSFG imaging was presented by Sagawa et al [130]. With a subnanosecond pulsed laser source and a supercontinuum, the authors obtained TSFG signals in combination with CARS, SHG and THG. They could observe TSFG in yeast cells despite the fact that their system was not optimized for imaging. Later on, the same group used this method to acquire TSFG spectra of different samples, including hemoglobin [131].
More recent studies have presented further analyses of TSFG for imaging applications. Potma et al. [132], focused on its sensitivity to vibrational levels. They worked in the C-H stretching range (2800 to 3000 cm^{-1}, [3.6, 3.3] µm, respectively), and reported the first TSFG images with vibrational contrast (resonance enhancement). Their study also showed spectral profiles obtained from images of lipids exhibiting resonant peaks. Using an improved setup with better spatial resolution [133], they successfully obtained vibrational images of biological objects such as lipid droplets. In this study, TSFG is combined with second-order sum frequency generation (SFG) and CARS signals, which provide complementary vibrational information.
Interestingly, Potma et al. reported that TSFG can be detected in bulk media in the moderatly focused regime, unlike the case of THG [132, 133]. To understand this observation, we can write the wavevector mismatch that needs to be cancelled in each case:

- **THG at $3\omega_1$:**
  $3(k_{\omega_1} - k_G) - k_{3\omega_1} = \dfrac{3\omega_1}{c}(n_{\omega_1} - n_{3\omega_1}) - 3k_G$
- **TSFG at $2\omega_1 + \omega_2$:**
  $2k_{\omega_1} + k_{\omega_2} - 3k_G - k_{2\omega_1+\omega_2} = \dfrac{1}{c}[2\omega_1 n_{\omega_1} + \omega_2 n_{\omega_2} - (2\omega_1 + \omega_2)n_{2\omega_1+\omega_2}] - 3k_G$
- **TSFG at $\omega_1 + 2\omega_2$:**
  $k_{\omega_1} + 2k_{\omega_2} - 3k_G - k_{\omega_1+2\omega_2} = \dfrac{1}{c}[\omega_1 n_{\omega_1} + 2\omega_2 n_{\omega_2} - (\omega_1 + 2\omega_2)n_{\omega_1+2\omega_2}] - 3k_G$

where we assumed that the two beam geometries (and Gouy shifts) are the same. From this expressions it can be seen that in the case of THG at $3\omega_1$ or at $3\omega_2$, isotropic normally dispersive media produce negative phase mismatch, preventing bulk signal. In the case of TSFG, however, even if the medium is normally dispersive, this dispersion could compensate for the Gouy shift and result in bulk TSFG signal. Although this is true in general, for tightly focused beams the Gouy shift is expected to dominate over dispersion. This is the case of our microscopy experiments described in the next sections, where we never observed bulk TSFG. We can therefore consider that in a high-NA microscope, the TSFG contrast mechanism is generally similar to that of THG, i.e. it highlights interfaces and heterogeneities.

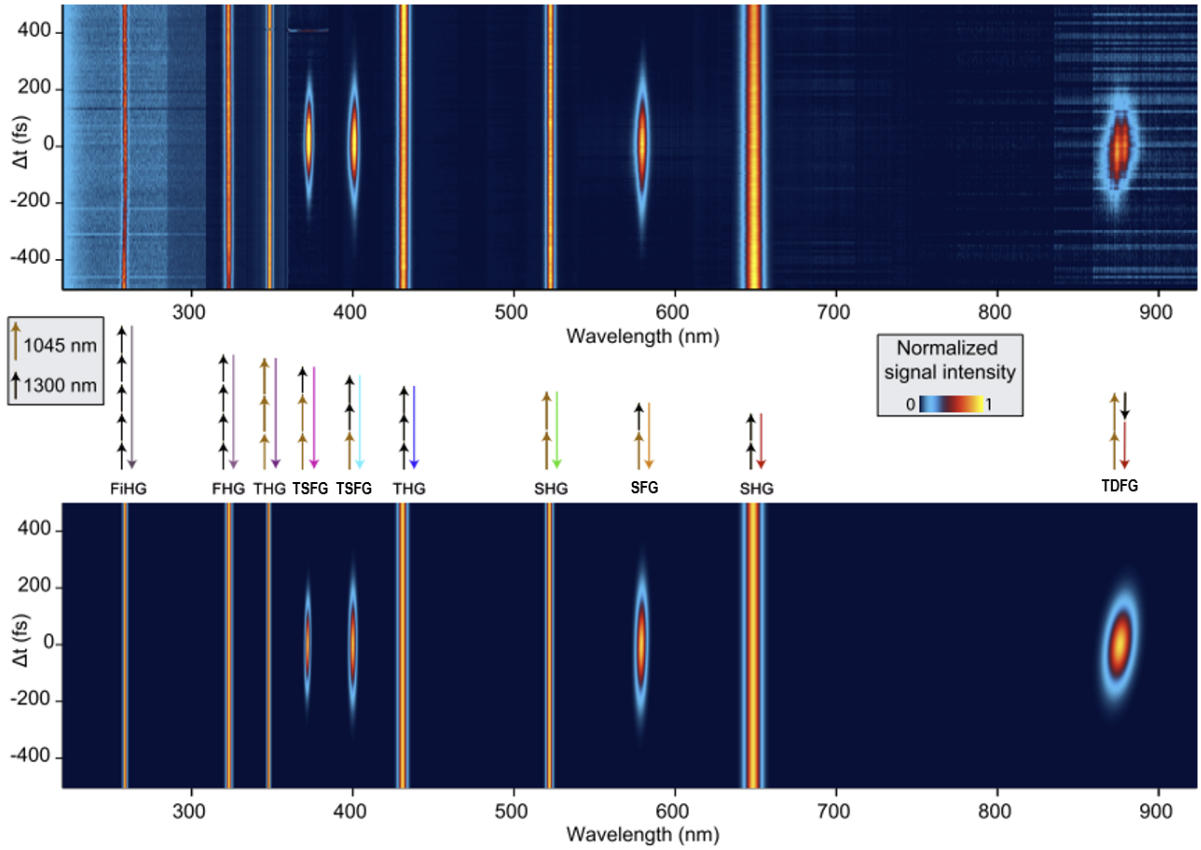

Figure 4.8: (Top) Intensity-normalized spectrograms obtained from a subdiffraction limited KNbO3 nanoparticles upon simultaneous 1045 and 1300 nm illumination. Direct harmonic signals (SHG, THG, fourth harmonic generation (FHG), fifth harmonic generation (FiHG)) appear as continuous vertical stripes as they do not depend on the relative pulse delay Δt, contrary to signals generated by the superposition of the 1045 and 1300 nm pulses (second order sum frequency generation (SFG) and four wave mixing processes: TSFG and TDFG) which display a clear Δt dependence. Note the absence of supercontinuum background and luminescence in the response. (Center) Photon-combinations leading to each distinct spectral element of the response. (Bottom) Simulated spectrograms. Adapted from [134].

In an even more recent study, Campagne et al [134] measured up to ten different coherent signals from nonlinear nanoparticles as a result of the mixing of two illumination wavelengths (Figure 4.8). They represent the coherent signals as a function of their wavelengths and of the temporal delay Δt between the two laser beams. The signals generated by a single laser beam (vertical traces with no dependence on Δt) are easily distinguished

from those depending on both illumination wavelengths. Indeed, the latter are maximized when the two beams are synchronized and vanish without temporal overlap. This demonstration is particularly elegant, although the experimental setup in this study was not optimized for imaging.
Apart from these few studies, TSFG has not been explored as a contrast modality for microscopy. In the next sections, we describe original developments achieved during this thesis project. First, we describe the implementation of a new strategy for one-shot colour TSFG-THG imaging on an OPO-based microscope, and a systematic study of the signals as a function of experimental parameters. Then, we report a spectral study of hemoglobin TSFG-THG signals revealing the presence of absorption-induced resonances. Finally, we investigate the potential of this new contrast for blood imaging applications on OPO- and OPA-based setups. From now on, we will use the term TSFG microscopy to refer to the use of two-beam excitation resulting in the generation of four signals: THG_1, $TSFG_1$, $TSFG_2$ and THG_2 as defined in Figure 4.7.

2 Experimental characterisation of TSFG microscopy

In this section, we present the implementation of an efficient strategy for colour TSFG imaging on an OPO-based microscope. We then present a systematic study of the detected signals as a function of experimental parameters such as average power, pulse duration, incident polarisation and chromatic aberrations.

2.1 Description of the microscope

We first implemented TSFG imaging on a laser scanning microscope equipped with a wavelength tunable laser source that allows spectral analysis.

- **Laser source.** The illumination source was a commercial dual-output femtosecond OPO system (InSight X3, *Spectra Physics*) operating at 80 MHz repetition rate. The tunable (OPO beam) output on this laser is linearly polarized and tunable over the 680 - 1300 nm wavelength range. A dispersion pre-compensation system is also included in the laser, enabling to compress the pulse to a duration of ≈120 fs on the sample plane. The second output is derived from the fixed-wavelength pump. It provides a linearly polarised beam at a wavelength of 1045 nm (the pump beam) with 190 fs (80 MHz) pulses and a maximum average power of 5 W.

- **Beam conditioning paths.** The beam injection paths were redesigned to enable wavelength mixing and therefore TSFG imaging. As shown in Figure 4.9, the beams go through a power control system consisting of a motorized half wave plate and a polarizing beam splitter. The size and divergence of the beams are then adjusted with independent telescopes. Achromatic lenses (ACH-NIR 25x50 NIR-II, *Edmund Optics*) were installed to ensure good transmission over the whole available excitation wavelength range.
  A motorized, 22 cm long delay line (ODL220/M, *Thorlabs*) adding a maximum of 44 cm delay (in equivalent light-travelled distance) is available in the pump beam path. The relative delay between the two beams at the output of the laser varies from 0.99 to 1.23 m depending on the wavelength of the OPO. The delay line was aligned and calibrated to allow beam synchronisation at the sample plane over the entire wavelength range of the OPO.

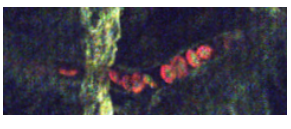

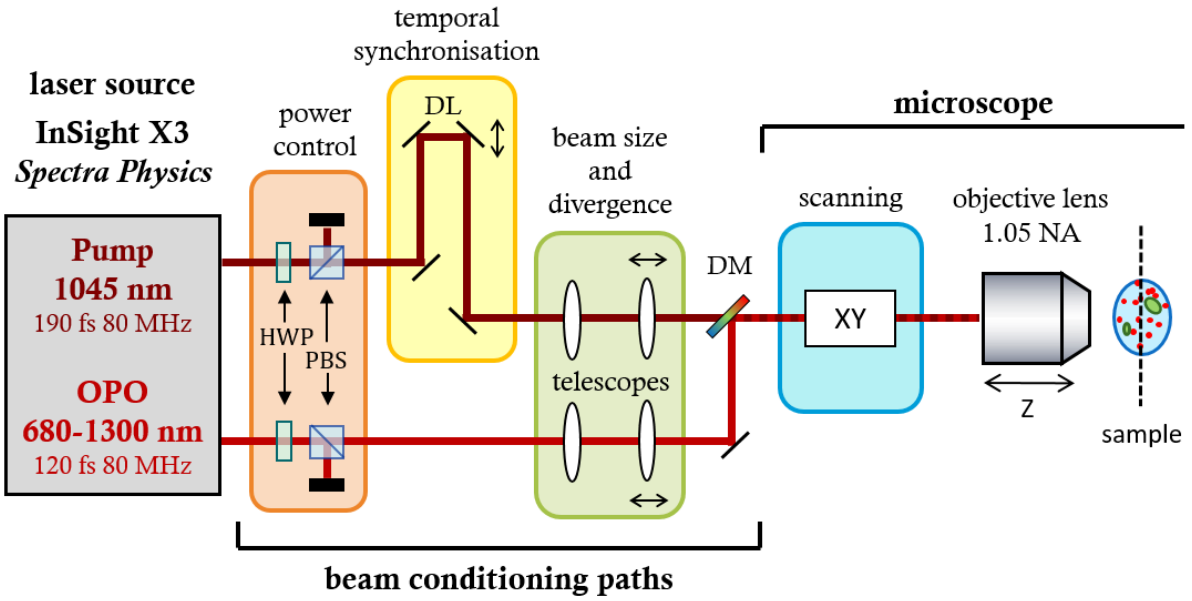

Figure 4.9: OPO-based excitation scheme for TSFG experiments. HWP: half-wave plate; PBS: polarising beam splitter; DM: dichroic mirror; DL: delay line.

Finally, the two beams were combined by a dichroic mirror (NFD01-1040-25x36, *Semrock*) transmitting all the wavelengths of the OPO except for a narrow (≈70 nm) band centered at 1040 nm which reflects the pump. Two mirrors on each beam enabled to independently adjust their position and angle at the entrance of the microscope.

- **Microscope.** The structure of this microscope (also designed by Pierre Mahou in our laboratory) used for the OPO-based experiments was similar to the one described in Chapter 2. Beam scanning was performed by a pair of non-resonant confocal galvanometric mirrors. The same water immersion objective was used (XLPLN25XWMP2, *Olympus*, 1.05 NA, 2 mm working distance), and mounted on a motorized axial stage.

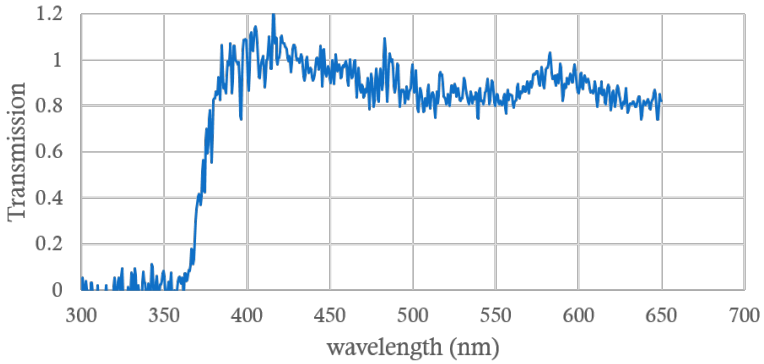

Figure 4.10: Transmission response of the condenser of our microscope. The other optics used in the microscope exhibit similar transmission with a strong decreased at $\lambda \lesssim 370$ nm.

- **Detection of TSFG and THG signals.**

We generally performed colour TSFG experiments by combining the pump wavelength $\lambda_1 = 1045\,\text{nm}$ and the OPO tuned to $\lambda_2 = 1300\,\text{nm}$. The resulting four wavelengths generated are then:

$$\lambda_{THG_1} = \frac{\lambda_1}{3} \approx 348\,\text{nm} \qquad \lambda_{THG_2} = \frac{\lambda_2}{3} \approx 433\,\text{nm}$$
$$\lambda_{TSFG_1} = \left(\frac{2}{\lambda_1} + \frac{1}{\lambda_2}\right)^{-1} \approx 373\,\text{nm} \qquad \lambda_{TSFG_2} = \left(\frac{1}{\lambda_1} + \frac{2}{\lambda_2}\right)^{-1} \approx 401\,\text{nm} \tag{4.7}$$

These are the same four wavelengths labelled as THG and TSFG in Figure 4.8.

Transmission of the detection optics (condenser, lenses) is strongly reduced in the UV range for wavelengths shorter than $\lambda = 370\,\text{nm}$, as seen in Figure 4.10. Therefore, detection of THG_1 was not practical and we focussed on the three remaining signals. We implemented three independent detectors in the transmission path to allow the simultaneous detection of TSFG_1, TSFG_2, and THG_2. We chose lenses with good transmission down to 370 nm (25mm Dia. UV-VIS coated, Near UV achromatic Lens, *Edmund Optics*). The detectors used in this microscope were PMTs operating in photon counting mode (P25PC, *Sens-tech, UK*).

To ensure that we were specifically detecting the coherent signals of interest, we used narrow bandpass filters: 370 ± 5, 400 ± 6, 434 ± 8.5nm. For comparison, the laser spectral widths are less than 10 nm resulting in a spectral width of $\approx 3\,\text{nm}$ for the third-order signals. As shown in Figure 4.11, the detection path splits the signal using two dichroic mirrors centered at 414 and 389 nm. The exact references of the filters and the dichroic mirrors were: FF01-373/10-25, FF01-400/12-25, FF01-434/17-25, FF414-Di01-25x36 and FF389-Di01-25x36, *Semrock*.

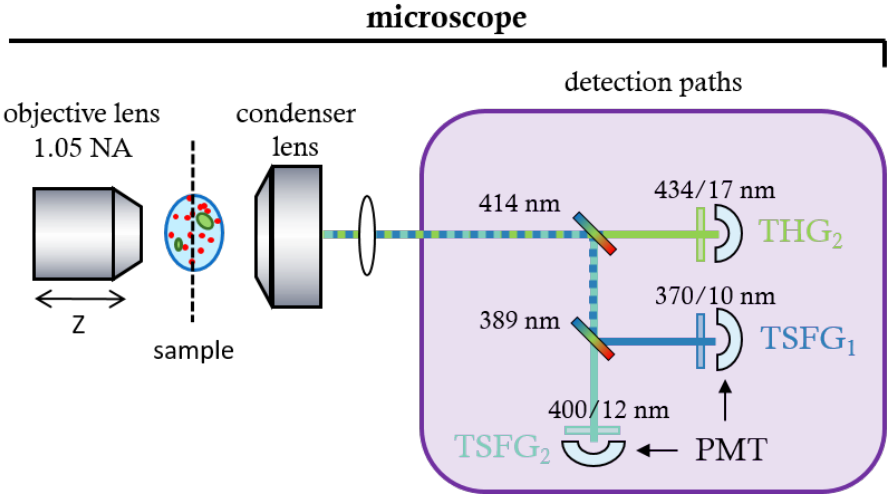

Figure 4.11: Schematic view of the three forward detection channels and filters.

2.2 Alignment Procedure

In this section we describe the alignment procedure required to obtain TSFG by mixing the pump (λ_1 =1045 nm) and the OPO (λ_2 =1300 nm). This experiment requires a precise spatial 3D co-alignment and temporal synchronisation of the two excitation beams.

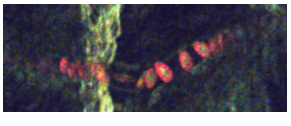

The sample used for co-alignment consists of multicolour labelled beads (1 µm of diameter (TetraSpeck Microspheres 1 µm, *ThermoFisher Scientific*)) embedded in agarose and mounted between a slide and a coverglass.

1. **Power, spatial resolution and spatial overlap**
   First of all, we adjusted the telescope on the OPO path to get the maximum axial resolution without losing power. The divergence of the pump beam was adjusted using the telescope to match the focal planes of the pump and the OPO beams. Their axial mismatch was measured by imaging a single bead with the two beams. In Figure 4.12, the axial profiles of one bead demonstrate a good axial overlap.

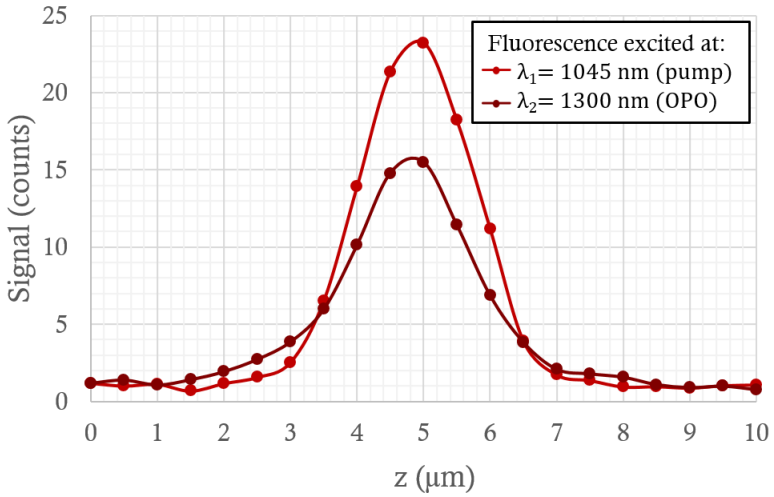

Figure 4.12: Axial profile of a single 1 µm bead accounting for the axial resolution and co-alignment of the two excitation beams.

   The measured axial resolutions were 2.2 µm and 2.1 µm for the pump and OPO, respectively. The z-mismatch was smaller than these measured resolutions. The maximum power available at the sample plane was 1.03 W for the pump (at 1045 nm) and 95 mW for the OPO (at 1300 nm).
   To obtain a precise lateral co-alignment of the beams, we imaged one bead at the center of the FOV with the two beams. Both signals were detected on the same channel and we adjusted the injection mirrors to make the two images overlap.

2. **Temporal synchronisation**
   To detect TSFG, the two excitation pulses must be synchronized with the delay line. First, a water-glass interface was placed at the focal plane (which can be done with THG imaging of the OPO beam). Then, the delay line was swept while imaging continuously to find the position at which the two beams overlap in time, giving rise to TSFG. Finally, fine tuning maximizes this signal as shown in Figure 4.13.

2.3 TSFG signal characterisation

In this section we analyse the dependence of THG and TSFG on the laser parameters. In the following calculations, P_1, I_1, ω_1 and τ_1 stand for the average power, intensity, frequency and pulse duration of the pump, respectively, whereas P_2, I_2, ω_2 and τ_2 are

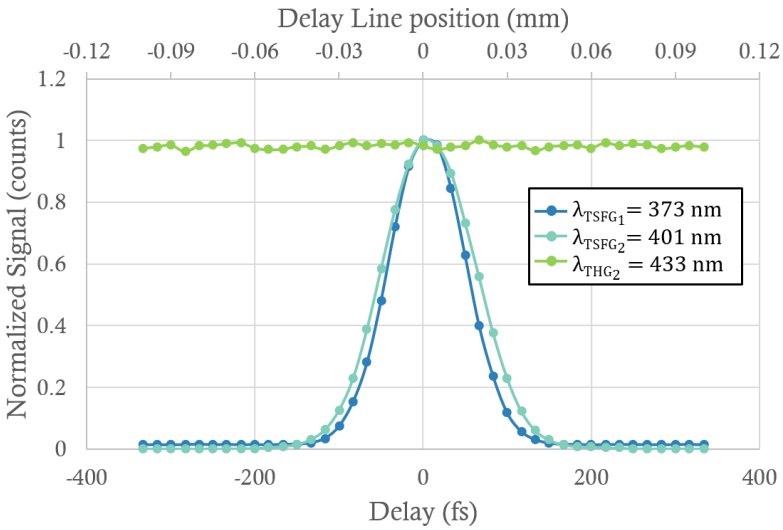

Figure 4.13: TSFG and THG signals (373, 401 and 433 nm) excited at λ_1 =1045 nm and λ_2 =1300 nm measured on a water-glass interface depending on the delay line position. TSFG signals decay rapidly with delay when desynchronizing the pulses.

the average power, intensity and frequency of the OPO beam, respectively. We consider common repetition rate $1/T$ and a temporal gaussian profile:

$$I_1(t) = I_0 \frac{T}{\tau_1} \frac{1}{\sqrt{2\pi}} e^{-\frac{t^2}{2\tau_1^2}}.$$

The average excitation intensity is:

$$\langle I_1 \rangle = \frac{\int_{-T/2}^{+T/2} I_1(t)dt}{T/2 - (-T/2)} = I_0 \frac{T}{\tau_1} \frac{1}{T\sqrt{2\pi}} \int_{-T/2}^{+T/2} e^{-\frac{t^2}{2\tau_1^2}} dt = I_0.$$

We assume that there is no interaction between pulses, thus $\tau_1 \ll T$. In this case the integral limits can be extended to $\pm\infty$. We have then used the result $\int_{-\infty}^{+\infty} e^{-\alpha t^2} dt = \sqrt{\pi/\alpha}$ with $\alpha = 1/2\tau_1^2$.
Now we calculate the THG signal at $3\omega_1$. The detection averages the signal, thus:

$$S_{THG_1} \propto \langle I_1^3 \rangle = \left(\langle I_1 \rangle \frac{T}{\tau_1}\right)^3 \frac{1}{(\sqrt{2\pi})^3} \frac{1}{T} \int_{-T/2}^{+T/2} e^{-\frac{3t^2}{2\tau_1^2}} dt = \left(\frac{T}{\tau_1}\right)^2 \langle I_1 \rangle^3 \frac{1}{2\pi\sqrt{3}},$$

in accordance to the expressions presented in Table 1.1 in Chapter 1.
For TSFG at frequency $2\omega_1 + \omega_2$:

$$S_{TSFG_1} \propto \langle I_1^2 I_2 \rangle = \left(\langle I_1 \rangle \frac{T}{\tau_1}\right)^2 \left(\langle I_2 \rangle \frac{T}{\tau_2}\right) \frac{1}{(\sqrt{2\pi})^3} \frac{1}{T} \int_{-T/2}^{+T/2} e^{-(\frac{1}{\tau_1^2} + \frac{1}{2\tau_2^2})t^2} dt =$$

$$= \frac{T^3\sqrt{3}}{\tau_1\sqrt{\tau_1^2 + 2\tau_2^2}} \langle I_1 \rangle^2 \langle I_2 \rangle \frac{1}{2\pi\sqrt{3}}.$$

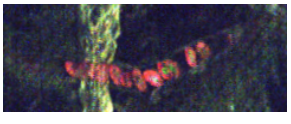

Using similar calculations for the two other signals, we obtain the following expressions:

$$\begin{aligned} S_{THG_1} &\propto \left(\frac{T}{\tau_1}\right)^2 \langle I_1\rangle^3 & S_{THG_2} &\propto \left(\frac{T}{\tau_2}\right)^2 \langle I_2\rangle^3 \\ S_{TSFG_1} &\propto \frac{9\sqrt{3}\,T^2}{\tau_1\tau_2\sqrt{(\tau_1/\tau_2)^2+2}}\langle I_1\rangle^2\langle I_2\rangle & S_{TSFG_2} &\propto \frac{9\sqrt{3}\,T^2}{\tau_1\tau_2\sqrt{(\tau_2/\tau_1)^2+2}}\langle I_1\rangle\langle I_2\rangle^2 \end{aligned} \tag{4.8}$$

These expressions can be written in terms of the average power of the lasers:

$$\begin{aligned} S_{THG_1} &\propto \left(\frac{T}{\tau_1}\right)^2 \langle P_1\rangle^3 & S_{THG_2} &\propto \left(\frac{T}{\tau_2}\right)^2 \langle P_2\rangle^3 \\ S_{TSFG_1} &\propto \frac{9\sqrt{3}\,T^2}{\tau_1\tau_2\sqrt{(\tau_1/\tau_2)^2+2}}\langle P_1\rangle^2\langle P_2\rangle & S_{TSFG_2} &\propto \frac{9\sqrt{3}\,T^2}{\tau_1\tau_2\sqrt{(\tau_2/\tau_1)^2+2}}\langle P_1\rangle\langle P_2\rangle^2 \end{aligned} \tag{4.9}$$

In the two following sections, we provide an experimental demonstration of the dependence of these signals on laser power and pulse duration.
We define two working modes on the microscope:

- **Single-beam THG mode.** In this mode, only the OPO beam is used. This allows to retrieve spectral information sequentially by tuning the excitation wavelength.
- **Wavelength mixing mode.** In this mode, the OPO beam is set to $\lambda_2 = 1300\,\text{nm}$ and overlapped with the pump ($\lambda_1 = 1045\,\text{nm}$) to produce TSFG. Three images are detected simultaneously at $\lambda_{TSFG_1} = 373\,\text{nm}$, $\lambda_{TSFG_2} = 401\,\text{nm}$ and $\lambda_{THG_2} = 433\,\text{nm}$. The narrow detection filters described previously are used in this mode. The fourth generated signal at $\lambda_{THG_1} = 348\,\text{nm}$ is not well transmitted by the optics on the detection system (Figure 4.10) and thus it is not used in this work.

2.3.1 Dependence on the excitation power

One first feature that we experimentally confirmed is the dependence of the signals on the excitation laser power. This demonstration is relatively easy to achieve in wavelength mixing mode. We detected simultaneous TSFG_1, TSFG_2 and THG_2 signals from polystyrene beads mounted in an agarose gel. We recorded series of such images while varying the excitation laser power.
The measured signals were fitted with a power law $S \propto P^\kappa$. Figure 4.14.a shows the variation of the three signals when increasing the pump power P_1. As expected, the THG_2 signal does not depend on this beam (power law $\kappa = 0$). On the other hand, the two TSFG signals increase with a power law of order $\kappa \approx 1$ and $\kappa \approx 2$ corresponding to the number of pump photons involved in the processes. Indeed, the signal resulting from the sum $2\omega_P + \omega_{OPO}$ (at $\lambda_{TSFG_1} = 373\,\text{nm}$) depends quadratically on the pump power whereas the signal resulting from the combination $\omega_P + 2\omega_{OPO}$ (at $\lambda_{TSFG_2} = 401\,\text{nm}$) grows linearly with the pump power, as shown by equations 4.9.
Similarly, Figure 4.14.b presents the behaviour of the three signals with increasing OPO power P_2. This beam being involved in the three processes, all power law orders are different from zero. As expected, $\kappa \approx 1$ for the sum at $\lambda_{TSFG_1} = 373\,\text{nm}$ and $\kappa \approx 2$ for the second TSFG signal at $\lambda_{TSFG_2} = 401\,\text{nm}$. In the case of THG_2, we retrieve the cubic

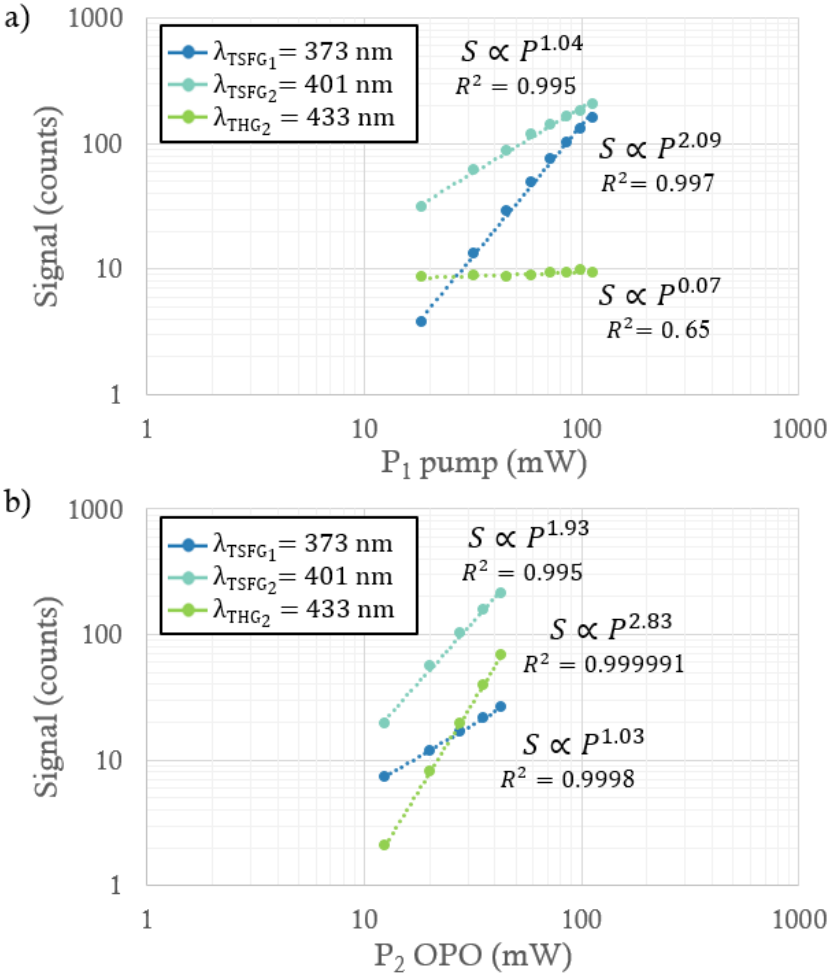

Figure 4.14: Signal dependence on the average power of the pump P_1 (a) or of the OPO P_2 (b). The THG and TSFG signals were measured on 1 um polystyrene beads.

power law ($\kappa \approx 3$) as expected.

Together, these experiments validate the power dependence of the signals and demonstrate the detection of TSFG using wavelength mixing.

2.3.2 Dependence on pulse duration

The aim of this section is to experimentally validate that the signal dependence on the relative pulse duration of the two beams is governed by the expressions 4.9. This verification is less straightforward than in the previous section because we do not have a direct control on the duration of the pulses.
The strategy here is to compare images acquired in the two different working modes, single-beam THG and wavelength mixing, at the two TSFG wavelengths, λ_{TSFG_1} = 373 nm and λ_{TSFG_2} = 401 nm.

We can simplify Eq. 4.9 assuming $\langle P_1 \rangle = \langle P_2 \rangle = 1$ and compare the signal acquired at the same detection wavelength with different modes: wavelength mixing (S_{mix}) and single-beam THG (S_{THG}). The detection wavelength is indicated in brackets. With this notation, $S_{THG}(\lambda_{TSFG_1=373\,\mathrm{nm}})$ is the THG signal excited at 1120 nm, and $S_{THG}(\lambda_{TSFG_2=401\,\mathrm{nm}})$

is the THG signal excited at 1200 nm as represented in the energy schemes in Figure 4.15.a. We obtain the following expressions:

$$\frac{S_{mix}(\lambda_{TSFG_1})}{S_{THG}(\lambda_{TSFG_1})} = \frac{9\sqrt{3}\,\alpha}{\sqrt{1/\alpha^2+2}} \qquad \frac{S_{mix}(\lambda_{TSFG_2})}{S_{THG}(\lambda_{TSFG_2})} = \frac{9\sqrt{3}\,\alpha}{\sqrt{\alpha^2+2}} \tag{4.10}$$

where we have defined $\alpha \equiv \tau_2/\tau_1 = \tau_{OPO}/\tau_{pump}$. These two expressions are plotted in Figure 4.15.b and reflect the enhancement factor for mixing TSFG signals compared to single-beam THG excitation. We observe that for $\alpha = 1$ ($\tau_1 = \tau_2$), the two TSFG signals present the same enhancement factor. This corresponds to an experimental situation where temporal overlap is optimized.

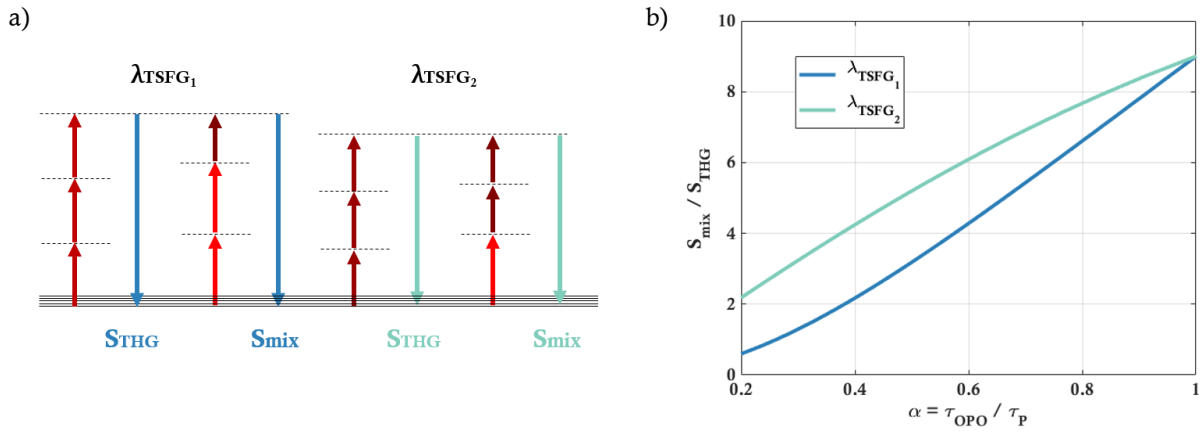

Figure 4.15: Variation of the mixing TSFG signal to single-beam THG signal ratio as a function of α (the ratio of the pulse duration of the two excitation beams).

In this analysis, we have assumed that τ_{OPO} is constant through the entire OPO wavelength range. However, this is not the case in our microscope. To estimate the effective value of τ_{OPO} for our system, we measured the pulse duration at the sample plane as a function of λ_{OPO}. These measurements are shown in Figure 4.16 for the wavelength range concerning this project. The pulse duration measured on the optical table is also displayed. The difference between the two curves reflect the dispersion induced by the microscope.
The pulse duration not being constant for the different wavelengths, a correction must be added to expressions 4.10. Then, the effective enhancement factors f_{TSFG_1} and f_{TSFG_2} become:

$$f_{\mathrm{TSFG}_1} = \frac{S_{mix}(\lambda_{TSFG_1})}{S_{THG}(\lambda_{TSFG_1})} = \frac{9\sqrt{3}\,\alpha'\beta'}{\sqrt{1/\alpha^2+2}} \qquad f_{\mathrm{TSFG}_2} = \frac{S_{mix}(\lambda_{TSFG_2})}{S_{THG}(\lambda_{TSFG_2})} = \frac{9\sqrt{3}\,\alpha''\beta''}{\sqrt{\alpha^2+2}} \tag{4.11}$$

where $\alpha \equiv \dfrac{\tau_{OPO_{1300}}}{\tau_{pump}} = 0.608$, $\alpha' \equiv \dfrac{\tau_{OPO_{1120}}}{\tau_{pump}} = 0.475$, $\alpha'' \equiv \dfrac{\tau_{OPO_{1200}}}{\tau_{pump}} = 0.529$,
$\beta' \equiv \dfrac{\tau_{OPO_{1120}}}{\tau_{OPO_{1300}}} = 0.781$ and $\beta'' \equiv \dfrac{\tau_{OPO_{1200}}}{\tau_{OPO_{1300}}} = 0.460$ from the measurements in Figure 4.16.
The resulting enhancement factors of the two TSFG signals at $\lambda_{TSFG_1} = 373$ nm and

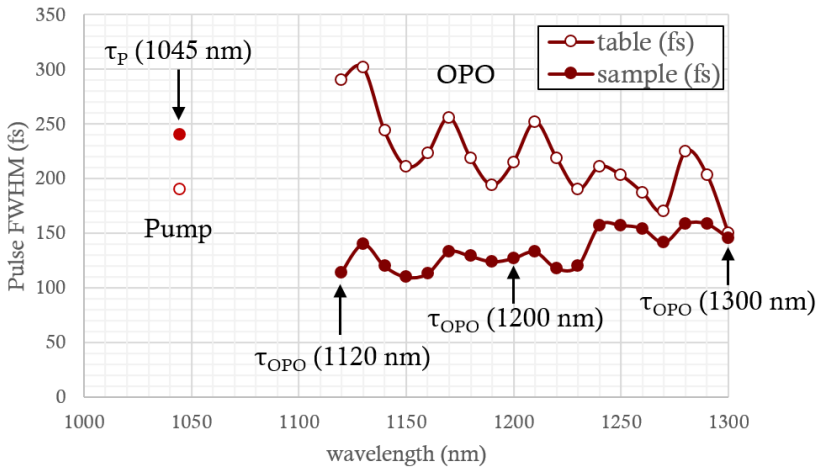

Figure 4.16: Autocorrelator measurements on the optical table and on the sample plane in function of the wavelength. The isolated points at 1045 nm correspond to the pump, which does not include a dispersion compensation element. The joined series of points spanning from 1120 to 1300 nm are measurements on the OPO. The pre-compensation system was tuned to achieve the shortest pulses at the sample plane to maximize the signals.

$\lambda_{TSFG_2} = 401\,\text{nm}$ with respect to the single-beam THG signals at the same wavelengths (i.e. excited with the OPO set at 1120 and 1200 nm, respectively) are:

$$f_{TSFG_1} = \frac{9\sqrt{3}\,\alpha'\beta'}{\sqrt{1/\alpha^2 + 2}} \approx 2.7 \qquad f_{TSFG_2} = \frac{9\sqrt{3}\,\alpha''\beta''}{\sqrt{\alpha^2 + 2}} \approx 4.7 \tag{4.12}$$

The dependence of the signals on the relative duration of the pulses can be evaluated by comparing these predicted values to the ratios of images taken with the two different acquisition modes. Two images were acquired simultaneously at 373 and 401 nm in wavelength mixing mode (with the OPO set at $\lambda_2 = 1300\,\text{nm}$) and two additional images were acquired at the same detection wavelengths sequentially in single-beam THG mode (with no pump and with the OPO tuned to 1120 and 1200 nm, respectively). As a control, we also recorded the image at 433 nm in the wavelength mixing mode and compared it with a supplementary image at the same detection wavelength acquired in single-beam THG mode (OPO set to $\lambda_2 = 1300\,\text{nm}$ and no pump). The corresponding enhancement factor can be defined as:

$$f_{THG_2} = \frac{S_{mix}(\lambda_{THG_2})}{S_{THG}(\lambda_{THG_2})} = 1 \tag{4.13}$$

This ratio is equal to one because the signals detected at 433 nm using both configurations ($S_{mix}(\lambda_{THG_2})$ and $S_{THG}(\lambda_{THG_2})$) are in fact both single-beam THG signals. Three resulting images were computed by dividing the wavelength mixing TSFG images by the single-beam THG images at the corresponding wavelengths. To avoid chromatic aberrations effects (studied later in this chapter) only the central 1/3 of the FOV was considered for this analysis. In Figure 4.17, the pixel distribution of these three ratio images is presented. A gaussian fit was performed on the histograms to determine the measured values. The half with at half maximum of the fitted curves can account for the uncertainties in this measurement. Hence, the measured values of the enhancement factors are:

$$f_{TSFG_1} = 2.50 \pm 0.66 \qquad f_{TSFG_2} = 4.33 \pm 1.38 \qquad f_{THG_2} = 0.96 \pm 0.19 \tag{4.14}$$

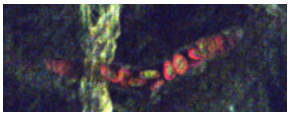

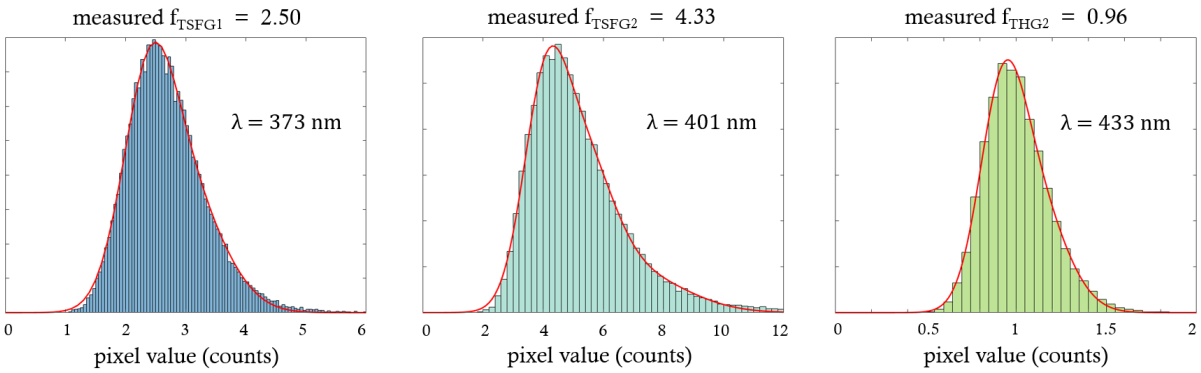

Figure 4.17: Pixel value distribution of the ratio mixing/single-beam-THG images for the three wavelengths.

We see that the experimental measurements of the enhancement factors are very close to the numerical calculation in Equations 4.12 and 4.13.

We conclude that these results confirm our theoretical prediction of the dependence of TSFG signals on the pulse duration of the two beams: matching the pulse duration is a means to optimize these signals; alternatively, mismatching the pulse duration could be a way to change the ratio between the two TSFG signals.

2.3.3 Effect of the polarisation directions

In this section, we briefly investigate the effect of the relative incident polarisations of the two excitation beams on TSFG signal. For this purpose, we introduced a HWP in the OPO path. The orientation of the linear polarisation of this beam was turned relatively to the orientation of the pump polarisation while acquiring images in wavelength mixing mode. The resulting signal modulation is shown in Figure 4.18.

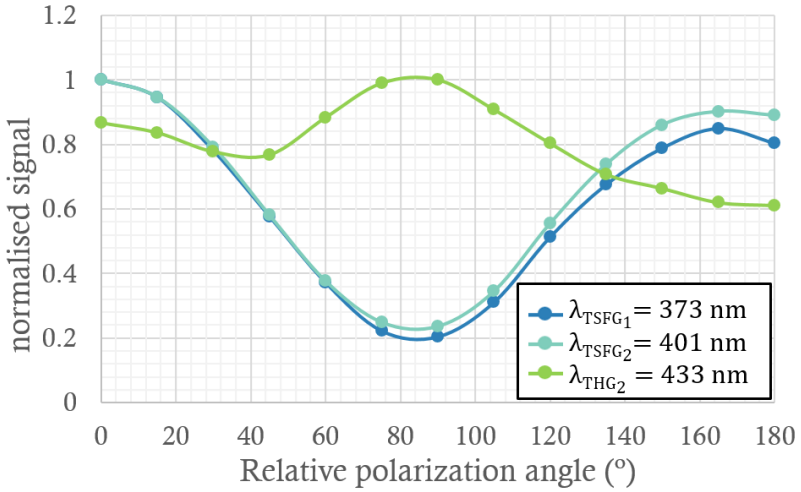

Figure 4.18: Effect of the relative polarization of the excitation beams on TSFG signals. $TSFG_1$, $TSFG_2$ and THG_2 signals measured on a zebrafish RBC as a function of the relative polarization between excitation beams. TSFG signals are maximized for parallel polarizations of the excitation beams.

This measurement indicates that TSFG signals are maximized when the polarisations of

the two excitation beams are parallel, and minimized when they are orthogonal. We note that polarization states were not perfectly linear in this experiment. Indeed, THG signal is not expected to change when rotating the OPO polarisation. The observed ≈ 30% THG modulation is in fact due to polarization ellipticity. We confirmed this hypothesis using a polarimeter (a polariser and a power meter placed on the sample plane). Polarization ellipticity was measured for each position of the HWP as $\epsilon = P_{max}/P_{min}$, where P_{max} and P_{min} are the maximum and minimum values on the modulation curve measured at the sample plane. Measured ellipticities are shown in Figure 4.19.

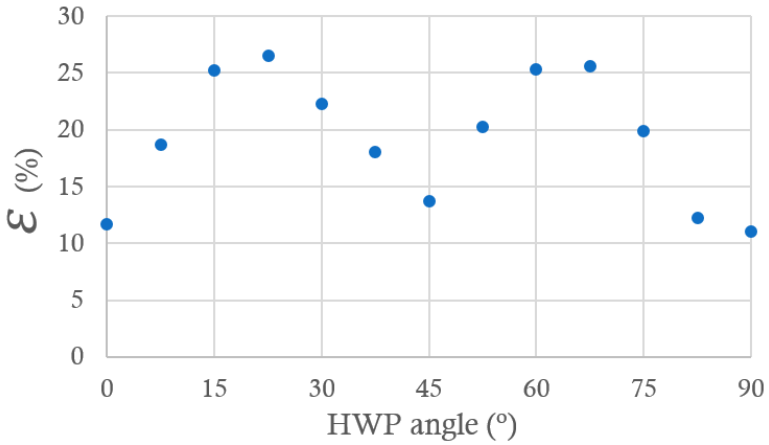

Figure 4.19: Ellipticity for each of the angles of the HWP, exceeding 25 % in some cases.

Nevertheless, this investigation confirms that TSFG should generally be implemented with parallel beam polarisations to maximize signal.

2.3.4 Effect of chromatic aberrations

To finalise the characterisation of TSFG as a function of the experimental microscope parameters, we analysed the effect of chromatic aberrations. From the past expertise of our laboratory, we knew that in two-photon wavelength mixing experiments, chromatic aberrations limit the usable lateral field of view (FOV), i.e. the FOV where the mixing process is efficient. Here, because we work with a third-order contrast mechanism, we anticipated that chromatic aberrations can significantly reduce the usable FOV.
We estimated the axial resolution degradation and the chromatic shift between the two beams depending on the position within the FOV. For this purpose, a 3D distribution of multicolour 1 µm beads in an agarose gel was imaged sequentially with the two laser beams as z-stacks. The images were then analysed with an automated multi-PSF metrology code previously developed in our laboratory [135]. Its principle is to localize a large number of beads in the imaged volume, and to measure the axial dimension of the PSF for each beam at all positions in the image. The code also calculates the chromatic lateral shift of the beams from the spatial shift of the two images. Figures 4.20 and 4.21 show the results for x and for y directions respectively.
In both cases, we observe that δz starts to be degraded at a distance of ≈ 230 µm from the center of the FOV. Given that the FOV dimensions are 770 x 770 µm^2 in this microscope, no axial resolution degradation was observed in the central ≈ 60 % region of the FOV. The degradation in the edges is probably due to the mirror placed between the scanners

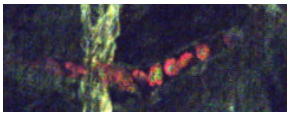

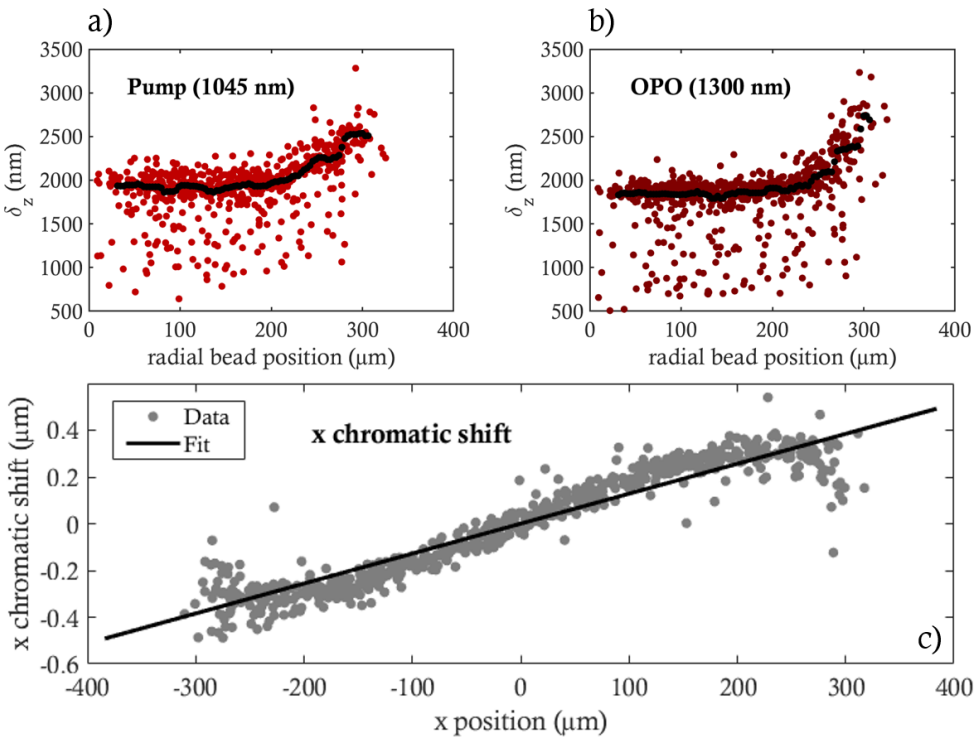

Figure 4.20: Statistical measurement of the axial PSF and its lateral degradation away from the center of the FOV along x in the case of the pump (a) and of the OPO at 1300 nm (b). Chromatic shift of the two lasers along x (c).

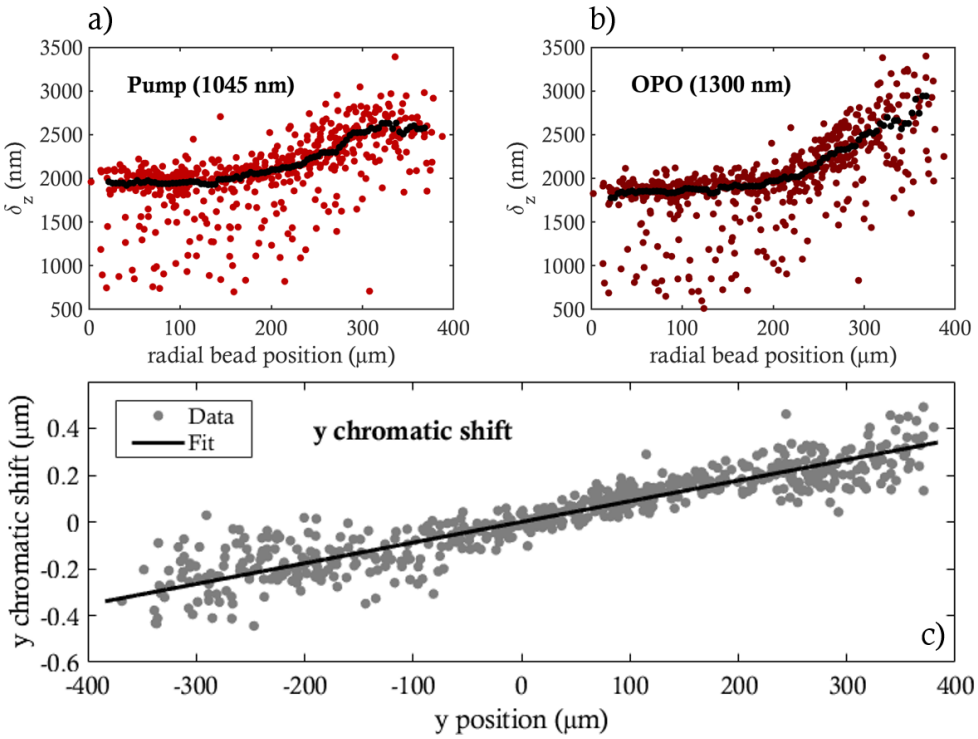

Figure 4.21: Statistical measurement of the axial PSF and its lateral degradation away from the center of the FOV along y in the case of the pump (a) and of the OPO at 1300 nm (b). Chromatic shift of the two lasers along y (c).

and the objective resulting in vignetting of the beams. This mirror may also be responsible for the smaller FOV observed along x compared to y. Indeed, its rectangular shape clips the beam in the x direction for lower scan angles than in the y direction. Figures 4.20.c and 4.21.c indicate that there is a maximum lateral shift between the two beams of 0.4 µm. In what follows, we analyse the effect of this lateral shift on TSFG signals.

To understand the effect of this chromatic shift on TSFG, we first performed a simple simulation. We considered a 1D model in which the excitation beams are represented by their gaussian spatial profiles. In Figure 4.22, the two laser Gaussian profiles are plotted with no lateral shift and with the maximum measured lateral shift of 0.4 µm (obtained from Figures 4.20.c and 4.21.c).

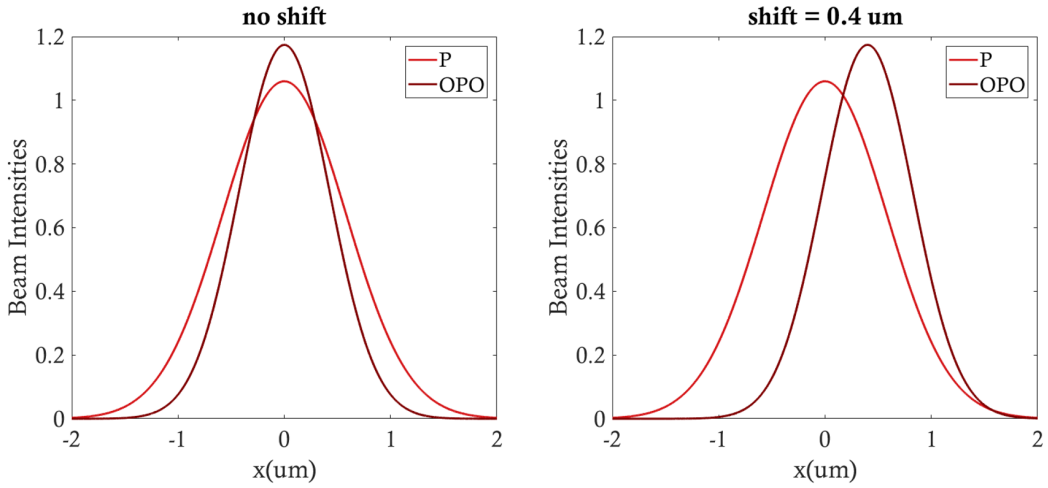

Figure 4.22: Pump and OPO Gaussian distributions coaligned (left) and with a 0.4 µm lateral shift (right). The FWHM are ≈ 1.4 µm and ≈ 1 µm for the pump and OPO respectively. The normalisation constant was arbitrarily chosen such that the two THG signals are normalised.

Nonlinear signal distributions are obtained as the product of these Gaussian functions raised to the number of photons involved in the process. For example, the signal distribution at λ_{TSFG_1} is the product of the pump Gaussian profile squared and the OPO Gaussian profile. Figure 4.23 represents the triple products which can be understood as the amplitudes of the generated signals. The FWHM used to build these Gaussian profiles were deduced from measured 2P lateral resolutions ($\delta_{xy} \approx 1$ µm for the pump and $\delta_{xy} \approx 0.7$ µm for the OPO) on beads from the images discussed above. With lateral mismatch of the two lasers, the TSFG signals are less efficient whereas the THG signals remain constant.
The resulting signal in each case is given by the integral of this triple product. Figure 4.24 shows the integral of the signal Gaussian profiles in Figure 4.23. This corresponds to the acquired signal and depends on the lateral shift. All the signals have been normalized to enable comparisons.
According to this simulation, at the edges of our FOV where the lateral shift reaches 0.4 µm, the TSFG signal is expected to drop to ≈ 80 % of its value at the center of the FOV.

To check if this model explains the TSFG signal loss at the edge of the FOV, we compared this last result with experimental data. Figure 4.25 shows the x and y profiles of the

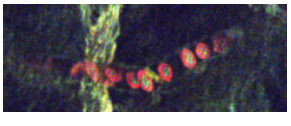

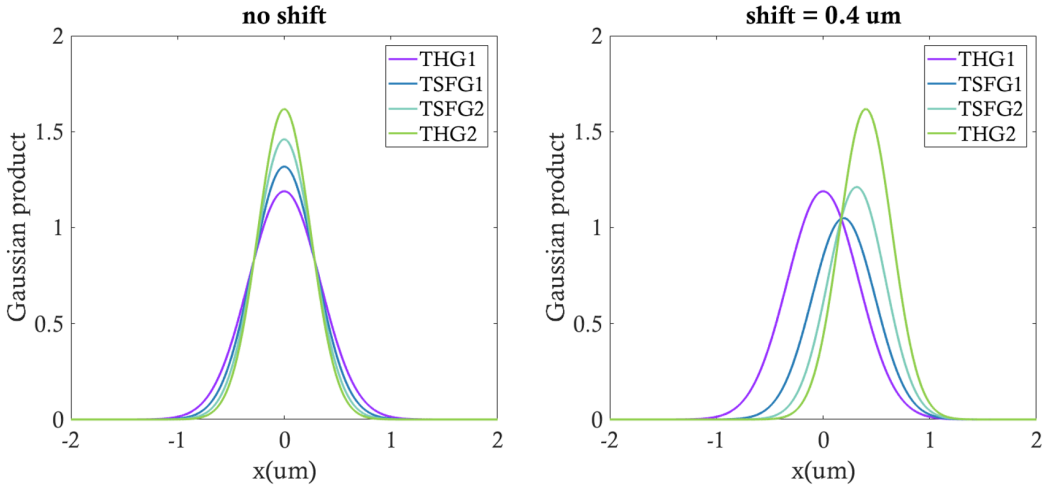

Figure 4.23: Third order product combination of the Gaussian excitations in Figure 4.22 with no shift and with a 0.4 µm lateral shift. The normalization constant was arbitrarily chosen such that the two THG signals are normalized.

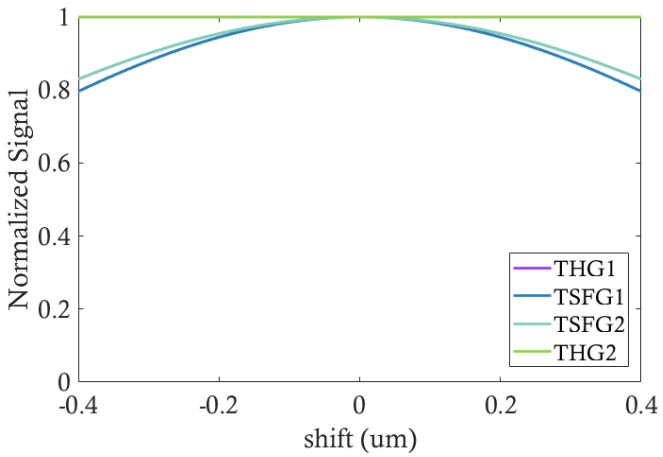

Figure 4.24: Integral of the third order products shown in Figure 4.23 for a shift comprised from 0 to 0.4 µm. The curves were normalised to 1.

z-projection of the wavelength mixing mode signals obtained by scanning a horizontal water-glass interface.

Figure 4.26 shows TSFG profiles of Figure 4.25 normalized by the THG signal. The TSFG signals drop is on the same order of magnitude as the one predicted by the model, which confirms the model validity for evaluating the effects of chromatic aberrations.

Overall, this investigation of chromatic aberrations shows that they have a limited effect in our experimental setup. This good performance is certainly due to the choice of the objective lens. We nevertheless observe a significant loss of signal at the edges of the FOV that is not due to chromatic aberrations but could be due to beam vignetting during scanning. To circumvent this limitation we can either limit the imaging to the center of the FOV or compensate for this non-homogeneous response by image post- processing (see Section 3.2).

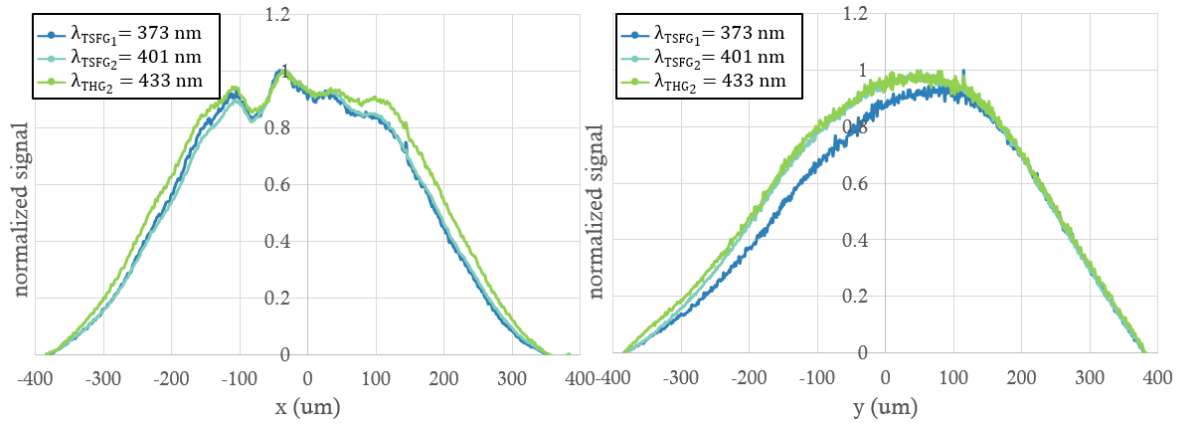

Figure 4.25: THG and TSFG profiles along x and y through the FOV, acquired as the z-projection of a water-glass horizontal interface.

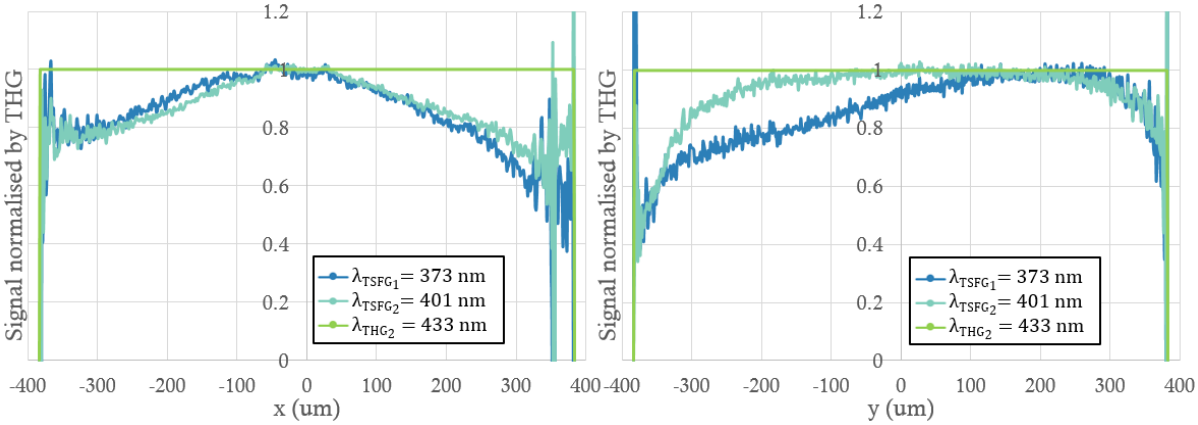

Figure 4.26: THG and TSFG profiles along x and y through the full FOV, normalized by the THG.

Together, with the results presented in this section we confirmed that we implemented an efficient experimental method providing one-shot (simultaneous) imaging of three TSFG-THG signals at different wavelengths. We analysed how to optimise its efficiency by adjusting the beam overlap and synchronisation, the incident polarisation and correcting for inhomogeneous signal distribution within the FOV.

3 Specific and functional TSFG imaging of hemoglobin in RBCs in vivo

In the followings sections, we present the application of TSFG for imaging hemoglobin *in vivo*. In Section 3.1, we first measure single-beam THG spectra of fully oxygenated and fully deoxygenated RBCs and we evidence THG resonance near the Soret band. We then show that our colour TSFG method has the potential to probe three wavelengths simultaneously, and to retrieve spectral information in a one-shot experiment. In Section 3.2, we show that TSFG can be used for selective blood detection in live zebrafish embryos with high temporal resolution. In Section 3.3, we show that TSFG can be used to monitor RBC oxygenation state in live zebrafish embryos. For this work, we used the same optical setup as presented in the previous section. Finally, in Section 3.4, we adapt our TSFG

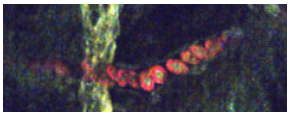

method to epidetected imaging in the OPA-based 3P microscope presented in Chapter 2, and we show that TSFG can be applied to deep-tissue blood imaging in live zebrafish adults.

3.1 Third order signal enhancement in the Soret bands

We have seen in Figure 4.1 that the linear absorption spectrum of hemoglobin presents a strong absorption peak centered at 415 nm when it is in its oxygenated state and at 430 nm when it is in its deoxygenated state. Here, we want to test if these absorption peaks of hemoglobin could resonantly enhance THG in a wavelength-dependent manner, and account for the RBC signal reported in a few studies such as [129]. If such a resonance is present, a second question is whether a significant difference can be detected between the two oxygenation states of hemoglobin which could be used for functional THG imaging (Sections 3.1.1 and 3.1.2). Finally, we want to explore the possibility of using TSFG to retrieve this spectral information in RBCs through a simultaneous measurement at three wavelengths (Section 3.1.3).

3.1.1 Isolated RBCs sample preparation

We measured THG spectra of RBC from two different species: human and zebrafish. One important difference between the two is that zebrafish RBCs have a nucleus, unlike mammalian RBCs. The preparation protocol to obtain RBCs in fully oxygenated and fully deoxygenetated states was established by Michel NÃ©grerie, INSERM researcher at LOB, and is described below.

- **Human RBCs**
  Fresh whole blood samples from different anonymised patients were purchased (*Cerba Xpert*) and received at the laboratory. As we have presented in Section 1.1, RBCs have naturally the ability of storing oxygen. Their hemoglobin is therefore in an oxygenated state at atmospheric pressure. This was confirmed with a linear spectrophotometer (Shimadzu UV-1700, *Pharmaspec*), and thus no special preparation is needed to obtain oxyhemoglobin. The cells were embedded in an agarose gel ($\approx$ 19 µL of blood in 500 µL of gel) to prevent them from moving during image acquisition. Low melting agarose ($T_{congealing}$ = 26 °C to 30 °C) was used to keep the cells at physiological temperature. The gel was a 2 % agarose solution: 2 g of agarose for 100 mL of Ringer's solution (an isotonic solution for RBC). The gel was mounted in a channel slide (μ-Slide Luer Glass Bottom, *IBIDI*) as represented in Figure 4.27. The channel thickness was 0.4 µm with the top made of a #1.5 glass coverslip ($\approx$ 170 µm). Two inlets allowed the filling of the chamber and were then sealed with caps.
  To obtain RBCs in deoxygenated state, the oxygen molecules need to be forced out of the hemoglobin. This was achieved with the help of Michel NÃ©grerie. The isotonic solution containing RBCs in agarose was degassed and put under argon while kept at 42 °C. A solution of sodium hydrosulfite ($Na_2S_2O_4$, 92 mM in Ringer's solution) was prepared and also degassed in vacuum ($\approx$ 50 Pa) and kept under argon ($\approx 1.3 \times 10^5$ Pa). Then, 25 µL of this reducing agent were injected on the agarose solution containing RBCs at 42 °C resulting in a final concentration of $\approx$ 4.4 mM in hydrosulfite and $\approx$ 1.9 % in agarose. The sealed channel was also degassed in

vacuum and filled with argon. The deoxygenated RBCs in solution were transferred with a syringe (gastight, *Hamilton*) inside the channel through the rubber cap, which was finally sealed with vacuum silicon paste. This provided sufficient tightness to keep the cells in deoxygenated state for the duration of the imaging session (≈ 20 min).

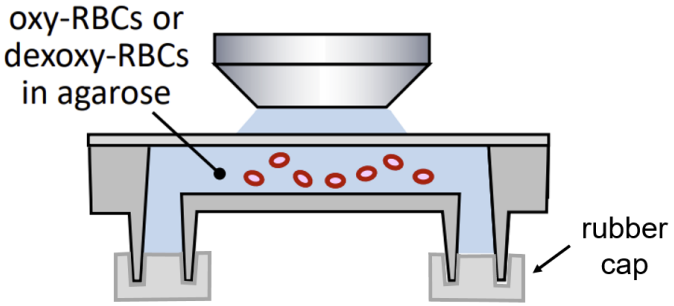

Figure 4.27: Channel Slide used as a sealed chamber for RBCs imaging in oxygenated and deoxygenated conditions.

- **Zebrafish RBCs**
  Zebrafish RBCs were obtained from wild-type adult zebrafish from our facility which were destined to euthanasia because of their age. Blood was obtained following the procedure described in [136]. After euthanasia by thermal shock in cold water ($T = 0\,°C$ to $4\,°C$) during 10 min, the fish body was wiped to remove the remaining water. Then, the tail was amputated with a sharp scalpel cut through the very posterior end of the dorsal aorta. With a micropipette, between 5 and 20 µL of blood could be obtained from the incision. To avoid coagulation, this volume was rapidly diluted in 200 µL of isotonic solution (Rainbow trout solution described in [137]). This solution was then used to constitute a $\approx 2\,\%$ agarose gel. From this point, we followed the same protocol to obtain oxygenated and deoxygenated hemoglobin as described for human RBC.

The linear absorption spectrum of each sample was measured on the spectrophotometer before and after imaging to verify its oxygenation state.

3.1.2 THG spectra near the Soret band

THG spectra were acquired in single-beam THG mode. The samples were imaged with the OPO beam tuned sequentially from 1120 to 1300 nm with steps of 10 nm (i.e. from 373.33 to 433.33 nm with steps of ≈ 3.33 nm in THG).[2] These limits were given by the optics transmission in the UV range (as shown in Figure 4.10) and by the highest wavelength available in the OPO (1300 nm). z-stacks of the samples were taken at 200 kHz pixel rate, 1 µm voxel depth and with an average power of 20 mW at the sample plane (maximum 45 mW). Hemoglobin absorption is maximal at the Soret peaks. To avoid artefacts due to THG light reabsorption by hemoglobin, we imaged cells close to the bottom of the chamber, with no other cells underneath.

[2]In the case of deoxygenated RBCs, the spectral step is twice as large to reduce the total imaging time to ≈ 20 min. After this delay, we observed that the non-perfect tightness of the chamber results in RBCs becoming oxygenated.

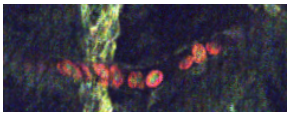

According to Equations 4.9, the images were divided by the cube of the laser power and multiplied by the square of the pulse duration to make them comparable. Using FIJI software, a region of interest (ROI) was hand-drawn for each RBC using a z-projection of all planes. The average value for several cells is plotted in Figures 4.28 and 4.29 along with the linear spectrum. In the absence of resonance we expect a flat THG

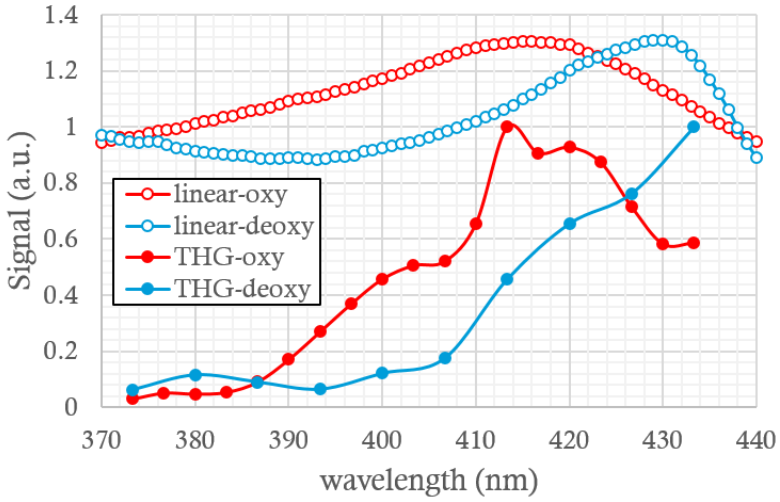

Figure 4.28: Linear and THG spectra measured on isolated human RBCs from different patients in oxygenated and deoxygenated states. Linear spectra are displayed with an arbitrary offset.

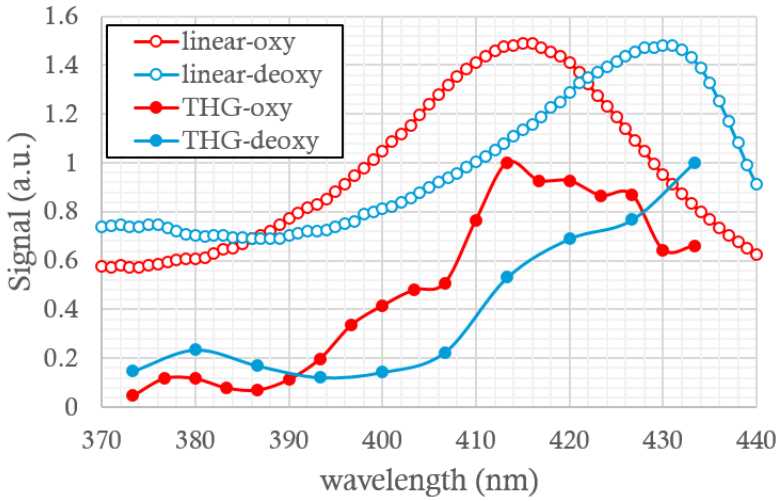

Figure 4.29: Linear and THG spectra measured on isolated zebrafish RBCs from different fish in oxygenated and deoxygenated states. Linear spectra are displayed with an arbitrary offset.

spectrum with no wavelength dependence. However, as shown in Figures 4.28 and 4.29, THG spectra from RBCs exhibit large variations which follow the profile of the linear spectra. A 20-fold THG enhancement is observed between 380 nm and the 415 - 430 nm region. This observation suggests that there is an efficient hemoglobin-mediated three-photon resonance enhancement of THG due to the Soret band absorption. Moreover, the

two oxygenation states present significant THG spectral differences, which confirm this interpretation and further suggests a potential way to distinguish between oxygenation states. We attribute the non smoothness of our THG spectra to uncertainties in excitation power and pulse duration measurements.
The Soret resonance also affects the contrast in wavelength-resolved THG images. Figure 4.30 presents THG images of a human RBC recorded in the excitation range 1120 - 1300 nm, corresponding to THG at 373 - 433 nm. Images are normalized to their maxima (the actual THG signal is 20x higher at 415 nm, as shown in Figure 4.28). We see that far from resonance (at short wavelengths), external RBC interfaces are well visible. On-resonance, the image contrast is largely altered.

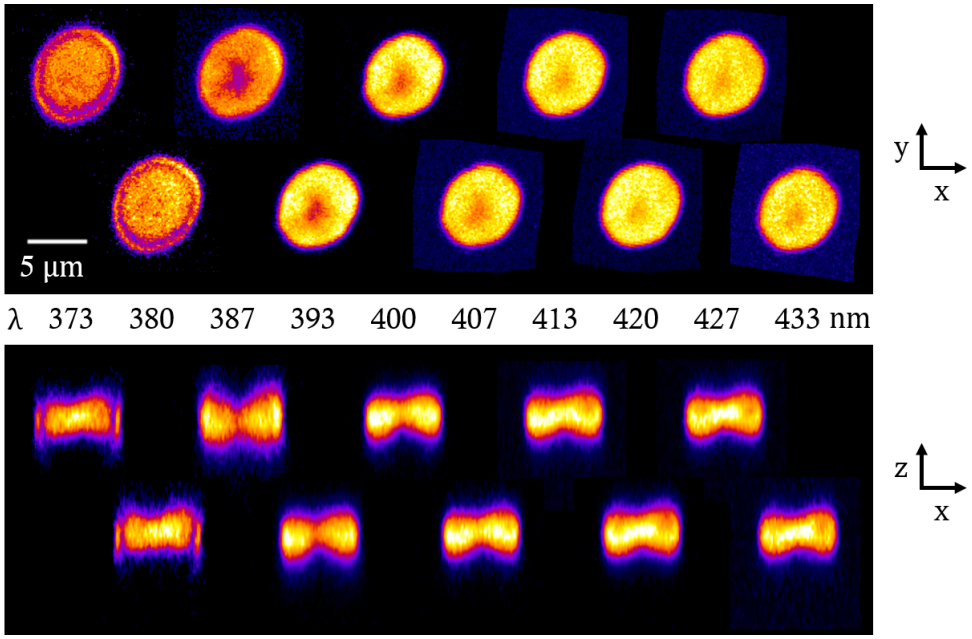

Figure 4.30: THG images from an isolated oxygenated human RBC recorded with excitation wavelengths in the 1120 - 1300 nm range, corresponding to THG in the 373 - 433 nm range. An average projection along the z axis is presented on the top image, while a projection along y is shown in the bottom image. Images are normalized to their maximum values.

Similar contrast variations are visible in THG images of zebrafish RBCs, as shown in Figure 4.31: THG signals from nucleus-cytoplasm interfaces are detected far from resonance, and are masked by resonantly-enhanced signals when the excitation wavelength matches the triple of the Soret band.
Together, these experiments demonstrate that: (i) THG is resonantly enhanced in hemoglobin in a wavelength-dependent manner related to absorption in the Soret band; (ii) maximum THG is observed when the excitation wavelength matches the triple of the Soret peak, suggesting a 3-photon resonance; (iii) this resonance does not depend on RBC type and is similar in human and in zebrafish; and (iv) the oxygenation state of RBCs can be probed using THG imaging at different wavelengths.

3.1.3 TSFG spectra near the Soret band

Based on the results of the previous section, we now explore if TSFG signals exhibit the same wavelength dependence as THG. Then, we investigate if the accessible wavelengths

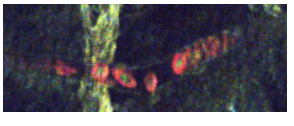

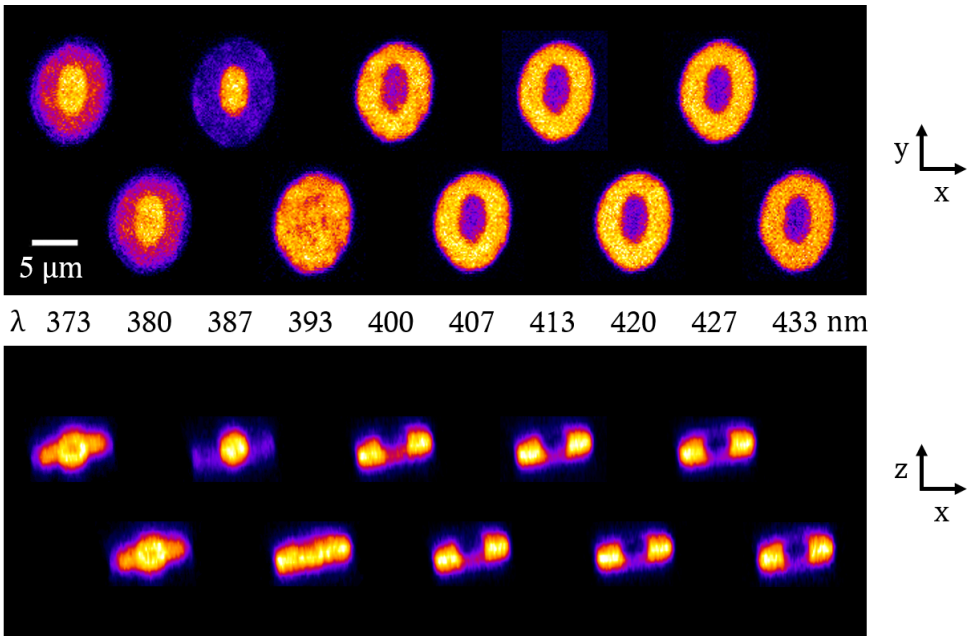

Figure 4.31: THG images from an isolated oxygenated zebrafish RBC recorded with excitation wavelengths in the 1120 - 1300 nm range, corresponding to THG in the 373 - 433 nm range. An average projection along the z axis is presented on the top image, while a projection along y is shown in the bottom image. Images are normalized to their maximum values.

in our microscope resulting from wavelength mixing allow to probe the oxygenation state of hemoglobin.

Oxygenated and deoxygenated samples of isolated RBCs from zebrafish were mounted in agarose as described in Section 3.1.1. The spectrum measurement started in wavelength mixing mode with the OPO wavelength set to 1300 nm. We then scanned the OPO wavelength down to 1250 nm by steps of 10 nm. For each wavelength, we adjusted the delay line to ensure optimal temporal matching of the OPO and pump pulses and we recorded three simultaneous images based on $TSFG_1$, $TSFG_2$ and THG_2 signals.

Figure 4.32 shows the spectra of oxy- and deoxygenated RBCs obtained for the three signals using wavelength mixing mode. They are similar to corresponding portions of the spectra measured in single-beam THG mode (Figure 4.29), and are correlated with the linear absorption spectra of oxy- and deoxyhemoglobin. We note that the difference between oxy- and deoxyhemoglobin is strongest for the OPO set to $\lambda_2 = 1300$ nm.

We also confirmed that imaging a RBC on-resonance and off-resonance at the same wavelength in THG or TSFG microscopy gives rise to very similar contrasts. Figure 4.33 shows THG and TSFG images at 373 and at 400 nm of the same RBC. We conclude that the two contrasts are essentially equivalent for imaging applications.

In conclusion, we demonstrated in Section 3.1 the wavelength-dependent resonant enhancement of THG and TSFG signals due to hemoglobin in RBCs. Importantly, we showed that using our colour TSFG method (wavelength mixing mode), we can simultaneously record one off-resonance signal (at 373 nm) and two on-resonance signals (at 401 and 433 nm) encompassing the Soret band. As we will see in the next section, this one-shot spectroscopic measurement is particularly interesting for probing flowing objects such as RBCs *in vivo*. We also found that with our setup, the contrast between oxygenated and deoxygenated states of hemoglobin is maximized for excitation at $\lambda_1 = 1045$ nm and

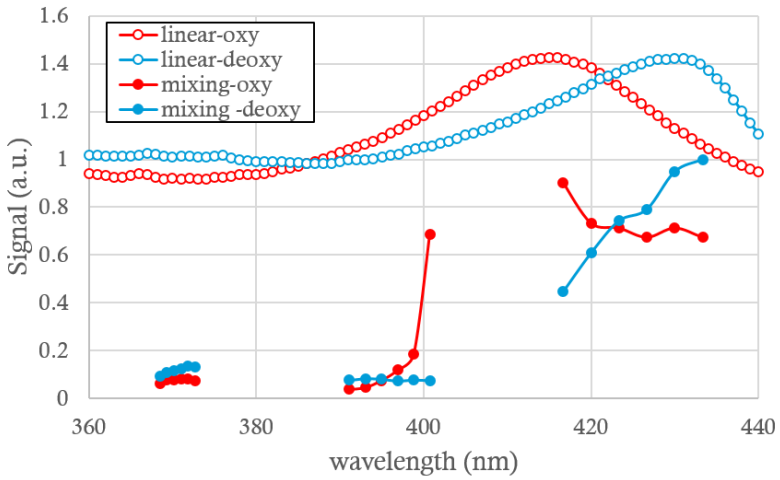

Figure 4.32: TSFG spectra measured on oxygenated and deoxygenated zebrafish RBCs.

Pump:	OFF	1045 nm	OFF	1045 nm
OPO:	1120 nm	1300 nm	1200 nm	1300 nm
Signal:	373 nm	373 nm	400 nm	400 nm

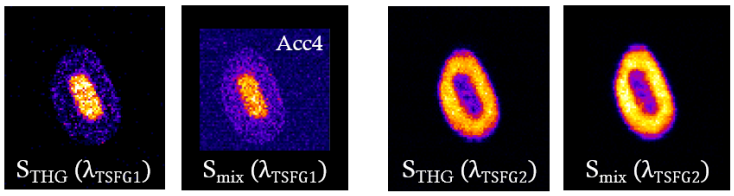

Figure 4.33: TSFG and THG images at 373 and at 400 nm revealing the similarity between the two contrasts. We note that the TSFG image at 373 nm was acquired with four accumulations to avoid photodamage, hence the higher background level.

$\lambda_2 = 1300\,\text{nm}$.

3.2 Specific imaging of RBCs using TSFG microscopy in live embryos

In this section we present how the TSFG resonant enhancement due to hemoglobin can be used for label-free segmentation of flowing RBCs in live zebrafish embryos.

We performed a series of experiments on zebrafish embryos at 2 dpf. We used the *Casper* mutant line, which is free from skin pigmentation [138]. Embryos were dechorionated, anesthetized (0.016 % tricaine, *Sigma Aldrich*), and mounted in a 2 % agarose gel with tricaine (also at 0.016 %) on a glass bottom dish allowing transmission imaging. While the agarose was still liquid, embryos were oriented on their lateral side using an eyelash. Special care was taken to position the dorsal aorta (DA) and the posterior cardinal vein (PCV) in the same horizontal plane so that they could be imaged simultaneously. This region of interest is indicated as a red box in Figure 4.34. After the agarose became solid, the dish was filled with embryo mounting solution as the immersion medium for imaging. In the microscope, the embryos were mounted with their anteroposterior axis orthogonal to the fast scan axis. In this orientation, the blood flow was also perpendicular to the fast

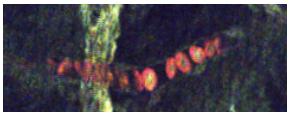

scan axis, which allowed imaging more red blood cells with less scanning artifacts. We then acquired time series of the three simultaneous images, and measured beam powers after the objective for subsequent normalization.

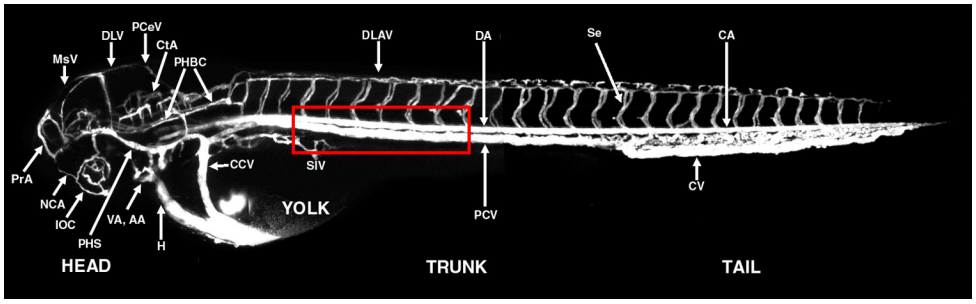

Figure 4.34: Lateral view of the vascular system of a zebrafish embryo at 2.5 dpf. The red boxed region represents our region of interest. Adapted from [139].

A typical three-channel image extracted from a time series is shown in Figure 4.35. The upper vessel closer to the notochord is the artery. Because of the pulsed arterial flow and the constant laser scanning speed, RBCs in the artery sometimes appear elongated in the images. In contrast, blood flow in the vein is constant. It can also be seen that the $TSFG_1$ image at 373 nm is weaker than the two other channels because of poor optics transmission at this wavelength. Nevertheless, flowing RBCs can be imaged simultaneously at the three wavelenghts despite their motion during image acquisition.

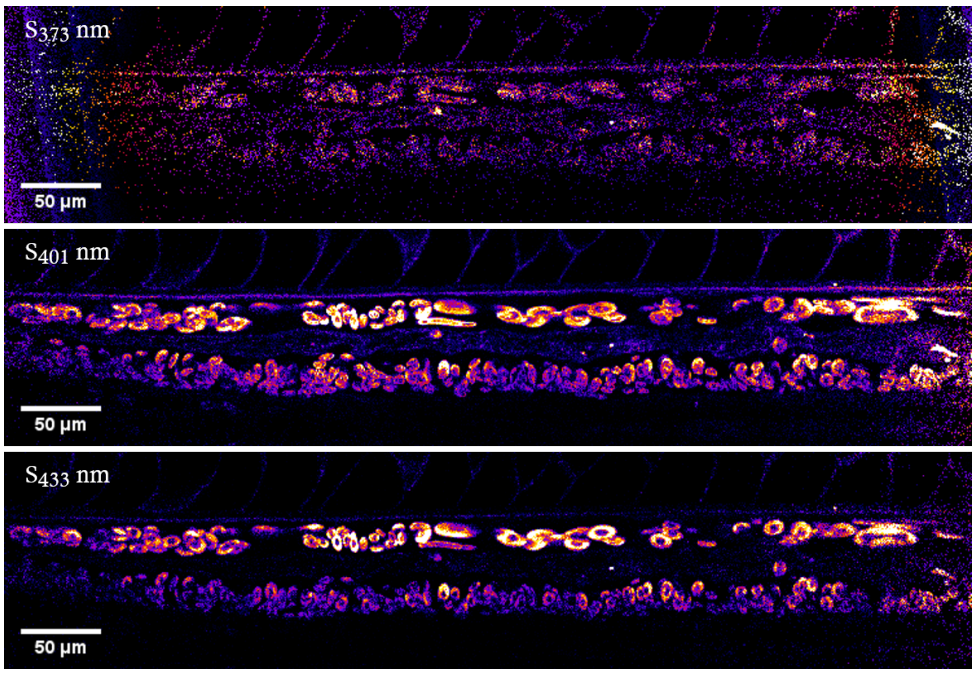

Figure 4.35: Three flat field corrected images of a 2dpf embryo detected simultaneously in wavelength mixing mode.

When using the wavelength mixing mode (1045 nm + 1300 nm excitation), the $TSFG_2$ and THG_2 signals detected at 401 and 433 nm lie in the resonant part of the hemoglobin

spectrum. In contrast, the $TSFG_1$ signal detected at 373 nm is far from the Soret resonance (Figure 4.32). Since the three images are recorded simultaneously, one simple possibility to detect RBCs is to compare resonant and non-resonant signals at the pixel scale. In principle, an "enhancement" image $S_{\text{enhancement}}$ can be calculated by dividing the sum of the two on-resonance images (S_{401} and S_{433}) by the off-resonance image (S_{373}):

$$S_{\text{enhancement}} = (S_{401} + S_{433})/S_{373} = (S_{TSFG_2} + S_{THG_2})/S_{TSFG_1} \tag{4.15}$$

According to the results of the previous section, this enhancement ratio is expected to be large in RBCs.

We therefore processed these image sequences as follows.

Flat field correction

First, we implemented a step of numerical flat field correction. As we have seen in section 2.3.4, vignetting, field curvature and chromatic aberrations result in inhomogenous TSFG and THG signal levels within the FOV (Figure 4.25). To compensate for this inhomogeneity, we obtained reference profiles by recording a z-stack of the TSFG signals from a horizontal water-glass interface. We used the z-projection of these images as an estimation of the inhomogeneous signal profiles across the FOV, and used them for normalization. The benefit of this flat-field correction step is shown in Figure 4.36.

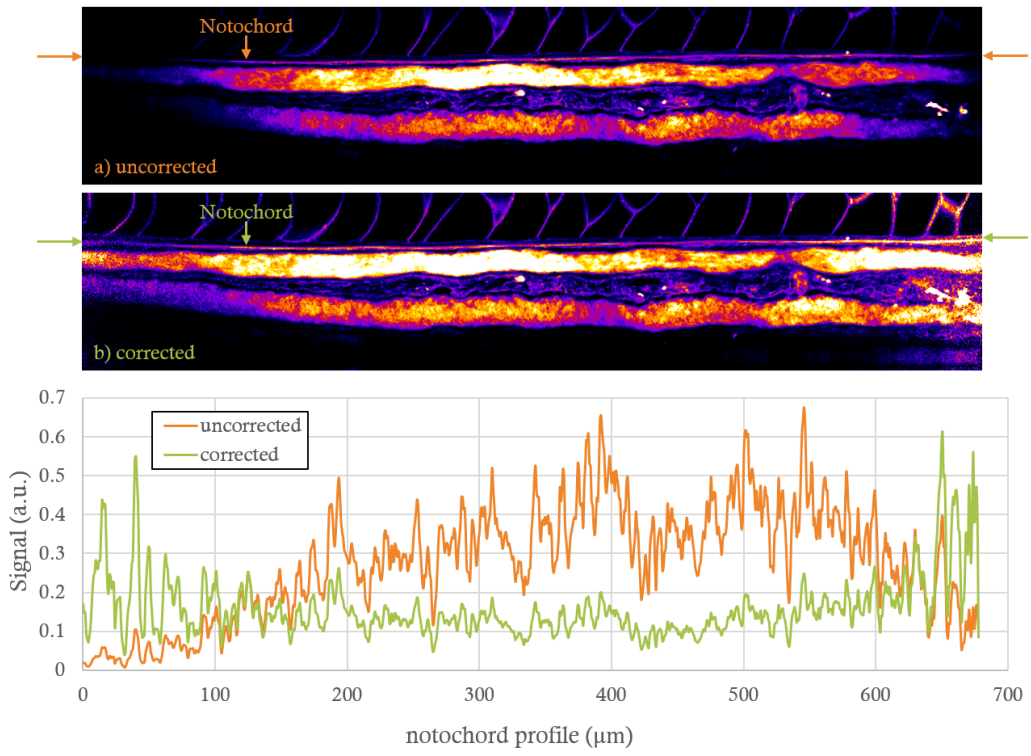

Figure 4.36: TSFG signal along the notochord edge of a 2dpf zebrafish embryo, before (a) and after (b) flat field correction.

Blood vessel and RBC segmentation

We then calculated the sum of the on-resonance images ($S_{401} + S_{433}$), and the $S_{\text{enhancement}}$ time series $(S_{401} + S_{433})/S_{373}$ as previously mentioned. We calculated two different binary

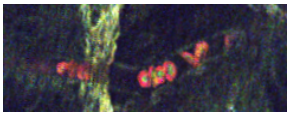

masks from this data. A vessel mask was obtained by computing the time projection of the $S_{\text{enhancement}}$ image series and applying a binary threshold (Figure 4.37.b-c). A RBC mask was obtained at each time point by first multiplying the $S_{\text{enhancement}}$ time series by the vessel binary mask, then applying a binary threshold, and finally a dilation-erosion binary filter to remove isolated pixels.

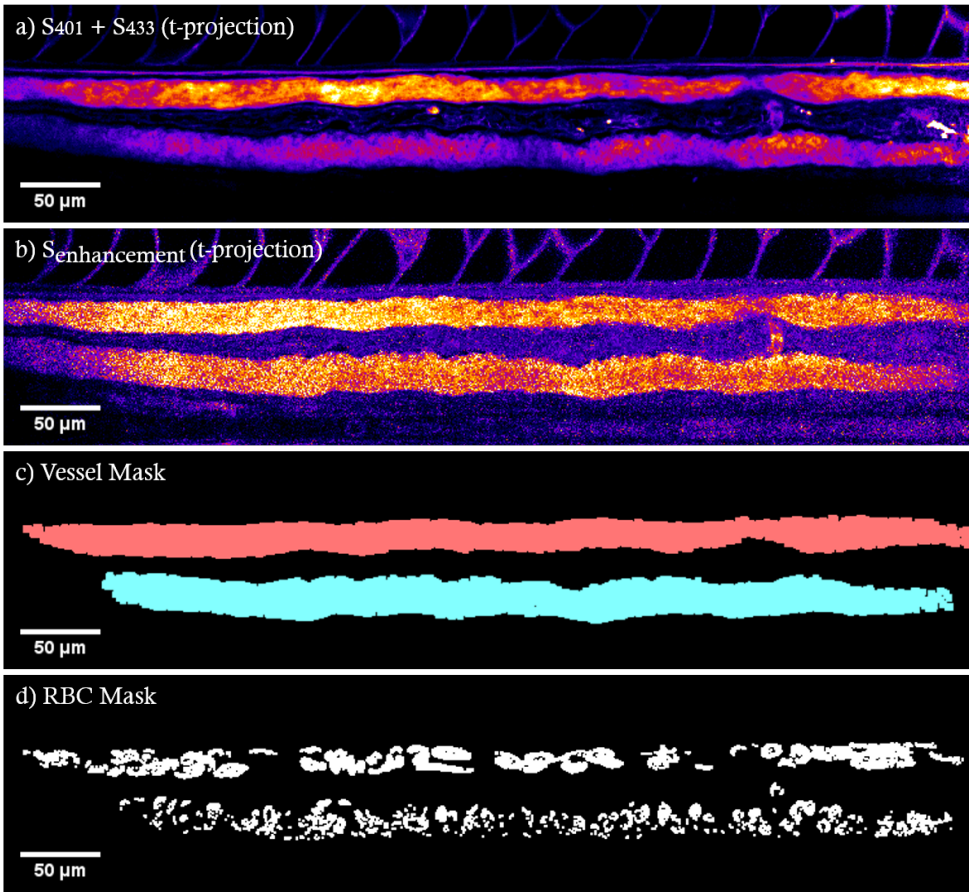

Figure 4.37: a) Time-projected sum of the on-resonance images (at 401 at 433 nm) from a series of 30 frames. b) $S_{\text{enhancement}}$ time-projected image calculated as the ratio between on-resonance and off-resonance images. c) Vessel mask obtained by applying a binary threshold to (b). Vessel identification (red for the artery, blue for the vein) is done manually. d) RBC mask for the image in Figure 4.35.

It is remarkable that RBC pixels could be automatically detected in individual frames of the time series by taking advantage of the simultaneity of the spectroscopic imaging process. To confirm the specificity of RBC detection, we compared TSFG imaging with fluorescence imaging of labelled RBCs. We imaged gata1-dsRed zebrafish embryos exhibiting red fluorescence labelling of RBCs [140]. The 2PEF signal was excited by the pump at 1045 nm and simultaneously collected on a fourth channel in epidetection (Figure 4.38.a).
The RBC mask applied to the resonant image is shown in Figure 4.38.b in fire colourmap. It is superimposed to the structural image obtained by time projection of S_{TSFG_1} (Figure 4.38.b in grey). The good correlation between the two images confirms the specificity of TSFG imaging for RBC detection based on resonant TSFG in hemoglobin.

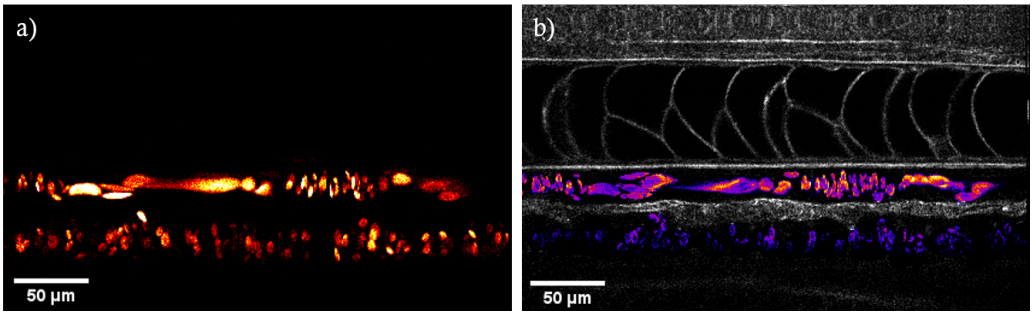

Figure 4.38: RBC segmentation in a gata1-dsRed embryo using red fluorescence from RBCs (a) and using TSFG imaging (b). This zebrafish line is not pigmentation-free and was treated with PTU (1-phenyl 2-thiourea) to remove pigments [141].

In short, we have demonstrated a novel label-free technique allowing automated segmentation of flowing RBCs and blood vessels in zebrafish embryos.
To further illustrate the potential of TSFG microscopy for blood detection, we imaged an entire zebrafish embryo. Figure 4.39 shows the three combined signals recorded in a tile-like manner over a large volume (3.53 mm x 1.40 mm x 55 µm). The image was obtained by recording a mosaic of 30 3D tiles (768 µm x 768 µm x 55 µm) and stitching them together. This preliminary demonstration suggests that the entire vascular system of the embryo could be imaged without requiring fluorescent labelling.

Figure 4.39: Mosaic image assembled from TSFG images at 373 nm (blue) and at 401 nm (green) and THG images at 433 nm (red). The image shows a z-projection of 12 different planes separated by a step of 5 µm.

Together, the results presented in this section demonstrate that TSFG microscopy can provide a label-free hemoglobin-sensitive contrast and allows automated segmentation of flowing RBCs in a living organism.

3.3 Probing RBC oxygenation in vivo

In this section we now explore the use of TSFG for probing the oxygenation state of RBCs in vivo. Similarly to the spectroscopic techniques discussed in Section 1.1.1, we want to use the spectral differences between oxy- and deoxyhemoglobin to probe its oxygenation state. According to the measured TSFG spectra from zebrafish RBCs (Figure 4.32),

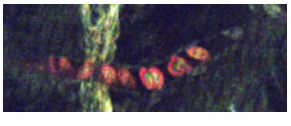

oxygenated RBCs exhibit larger signal at 401 nm than deoxygenated RBCs, and the opposite is observed at 433 nm. We therefore propose to use the ratio of these two signals as a probe of oxygenation. We define an oxygenation parameter:

$$R = \frac{S_{401}}{S_{433}} = \frac{S_{TSFG_2}}{S_{THG_2}}.$$

We expect $R_{oxy} > 1$ for oxygenated samples and $R_{deoxy} < 1$ for deoxygenated samples.

3.3.1 Oxygenation contrast in isolated RBCs

To check if the oxygenation state can be probed by TSFG microscopy, we first worked with samples exhibiting extreme hemoglobin oxygenation states. We imaged isolated zebrafish RBCs prepared as described in Section 3.1.1 in both fully oxygenated and fully deoxygenated states. These states were verified by spectrophotometer measurements before and after imaging. The MATLAB code written for blood detection was used to detect RBCs pixels in these images. For these pixels, we plotted the values of the image at 401 nm versus those at 433 nm. We then used a linear regression fit of the form $S_{401} = R \cdot S_{433}$ to determine an average value of the oxygenation parameter R. Figure 4.40 shows the pixels of two different RBCs extracted from the same zebrafish, and showing $R_{oxy} > 1 > R_{deoxy}$ consistently with the TSFG spectra.

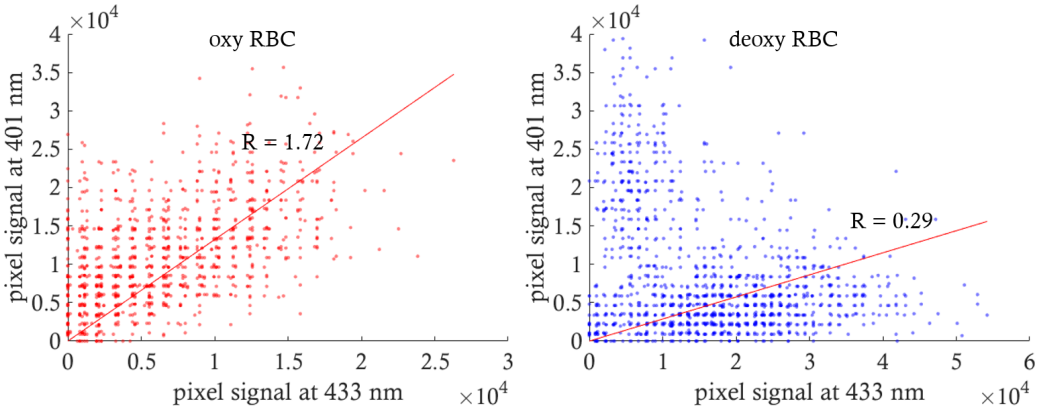

Figure 4.40: Example of the determination of the oxygenation parameter R for an oxygenated RBC (left) and a deoxygenated RBC (right). The pixel values at 401 and 433 nm are scattered on the plot. The cells were segmented with an individual mask using the resonant part of the signal as in Section 3.2.

This analysis was performed on 6 oxygenated and 8 deoxygenated individual RBCs *ex vivo*, all of them extracted from the same zebrafish. The R factors for all those measurements are represented in Figure 4.41.
Significant differences are observed between fully oxygenated and fully deoxygenated isolated RBCs. This result confirms that the oxygenation state of hemoglobin in isolated RBCs can be probed with TSFG microscopy.

3.3.2 Oxygenation contrast in normoxic 2dpf zebrafish

After this verification that TSFG imaging can probe the oxygenation state of isolated RBCs, we tried to extend this approach to *in vivo* imaging. We present here its first application to live 2dpf zebrafish embryos. We used TSFG imaging to estimate R in RBCs

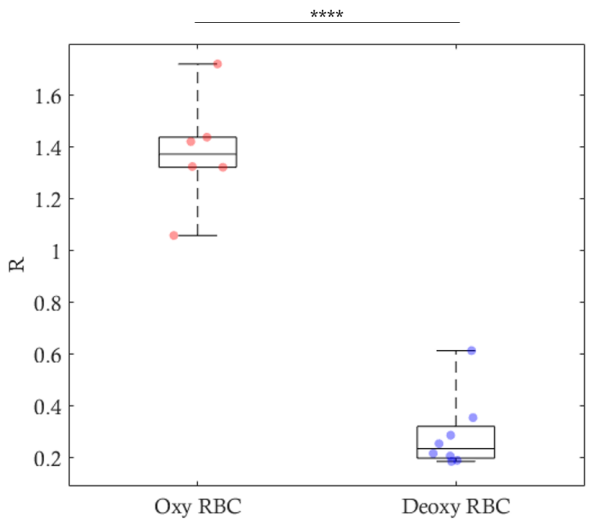

Figure 4.41: Results of oxygenation parameter measurements in 6 and 8 individual RBCs from the same zebrafish, prepared on fully oxygenated and fully deoxygenated states, respectively. Each point corresponds to the R parameter measured on the pixels from a segmented RBC as shown in Figure 4.40. The linear spectrum of each sample, measured before and after imaging, is equal to those in Figure 4.32. The p-value represented by the stars is the result of an unpaired, two-tailed, Whelch's t-test (unequal variances t-test): $p < 0.0001$.

flowing through the dorsal aorta (DA) and the posterior cardinal vein (PCV), anticipating that their oxygenation states could be different. Twenty embryos were mounted in agarose under normal oxygenation conditions as described in Section 3.2. Several t-stacks were acquired for each embryo in wavelength mixing mode and processed with the blood detection strategy. The RBC masks were combined with the vessel masks to identify all the pixels corresponding to RBCs in each vessel.

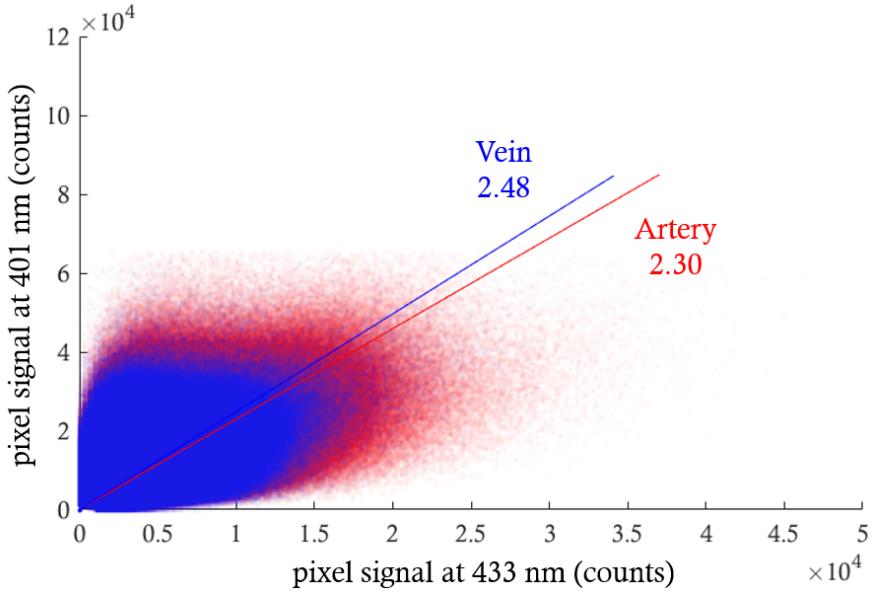

Figure 4.42: Oxygenation analysis for 20 embryos in normoxic conditions. The slopes account for the ensemble of the samples.

The ensemble of pixels measured for the DA and the PCV are shown as a scatter plot

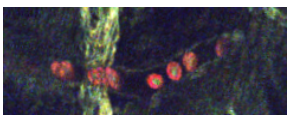

in Figure 4.42, where the values at 401 nm in the vertical axis are plotted against the values at 433 nm on the horizontal axis. The different oxygenation parameters (R values) of individual fish analysis are represented in Figure 4.43.

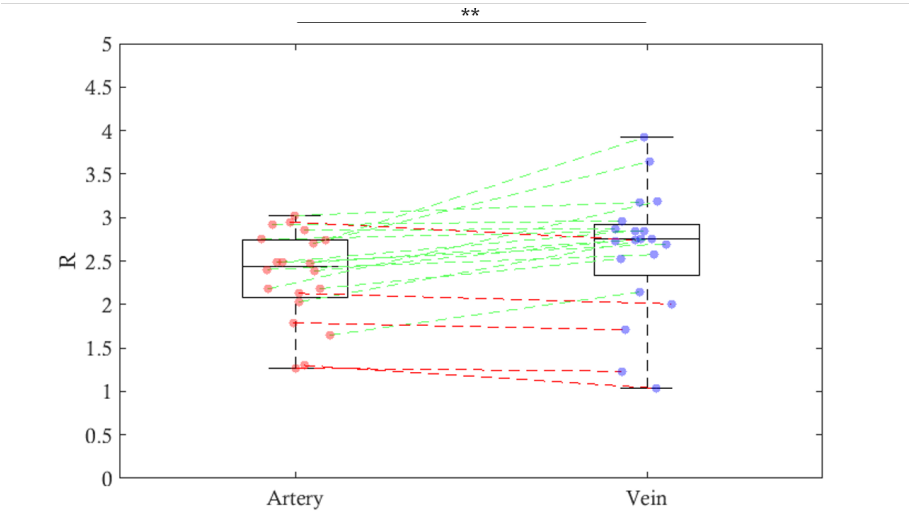

Figure 4.43: Results of oxygenation parameter measurements on 20 embryos. The dashed lines link the value of R for the artery and the vein of the same embryo (green for those following the average behaviour, red for the others). The p-value represented by the stars is the result of a paired, two-tailed, Student's t-test: $p < 0.01$.

DA and PCV were chosen as the positions in the vascular system in which we expected differences in oxygenation to be maximized. Indeed, the DA carries oxygenated blood from the heart to the body and the PCV carries deoxygenated blood flowing back to the heart. However, our result suggests that the oxygenation difference between the artery and the vein is in fact weak at this early stage of development. The statistical analysis done on the data represented in Figure 4.43 indicates that the differences we measured are significant and that the vein oxygenation state is slightly higher than that of the artery. To our knowledge, there is no previous measurement of this difference in oxygenation with a spectroscopic method, so a comparison is not possible. However, a weak difference between the oxygenation measured in the PCV and the cardiac region was reported using PLIM sensors [104]. This result can be explained by the fact that oxygenation at this stage happens mostly by diffusion through the tissues as discussed in Section 1.1.1. As a consequence, no strong difference between DA and PCV is observed. In addition, since the vein is located closer to the embryo surface, it can be slightly more oxygenated than the artery.

We measured that the R values in DA and PCV are high and close to those obtained in fully oxygenated isolated RBCs (Figure 4.41). We therefore conclude that hemoglobin in zebrafish embryos at this early stage is highly oxygenated. This observation is consistent with published data [101, 104].

3.3.3 Oxygenation dynamics in zebrafish embryos: cardiac arrest experiment

To investigate if TSFG microscopy can detect changes in RBCs oxygenation *in vivo* we attempted to disrupt oxygenation by blocking blood circulation. We induced transient reversible cardioplegia (cardiac arrest) in zebrafish embryos using a tricain overdose [142].

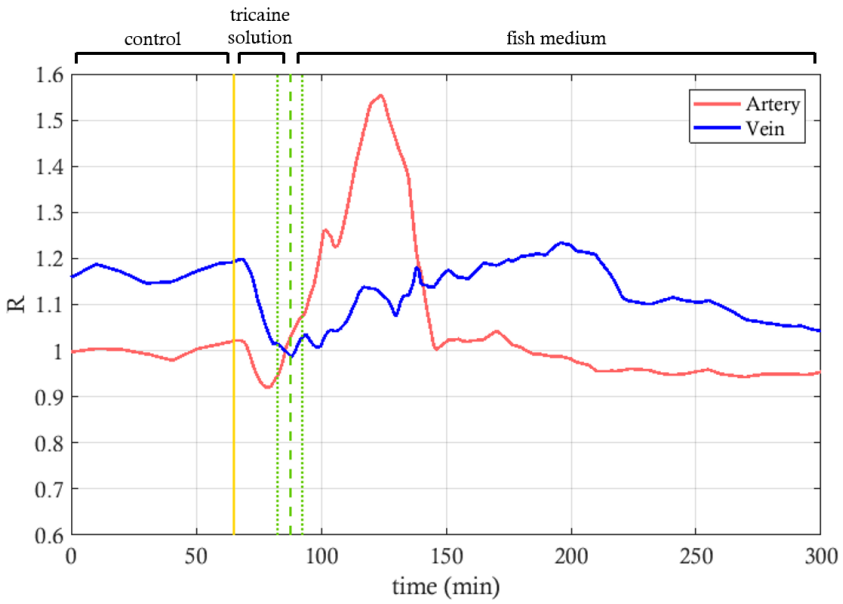

Figure 4.44: Artery and vein oxygenation evolution along time (left) and the difference between the two (right), average of 4 embryos, normalized to the artery control oxygenation parameter. The yellow vertical line indicates the moment when we induced an overdose of tricain (common for all the samples). The blue vertical line indicates the average time at which the sample is washed with fish medium without tricaine. The two blue lines on the sides indicate the shortest and the longest time on tricaine at 0.2 %.

The embryos were first mounted in normal conditions. Then, after one hour of imaging (an image series every 5 min) the immersion medium was replaced by a highly concentrated tricaine solution (0.2 %). After ≈ 20 min the blood flow stopped due to cardiac arrest and the tricaine was washed out using fish medium. Imaging continued as the heart beat and the normal blood flow recovered. Cardiac arrest did not exceed 30 min in any case and the embryo was imaged for several hours. The R values of the two vessels during these cardiac arrest experiments are presented in Figure 4.44 (average result of 4 embryos).

As anticipated, cardiac arrest induced significant changes in R and on the oxygenation state. However, the observed variation is difficult to interpret. Indeed, we first detected a weak decrease in R during cardiac arrest. However, the artery exhibited a strong increase in R after recovery of heart beat and blood flow. About 1 h later, the oxygenation of the artery returned to its baseline. This behaviour may be due to oxygen diffusion. Although this experiment indicated that TSFG microscopy probes dynamic changes in the RBCs, the response to a cardiac arrest is indirect and not described in the litterature. We therefore decided to implement a simpler hypoxia assay.

3.3.4 Oxygenation dynamics in zebrafish embryos: hypoxia experiment

To induce a strong deoxygenation of hemoglobin in live zebrafish embryos, we imaged embryos under hypoxia. This choice was motivated by the fact that oxygenation in early embryos is dominated by diffusion rather than by physiology.
2dpf zebrafish embryos were mounted as in Section 3.2 except that we used a specific sealed chamber (Figure 4.45). The bottom of the dish had a shallow circular step constituting a small well of ≈ 100 µL where the embryo and the agarose fit easily. In these experiments,

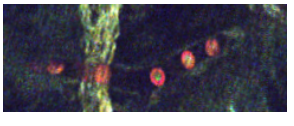

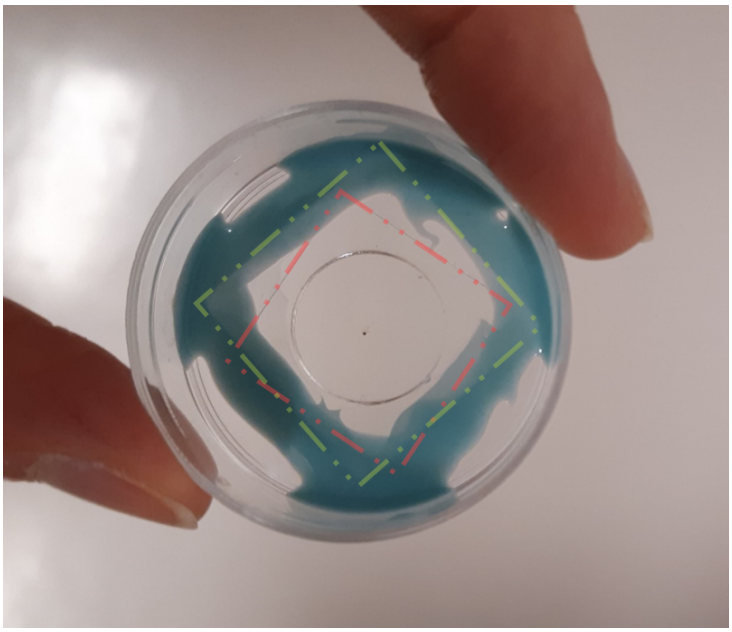

Figure 4.45: Embryo mounted on a sealed lab-made chamber to induce hypoxia. We can see the eye of the embryo as the small black point in the middle of the sample. The red dashed square indicates the bottom glass belonging to the dish and the green one indicates the one added after mounting the fish. The blue silicon paste is also visible.

the top of the well was covered with a coverglass and sealed with silicone (twinsil speed, *Picodent*) while the agarose was still liquid.
Less than ten minutes after mounting, the imaging session started with a t-stack of 30 images of a single plane within the vessels region. This measurement was repeated every 5 minutes. After several hours in the sealed chamber (ranging from 97 to 423 min depending on the embryo), the sample was taken away from the microscope. The top coverglass of the chamber was removed to stop hypoxia and recover normoxia. The dish was filled with mounting medium and placed back under the microscope, with the embryo still embedded in agarose to avoid movement. The same ROI was found and imaged again. The time between the last hypoxia image and the first one after opening the chamber was less than 15 min.

From the recorded images, we extracted the oxygenation parameter R for both the vein and the artery. The measurement of R along the whole experiment is shown in the case of one embryo in Figure 4.46. The values of R for control, hypoxia and recovery time points are summarized for 9 embryos in Figure 4.47.
We observed that the R values for the vein and the artery were very close at the beginning of the experiment (Figure 4.46), consistently with the experiments in normoxic embryos (Section 3.3.2). A significant oxygenation decrease (of almost 50 %) was observed in the artery and suggests that the limited oxygen supply inside the small chamber volume was being consumed by the embryo. After chamber opening, we observed a fast recovery (up to $\approx 90\,\%$) of the oxygenation parameter. This suggests that RBCs recover their oxygenation state very rapidly after hypoxia. Such a fast recovery is consistent with [104].
Figure 4.48 shows the evolution of the S_{401} and S_{433} signals independently during the hypoxia experiment. This analysis confirms that the two signals change in opposite directions during the experiment, and that our ratio-metric analysis is an effective way to

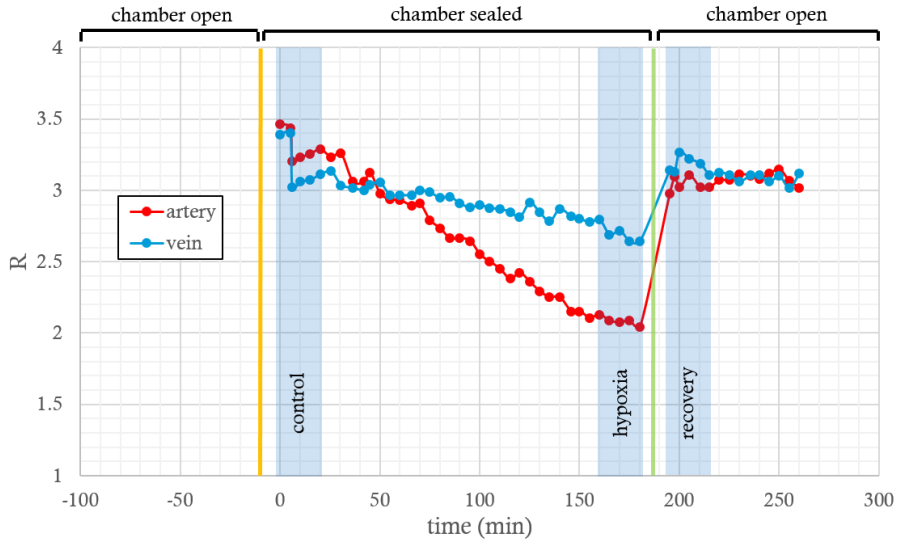

Figure 4.46: Oxygenation parameter dynamics of a 2dpf zebrafish embryo along $\approx 4\,\mathrm{h}$. The yellow vertical line at $t = -10\,\mathrm{min}$ indicates the moment of sealing the chamber and the green vertical line at $t = 182\,\mathrm{min}$ indicates the moment when the chamber opens.

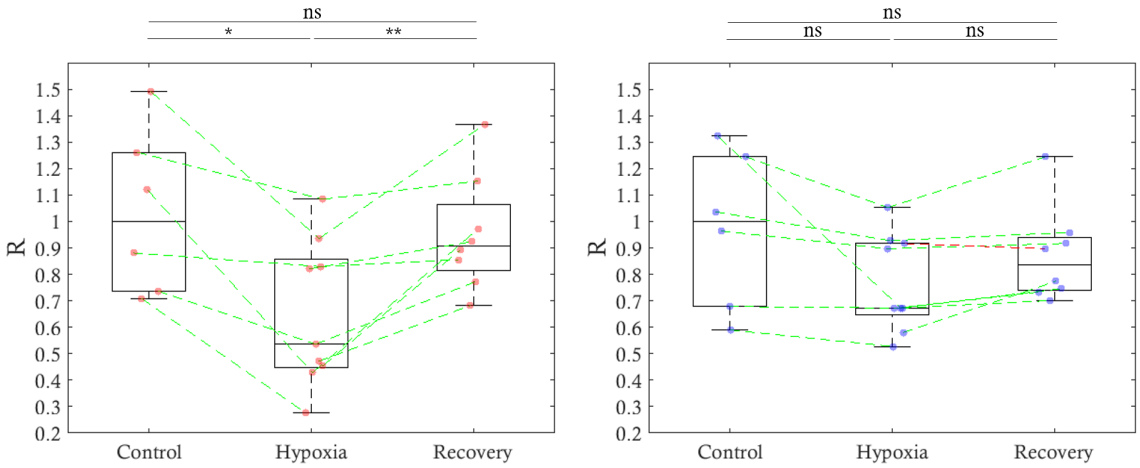

Figure 4.47: Oxygenation parameter for control, hypoxia and normoxia recovery time points defined in Figure 4.46 measured on zebrafish embryos (artery, left and vein, right). Because the experiments on different zebrafish were parallelized, only specific time points were acquired for several fish instead of imaging through the whole dynamics of the process. The values are an average of several points spanning 25 min at maximum, and the control oxygenation median was normalized to 1. The test performed here was a mixed-effects model, more capable of dealing with missing data as compared to ANOVA tests.

maximize the oxygenation contrast in such dynamic experiments.

Together, the experiments presented in Section 3.3 provide promising results towards functional TSFG microscopy. We have shown that this strategy can probe the oxygenation state of hemoglobin in isolated RBCs *ex vivo*. Although it was not straightforward to implement a first demonstration *in vivo*, we successfully detected significant variations of the hemoglobin oxygenation state in the artery of live early embryos under hypoxia.

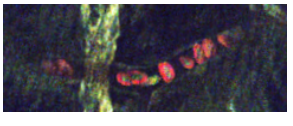

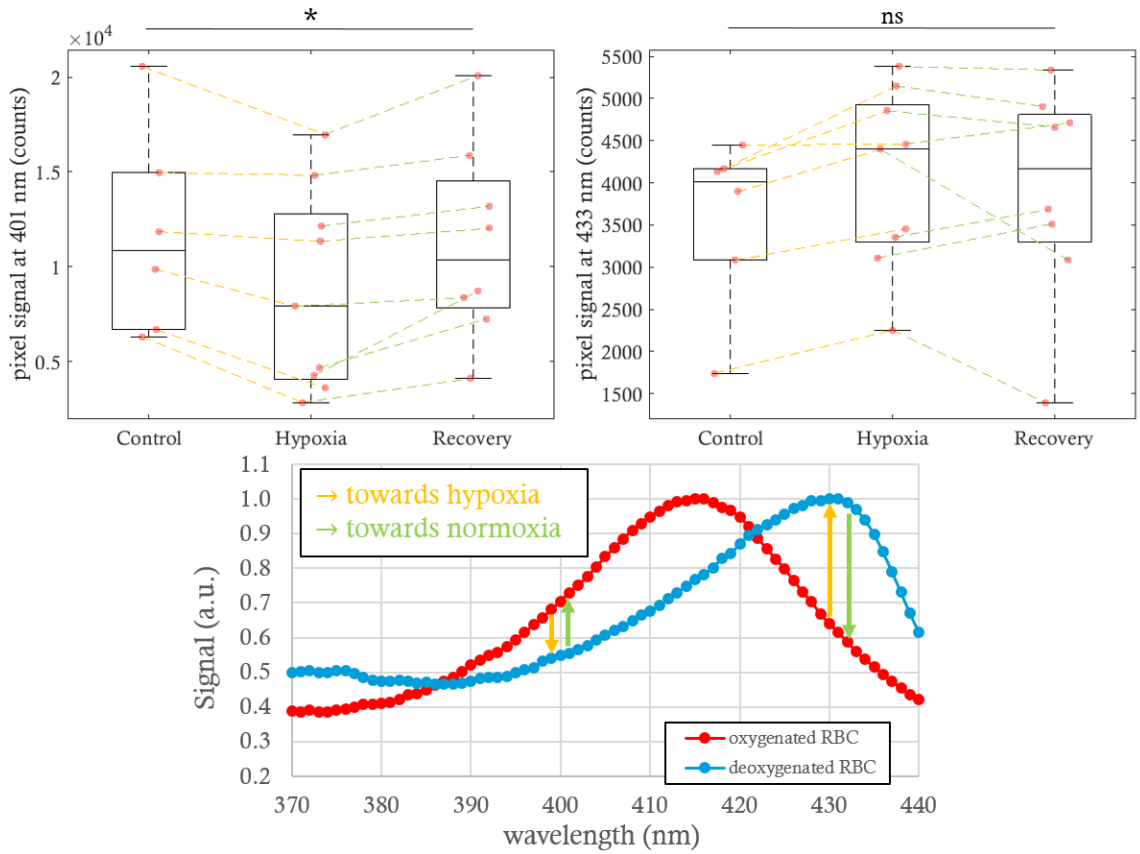

Figure 4.48: Absolute Signal at 401 (top left) and 433 nm (top right) measured on the artery. The star indicates $p < 0.05$ for a one-way, paired ANOVA test. Linear fully oxygenated and fully de-oxygenated spectra in zebrafish RBCs (bottom). The arrows indicate the transition from one state to the other.

3.4 Deep-tissue blood imaging with TSFG

Finally, we transposed TSFG microscopy to deep-tissue imaging by implementing this new modality on the OPA-based microscope presented in Chapter 2. We adapted the method to epidetection, and imaged the brain of a live adult zebrafish in collaboration with Nicolas Dray (Institut Pasteur).

In this microscope, the pump and OPA wavelengths are centered at 1030 nm and 1300 nm respectively. The resulting TSFG wavelengths are then: $\lambda_{TSFG_1} = 370$ nm and $\lambda_{TSFG_2} = 402$ nm. The narrow band detection filters used on the OPO system were therefore also suited to collect these signals. As the sample is thick and not transparent, we collected the backscattered forward-directed signals.

A male *casper* mutant (without pigmentation) was maintained in 0.2 % tricaine solution. After a few minutes, the fish stopped moving and was mounted in a dish also filled with tricaine solution. Two pieces of foam attached to the dish held it from both sides and kept its head up for imaging. A picture of this setup is shown in Figure 4.49. With the help of an IR camera installed on the microscope, we located the position of the telencephalon, a region of the forebrain presenting a relatively flat surface which limits optical aberrations.

To confirm whether the strong hemoglobin-specific resonance of TSFG could be detected as in the other microscope, we first imaged superficial blood vessels that irrigate the skin covering areas above the skull. An example is shown in Figure 4.50.

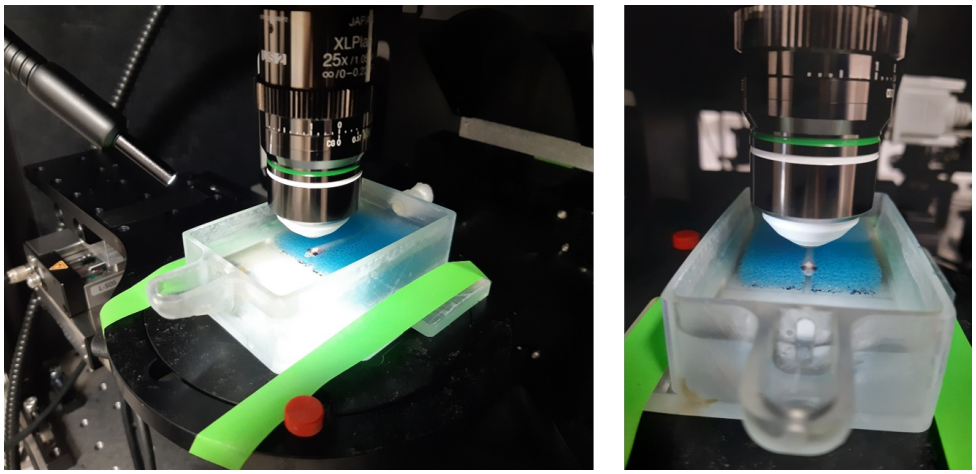

Figure 4.49: Pictures of an adult zebrafish mounted for imaging. The brain is kept as horizontal as possible using the foam sample holder while completely immersed in the tricaine solution.

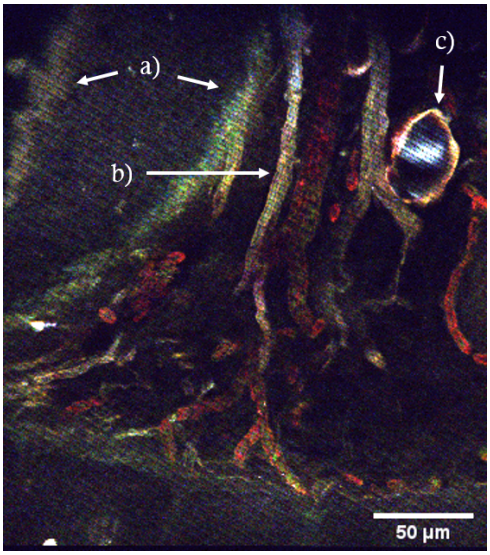

Figure 4.50: Sub-skin vessels (z ≈ 50 µm) with wavelength mixing contrast. Red: THG at 433 nm, green: TSFG at 402 nm, blue: TSFG at 370 nm.

S_{THG_2} (at $\lambda = 433$ nm shown in red in Figure 4.50) appears specific to blood vessels confirming the spectral resonance. S_{TSFG_2} (at 402 nm, in green) is localized on the nuclei and membrane of the RBCs. In the images obtained with this microscope, we notice weaker resonance of hemoglobin at this wavelength compared to the results obtained on the OPO system (described in Section 2.1). This might be due to broader spectral bandwidths associated to shorter temporal profiles. Some other structures are visible. Those appearing white in the image present the same amount of signal in the three channels, corresponding to non-resonant signal. This is the case of skull interfaces (Figure 4.50.a) or myelin fibers (Figure 4.50.b). A lipid droplet presenting strong interface signal and characterized by the presence of blue endogenous fluorescence is also visible (Figure 4.50.c).

We then demonstrated RBCs and blood vessel segmentation in thick samples. Since S_{TSFG_2} at 402 nm exhibited reduced resonance, when building the vessel mask, this image was used as non-resonant signal together with S_{TSFG_1} at 370 nm. We defined here a resonance enhancement image as:

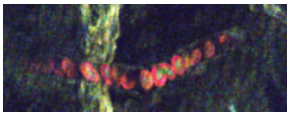

$$S_{\text{enhancement}} = \mathrm{S}_{433}/(\mathrm{S}_{370} + \mathrm{S}_{402}) = \mathrm{S}_{\mathrm{THG}_2}/(\mathrm{S}_{\mathrm{TSFG}_1} + \mathrm{S}_{\mathrm{TSFG}_2}). \tag{4.16}$$

Figure 4.51 presents blood vessel segmentation from other non-resonant signals such as skull interface (a) or myelinated nerve fibers (b).

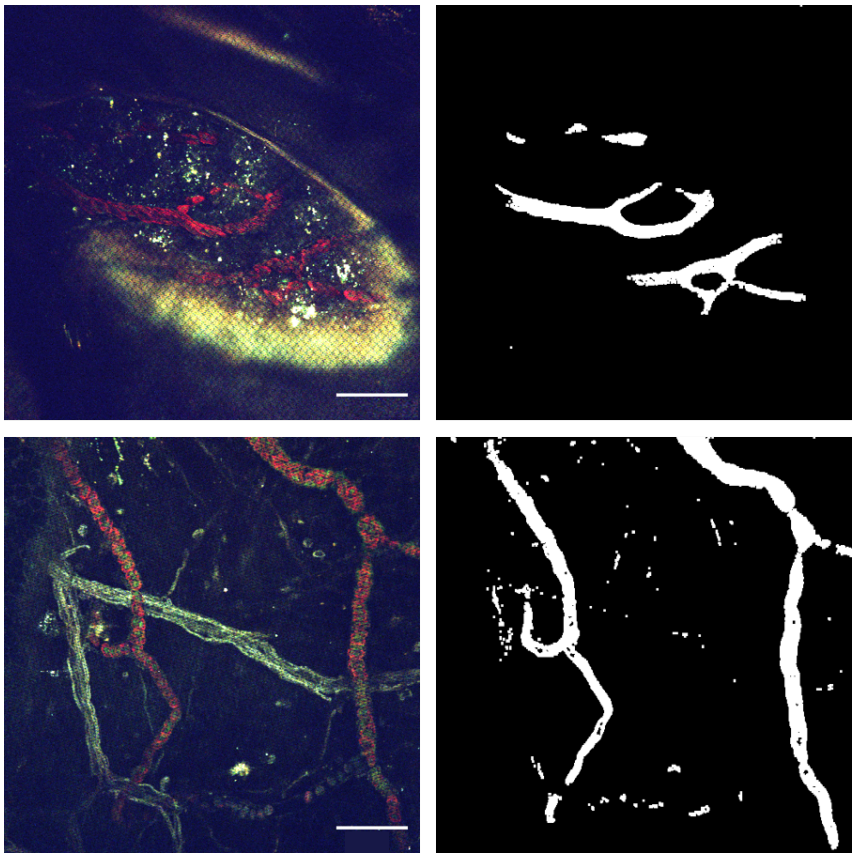

Figure 4.51: Blood vessel segmentation using TSFG microscopy. The signal from non-resonant structures is filtered out when calculating $S_{\text{enhancement}}$. Red: THG at 433 nm, green: TSFG at 402 nm, blue: TSFG at 370 nm. Scale bar 50 µm.

To build a RBCs mask from the segmented vessel regions we can either use the definition in Equation 4.15 which considers TSFG_2 at 402 nm as mostly resonant (Figure 4.52.a), or the one in Equation 4.16, which considers it mostly non-resonant (Figure 4.52.b). In the first case, the mask includes whole RBCs whereas the second case allows segmentation of body cells without the nuclei. In the bottom right side of this thesis we have included a time lapse of this region of interest as a flipbook.
All these images were recorded on the first ≈ 150 µm under the surface and with typical average powers: $P_P \approx 2$ mW and $P_{OPA} \approx 10$ mW. These power levels are compatible with *in vivo* imaging.

In what follows, we present images obtained at larger imaging depths. A large depth of the telencephalon was imaged as a series of 12 successive z-stacks for which the excitation power was increased with imaging depth. The step along z was $\Delta z = 2$ µm and the maximum imaging depth was ≈ 700 µm under the skin surface.

Image processing was performed as follows. We first linearised the images according to the detection response calibrated in Chapter 2 (see Figure 2.20 in Section 4.2.3). Then, we

Figure 4.52: 30 µm deep image of RBCs flowing through a blood vessel and the corresponding RBCs mask built automatically with MATLAB code: option including the nuclei (center) and option without the nuclei (right). Red: THG at 433 nm, green: TSFG at 402 nm, blue: TSFG at 370 nm. The specificity of this contrast to hemoglobin highlights RBCs in red and green while the nervous structures appear in white. Scale bar 50 µm.

normalised the 12 successive z-stacks by the excitation power according to the dependences of each signal studied in Section 2.3.1. The resulting image stack exhibited an exponential decay for each signal with imaging depth (Figure 4.53, left). This profile was then fitted with an exponential model (each channel separately) of the form $S = S_0 * exp(-3z/ls)$ and smoothed to compensate for signal discontinuities caused by experimental uncertainties on the excitation power or imaging depth (Figure 4.53, right).

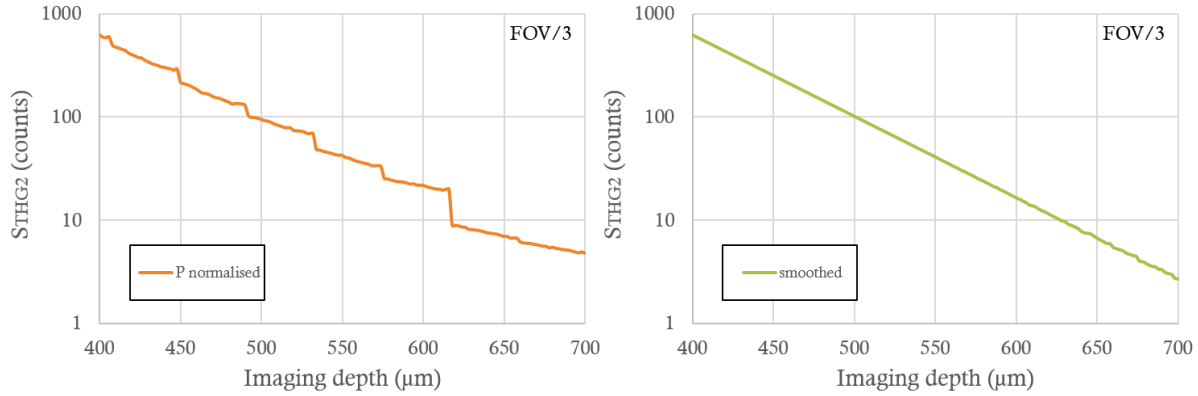

Figure 4.53: Axial profile of S_{THG_2} at 433 nm, averaged on the central third of the field of view (left). The same profile after being smoothed to an exponential decrease (right).

The l_s parameter of the fit can be interpreted as a rough estimate of the scattering length (Assuming a homogeneous signal, constant effective NA with depth, and no absorption or aberrations). We estimated ls to be in the range 130 - 160 µm. This value indicates the rate at which the laser power should be increased in depth to keep a constant detected signal. Moreover, it can be used to flatten the signal profile in depth (Figure 4.54).

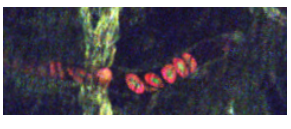

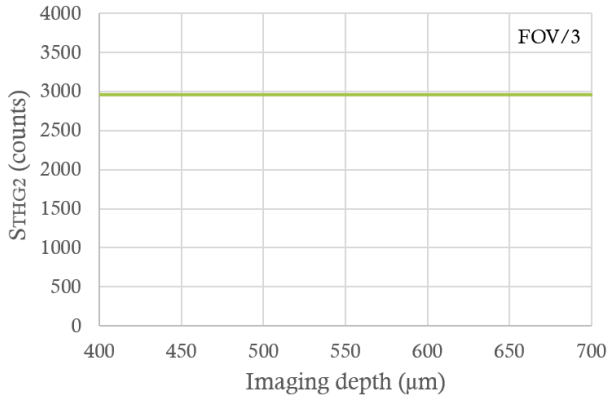

Figure 4.54: Axial profile of S_{THG_2} at 433 nm after flattening correction averaged on the central third of the field of view.

Finally, a z-stitching of the 3D tiles was performed through 3D registration using rigid body transformations (Figure 4.55.a presents a xz re-sliced view). The two interfaces of the skull are visible at $z \approx 180\,\mu m$. The figure also shows four xy images with specific details. They confirm that individual RBC can be distinguished at an imaging depth of 398 and 500 µm through skull. Some white (non-resonant) structures are also visible in the telencephalon, probably corresponding to myelinated fibers.
Blood vessels were detected at least up to imaging depths of $\approx 600\,\mu m$ (Figure 4.55.d). Myelinated fibers were detected at a depth of $\approx 672\,\mu m$ (Figure 4.55.e). The maximum powers used at deeper planes were: $P_P = 61.15\,mW$ and $P_{OPA} = 74\,mW$, adding to a total of 135 mW, which remains compatible with *in vivo* imaging.
Finally, in Figure 4.56 we present volume renderings of the three independent signals and a composite. The complementarity of these images is well illustrated in the composite, where RBC and other structures can be distinguished thanks to their different "TSFG ratios".
Finally, we were able to automatically detect RBCs by using these combined images. In Figure 4.57.a we present the result of the operation $S_{THG_2} - S_{TSFG_2}$. This method proved more straightforward for this dataset than the one described in Equations 4.15 and 4.16 due to the comparatively strong RBC signal values in the resonant stack, and low background values around the telencephalon. Away from the brain surface, the operation in Equation 4.16 provides a very efficient detection of individual RBCs even at large depths (Figure 4.57.b).
In conclusion, we have implemented our colour TSFG imaging modality on an OPA-based microscope also adapted for 3P microsocpy. We demonstrated that hemoglobin specific imaging of blood vessels and RBCs is possible deep inside the brain of a live adult zebrafish.

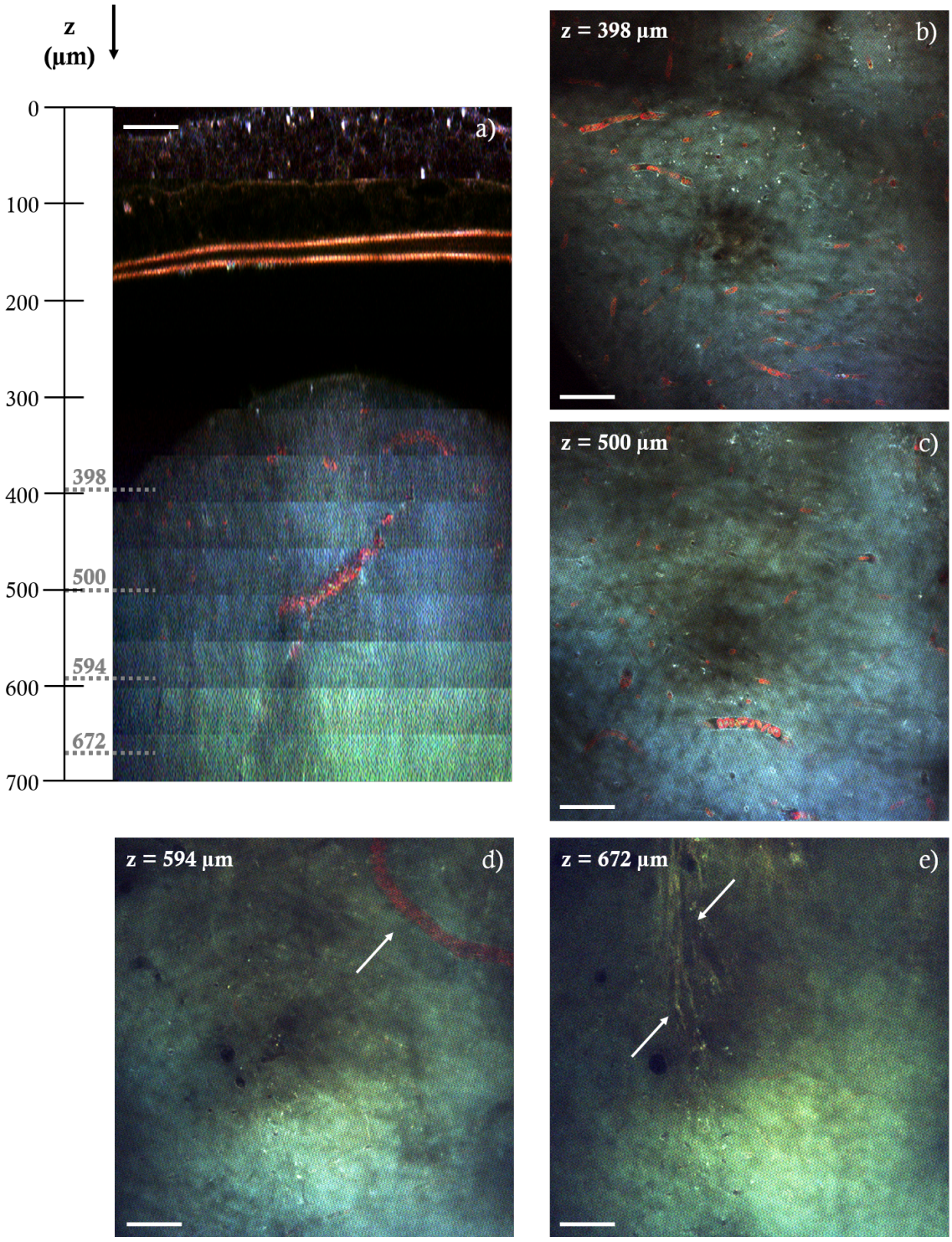

Figure 4.55: Resulting z-stack acquired on the telencephalon after the discussed corrections. Axial xz view (a) and slices xy at 398 (b), 500 (c), 594 (d) and 672 µm (e). Red: S_{THG_2} at 433 nm, green: S_{TSFG_2} at 402 nm, blue: S_{TSFG_1} at 370 nm. Scale bar 50 µm.

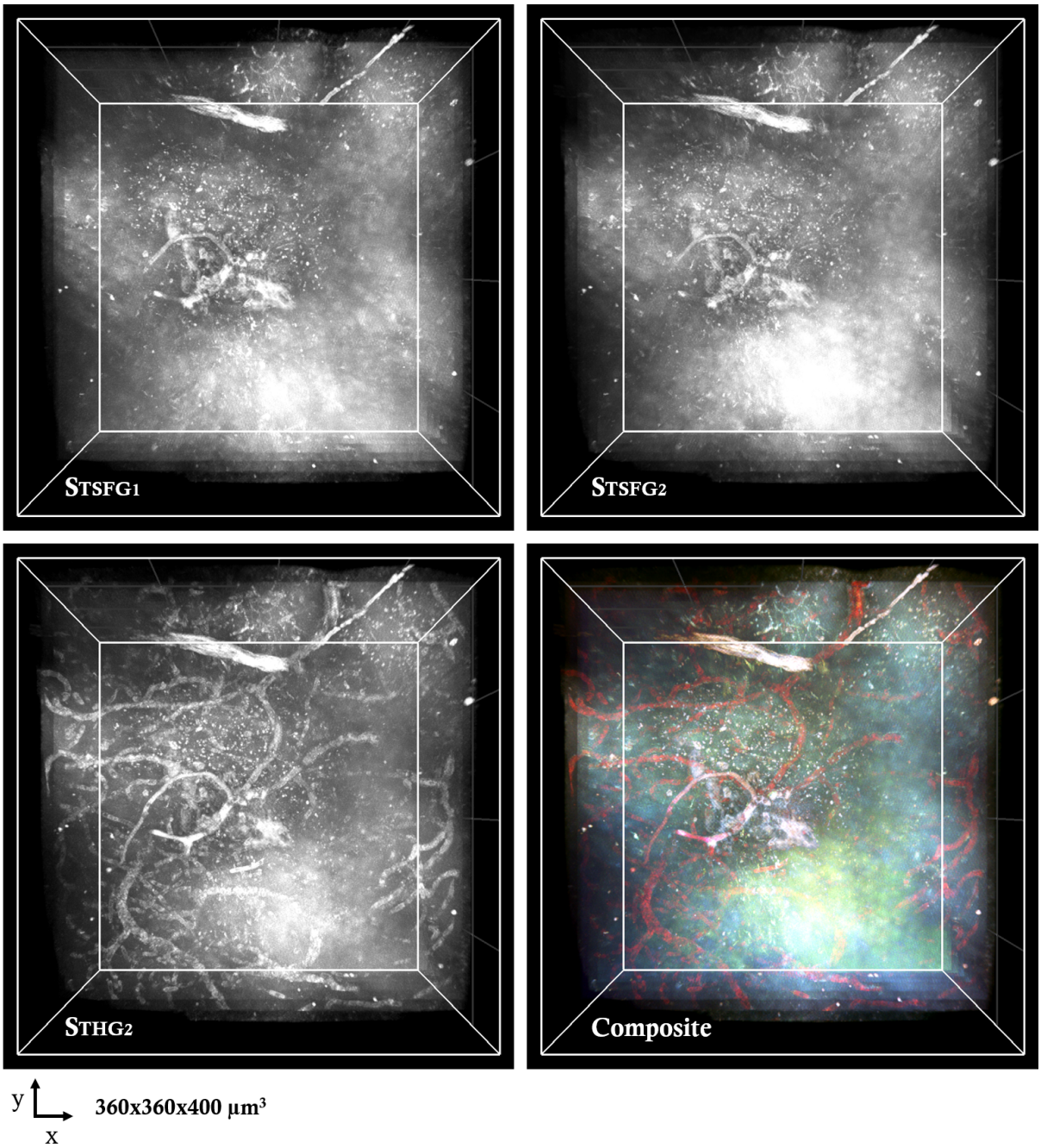

Figure 4.56: Volume views of the three independent channels S_{TSFG_1}, S_{TSFG_2} and S_{THG_2} visualised with Imaris (z-projection mode: maximum intensity). The combination of the three channels is shown in the bottom right side of the image. Red: S_{THG_2} at 433 nm, green: S_{TSFG_2} at 402 nm, blue: S_{TSFG_1} at 370 nm.

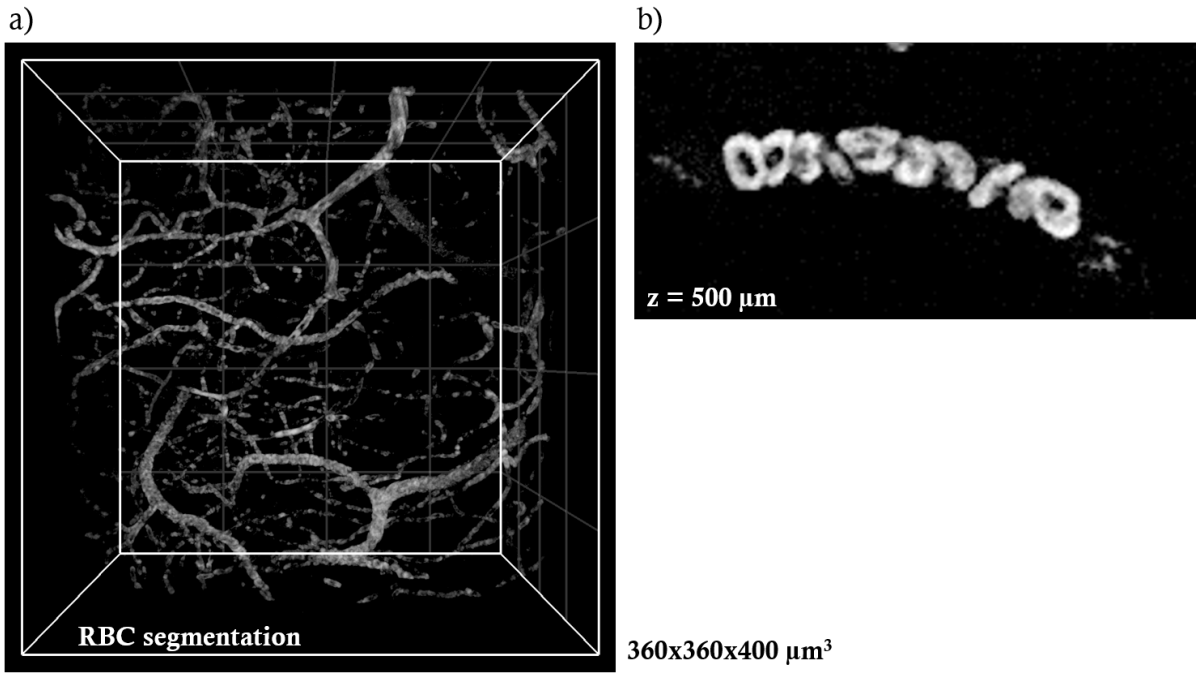

Figure 4.57: a) Segmentation of RBCs obtained with Imaris as $S_{THG_2} - S_{TSFG_2}$. A median filter of 3x3 pixels was also applied to smooth the image. b) Detail at $z = 500\,\mu\text{m}$ showing segmentation of individual RBC using Equation 4.16.

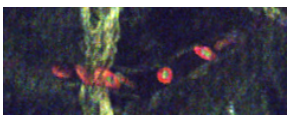

4 Conclusion and perspectives of Chapter 4

In this chapter we proposed to extend the number of observable parameters in 3P microscopy by demonstrating third-order sum frequency generation (TSFG) as a new contrast mechanism. We described an additional experimental setup, based on an OPO tunable source. We demonstrated the forward detection of TSFG signals and presented their detailed characterisation as a function of the excitation power, the pulse duration, the incident polarisation and the chromatic aberrations. Since TSFG is generated by wavelength mixing of two illumination beams, up to four signals can be obtained simultaneously and detected at different wavelengths: two THG signals and two TSFG signals (see Figure 4.7). We called TSFG microscopy or colour TSFG microscopy, the imaging method using several of these simultaneous third-order coherent signals detected at different wavelengths. Then, we confirmed that the contrast provided by THG and TSFG generated at the same wavelength is equivalent and that both exhibit a three-photon resonance enhancement due to hemoglobin. This enhancement occurs when real energy transitions exist close to the virtual electronic levels involved in THG (see Figure 4.6.a). In the particular case of hemoglobin absorption spectrum, there is a strong absorption band around 415-430 nm known as the Soret band. Therefore, we showed that both THG and TSFG signals from RBCs generated in this wavelength range are enhanced compared to other wavelengths. In this case, colour TSFG microscopy becomes a powerful tool to image RBCs since it provides several simultaneous images with different features without labelling. Indeed, by selecting de combination of wavelengths used to generate TSFG with respect to the Soret band, TSFG microscopy enables (i) imaging of moving RBCs circulating in the bloodstream with high-specificity and (ii) label-free functional imaging of blood oxygenation levels.

Specific imaging of hemoglobin and red blood cell segmentation
To demonstrate specific imaging of hemoglobin in live zebrafish, we performed TSFG imaging of blood vessels with two beams at 1045 and 1300 nm resulting in the detection of signals including resonant and non-resonant contributions (S_{TSFG_2} at 401 nm and S_{THG_2} at 433 nm), as well as purely non-resonant signals (S_{TSFG_1} at 373 nm). While the resonant signal is specifically localised in RBCs, non-resonant contributions provide contrast commonly obtained in THG microscopy, such as that from lipid bodies or myelin. We demonstrated by processing such imaging data, that it is possible to segment individual RBCs and separate them from non-resonant signals. By comparing this strategy with the imaging of fluorescently labelled RBCs, we demonstrated the high-specificity of this label-free approach. In the specific case of gata1-dsRed zebrafish line, a commonly used fluorescence strategy to label RBCs, we showed that TSFG imaging provides a higher sensitivity with fewer false negatives (RBCs without detected signal). In addition, we showed that the high temporal resolution of this strategy is an additional advantage of TSFG microscopy. Indeed, since all signals are detected simultaneously and without requiring to tune the laser wavelength, the temporal resolution is sufficient to detect RBCs moving through the bloodstream at high speed. To illustrate this capability, we first demonstrated hemoglobin specificity of TSFG microscopy by imaging RBCs in live 2dpf zebrafish embryos using an OPO system. This first study indicated that the wavelengths avail-

able in the OPA system described in Chapter 2 (1030 and 1300 nm) are well adapted for TSFG imaging of hemoglobin. Based on this observation, we used the OPA system and epidetection (presented in Chapter 2) to perform deep-tissue TSFG imaging and demonstrated label-free specific imaging of RBCs in a live adult zebrafish brain through the skull.

Functional imaging of hemoglobin oxygenation

The hemoglobin linear absorption spectrum exhibits differences in the Soret band depending on its oxygenation state, with a maximum at 415 nm when it is fully oxygenated and at 430 nm when it is fully deoxygenated. Such difference can be used to probe the oxygenation state of hemoglobin. In this chapter, we therefore explored the possibility to perform functional label-free imaging of hemoglobin oxygenation using TSFG microscopy. We first demonstrated that similar spectral differences are also present in the THG and TSFG spectra of both human and zebrafish isolated RBCs. We showed that the ratio of images acquired at specific wavelengths located on the resonant part of the spectrum depends on the oxygenation state of hemoglobin and can be used as an oxygenation indicator. Such result was first obtained by imaging isolated RBCs *in vitro* in fully oxygenated or deoxygenated state. We then further confirmed the potential of this approach by detecting a significant difference of oxygenation state when imaging circulating RBCs in live 2dpf zebrafish embryos in normal or hypoxic conditions. To further explore the sensitivity of this approach, we compared measurements performed in the artery and the vein of the embryo in normoxic conditions. We observed a higher oxygenation state in the vein than in the artery. Such surprising result could be due to the fact that at this very early stage of development and due to the small size of the embryo, oxygen transport is achieved by diffusion through the tissues instead of convection through the bloodstream. In addition, we performed experiments of transient cardiac arrest. However, since the oxygenation state in the zebrafish at this early stage is not completely known, this investigation requires more experiments to reach a biological conclusion.

Discussion and perspectives

Considering the functional application of TSFG microscopy presented here, one could think a simpler system using only THG signals with two excitation beams at 1200 and 1300 nm and without requiring wavelength mixing. Indeed, it would provide equivalent signals to TSFG using 1045 and 1300 nm to perform oxygenation probing. However, our strategy based on TSFG has several important advantages. First, the simultaneous combination of 1045 and 1300 nm beams is easier to obtain with available laser sources. Indeed, 1045 nm is the wavelength of the pump laser used to generate higher wavelength beams in most OPO and OPA systems. In addition, as can be seen in Figure 1.23, 1200 nm corresponds to a maximum of water absorption that can be avoided by using an excitation at 1045 nm. Therefore, TSFG should induce less thermal effects. In our in-depth application, the total average power used at the sample surface did not exceed 135 mW, which is comparable with the values reported in the literature [143]. Finally, TSFG also provides a fully non-resonant image that can be used for RBC segmentation in parallel to the functional imaging of the oxygenation state. Therefore, to combine the specific and the functional imaging of hemoglobin, three signals at three different wavelengths are needed, and they are

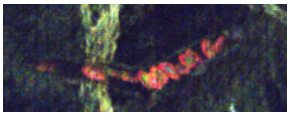

provided by the wavelength mixing scheme.
As a first perspective of this work, we plan to apply the functional imaging capability of TSFG microscopy to adult zebrafish. We will try to induce hypoxia to a zebrafish while imaging blood vessels inside its brain and see whether significant differences are observed due to the disruption of the oxygenation conditions. This would demonstrate that TSFG functional imaging can be performed in depth. A second perspective of this project is to estimate the accuracy of the oxygenation measurement obtained with TSFG microscopy. This could be done by comparing the measurements with existing phosphorescent oxygenation sensors.
To further extend the number of observable parameters, several strategies might be interesting to explore. First, we might try to extract more information from the three images acquired in TSFG microscopy. As shown in Figure 4.58, several features can be extracted from these images. The image in the bottom left shows a strong signal from myelinated fibers and other non-resonant structures. RBC segmentation is more efficient in the middle bottom image, which is the one used for blood detection in this project. The bottom right image is another image combination enhancing a signal that might be autofluorescence. Another very interesting perspective of this study is the combination of our blood oxygenation measurement with calcium indicators of neuronal activity. This combination is particularly well suited since the optimal wavelength for 3P excitation of neuronal activity markers is in the 1300 - 1320 nm range [144], which is already used in our method. For this reason, the straightforward addition of a green detection channel would allow to investigate the correlation between blood oxygenation levels and neuronal activity. In addition, THG has also been used to quantify hemodynamics by measuring blood velocity in murine cortical vessels [145, 146]. Such analysis is compatible with both oxygenation and neural activity probing. Together, it would provide a powerful strategy for functional imaging in neuroscience.
A final perspective of this work is to extend TSFG imaging to target other molecules. Absorption peaks are present in other pigments such as chlorophyll, involved in photosynthesis. Along this line, Figure 4.59 shows two TSFG images of zebrafish skin which exhibit spectroscopic contrast, possibly due to resonant effects.

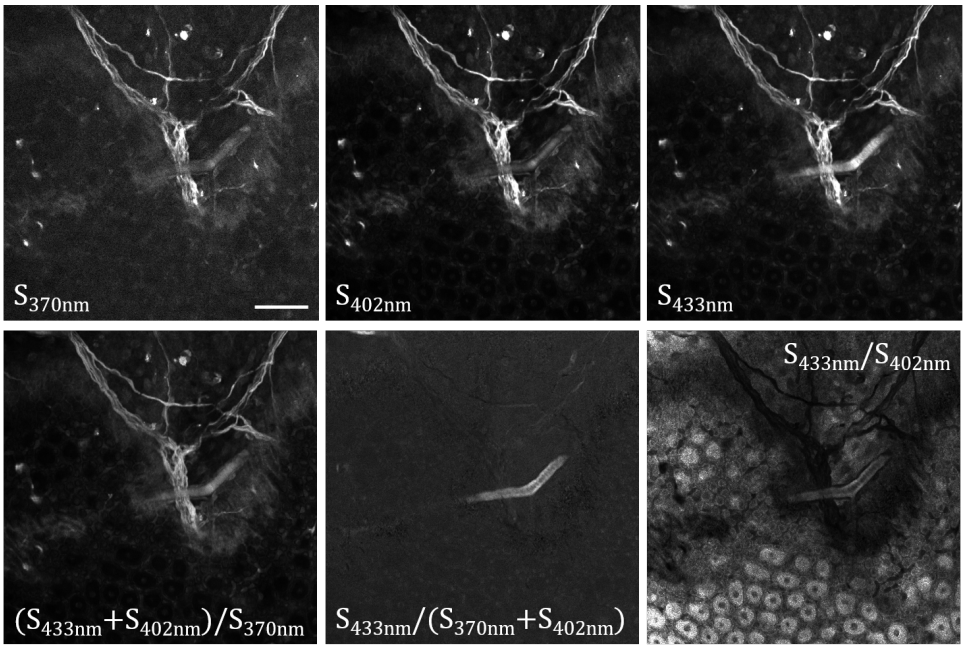

Figure 4.58: The three detected signals and three different combinations we can calculate from them. The operation performed on each combination is written in expressions where each image is represented by its wavelength. We can appreciate that each combination enhances different structures on the image. Scale bar 50 µm.

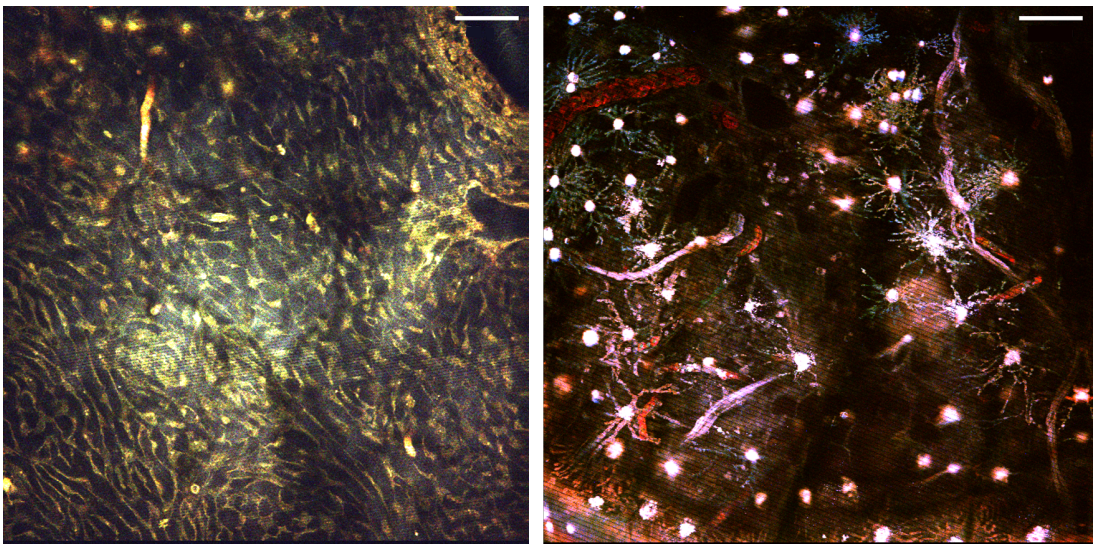

Figure 4.59: Images taken on the skin of an adult zf in which apart from RBC, some other structures present a strong signal. Red: THG at 433 nm, green: TSFG at 402 nm, blue: TSFG at 370 nm. Scale bar 50 µm.

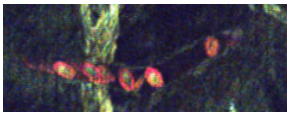

Chapter 5

General conclusion and perspectives

Three-photon (3P) microscopy is an emerging and promising technique for deep-tissue biological imaging. However, its implementation raises several experimental challenges. In this thesis work, we tackled several bottlenecks currently limiting its development: (i) the laser source and (ii) the nature and number of the detectable signals.

First, to efficiently produce third order nonlinear optical processes such as three-photon absorption or third-harmonic generation deep inside scattering samples, laser pulses of high energy and high peak intensity are required. Such pulses are typically provided by laser sources working in the MHz repetition rate range. In addition, deeper imaging is achieved by using excitation in the 1300 and 1700 nm wavelength ranges due to reduced scattering and absorption. For these reasons, the sources currently used in 2P microscopy, typically working at 80 MHz repetition rate and 900 - 1200 nm wavelength range, are not adapted for 3P imaging. In this work, we have discussed the use of an original multibeam laser source prototype developed by our collaborators at LCF. We implemented and optimized a dedicated microscope and found that despite its promising characteristics, the initial version of this source had important stability issues which prevented its use for biological applications. Based on our feedback and iterations, further technological developments resulted in a commercial product finally released at the end of 2021. We think that this type of multibeam laser source is of great interest for multicolour multiphoton applications. We note that in future versions of OPAs for in-depth microscopy, interesting additional features could be the ability to tune the repetition rate, and the integration of high-speed power control systems.

An important part of this thesis work has been devoted to the extension of the number of observable parameters in 3P microscopy. Motivated by the lack of published data on 3P excitation of blue fluorescent proteins, we investigated the possibility of using the pump beam at 1030 nm of our source for this purpose. We successfully demonstrated 3P excitation of EBFP2, mCerulean and mTurquoise2 at 1030 nm. We identified their 3P excitation regimes and reported preliminary demonstrations of 3P blue fluorescence imaging in depth. The second approach we explored is the use of spectroscopic third-order coherent contrast. We investigated the use of TSFG to perform specific and functional label-free imaging of red blood cells. Indeed, TSFG microscopy provides up to four signals at different wavelengths, which can be used for fast spectral investigation. We showed resonance enhancement of the third-order nonlinear susceptibility when imaging hemoglobin in red blood cells. We then demonstrated that this property can be exploited to ob-

tain highly specific and sensitive imaging of RBCs and their segmentation *in vivo*. This imaging strategy has been successfully applied to detect flowing RBCs deep inside an adult zebrafish brain. In addition, we also investigated the potential of TSFG imaging for functional imaging of the oxygenation state of hemoglobin. The demonstration of specific and functional *in vivo* imaging using coherent nonlinear signals is novel, and the high spatio-temporal resolution of our approach opens the way to promising applications. As a perspective, our colour TSFG imaging approach could be combined with colour fluorescence imaging taking advantage of the same excitation scheme. Considering that up to 4 spectral bands are accessible with dual-beam three-photon excitation, the additional heating associated with this illumination regime could be an acceptable inconvenient when put in balance with the gain in information content.

Overall, this work has contributed to the development and optimisation of 3P microscopy. It has demonstrated the potential of dual-beam excitation for label free specific and functional imaging based on TSFG and for colour fluorescence imaging. It should open the way to several technological and applicative developments which would further contribute to make visible the invisible.

Bibliography

[1] Jean Livet, Tamily A Weissman, Hyuno Kang, Ryan W Draft, Ju Lu, Robyn A Bennis, Joshua R Sanes, and Jeff W Lichtman. Transgenic strategies for combinatorial expression of fluorescent proteins in the nervous system. Nature, 450(7166):56–62, 2007. 5, 61, 71

[2] Margaux Schmeltz. Microscopie de second harmonique résolue en polarisations linéaire et circulaire pour caractériser l'organisation 3D du collagène. PhD thesis, Université Paris Saclay (COmUE), 2019. 5

[3] Jens L Franzen, Philip D Gingerich, Jörg Habersetzer, Jørn H Hurum, Wighart Von Koenigswald, and B Holly Smith. Complete primate skeleton from the middle eocene of messel in germany: morphology and paleobiology. PLoS one, 4(5):e5723, 2009. 5

[4] Marvin Minsky. Memoir on inventing the confocal scanning microscope. Scanning, 10(4):128–138, 1988. 5

[5] Omar E Olarte, Jordi Andilla, Emilio J Gualda, and Pablo Loza-Alvarez. Light-sheet microscopy: a tutorial. Advances in Optics and Photonics, 10(1):111–179, 2018. 6, 7

[6] Elena Remacha, Lars Friedrich, Julien Vermot, and Florian O Fahrbach. How to define and optimize axial resolution in light-sheet microscopy: a simulation-based approach. Biomedical optics express, 11(1):8–26, 2020. 7

[7] Maria Göppert-Mayer. Über elementarakte mit zwei quantensprüngen. Annalen der Physik, 401(3):273–294, 1931. 7

[8] Winfried Denk, James H Strickler, and Watt W Webb. Two-photon laser scanning fluorescence microscopy. Science, 248(4951):73–76, 1990. 7

[9] Warren R Zipfel, Rebecca M Williams, and Watt W Webb. Nonlinear magic: multiphoton microscopy in the biosciences. Nature biotechnology, 21(11):1369–1377, 2003. 8, 16, 17

[10] Nancy E. and Peter C. Meinig School of Biomedical Engineering. 2p cross-section spectra data sets. 8

[11] Delphine Débarre. Microscopie par génération de troisième harmonique appliquée à la biologie. PhD thesis, 2006. Thèse de doctorat, École polytechnique 2006. 8, 52, 94

[12] Steven L Jacques. Optical properties of biological tissues: a review. Physics in Medicine & Biology, 58(11):R37, 2013. 9, 10, 31

[13] Willy Supatto, Thai V Truong, Delphine Débarre, and Emmanuel Beaurepaire. Advances in multiphoton microscopy for imaging embryos. Current opinion in genetics & development, 21(5):538–548, 2011. 10

[14] Patrick Theer and Winfried Denk. On the fundamental imaging-depth limit in two-photon microscopy. JOSA A, 23(12):3139–3149, 2006. 10, 23

[15] Fritjof Helmchen and Winfried Denk. Deep tissue two-photon microscopy. Nature methods, 2(12):932–940, 2005. 10, 51

[16] Periklis Pantazis and Willy Supatto. Advances in whole-embryo imaging: a quantitative transition is underway. Nature Reviews Molecular Cell Biology, 15(5):327–339, 2014. 11

[17] Shmuel Roth and Isaac Freund. Second harmonic generation in collagen. The Journal of chemical physics, 70(4):1637–1643, 1979. 11

[18] Yici Guo, PP Ho, H Savage, D Harris, P Sacks, S Schantz, Feng Liu, N Zhadin, and RR Alfano. Second-harmonic tomography of tissues. Optics Letters, 22(17):1323–1325, 1997. 11

[19] Paul J Campagnola, Andrew C Millard, Mark Terasaki, Pamela E Hoppe, Christian J Malone, and William A Mohler. Three-dimensional high-resolution second-harmonic generation imaging of endogenous structural proteins in biological tissues. Biophysical journal, 82(1):493–508, 2002. 11

[20] Y Barad, Henryk Eisenberg, M Horowitz, and Yaron Silberberg. Nonlinear scanning laser microscopy by third harmonic generation. Applied Physics Letters, 70(8):922–924, 1997. 11

[21] M Müller, J Squier, KR Wilson, and GJ Brakenhoff. 3d microscopy of transparent objects using third-harmonic generation. Journal of microscopy, 191(3):266–274, 1998. 11, 94

[22] Michael D Duncan, J Reintjes, and TJ Manuccia. Scanning coherent anti-stokes raman microscope. Optics letters, 7(8):350–352, 1982. 11

[23] Andreas Zumbusch, Gary R Holtom, and X Sunney Xie. Three-dimensional vibrational imaging by coherent anti-stokes raman scattering. Physical review letters, 82(20):4142, 1999. 11

[24] Andreas Volkmer, Ji-Xin Cheng, and X Sunney Xie. Vibrational imaging with high sensitivity via epidetected coherent anti-stokes raman scattering microscopy. Physical Review Letters, 87(2):023901, 2001. 11

[25] Pierre Mahou. Microscopie non linéaire de tissus biologiques: excitation multicouleur, faisceaux de Bessel, et excitation en nappe de lumière. PhD thesis, Ecole Polytechnique X, 2012. 13

[26] Martin Oheim, Emmanuel Beaurepaire, Emmanuelle Chaigneau, Jerome Mertz, and Serge Charpak. Two-photon microscopy in brain tissue: parameters influencing the imaging depth. Journal of neuroscience methods, 111(1):29–37, 2001. 13

[27] Demirhan Kobat, Michael E Durst, Nozomi Nishimura, Angela W Wong, Chris B Schaffer, and Chris Xu. Deep tissue multiphoton microscopy using longer wavelength excitation. Optics express, 17(16):13354–13364, 2009. 13, 14

[28] David Kleinfeld, Partha P Mitra, Fritjof Helmchen, and Winfried Denk. Fluctuations and stimulus-induced changes in blood flow observed in individual capillaries in layers 2 through 4 of rat neocortex. Proceedings of the National Academy of Sciences, 95(26):15741–15746, 1998. 14

[29] Fritjof Helmchen, Karel Svoboda, Winfried Denk, and David W Tank. In vivo dendritic calcium dynamics in deep-layer cortical pyramidal neurons. Nature neuroscience, 2(11):989–996, 1999. 14

[30] M Müller, J Squier, R Wolleschensky, U Simon, GJ Brakenhoff, et al. Dispersion pre-compensation of 15 femtosecond optical pulses for high-numerical-aperture objectives. Journal of microscopy, 191(2):141–150, 1998. 14

[31] David N Fittinghoff, Andrew C Millard, Jeffery A Squier, and M Muller. Frequency-resolved optical gating measurement of ultrashort pulses passing through a high numerical aperture objective. IEEE Journal of Quantum Electronics, 35(4):479–486, 1999. 14

[32] Emmanuel Beaurepaire, Martin Oheim, and Jerome Mertz. Ultra-deep two-photon fluorescence excitation in turbid media. Optics Communications, 188(1-4):25–29, 2001. 14, 15

[33] Patrick Theer, Mazahir T Hasan, and Winfried Denk. Two-photon imaging to a depth of 1000 μm in living brains by use of a ti: Al 2 o 3 regenerative amplifier. Optics letters, 28(12):1022–1024, 2003. 14, 15, 16, 23, 24

[34] Nicholas G Horton, Ke Wang, Demirhan Kobat, Catharine G Clark, Frank W Wise, Chris B Schaffer, and Chris Xu. In vivo three-photon microscopy of subcortical structures within an intact mouse brain. Nature photonics, 7(3):205–209, 2013. 16, 22, 24, 29

[35] Tianyu Wang and Chris Xu. Three-photon neuronal imaging in deep mouse brain. Optica, 7(8):947–960, 2020. 23, 24, 31, 32, 33, 74

[36] Demirhan Kobat, Nicholas G Horton, and Chris Xu. In vivo two-photon microscopy to 1.6-mm depth in mouse cortex. Journal of biomedical optics, 16(10):106014, 2011. 23

[37] Kevin Takasaki, Reza Abbasi-Asl, and Jack Waters. Superficial bound of the depth limit of two-photon imaging in mouse brain. Eneuro, 7(1), 2020. 24

[38] Tianyu Wang, Chunyan Wu, Dimitre G Ouzounov, Wenchao Gu, Fei Xia, Minsu Kim, Xusan Yang, Melissa R Warden, and Chris Xu. Quantitative analysis of 1300-nm three-photon calcium imaging in the mouse brain. Elife, 9:e53205, 2020. 24, 31

[39] Hongji Liu, Xiangquan Deng, Shen Tong, Chen He, Hui Cheng, Ziwei Zhuang, Mengyao Gan, Jia Li, Weixin Xie, Ping Qiu, et al. In vivo deep-brain structural and hemodynamic multiphoton microscopy enabled by quantum dots. Nano letters, 19(8):5260–5265, 2019. 24

[40] Alfred Vogel and Vasan Venugopalan. Mechanisms of pulsed laser ablation of biological tissues. Chemical reviews, 103(2):577–644, 2003. 27

[41] Mengran Wang, Chunyan Wu, David Sinefeld, Bo Li, Fei Xia, and Chris Xu. Comparing the effective attenuation lengths for long wavelength in vivo imaging of the mouse brain. Biomedical optics express, 9(8):3534–3543, 2018. 27, 28

[42] Khmaies Guesmi, Lamiae Abdeladim, Samuel Tozer, Pierre Mahou, Takuma Kumamoto, Karolis Jurkus, Philippe Rigaud, Karine Loulier, Nicolas Dray, Patrick Georges, et al. Dual-color deep-tissue three-photon microscopy with a multiband infrared laser. Light: Science & Applications, 7(1):1–9, 2018. 27, 29, 37, 75

[43] David L Wokosin, Victoria E Centonze, Sarah Crittenden, and John White. Three-photon excitation fluorescence imaging of biological specimens using an all-solid-state laser. Bioimaging, 4(3):208–214, 1996. 29

[44] Stefan W Hell, Karsten Bahlmann, Martin Schrader, Aleksi Soini, Henryk M Malak, Ignacy Gryczynski, and Joseph R Lakowicz. Three-photon excitation in fluorescence microscopy. Journal of Biomedical Optics, 1(1):71–74, 1996. 29

[45] Chris Xu, Warren Zipfel, Jason B Shear, Rebecca M Williams, and Watt W Webb. Multiphoton fluorescence excitation: new spectral windows for biological nonlinear microscopy. Proceedings of the National Academy of Sciences, 93(20):10763–10768, 1996. 29, 70

[46] Dimitre G Ouzounov, Tianyu Wang, Mengran Wang, Danielle D Feng, Nicholas G Horton, Jean C Cruz-Hernández, Yu-Ting Cheng, Jacob Reimer, Nishimura Nozomi Tolias, Andreas S, and Chris Xu. In vivo three-photon imaging of activity of gcamp6-labeled neurons deep in intact mouse brain. Nature methods, 14(4):388–390, 2017. 29, 30

[47] Tianyu Wang, Dimitre G Ouzounov, Chunyan Wu, Nicholas G Horton, Bin Zhang, Cheng-Hsun Wu, Yanping Zhang, Mark J Schnitzer, and Chris Xu. Three-photon imaging of mouse brain structure and function through the intact skull. Nature methods, 15(10):789–792, 2018. 30

[48] Delphine Debarre, Nicolas Olivier, Willy Supatto, and Emmanuel Beaurepaire. Mitigating phototoxicity during multiphoton microscopy of live drosophila embryos in the 1.0–1.2 μ m wavelength range. PLoS One, 9(8):e104250, 2014. 30, 60

[49] George M Hale and Marvin R Querry. Optical constants of water in the 200-nm to 200-μm wavelength region. Applied optics, 12(3):555–563, 1973. 31

[50] Nienke Bosschaart, Gerda J Edelman, Maurice CG Aalders, Ton G van Leeuwen, and Dirk J Faber. A literature review and novel theoretical approach on the optical properties of whole blood. Lasers in medical science, 29(2):453–479, 2014. 31

[51] Kaspar Podgorski and Gayathri Ranganathan. Brain heating induced by near-infrared lasers during multiphoton microscopy. Journal of neurophysiology, 116(3):1012–1023, 2016. 31

[52] Keith Berland and Guoqing Shen. Excitation saturation in two-photon fluorescence correlation spectroscopy. Applied optics, 42(27):5566–5576, 2003. 32

[53] Murat Yildirim, Hiroki Sugihara, Peter TC So, and Mriganka Sur. Functional imaging of visual cortical layers and subplate in awake mice with optimized three-photon microscopy. Nature communications, 10(1):1–12, 2019. 32

[54] Xiaojun Cheng, Sanaz Sadegh, Sharvari Zilpelwar, Anna Devor, Lei Tian, and David A Boas. Comparing the fundamental imaging depth limit of two-photon, three-photon, and non-degenerate two-photon microscopy. Optics letters, 45(10):2934–2937, 2020. 34

[55] Robert W. Boyd. Nonlinear optics. Elsevier, Academic Press, 3. ed edition, 2008. 40, 41, 92, 93, 96

[56] RL Fork, OE Martinez, and JP Gordon. Negative dispersion using pairs of prisms. Optics letters, 9(5):150–152, 1984. 48

[57] Bernard Richards and Emil Wolf. Electromagnetic diffraction in optical systems, ii. structure of the image field in an aplanatic system. Proceedings of the Royal Society of London. Series A. Mathematical and Physical Sciences, 253(1274):358–379, 1959. 51

[58] Lukas Novotny and Bert Hecht. Principles of nano-optics. Cambridge university press, 2012. 51

[59] Marcel Leutenegger, Ramachandra Rao, Rainer A Leitgeb, and Theo Lasser. Fast focus field calculations. Optics express, 14(23):11277–11291, 2006. 51

[60] Nicolas Olivier. Mécanismes de contraste et contrôle du front d'onde en microscopie non linéaire cohérente. Thèses, École Polytechnique X, November 2009. 52

[61] Pierre Mahou, Maxwell Zimmerley, Karine Loulier, Katherine S Matho, Guillaume Labroille, Xavier Morin, Willy Supatto, Jean Livet, Delphine Débarre, and Emmanuel Beaurepaire. Multicolor two-photon tissue imaging by wavelength mixing. Nature methods, 9(8):815–818, 2012. 53, 84

[62] Nicolas Olivier, Miguel A Luengo-Oroz, Louise Duloquin, Emmanuel Faure, Thierry Savy, Israël Veilleux, Xavier Solinas, Delphine Débarre, Paul Bourgine, Andrés Santos, Nadine Peyréras, and Emmanuel Beaurepaire. Cell lineage reconstruction of early zebrafish embryos using label-free nonlinear microscopy. Science, 329(5994):967–971, 2010. 59, 90

[63] Delphine Débarre, Willy Supatto, Emmanuel Farge, Bruno Moulia, Marie-Claire Schanne-Klein, and Emmanuel Beaurepaire. Velocimetric third-harmonic generation microscopy: micrometer-scale quantification of morphogenetic movements in unstained embryos. Optics letters, 29(24):2881–2883, 2004. 60

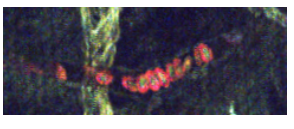

[64] Karine Loulier, Raphaëlle Barry, Pierre Mahou, Yann Le Franc, Willy Supatto, Katherine S Matho, Siohoi Ieng, Stéphane Fouquet, Elisabeth Dupin, Ryad Benosman, et al. Multiplex cell and lineage tracking with combinatorial labels. Neuron, 81(3):505–520, 2014. 61

[65] Talley J Lambert. Fpbase: a community-editable fluorescent protein database. Nature methods, 16(4):277–278, 2019. 66, 69, 72

[66] X Michalet, FF Pinaud, LA Bentolila, JM Tsay, SJJL Doose, JJ Li, G Sundaresan, AM Wu, SS Gambhir, and S Weiss. Quantum dots for live cells, in vivo imaging, and diagnostics. science, 307(5709):538–544, 2005. 68

[67] Cristian T Matea, Teodora Mocan, Flaviu Tabaran, Teodora Pop, Ofelia Mosteanu, Cosmin Puia, Cornel Iancu, and Lucian Mocan. Quantum dots in imaging, drug delivery and sensor applications. International journal of nanomedicine, 12:5421, 2017. 68

[68] Nathan C Shaner, Paul A Steinbach, and Roger Y Tsien. A guide to choosing fluorescent proteins. Nature methods, 2(12):905–909, 2005. 69

[69] Roger Y Tsien. Constructing and exploiting the fluorescent protein paintbox (nobel lecture). Angewandte Chemie International Edition, 48(31):5612–5626, 2009. 69

[70] Roger Y Tsien. The green fluorescent protein. Annual review of biochemistry, 67(1):509–544, 1998. 69

[71] Dmitriy M Chudakov, Mikhail V Matz, Sergey Lukyanov, and Konstantin A Lukyanov. Fluorescent proteins and their applications in imaging living cells and tissues. Physiological reviews, 90(3):1103–1163, 2010. 69

[72] Chris Xu, Jeffrey Guild, Watt W Webb, and Winfried Denk. Determination of absolute two-photon excitation cross sections by in situ second-order autocorrelation. Optics letters, 20(23):2372–2374, 1995. 70

[73] M Drobizhev, S Tillo, NS Makarov, TE Hughes, and A Rebane. Absolute two-photon absorption spectra and two-photon brightness of orange and red fluorescent proteins. The Journal of Physical Chemistry B, 113(4):855–859, 2009. 70

[74] Mikhail Drobizhev, Nikolay S Makarov, Shane E Tillo, Thomas E Hughes, and Aleksander Rebane. Two-photon absorption properties of fluorescent proteins. Nature methods, 8(5):393–399, 2011. 70

[75] Jason B Shear, Edward B Brown, and Watt W Webb. Multiphoton-excited fluorescence of fluorogen-labeled neurotransmitters. Analytical chemistry, 68(10):1778–1783, 1996. 70

[76] S Maiti, Jason B Shear, RM Williams, WR Zipfel, and Watt W Webb. Measuring serotonin distribution in live cells with three-photon excitation. Science, 275(5299):530–532, 1997. 70

[77] Li-Chung Cheng, Nicholas G Horton, Ke Wang, Shean-Jen Chen, and Chris Xu. Measurements of multiphoton action cross sections for multiphoton microscopy. Biomedical optics express, 5(10):3427–3433, 2014. 70, 74, 75

[78] Hongji Liu, Jiaqi Wang, Xiao Peng, Ziwei Zhuang, Ping Qiu, and Ke Wang. Ex and in vivo characterization of the wavelength-dependent 3-photon action cross-sections of red fluorescent proteins covering the 1700-nm window. Journal of biophotonics, 11(7):e201700351, 2018. 70

[79] Xiangquan Deng, Ziwei Zhuang, Hongji Liu, Ping Aiu, and Ke Wang. Measurement of 3-photon excitation and emission spectra and verification of kasha s rule for selected fluorescent proteins excited at the 1700-nm window. Optics express, 27(9):12723–12731, 2019. 70, 71, 74

[80] Michael Kasha. Characterization of electronic transitions in complex molecules. Discussions of the Faraday society, 9:14–19, 1950. 70

[81] Oksana M Subach, Illia S Gundorov, Masami Yoshimura, Fedor V Subach, Jinghang Zhang, David Grüenwald, Ekaterina A Souslova, Dmitriy M Chudakov, and Vladislav V Verkhusha. Conversion of red fluorescent protein into a bright blue probe. Chemistry & biology, 15(10):1116–1124, 2008. 72

[82] Hui-wang Ai, Nathan C Shaner, Zihao Cheng, Roger Y Tsien, and Robert E Campbell. Exploration of new chromophore structures leads to the identification of improved blue fluorescent proteins. Biochemistry, 46(20):5904–5910, 2007. 72

[83] Paula J Cranfill, Brittney R Sell, Michelle A Baird, John R Allen, Zeno Lavagnino, H Martijn De Gruiter, Gert-Jan Kremers, Michael W Davidson, Alessandro Ustione, and David W Piston. Quantitative assessment of fluorescent proteins. Nature methods, 13(7):557–562, 2016. 72

[84] Joachim Goedhart, David Von Stetten, Marjolaine Noirclerc-Savoye, Mickaël Lelimousin, Linda Joosen, Mark A Hink, Laura Van Weeren, Theodorus WJ Gadella, and Antoine Royant. Structure-guided evolution of cyan fluorescent proteins towards a quantum yield of 93%. Nature communications, 3(1):1–9, 2012. 72

[85] Te-Tuan Yang, Linzhao Cheng, and Steven R Kain. Optimized codon usage and chromophore mutations provide enhanced sensitivity with the green fluorescent protein. Nucleic acids research, 24(22):4592–4593, 1996. 72

[86] Karen S Sarkisyan, Alexander S Goryashchenko, Peter V Lidsky, Dmitry A Gorbachev, Nina G Bozhanova, Andrey Yu Gorokhovatsky, Alina R Pereverzeva, Alina P Ryumina, Victoria V Zherdeva, Alexander P Savitsky, et al. Green fluorescent protein with anionic tryptophan-based chromophore and long fluorescence lifetime. Biophysical journal, 109(2):380–389, 2015. 72

[87] Nathan C Shaner, Robert E Campbell, Paul A Steinbach, Ben NG Giepmans, Amy E Palmer, and Roger Y Tsien. Improved monomeric red, orange and yellow fluorescent proteins derived from discosoma sp. red fluorescent protein. Nature biotechnology, 22(12):1567–1572, 2004. 72

[88] Ekaterina M Merzlyak, Joachim Goedhart, Dmitry Shcherbo, Mariya E Bulina, Aleksandr S Shcheglov, Arkady F Fradkov, Anna Gaintzeva, Konstantin A Lukyanov, Sergey Lukyanov, Theodorus WJ Gadella, et al. Bright monomeric red fluorescent protein with an extended fluorescence lifetime. Nature methods, 4(7):555–557, 2007. 72

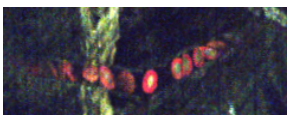

[89] Mengran Wang, Minsu Kim, Fei Xia, and Chris Xu. Impact of the emission wavelengths on in vivo multiphoton imaging of mouse brains. Biomedical optics express, 10(4):1905–1918, 2019. 74

[90] William P Dempsey, Lada Georgieva, Patrick M Helbling, Ali Y Sonay, Thai V Truong, Michel Haffner, and Periklis Pantazis. In vivo single-cell labeling by confined primed conversion. Nature methods, 12(7):645–648, 2015. 77

[91] Kathryn S McClelland, Ee Ting Ng, and Josephine Bowles. Agarose/gelatin immobilisation of tissues or embryo segments for orientated paraffin embedding and sectioning. Differentiation, 91(4-5):68–71, 2016. 80

[92] Amanda J Bares, Menansili A Mejooli, Mitchell A Pender, Scott A Leddon, Steven Tilley, Karen Lin, Jingyuan Dong, Minsoo Kim, Deborah J Fowell, Nozomi Nishimura, et al. Hyperspectral multiphoton microscopy for in vivo visualization of multiple, spectrally overlapped fluorescent labels. Optica, 7(11):1587–1601, 2020. 84

[93] Junyoung Seo, Yeonbo Sim, Jeewon Kim, Hyunwoo Kim, In Cho, Young-Gyu Yoon, and Jae-Byum Chang. Picasso: Ultra-multiplexed fluorescence imaging of biomolecules through single-round imaging and blind source unmixing. bioRxiv, 2021. 84

[94] Steven L Jacques. Optical properties of biological tissues: a review. Physics in Medicine and Biology, 58(11):R37–R61, may 2013. 86

[95] Gerard J. Tortora and Sandra Reynolds Grabowski. Introduction to the human body: the essentials of anatomy and physiology. J. Wiley & Sons, 6th ed edition, 2004. 87

[96] Handbook of Metalloproteins. John Wiley & Sons, Ltd, Apr 2006. 87

[97] Hui Chen, Masao Ikeda-Saito, and Sason Shaik. Nature of the fe- o2 bonding in oxy-myoglobin: effect of the protein. Journal of the American Chemical Society, 130(44):14778–14790, 2008. 88

[98] J.L. Soret. Analyse spectrale: sur le spectre d'absorption du sang dans la partie violette et ultra-violette. Comptes rendus hebdomadaires des séances de l'Académie des sciences - publiés... par MM. les secrétaires perpétuels, 97:1269–1273, Dec 1883. 88

[99] Marco Ferrari and Valentina Quaresima. A brief review on the history of human functional near-infrared spectroscopy (fnirs) development and fields of application. Neuroimage, 63(2):921–935, 2012. 88

[100] Cristina Udina, Stella Avtzi, Turgut Durduran, Roee Holtzer, Andrea L Rosso, Carmina Castellano-Tejedor, Laura-Monica Perez, Luis Soto-Bagaria, and Marco Inzitari. Functional near-infrared spectroscopy to study cerebral hemodynamics in older adults during cognitive and motor tasks: a review. Frontiers in aging neuroscience, 11:367, 2020. 88

[101] Sandra Grillitsch, Nikolaus Medgyesy, Thorsten Schwerte, and Bernd Pelster. The influence of environmental p o2 on hemoglobin oxygen saturation in developing zebrafish danio rerio. Journal of experimental biology, 208(2):309–316, 2005. 88, 126

[102] Bernd Pelster and Warren W Burggren. Disruption of hemoglobin oxygen transport does not impact oxygen-dependent physiological processes in developing embryos of zebra fish (danio rerio). Circulation research, 79(2):358–362, 1996. 89

[103] Tatiana V Esipova, Alexander Karagodov, Joann Miller, David F Wilson, Theresa M Busch, and Sergei A Vinogradov. Two new 'protected' oxyphors for biological oximetry: properties and application in tumor imaging. Analytical chemistry, 83(22):8756–8765, 2011. 89

[104] Shih-Hao Huang, Chu-Hung Yu, and Yi-Lung Chien. Light-addressable measurement of in vivo tissue oxygenation in an unanesthetized zebrafish embryo via phase-based phosphorescence lifetime detection. Sensors, 15(4):8146–8162, 2015. 89, 126, 128

[105] Arnold D Estrada, Adrien Ponticorvo, Tim N Ford, and Andrew K Dunn. Microvascular oxygen quantification using two-photon microscopy. Optics letters, 33(10):1038–1040, 2008. 89

[106] Sava Sakadžić, Emmanuel Roussakis, Mohammad A Yaseen, Emiri T Mandeville, Vivek J Srinivasan, Ken Arai, Svetlana Ruvinskaya, Anna Devor, Eng H Lo, Sergei A Vinogradov, et al. Two-photon high-resolution measurement of partial pressure of oxygen in cerebral vasculature and tissue. Nature methods, 7(9):755–759, 2010. 89

[107] Tatiana V Esipova, Matthew JP Barrett, Eva Erlebach, Artëm E Masunov, Bruno Weber, and Sergei A Vinogradov. Oxyphor 2p: a high-performance probe for deep-tissue longitudinal oxygen imaging. Cell Metabolism, 29(3):736–744, 2019. 89

[108] Qingguang Zhang, Morgane Roche, Kyle W Gheres, Emmanuelle Chaigneau, Ravi T Kedarasetti, William D Haselden, Serge Charpak, and Patrick J Drew. Cerebral oxygenation during locomotion is modulated by respiration. Nature communications, 10(1):1–15, 2019. 89

[109] Rebecca M Williams, Warren R Zipfel, and Watt W Webb. Interpreting second-harmonic generation images of collagen i fibrils. Biophysical journal, 88(2):1377–1386, 2005. 90

[110] Stéphane Bancelin, Carole Aimé, Ivan Gusachenko, Laura Kowalczuk, Gaël Latour, Thibaud Coradin, and Marie-Claire Schanne-Klein. Determination of collagen fibril size via absolute measurements of second-harmonic generation signals. Nature communications, 5(1):1–8, 2014. 90

[111] Shih-Peng Tai, Tsung-Han Tsai, Wen-Jeng Lee, Dar-Bin Shieh, Yi-Hua Liao, Hsin-Yi Huang, Kenneth Y-J Zhang, Hsiang-Lin Liu, and Chi-Kuang Sun. Optical biopsy of fixed human skin with backward-collected optical harmonics signals. Optics express, 13(20):8231–8242, 2005. 90

[112] Alvin T Yeh, Nader Nassif, Aikaterini Zoumi, and Bruce J Tromberg. Selective corneal imaging using combined second-harmonic generation and two-photon excited fluorescence. Optics letters, 27(23):2082–2084, 2002. 90

[113] Sergey V Plotnikov, Andrew C Millard, Paul J Campagnola, and William A Mohler. Characterization of the myosin-based source for second-harmonic generation from muscle sarcomeres. Biophysical journal, 90(2):693–703, 2006. 90

[114] William Mohler, Andrew C Millard, and Paul J Campagnola. Second harmonic generation imaging of endogenous structural proteins. Methods, 29(1):97–109, 2003. 90

[115] Delphine Débarre, Willy Supatto, Ana-Maria Pena, Aurélie Fabre, Thierry Tordjmann, Laurent Combettes, Marie-Claire Schanne-Klein, and Emmanuel Beaurepaire. Imaging lipid bodies in cells and tissues using third-harmonic generation microscopy. Nature methods, 3(1):47–53, 2006. 90, 94

[116] Shi-Wei Chu, Szu-Yu Chen, Tsung-Han Tsai, Tzu-Ming Liu, Cheng-Yung Lin, Huai-Jen Tsai, and Chi-Kuang Sun. In vivo developmental biology study using noninvasive multi-harmonic generation microscopy. Optics express, 11(23):3093–3099, 2003. 90

[117] Chi-Kuang Sun, Shi-Wei Chu, Szu-Yu Chen, Tsung-Han Tsai, Tzu-Ming Liu, Chung-Yung Lin, and Huai-Jen Tsai. Higher harmonic generation microscopy for developmental biology. Journal of structural biology, 147(1):19–30, 2004. 90

[118] Conor L Evans, Xiaoyin Xu, Santosh Kesari, X Sunney Xie, Stephen TC Wong, and Geoffrey S Young. Chemically-selective imaging of brain structures with cars microscopy. Optics express, 15(19):12076–12087, 2007. 90

[119] Joséphine Morizet. Microscopie par génération de troisième harmonique résolue en polarisation pour l'imagerie de la myéline et des biocristaux. PhD thesis, Institut polytechnique de Paris, 2020. 93

[120] Nicolas Olivier, Delphine Débarre, and Emmanuel Beaurepaire. THG microscopy of cells and tissues: contrast mechanisms and applications. In Francesco S . Pavone and Paul J . Campagnola, editors, Second Harmonic Generation Imaging, pages 51–80. Taylor & Francis, 2013. 94

[121] Ji-Xin Cheng and X Sunney Xie. Green's function formulation for third-harmonic generation microscopy. JOSA B, 19(7):1604–1610, 2002. 94

[122] Delphine Débarre, Nicolas Olivier, and Emmanuel Beaurepaire. Signal epidetection in third-harmonic generation microscopy of turbid media. Optics express, 15(14):8913–8924, 2007. 94

[123] Matthew J Farrar, Frank W Wise, Joseph R Fetcho, and Chris B Schaffer. In vivo imaging of myelin in the vertebrate central nervous system using third harmonic generation microscopy. Biophysical journal, 100(5):1362–1371, 2011. 94

[124] Andrew C Millard, Paul W Wiseman, David N Fittinghoff, Kent R Wilson, Jeffrey A Squier, and Michiel Müller. Third-harmonic generation microscopy by use of a

compact, femtosecond fiber laser source. Applied optics, 38(36):7393–7397, 1999. 94

[125] Che-Hang Yu, Shih-Peng Tai, Chun-Ta Kung, Wen-Jeng Lee, Yi-Fan Chan, Hsiang-Lin Liu, Jiun-Yi Lyu, and Chi-Kuang Sun. Molecular third-harmonic-generation microscopy through resonance enhancement with absorbing dye. Optics letters, 33(4):387–389, 2008. 95

[126] Jonathan M Bélisle, Santiago Costantino, Mara L Leimanis, Marie-Josée Bellemare, D Scott Bohle, Elias Georges, and Paul W Wiseman. Sensitive detection of malaria infection by third harmonic generation imaging. Biophysical journal, 94(4):L26–L28, 2008. 95

[127] Richard D Schaller, Justin C Johnson, and Richard J Saykally. Nonlinear chemical imaging microscopy: near-field third harmonic generation imaging of human red blood cells. Analytical chemistry, 72(21):5361–5364, 2000. 95

[128] G Omar Clay, Andrew C Millard, Chris B Schaffer, Juerg Aus-der Au, Philbert S Tsai, Jeffrey A Squier, and David Kleinfeld. Spectroscopy of third-harmonic generation: evidence for resonances in model compounds and ligated hemoglobin. JOSA B, 23(5):932–950, 2006. 95

[129] Chieh-Feng Chang, Che-Hang Yu, and Chi-Kuang Sun. Multi-photon resonance enhancement of third harmonic generation in human oxyhemoglobin and deoxyhemoglobin. Journal of biophotonics, 3(10-11):678–685, 2010. 95, 96, 114

[130] Hiroki Segawa, Masanari Okuno, Hideaki Kano, Philippe Leproux, Vincent Couderc, and Hiro-o Hamaguchi. Label-free tetra-modal molecular imaging of living cells with cars, shg, thg and tsfg (coherent anti-stokes raman scattering, second harmonic generation, third harmonic generation and third-order sum frequency generation). Optics express, 20(9):9551–9557, 2012. 97

[131] Hiroki Segawa, Naoki Fukutake, Philippe Leproux, Vincent Couderc, Takeaki Ozawa, and Hideaki Kano. Electronically resonant third-order sum frequency generation spectroscopy using a nanosecond white-light supercontinuum. Optics express, 22(9):10416–10429, 2014. 97

[132] Adam M Hanninen, Richard C Prince, and Eric O Potma. Triple modal coherent nonlinear imaging with vibrational contrast. IEEE Journal of Selected Topics in Quantum Electronics, 25(1):1–11, 2018. 97

[133] Adam M Hanninen, Richard C Prince, Raul Ramos, Maksim V Plikus, and Eric O Potma. High-resolution infrared imaging of biological samples with third-order sum-frequency generation microscopy. Biomedical optics express, 9(10):4807–4817, 2018. 97

[134] Gabriel Campargue, Luca La Volpe, Gabriel Giardina, Geoffrey Gaulier, Fiorella Lucarini, Ivan Gautschi, Ronan Le Dantec, Davide Staedler, Dario Diviani, Yannick Mugnier, et al. Multiorder nonlinear mixing in metal oxide nanoparticles. Nano Letters, 20(12):8725–8732, 2020. 98

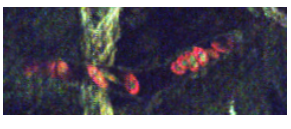

[135] Pierre Mahou, Guy Malkinson, Élodie Chaudan, Thierry Gacoin, Emmanuel Beaurepaire, and Willy Supatto. Metrology of multiphoton microscopes using second harmonic generation nanoprobes. Small, 13(42):1701442, 2017. 109

[136] Gabriela L. Pedroso, Thais O. Hammes, Thayssa D.C. Escobar, Laisa B. Fracasso, Luiz Felipe Forgiarini, and Themis R. da Silveira. Blood collection for biochemical analysis in adult zebrafish. Journal of Visualized Experiments, (63):3865, May 2012. 115

[137] Stéphane Egee. Mise en évidence des voies de conductance dans les érythrocytes nucléés de poissons (Oncorhynchus mykiss) : implication dans la régulation du volume cellulaire. Thèses, Université de Bretagne Occidentale, December 1998. 115

[138] Richard Mark White, Anna Sessa, Christopher Burke, Teresa Bowman, Jocelyn LeBlanc, Craig Ceol, Caitlin Bourque, Michael Dovey, Wolfram Goessling, Caroline Erter Burns, et al. Transparent adult zebrafish as a tool for in vivo transplantation analysis. Cell stem cell, 2(2):183–189, 2008. 119

[139] Sumio Isogai, Masaharu Horiguchi, and Bant M. Weinstein. The vascular anatomy of the developing zebrafish: An atlas of embryonic and early larval development. Developmental Biology, 230(2):278–301, Feb 2001. 120

[140] David Traver, Barry H Paw, Kenneth D Poss, W Todd Penberthy, Shuo Lin, and Leonard I Zon. Transplantation and in vivo imaging of multilineage engraftment in zebrafish bloodless mutants. Nature immunology, 4(12):1238–1246, 2003. 122

[141] Johnny Karlsson, Jonas von Hofsten, and Per-Erik Olsson. Generating transparent zebrafish: a refined method to improve detection of gene expression during embryonic development. Marine biotechnology, 3(6):522–527, 2001. 123

[142] David W Staudt, Jiandong Liu, Kurt S Thorn, Nico Stuurman, Michael Liebling, and Didier YR Stainier. High-resolution imaging of cardiomyocyte behavior reveals two distinct steps in ventricular trabeculation. Development, 141(3):585–593, 2014. 126

[143] Dawnis M Chow, David Sinefeld, Kristine E Kolkman, Dimitre G Ouzounov, Najva Akbari, Rose Tatarsky, Andrew Bass, Chris Xu, and Joseph R Fetcho. Deep three-photon imaging of the brain in intact adult zebrafish. Nature methods, 17(6):605–608, 2020. 139

[144] Dimitre G Ouzounov, Tianyu Wang, Chunyan Wu, and Chris Xu. Gcamp6 δf/f dependence on the excitation wavelength in 3-photon and 2-photon microscopy of mouse brain activity. Biomedical optics express, 10(7):3343–3352, 2019. 140

[145] Sung Ji Ahn, Nancy E Ruiz-Uribe, Baoqiang Li, Jason Porter, Sava Sakadzic, and Chris B Schaffer. Label-free assessment of hemodynamics in individual cortical brain vessels using third harmonic generation microscopy. Biomedical Optics Express, 11(5):2665–2678, 2020. 140

[146] Hongji Liu, Xinlin Chen, Xiangquan Deng, Ziwei Zhuang, Shen Tong, Weixin Xie, Jia Li, Ping Qiu, and Ke Wang. In vivo deep-brain blood flow speed measurement through third-harmonic generation imaging excited at the 1700-nm window. Biomedical Optics Express, 11(5):2738–2744, 2020. 140

ECOLE DOCTORALE

Titre : Microscopie à trois photons : instrumentation et extension des paramètres observables
Mots clés : Microscopie multiphoton, Microscopie à trois photons, Microscopie THG, Optique non linéaire, Imagerie biologique, cerveau de souris, poisson-zèbre

Résumé : La microscopie multiphotonique est la technique de référence pour l'imagerie de fluorescence des tissus intacts. Il a récemment été démontré que la microscopie à trois photons (3P) offre un contraste supérieur à l'imagerie à deux photons (2P) à grande profondeur dans les milieux diffusants densément marqués. Cet avantage est dû au meilleur confinement de l'excitation 3P et à la diffusion réduite aux longueurs d'onde utilisées. Bien que cette approche prometteuse ait permis d'atteindre des profondeurs d'imagerie supérieures au millimètre dans le cerveau de souris, elle n'est pas encore complètement stabilisée technologiquement, et manque de modalités d'imagerie multicolore. Dans ce travail, nous explorons l'extension du nombre de signaux et de paramètres qui peuvent être utilisés en microscopie 3P des tissus profonds. Dans un premier chapitre, nous introduisons les concepts impliqués dans la microscopie 3P et nous analysons les paramètres limitant la profondeur d'imagerie. Dans un second chapitre, nous décrivons la construction et l'optimisation d'un microscope 3P utilisant une nouvelle génération d'amplificateurs paramétriques optiques (OPA) multifaisceaux adaptés à l'excitation 3P dans la gamme proche infrarouge. Nous discutons notamment les questions liées à la stabilité de la source, la compensation de la dispersion et la combinaison des faisceaux dans le microscope. Dans les deux derniers chapitres, nous présentons les résultats de deux projets visant à étendre les signaux utilisables dans un système 3P. Dans le troisième chapitre, nous explorons l'efficacité de l'excitation 3P à 1030 nm de plusieurs protéines fluorescentes (FPs) bleues, afin de compléter les études précédentes rapportant l'excitation 3P des FPs vertes et rouges, respectivement à 1300 et 1700 nm. Nous identifions des FPs bleues présentant une efficacité d'excitation et produisant un niveau de signal comparable aux protéines vertes et rouges. Ces résultats encourageants ouvrent des perspectives pour la microscopie 3P en couleur. Dans le quatrième chapitre, nous explorons la possibilité d'une imagerie cohérente multicolore basée sur la génération de somme de fréquences du troisième ordre. Nous montrons que cette nouvelle modalité de contraste sans marquage révèle les vaisseaux sanguins avec une possibilité d'imagerie fonctionnelle, et qu'elle peut être directement intégrée sur un microscope 3P. Globalement, le travail décrit dans cette thèse étend le nombre de signaux qui peuvent être sondés en microscopie en profondeur des tissus diffusants.

Title : Three-photon microscopy: instrumentation and extension of the observable parameters
Keywords : Multiphoton microscopy, Three-photon microscopy, THG microscopy, Nonlinear optics, Biological imaging, mouse brain, zebrafish

Abstract : Multiphoton microscopy is the reference technique for fluorescence imaging of intact tissues. Three-photon (3P) microscopy was recently demonstrated as providing superior contrast than two-photon (2P) imaging at large depths in densely labelled scattering media. This advantage is due to the superior confinement of the 3P excitation and the reduced scattering experienced at longer wavelengths. Although this promising approach has made it possible to reach imaging depths beyond one millimetre in the mouse brain, it is not yet fully mature technologically and lacks efficient multicolor imaging modalities. In this work, we explore the extension of the number of signals and parameters that can be used in deep-tissue 3P microscopy. In a first chapter, we introduce the concepts underlying 3P microscopy and we analyse the parameters limiting imaging depth. In a second chapter, we describe the construction and optimization of a 3P microscope based on a new generation of multibeam optical parametric amplifier (OPA) source adapted for 3P excitation in the short-wavelength infrared range. We pay particular attention to source stability, dispersion compensation, and beam combination in the microscope. In the two remaining chapters, we present the results of two projects aiming at extending the signals usable in a 3P system. In the third chapter, we explore the 3P excitation efficiency of several blue fluorescent proteins (FPs) with 1030 nm light, in order to complement previous studies reporting 3P excitation of green and red FPs at 1300 and 1700 nm, respectively. We identify efficiently excited blue FPs producing signal levels comparable to green and red proteins. These encouraging results open perspectives for multicolor 3P microscopy. In the fourth chapter, we explore the possibility of multicolor coherent imaging based on third-order sum-frequency generation. We show that this new contrast modality provides label-free contrast highlighting blood vessels with a possibility of functional imaging, and that it can be directly integrated on a 3P microscope. Overall, the work described in this thesis extends the number of signals that can be probed in deep-tissue microscopy.

Institut Polytechnique de Paris 91120 Palaiseau, France